Computational modelling of the effect of surfaces on polyvinyldenedifluoride

Francesco Pelizza

Department of Chemical and Process Engineering
University of Strathclyde

This dissertation is submitted for the degree of
Doctor of Philosophy

September 2018

I would like to dedicate this thesis to my lovely parents for being near to me at any step of my life, supporting me and giving all the resources they could. Giving me much more than what I have asked and deserved, they taught me how love, union, dedication and faith in your family is such an important matter of life that nothing else should take priority over this. At least I hope to have them rewarded with the perseverance and passion I put in my life challenges.

Declaration

I hereby declare that except where specific reference is made to the work of others, the contents of this dissertation are original and have not been submitted in whole or in part for consideration for any other degree or qualification in this, or any other university. This dissertation is my own work and contains nothing which is the outcome of work done in collaboration with others, except as specified in the text and Acknowledgements. This dissertation contains fewer than 65,000 words including appendices, bibliography, footnotes, tables and equations and has fewer than 150 figures.

Francesco Pelizza
September 2018

Acknowledgements

I would like to acknowledge all the people of my research group with who I shared many interesting scientific opinions. Mostly, my supervisor Dr. Karen Johnston that put a lot of dedication and punctuality in following me in my PhD project, teaching, advising and reviewing my work.

Strong acknowledgements goes to Dr. Demostenes Kivotides for being a friend, a mentor and eclectic person to talk to along my PhD esperience, for sharing resources and scientific passion with me. Special acknowledgements goes to Dr. Leo Lue and Dr. Ashleigh Fletcher for all the support, patience, professionalism and good sense they applied to support me many times. I owe my thanks also to other departmental staff such as Dr. Miguel Jorge, Dr. Esther Medina-Ventura and Dr. Paul Mulheran.

I finally acknowledge my dearest and nearest friends Ivan Alejandro Principe and Andrea Tasca for making my life in Glasgow more happy and coloured for the feelings, passions and moments shared, especially, the amazing summer of 2016. I also thanks Maryam Derkani, Dr. Javier Cardona, Calum Williams, Fraser Baigent and all the other PhD students of the Chemical and Process Engineering department.

Abstract

The physical properties of polyvinyldenedifluoride (PVDF) polymorphs and the effect of surfaces on PVDF properties have been investigated with computational modelling to address crystallinity issues that such semi-crystalline polymer presents. Indeed, PVDF has the potential to support new technology generation of flexible electronic devices, but to prepare reliable devices made with PVDF, such polymer needs to be sampled at high crystalline grade. As PVDF is a semi-crystalline polymer its intrinsic flexibility represents a major advantage for flexible electronics which also increases manufacturing complexity of such material. To understand the crystalline behaviour of PVDF it is necessary to computationally investigate its fundamental physical properties per each of its crystal phase and the main behaviour of PVDF in conditions of finite temperature.

Density functional theory (DFT) calculations has been used as a quantum mechanical (QM) tool to solve the electronic structures of PVDF polymorphs obtaining structural information such as geometries, energetics, spontaneous polarisation and vibrational frequencies. Furthermore the impact of including van der Waals (vdW) forces in DFT was evaluated showing that the vdW-DF DFT functional had the best physical properties prediction agreement with experimental observations. The vibrational frequencies of all PVDF polymorphs were computationally determined to verify the metastability of every crystal phase determined in the present study. Furthermore, the vibrational frequencies determination allowed to enrich the knowledge about adsorption peaks that each PVDF structure possesses to ease the computation to experimental IR spectra comparison.

The optimised geometries of PVDF crystals obtained from the DFT investigation have been scaled to molecular dynamics (MD) since it represents a time consistent methodology to follow the evolution of molecular interactions between particles. The interest was to compute the finite temperature dynamics, ensuring the use of the best performing force field and to gather new knowledge about the crystalline phase formation of PVDF liquid melts under different conditions such as bulk and confined between surface layers. The effect of polymer confinement and surface/polymer electrostatics interaction were evaluated in such study showing that electrostatics played a main role in driving the formation of highly crystalline PVDF systems.

Table of contents

List of figures xv

List of tables xxv

1 Introduction 5
- 1.1 Fields of application of flexible ferroelectric devices . . . 5
- 1.2 Ferroelectricity . . . 6
- 1.3 FE materials . . . 8
- 1.4 Ferroelectric polymers . . . 9
- 1.5 Aims . . . 10
- 1.6 Thesis structure . . . 11

2 Literature review 13
- 2.1 Crystallinity and ferroelectric properties of PVDF . . . 13
  - 2.1.1 Crystal phases . . . 15
- 2.2 Polymorphs identification . . . 21
- 2.3 Crystallinity control . . . 23
  - 2.3.1 Mechanical stretching . . . 24
  - 2.3.2 Poling . . . 26
  - 2.3.3 Solvent effects . . . 27
  - 2.3.4 Spin coating, thermal annealing and shear stress . . . 28
- 2.4 Additives effects on PVDF . . . 29
  - 2.4.1 Ionic molecules as additives to PVDF solutions . . . 29
  - 2.4.2 Nanoclays, zeolites and perovskites as additives . . . 31
  - 2.4.3 Silicon nanoparticles as additives . . . 34
  - 2.4.4 Palladium Chloride nanoparticles as additives . . . 35
- 2.5 PVDF on surfaces . . . 39
  - 2.5.1 Evaporated oligomers on glass substrates . . . 43

2.6 PVDF computational studies . . . 44
- 2.6.1 Crystal structures . . . 45
- 2.6.2 Crystal properties . . . 45
- 2.6.3 Phase transformation mechanisms . . . 46
- 2.6.4 Solid and liquid bulk properties . . . 47
- 2.6.5 Surface studies . . . 48

2.7 Summary . . . 48
2.8 Objectives . . . 49

3 Methodology 51

3.1 Density functional theory . . . 52
- 3.1.1 Born-Openheimer approximation, core particles as pseudopotentials, Bloch's theorem and unit cell . . . 53
- 3.1.2 The Kohn-Sham equation . . . 56
- 3.1.3 The Exchange-Correlation functional . . . 58
- 3.1.4 Reciprocal lattice, k-point sampling and energy cutoff . . . 60
- 3.1.5 The Brillouin zone, gamma point and bands structure . . . 62

3.2 The Berry's geometry polarisation phase theory . . . 63
3.3 Vibrational frequencies . . . 65
3.4 Quantum ESPRESSO . . . 68
- 3.4.1 Methods applied to DFT calculations . . . 68

3.5 Molecular dynamics . . . 70
- 3.5.1 Molecular dynamics general settings . . . 71
- 3.5.2 Force field definition . . . 72

3.6 Literature force fields . . . 74
- 3.6.1 MSXX . . . 74
- 3.6.2 Byutner and Smith . . . 77
- 3.6.3 OPLS . . . 77

3.7 Molecular dynamics data analysis techniques . . . 79

4 DFT study of bulk crystalline PVDF 85

4.1 Lattice structures . . . 86
4.2 Cohesive energies . . . 95
4.3 Phase energies . . . 96
4.4 Spontaneous polarisation . . . 98
4.5 Electronic structures . . . 102
4.6 Vibrational frequencies . . . 106

4.6.1 Vibrational frequencies of the β-phase 107
4.6.2 Vibrational frequencies of the ζ-phase 110
4.6.3 Vibrational frequencies of the α-phase 112
4.6.4 Vibrational frequencies of the δ-phase 114
4.6.5 Vibrational frequencies of the γ-phase 115
4.6.6 Vibrational frequencies of the ε-phase 119
4.7 Summary 119

5 Force fields performance on bulk PVDF 121
5.1 Crystal structures & energetics 122
5.1.1 Crystal structures 123
5.1.2 Cohesive and relative crystal energies 124
5.2 Liquid phase properties 127
5.2.1 Equilibration procedure 129
5.2.2 Physical properties distribution of PVDF liquid bulk 138
5.3 Summary 140

6 Surface study of PVDF oligomers 143
6.1 Surface model 143
6.2 Surface nanoconfinement effect on β-phase formation with uncharged graphene 146
6.3 Surface electrostatics effects on β-phase formation 150
6.4 Summary 161

7 Conclusions 165
7.1 Future work 168

References 171

Appendix A Plots, Tables and Figures 183
A.1 Convergence tests 183
A.2 Table of conversions and calculations 185
A.3 DFT additional data 186
A.3.1 Partial DOS using the PBE functional 186
A.3.2 Electronic structures performed with vdW-DF 190
A.3.3 Correlation Plots 195
A.3.4 Vibrational frequencies of the ε_{uu} and ε_{ud} crystals 197
A.4 Additional data of the liquid bulk equilibration phase 201
A.5 Additional data of the two graphene sheets surface model MD dynamics . . 207

Appendix B Papers published, due to submission and future publications 209
B.1 Publications of chapter 4 . . . 209
B.1.1 PVDF crystal structure study of α, δ and β phases using first principle vdW (published) . . . 209
B.1.2 PVDF crystal structure study of γ, ε and ζ crystals using first principle vdW (submitted) . . . 220
B.1.3 Vibrational frequencies of PVDF polymorphs (future publication) . 235
B.2 Publication of chapter 5 (future publication) . . . 235
B.3 Publication of chapter 6 (future publication) . . . 235

List of figures

1.1 Schematic diagram of a general hysteresis response of a ferroelectric material and all the properties the diagram can provide. B: Polarisation (μC cm^{-2}); H: Electric field (MV/m^{-2}); a: Starting neutral steady state where the medium has never been polarised or trespassed the Curie temperature; b/e: Maximum values of saturation of the dipole (μC cm^{-2}); c/f: Remnant polarisation after the applied electric potential vanished (μC cm^{-2}); d/g: Critical Coercive Field (MV/m^{-2}) able to induce a dipole inversion. 7

1.2 Sketch of the ferroelectric $BaTiO_3$ perovskites crytal unit where the dipole reorients with a small Ti displacement of ≈0.05Å. Ba: light blue; O: dark red; Ti: grey. 8

1.3 Sketch of a PVDF ferroelectric crystal phase where at the chain dipole inversion correspond an entire chain flip of ≈2.5Å. In here, the two chains showed has to be intended as one chain drawn in both ferroelectric configurations. F: light grey; C: yellow; H: light blue. 9

2.1 Left: Schematic spherulite aggregation model of non-FE α-PVDF lamellae structures with chains fractions falling into disordered amorphous regions taken from Broadhurst[1] *et al*; Right: Atomic Force Microscopy of a PVDF spin cast and rapidly annealed on a coated gold surface taken from Kang[2] *et al*. 14

2.2 The three backbone chains conformations of PVDF as full trans T (a), TG^+TG^- (b) and $T_3G^+T_3G^-$ (c). F: light grey; C: yellow; H: light blue. . . 15

2.3 A generic view of β-PVDF. a: front view including the crystal unit box; b: side view of one chain backbone trans bonds T; c: top view of the chains of the crystal unit box. F: light grey; C: yellow; H: light blue. 17

2.4 A generic view of α-PVDF. a: front view including the crystal unit box; b: top view of two chains backbone trans bonds TG^+TG^-. F: light grey; C: yellow; H: light blue. 18

2.5 A generic view of δ-PVDF. a: front view including the crystal unit box; b: top view of two chains backbone trans bonds $TG^{+}TG^{-}$. F: light grey; C: yellow; H: light blue. 19

2.6 A generic view of γ_{uu}-PVDF. a: front view including the crystal unit box; b: top view of two chains backbone trans bonds $T_3G^{+}T_3G^{-}$. F: light grey; C: yellow; H: light blue. 19

2.7 A generic view of γ_{ud}-PVDF. a: front view including the crystal unit box; b: top view of two chains backbone trans bonds $T_3G^{+}T_3G^{-}$. F: light grey; C: yellow; H: light blue. 20

2.8 A generic view of ε_{uu}-PVDF. a: front view including the crystal unit box; b: top view of two chains backbone trans bonds $T_3G^{+}T_3G^{-}$. F: light grey; C: yellow; H: light blue. 21

2.9 A generic view of ε_{ud}-PVDF. a: front view including the crystal unit box; b: top view of two chains backbone trans bonds $T_3G^{+}T_3G^{-}$. F: light grey; C: yellow; H: light blue. 21

2.10 FTIR spectra of a raw PVDF sample. Taken from Cai *et al*[3]. 22

2.11 Percentage of crystalline β-phase increase as function of Stretch ratio of a prepared thin film at different stretching speeds at room temperature. a: 0.18 cm min^{-1}; b: 0.6 cm min^{-1}; c: 1.02 cm min^{-1}; d: 2.04 cm min^{-1}. Taken from Caihong *et al*[4]. 26

2.12 Sample of PVDF/$BaTiO_3$ mixture rich in spherulite domains containing $BaTiO_3$ ceramic particles of average size of 500 nm. Taken from Mendes *et al*[5]. 33

2.13 FE-SEM images of (a) neat PVDF and (b) PdCl-NP-doped PVDF thin films. AFM topographic images (scan area 6 μm × 6 μm) of (c) neat PVDF and (d) corresponding line (roughness height at three different intersecting lines) profiles and (e) a PdCl-NP-doped PVDF thin film and (f) the corresponding line (roughness height at three different intersecting lines) profile. Taken from Mandal *et al*[6]. 36

2.14 DC-EFM images ((a, b) amplitude, (c, d) phase) of neat PVDF (left panel) and PdCl-NP-doped PVDF (right panel) thin films. Scan area: 6 μm × 6 μm. The corresponding line (marked with red lines) profiles are shown at the bottom (a, b) and in the middle (c, d) of the each image. (Bottom of c and d) Schematic illustrations of the orientation of the dipoles (cross-sectional view) along the marked lines shown in the DC-EFM images. Taken from Mandal *et al*[6]. 37

2.15 Schematic representation of the electrostatic interaction between the surface charges of nanoparticles and the CH_2/CF_2 dipoles of PVDF. Taken from Mandal *et al*[6]. 38
2.16 Schematic sketch to make visible the β-PVDF chains orientation. Taken from Cauda *et al*[7]. 40
2.17 SEM images of 3 wt % PVDF-TrFE on (a) SiO 2 and (b) CVD-graphene substrates thermally annealed at 200 °C for 30 min. The inset presented a schematic of the sample structures. Taken from Kang *et al*[8]. 41
2.18 (a) Grazing incidence reflection absorption (GIRAS) FTIR of the the inset of (b) displays a magnified image with the characteristic needlelike β crystals. (c) AFM images of a PVDF film spin cast and rapidly annealed on COOH-terminated SAMs treated Au substrate. AFM (d) and OM image show micropatterned β and α PVDF crystals. Taken from Kang *et al*[2]. 42
2.19 Schematic sketch of the ferroelectric device assembly. Pt/Co: Platinum Cobalt bottom electrode; VDF: VDF olygomers; Al: Aluminium top electrode; glass: glass support of the chip. Taken from Foreman *et al*[9]. 44
2.20 Left: Pyroelectric current of a dynamic heating of the chip sample showing the paraelectric phase transition at 75°C. Taken from Foreman *et al*[9] Right: XRD data for the as-grown VDF oligomer thin film. Taken from Foreman *et al*[9]. 44

3.1 Conceptualisation of a many body system seen in the DFT formalisms as the functional of the energy density of the system. Sketch inspired from [10]. . . 53
3.2 Graphical representation of a unit cell with a, b and c are the lattice vector and α, β and γ are the angles between the lattice vectors. Sketch made from Ashcroft's book [11]. 55
3.3 Typical self-consistent iterator to solve the KS equation. Taken from [10]. . . 57
3.4 Energy profile of van der Waals forces estimation as function of space comparing three different functionals such as PBE, vdW-DF and vdW-DF2 taken from Giannozzi[12]. 60
3.5 Left: Face Centred Cubic brillouin zone and k-path taken from Setyawan[13]. Right: Bands structures of the FCC gold geometry taken from Setyawan[13]. 62
3.6 Positive an negative charges coupling of many unit cells repeated in space. Taken from Martin[14]. 63

3.7 Left: Experimental measurement of the spontaneous polarisation of a medium. Right: Hysteresis loop retrievable from the experimental measurement of P which correspond to the double of the real P magnitude of the solid. Taken from Martin[14]. 64
3.8 Harmonic oscillator sketch. Taken from Ziman[15]. 67
3.9 Left: The van der Waals energy interaction contribution of non bonded particles as function of space. Taken from Martin [14]. Right: The Coulomb energy interaction contribution of non bonded particles as function of space. Taken from Martin [14]. 73
3.10 Schematic sketch of R_g (s) and R_e (r) identification. Taken from Rapaport[16]. 80
3.11 Dihedral distribution sketch of a polyisobutylene chain. Taken from Hari[17]. 81

4.1 A generic view of ζ-PVDF. a: front view including the crystal unit box; b: side view of one chain backbone trans bonds T; c: top view of the chains of the crystal unit box. F: light grey; C: yellow; H: light blue. 89
4.2 Phase energies of all PVDF polymorphs compared to literature DFT results. 98
4.3 Spontaneous Polarisation of all FE PVDF crystals predicted with the current DFT study. Volume has been normalised by the number of monomers present within each modelled crystal structure. 100
4.4 Bands structure and DOS states of β-PVDF comparing DFT and experimental results taken from Duan *et al*[18]. Duan's k-path: $\Delta(.5,\ .3,\ -.2) \rightarrow \Gamma(.0,\ .0,\ .0) \rightarrow Z(.5,\ .5,\ .0)$. Black dotted bars express the comparison of theoretical with experimental bands structure determination[19, 18] mapped into a Face-Centred Orthorombic lattice. 103
4.5 Orthorombic lattice structure and Brillouin zone of the β-phase. Taken from Setyawan *et al*[13]. 103
4.6 Bands structure and DOS states of β-PVDF predicted with the current DFT study using PBE. Red line: HOMO; Green line: LUMO. 104
4.7 Bands structure and DOS states of ζ-PVDF predicted with the current DFT study using PBE. Red line: HOMO; Green line: LUMO. 105
4.8 Bands structure and DOS states of α-PVDF predicted with the current DFT study using PBE. Red line: HOMO; Green line: LUMO. 105

5.1 Phase energy plot of all PVDF structures characterised using the three FFs and with literature comparison, the α-PVDF is the reference structure from which the zero has been set. Results are in comparison with DFT$_{vdW}$. DFT$_{vdW}$: DFT results from XC-f vdW-DF. The energy minimisation threshold was fixed to 4.18e-09 kJ mol^{-1}. 126

5.2 Cohesive energies of PVDF polymorphs per each FFs compared to DFT$_{vdW}$ results. Each backbone type (*e.g.* $T_3G^+T_3G^-$, TG^+TG^- and T) represent the relative reference from which to calculate the individual cohesive energies of each crystal phase grouped per backbone type. DFT$_{vdW}$: DFT results from XC-f vdW-DF. The energy minimisation threshold was fixed to 4.18e-09 kJ mol^{-1}. 127

5.3 Initial structure of the bulk model. A: *a*-axis; B: *b*-axis; C: *c*-axis. Green: Hydrogen; Purple, Cyan: Carbon; Pink: Fluorine. 129

5.4 Density versus time of bulk β-PDVF short chains during all heating approaches tested together with the complete liquid phase equilibration procedure using the B&S FF. High temperature annealing: constant thermal treatment to melt the chains; Cooling: cooling process to bring the system to 500 K; Fix at 500 K: steady dynamic run at the fixed temperature of 500 K; Equilibrium: Equilibrium of the liquid phase. 130

5.5 Density as function of time of bulk PDVF annealed at 800 K and cooled to to 500 K using 3 different cooling rates using the B&S FF. 132

5.6 R$_g$ as function of time of bulk PDVF annealed at 800 K and cooled to to 500 K using 3 different cooling rates using the B&S FF. 133

5.7 R$_g$ as function of time of the annealing temperatures from 500 K up to 900 K using the B&S FF. 134

5.8 Pictures of the initial melted PVDF system at 600 K using the B&S force field which has been switched after 40 ns of heating to the OPLS force field, then cooled down to 500 K in 10 ns and kept at such temperature per 30 ns. To follow the picture from the restart moment swithing B&S with OPLS until the OPLS steady state at 500 K. T0: initial zero time step of the system melted at 600 K for 40 ns with B&S restarted with OPLS (initial disorder of B&S); T1: system cooled at 580 K in 2 ns; T2: system cooled at 540 K in 6 ns; T3: system cooled at 520 K in 8 ns; T4: system constantly resting at 500 K per 15 ns; T5: final steady state after 30 ns constantly at 500 K. Green: Hydrogen; Purple, Cyan: Carbon; Pink: Fluorine. 137

5.9 Dihedrals backbone distribution of the bulk PVDF model of the annealing attempts of 500 K (solid), 800 K and 900 K (last 15 ns of annealing time) and the last 15 ns of the liquid phase equilibrated at 500 K (liquid) using the B&S FF. 139

6.1 Initial structure of the surface model. A: *a*-axis; B: *b*-axis; C: *c*-axis. Green: Hydrogen; Purple, Cyan: Carbon; Pink: Fluorine. 144
6.2 Average atoms number distribution as function of space along the *b*-axis of the liquid phase at 500 K using the B&S FF. Surface: Graphene Surface Layer; 6.4 Å: regions of space where the surface augment the atom number concentration due to surface-polymer attraction. The dashed line represents the averaged atoms distribution sum of carbon, fluorine and hydrogen atoms of the liquid phase equilibrium of the bulk model at 500 K. 146
6.3 PVDF chains averaged R_g distribution as function of space corresponding to the centre of mass of molecules calculated perpendicularly to the surface *b*-axis at 500 K using the B&S FF. The dashed line is the average R_g of the liquid bulk model at 500 K of Table 5.8. 147
6.4 PVDF chains averaged R_e distribution as function of space corresponding to the centre of mass of molecules calculated perpendicularly to the surface *b*-axis at 500 K using the B&S FF. The dashed line is the average R_e of the liquid bulk model at 500 K of Table 5.8. 148
6.5 Averaged dihedrals backbone distribution of the liquid PVDF surface model sandwiched in graphene sheets at 500 K using the B&S FF in comparison with the liquid bulk model at 500 K computed using B&S FF. 149
6.6 Snapshot of the liquid phase at 500 K of the PVDF film on an uncharged graphene sheet using the B&S FF. Green: Hydrogen; Purple, Cyan: Carbon; Pink: Fluorine. 150
6.7 Atoms distribution as function of space on the surface *b*-axis of the computed replica having two graphene sheets with Q: 0 using the B&S FF. 152
6.8 Trajectory snapshot side view of the computed replica with Q: 0 at the liquid phase equilibrium showing a generally disordered state of PVDF oligomers. Green: Hydrogen; Purple, Cyan: Carbon; Pink: Fluorine. 153
6.9 Trajectory snapshot top view of the computed replica with Q: 0 at the liquid phase equilibrium showing a generally disordered state of PVDF oligomers. Green: Hydrogen; Purple, Cyan: Carbon; Pink: Fluorine. 154
6.10 Atoms distribution as function of space on the surface *b*-axis of the computed replica having two graphene sheets with Q: 0.025 using the B&S FF. . . . 155

6.11 Atoms distribution as function of space on the surface *b*-axis of the computed replicas having two graphene sheets with Q: 0.05 using the B&S FF. 156
6.12 Atoms distribution as function of space on the surface *b*-axis of the computed replica having two graphene sheets with Q: 0.1 using the B&S FF. 157
6.13 Representative trajectory image side view of the computed replica with Q: 0.025 showing PVDF oligomers assuming the β-phase chains conformation on a charged graphene surface. Green: Hydrogen; Purple, Cyan: Carbon; Pink: Fluorine. 158
6.14 Representative trajectory image top view of the computed replica with Q: 0.025 showing PVDF oligomers assuming the β-phase chains conformation on a charged graphene surface. Green: Hydrogen; Purple, Cyan: Carbon; Pink: Fluorine. 159
6.15 Representative trajectory image side view of the computed replica with Q: 0.05 showing PVDF oligomers assuming the β-phase chains conformation on a charged graphene surface. Green: Hydrogen; Purple, Cyan: Carbon; Pink: Fluorine. 159
6.16 Representative trajectory image top view of the computed replica with Q: 0.05 showing PVDF oligomers assuming the β-phase chains conformation on a charged graphene surface. Green: Hydrogen; Purple, Cyan: Carbon; Pink: Fluorine. 160
6.17 Representative trajectory image side view of the computed replica with Q: 0.1 showing PVDF oligomers assuming the β-phase chains conformation on a charged graphene surface. Green: Hydrogen; Purple, Cyan: Carbon; Pink: Fluorine. 161
6.18 Representative trajectory image top view of the computed replica with Q: 0.1 showing PVDF oligomers assuming the β-phase chains conformation on a charged graphene surface. Green: Hydrogen; Purple, Cyan: Carbon; Pink: Fluorine. 162
6.19 Dihedral distribution of the last 15 ns of the liquid phase equilibrium at 500 K of the four computed replica with two graphene sheets bringing different charges using the B&S FF. 163

A.1 Convergence tests for the full trans backbone structure such as the β and ζ phases (12 atoms models: 12 milli Rydbergs tollerance), with the ideal kinetic energy cutoff of the charge density ten times the kinetic energy cutoff of the wavefunction (for US pseudopotentials). Left: Convergence overview; Right: Convergence zoomed in the milli Rydbergs range were cutoffs were accepted. 183
A.2 Convergence tests for the full trans backbone structure such as the α and δ phases (24 atoms models: 24 milli Rydbergs tollerance), with the ideal kinetic energy cutoff of the charge density ten times the kinetic energy cutoff of the wavefunction (for US pseudopotentials). Left: Convergence overview; Right: Convergence zoomed in the milli Rydbergs range were cutoffs were accepted. 184
A.3 Convergence tests for the full trans backbone structure such as the γ and ε phases (48 atoms models: 48 milli Rydbergs tollerance), with the ideal kinetic energy cutoff of the charge density ten times the kinetic energy cutoff of the wavefunction (for US pseudopotentials). Left: Convergence overview; Right: Convergence zoomed in the milli Rydbergs range were cutoffs were accepted. 184
A.4 Partial DOS s electrons projection of the β-phase using PBE. 186
A.5 Partial DOS p electrons projection of the β-phase using PBE. 187
A.6 Partial DOS s electrons projection of the ζ-phase using PBE. 187
A.7 Partial DOS p electrons projection of the ζ-phase using PBE. 188
A.8 Partial DOS s electrons projection of the α-phase using PBE. 188
A.9 Partial DOS p electrons projection of the α-phase using PBE. 189
A.10 Bands structure and DOS states of the β-phase using vdW-DF. 190
A.11 Partial DOS s electrons projection of the β-phase using vdW-DF. 190
A.12 Partial DOS p electrons projection of the β-phase using vdW-DF. 191
A.13 Bands structure and DOS states of the ζ-phase using vdW-DF. 191
A.14 Partial DOS s electrons projection of the ζ-phase using vdW-DF. 192
A.15 Partial DOS p electrons projection of the ζ-phase using vdW-DF. 192
A.16 Bands structure and DOS states of the α-phase using vdW-DF. 193
A.17 Partial DOS s electrons projection of the α-phase using vdW-DF. 193
A.18 Partial DOS p electrons projection of the α-phase using vdW-DF. 194
A.19 Correlation plot of the computed β-phase frequencies with the experimental frequencies. 195

A.20 Correlation plot of the computed α-phase frequencies with the experimental frequencies. 195

A.21 Correlation plot of the computed γ-phase frequencies with the experimental frequencies. 196

A.22 R_e as function of time of bulk PDVF annealed at 800 K and cooled to to 500 K using 3 different cooling rates using the B&S FF. 202

A.23 R_e as function of time of the annealing temperatures from 500 K up to 900 K using the B&S FF. 203

A.24 Density versus time of bulk β-PDVF short chains during hybrid equilibration procedure where the melted system was gathered from B&S force field dynamic at 600 K and passed into OPLS to cooling such disordered system steadily at 500 K. Heating at 600 K: thermal treatment at 600 K to melt the chains; Cooling: cooling process to bring the system to 500 K; Fix at 500 K: steady dynamic run at the fixed temperature of 500 K; Equilibrium: Equilibrium of the liquid phase. 204

A.25 Radius of gyration versus time of bulk β-PDVF short chains during hybrid equilibration procedure where the melted system was gathered from B&S force field dynamic at 600 K and passed into OPLS to cooling such disordered system steadily at 500 K. Heating at 600 K: thermal treatment at 600 K to melt the chains; Cooling: cooling process to bring the system to 500 K; Fix at 500 K: steady dynamic run at the fixed temperature of 500 K; Equilibrium: Equilibrium of the liquid phase. 205

A.26 End to end distance versus time of bulk β-PDVF short chains during hybrid equilibration procedure where the melted system was gathered from B&S force field dynamic at 600 K and passed into OPLS to cooling such disordered system steadily at 500 K. Heating at 600 K: thermal treatment at 600 K to melt the chains; Cooling: cooling process to bring the system to 500 K; Fix at 500 K: steady dynamic run at the fixed temperature of 500 K; Equilibrium: Equilibrium of the liquid phase. 206

A.27 Density as function of time of the four computed replica with graphene layers differently charged from a Q of 0 up to 0.1 (*e*) using B&S FF. 207

List of tables

2.1 Labelling map from the old numbering system to the modern Greek alphabet and space groups list of all PVDF crystal structures. Space groups of the present predicted PVDF geometries were verified using FINDSYM online software[20]. N: number of symmetry operations; *: also mentioned as Form IV in the case of few contemporary papers[21] of the past; $_{uu}$: up-up chain packing; $_{ud}$: up-down chain packing. 16

2.2 Resuming table of different post processing techniques to increase the PVDF sample crystallinity showing pros and cons of each technique and its applicability in flexible electronics. Appl.: Applicability of the technique to flexible electronics. 24

2.3 Percentage of crystalline β-phase increase as function of elongation speed: cm min^{-1}; Taken from Mohammadi *et al*[22]. 24

2.4 γ-phase content for PVDF with wt 0.5% of Montmorillonite nanocomposites obtained by recrystallisation after melting at different temperatures. It was reported that the samples crystallised after melting at 210 °C crystallised fully in the α-phase. The accuracy in estimating the β-phase content using FTIR has been evaluated to be $\approx$0.6%. Taken from Lopes *et al*[23]. 31

2.5 γ-phase content for the PVDF/NaY zeolite composites with different NaY content and crystallised after annealing at 190 °C and recrystallised. It was reported that the samples crystallised after annealing at 210 °C crystallised fully in the α-phase[23]. Taken from Lopes *et al*[24]. 32

2.6 β-phase content for the PVDF/BaTiO$_3$ mixture made with different percentage content of BaTiO$_3$ and different average particle sizes. Taken from Mendes *et al*[5]. 32

2.7 PVDF crystal phases content with increasing wt % of OMS by MQ-AN the thin film samples. Work made by Ramasundaram *et al*[25]. 34

3.1 Table of general parameters used to conduct calculations always used if not differently specified. wfc: Kinetic energy cutoff of the wavefunction; rho: Kinetic energy cutoff of the charge density; forces: Convergence threshold of forces acting on ions; tot. eng.: Total energy convergence threshold of the total energy of ions minimisation; Tot.Eng.: Total energy convergence threshold of the scf calculation; Mesh: k-points mesh of the Brillouin zone along x,y,and z axes, respectively; N$_K$: Number of k-points in the Brillouin zone. 69

3.2 Procedure description of calculation types. Calc. Type: Calculation Types. . 69

3.3 Table of parameters used to conduct specific types of calculations. N$_a$: Number of atoms; N$_b$: number of kohn-Sham states (bands). N$_{K+}$: Number of K-points added to any axis in the K-mesh for band and DOS; N$_{K+axis}$: number of K-points added to the polarisation axis for Berry phase calculation; tot.eng.: Total energy convergence threshold of the total energy in scf calculation; Tot.Eng.: Total energy convergence threshold for ions relaxation. 69

3.4 MSXX force field parameters made by Karasawa *et al*[26]. X: Cross term values of cross term potentials. *: Values adjusted in the present study to simulate finite chains length. The units of K,D, k_R,k_θ,A_{ij},C_{ij} are in kJ mol^{-1}. The units of R$_b$,ρ are in Å. The units of Θ_a D$_{C0}$, D$_{F0}$, D$_{H0}$ and D$_{RR}$ are in degrees. The units of Charge are in elementary charge (e). 76

3.5 Byutner & Smith force field parameters made by Byutner *et al*[27]. a: B&S original. b: Erdtman original. The units of K1, K2, K3, K4, K5, K6, A_{ij},C_{ij} are in kJ mol^{-1} and K_b, K_a in kJ mol^{-2}. The units of r_0 and ρ are in Å. The units of $\Theta_0$is in degrees. The units of Charge are in elementary charge (e). . 78

3.6 OPLS force field parameters used by Guryel *et al*[28]. The units of K_a, K_b andε are given in kJ mol^{-1}. The units of r_0 and σ are given in Å. The units of Θ_0 are given in degrees. The units of Charge are in elementary charge (e). 79

3.7 Examples of the conformation tensor of a system where all atoms moved stochastically far from their original place, showing the diagonal matrix is converged to one. Taken from Hari[17]. ^{a}: conformation tensor of x-axis C$_{xx}$; ^{b}: conformation tensor of y-axis C$_{yy}$; ^{c}: conformation tensor of z-axis C$_{zz}$. . 83

4.1 Lattice constants, angle β^o, and volume V, for the α-phase for different functionals compared to DFT and experimental results available in the literature. *: Estimated lattice accuracy from present convergence tests, see Tables A.1, A.2, A.3. 86

4.2 Lattice constants and volume V, for the δ-phase for different functionals compared to DFT and experimental results available in the literature. *: Estimated lattice accuracy from present convergence tests, see Tables A.1, A.2, A.3. 87

4.3 Lattice constants and volume V, for the β-phase for different functionals compared to DFT and experimental results available in the literature. *: Estimated lattice accuracy from present convergence tests, see Tables A.1, A.2, A.3. 88

4.4 Lattice constants and volume V, for the ζ-phase for different DFT functionals. 90

4.5 Lattice constants and volume V, for the γ_{uu}-phase for different functionals compared to DFT and experimental results available in the literature. *: Estimated lattice accuracy from present convergence tests, see Tables A.1, A.2, A.3. 90

4.6 Lattice constants and volume V, for the γ_{ud}-phase for different functionals compared to DFT and experimental results available in the literature. *: Estimated lattice accuracy from present convergence tests, see Tables A.1, A.2, A.3. 91

4.7 Lattice constants and volume V, for the ε_{uu}-phase for different functionals compared to DFT results available in the literature. *: Estimated lattice accuracy from present convergence tests, see Tables A.1, A.2, A.3. 92

4.8 Lattice constants and volume V, for the ε_{ud}-phase for different functionals compared to DFT and experimental results available in the literature. *: Estimated lattice accuracy from present convergence tests, see Tables A.1, A.2, A.3. 94

4.9 Cohesive energies of PVDF backbones, $\Delta_{TG^{+/-}}$ and $\Delta_{TTTG^{+/-}}$ isolated chains energies referred to the full trans chain energy Δ_T used as reference and compared to DFT results available in literature; Δ: kJ mol^{-1}. Acc.: The accuracy is normalised per chain's monomer, averaged for all chains types of the same functional and expressed in kJ mol^{-1}. XC: Exchange correlation functional. 96

4.10 Cohesive energies of all PVDF polymorphs compared to DFT results available in literature. Energy ranges are expressed in kJ mol^{-1}. Acc.: The accuracy is normalised per chain's monomer, averaged per all crystals of the same functional and expressed in kJ mol^{-1}. XC: Exchange correlation functional. Ref.: Reference. 97

4.11 Spontaneous polarisation of the β, δ, γ_{uu} and γ_{ud} phases compared with different DFT functionals and experiment from literature (where applicable). *: Evaporation of $[VDF]_{12/16}$ oligomers in vacuum for deposition on electrode substrate[29]. Acc.: The accuracy is normalised by the crystal unit, averaged for all crystals of the same functionals and expressed in μC cm^{-2}. 101

4.12 Vibrational frequencies of the β-PVDF primitive cell compared to previous calculated and observed values. The accuracy of peaks prediction of the present computation has been estimated to be 0.32 cm^{-1} for the β crystal. [a]: observed by other authors[30, 31] as the experimental peak at 600 cm^{-1}; [b]: Observed experimentally by Bormashenko *et al*[30] as the experimental peak at 511 cm^{-1}; [c]: Present vibrational frequencies scaled with the empirical factors used by Nakhmanson[32] to show how peaks would be like if scaled; IR: present IR peaks relative intensity. ν: stretching (a: symmetric, s: asymmetric); r: rocking; w: wagging; t: twisting; δ: bending; τ: torsional; L: librational. 108

4.13 Vibrational frequencies of the ζ-PVDF. IR: present IR peaks relative intensity. The accuracy of peaks prediction of the present computation has been estimated to be 0.24 cm^{-1} for the ζ crystal. ν: stretching (a: symmetric, s: asymmetric); r: rocking; w: wagging; t: twisting; δ: bending; τ: torsional; L: librational. 111

4.14 Vibrational frequencies of the α-PVDF. Frequencies are compared to previous calculated and observed values. The accuracy of peaks prediction of the present computation has been estimated to be 0.44 cm^{-1} for the α crystal. IR: present IR peaks relative intensity. ν: stretching (a: symmetric, s: asymmetric); r: rocking; w: wagging; t: twisting; δ: bending; τ: torsional; L: librational. 112

4.15 Vibrational frequencies of the δ-PVDF primitive cell. IR: present IR peaks relative intensity. The accuracy of peaks prediction of the present computation has been estimated to be 0.45 cm^{-1} for the δ crystal. ν: stretching (a: symmetric, s: asymmetric); r: rocking; w: wagging; t: twisting; δ: bending; τ: torsional; L: librational. 116

4.16 Vibrational frequencies of the γ-PVDF primitive cell. The accuracy of peaks prediction of the present computation has been estimated to be 0.81 cm^{-1} for the γ crystal. ν: stretching (a: symmetric, s: asymmetric); r: rocking; w: wagging; t: twisting; δ: bending; τ: torsional; L: librational. 116

5.1 DFT and MD lattice comparison of PVDF polymorphs compared with DFT$_{vdW}$ results and literature. DFT$_{vdW}$: DFT results from XC-f vdW-DF. . 123

5.2 Isolated chain energies of PVDF backbones in vacuum of $\Delta_{TG^{+/-}}$ and $\Delta_{TTTG^{+/-}}$ chains with isolated chain energy of Δ_T as relative zero. The unit of Δ is kJ mol^{-1}. 125

5.3 Cohesive energies of all PVDF polymorphs compared to MD results available in literature. Energies are expressed in kJ mol^{-1}. 125

5.4 Averaged properties of the B&S FF MD runs for different annealing temperatures from 500 K up to 900 K performed for 40 ns. T$_{ann}$: Annealing temperature. Std.: Standard deviation. 131

5.5 Averaged properties of the B&S FF MD runs of different cooling rates from 800 K to 500 K. Std.: Standard deviation. 134

5.6 B&S FF physical properties averages of the geometrically optimised β crystalline system and its conformation tensor. Geom. opt.: Data of the optimised geometry of β-PVDF 100% crystalline at 0 K before annealing started; Conformations tensor has been calculated on the optimised geometry at 0 K before annealing started. 135

5.7 MSXX-noX FF runs averaged properties of the full equilibration attempt. Cooling: cooling rates of 30 K ns^{-1}. Std.: Standard deviation. 136

5.8 Liquid phase equilibrium at 500 K of the PVDF bulk model using the B&S FF. Std.: Standard deviation. 139

6.1 OPLS Force Field vdW mixed parameters obtained using the mixing rules 6.1 and 6.2 to implement the LJ potential in the B&S FF. ε: kJ mol^{-1}; σ: Å;. 145

6.2 Conformation tensor by diagonal elements as function of space from bottom to top of the *b*-axis for the liquid phase equilibrium of the PVDF surface model using the B&S FF. 148

6.3 Statistics of the computed surface model using B&S FF, which have been perpetuated after the liquid phase equilibrium with the modification of charges from having two neutrally charged graphene sheets up to two graphene sheets with opposite charges magnitude to preserve system neutrality. A: Neutrally charged graphene sheets; B: Q=±0.025 charged graphene sheets; C: Q=±0.05 charged graphene sheets; D: Q=±0.1 charged graphene sheets; Std.: Standard deviation. 151

A.1 Table of conversion constants and calculations used in the thesis taken from the NIST CODATA database[33]. Std.: Standard deviation; R_g: Radius of gyration; R_e: End to end distance; Tensor: Conformation tensor 185

A.2 Vibrational frequencies of the ε_{uu}-PVDF. 197

A.3 Vibrational frequencies of the ε_{ud}-PVDF. 199

A.4 Conformation tensor for the B&S force field during fixed temperature dynamics runs. A: system cooled at 400 K in 10 ns after the 30 ns steady at 500 K and kept for 30 ns at 400 K where here the last 15 ns were showed; B:system cooled at 300 K in 10 ns after the 30 ns steady at 400 K and kept for 30 ns at 300 K where here the last 15 ns were showed. 202

A.5 Conformation tensor for the B&S force field during fixed temperature dynamics runs. A: constant heating at 600 K per 40 ns; B: cooling at 500 K in 10 ns; C: 15 ns stable at 500 K; D: extra 15 ns stable at 500 K. 202

Nomenclature

^{o}C	Temperature units in Celsius
K	Temperature units in Kelvin, 0 K = -273,15 ^{o}C
T_c	Curie temperature
T_m	Melting temperature
T_g	Transition glass temperature
eV	Energy gained by an electron moving into vacuum under a potential of 1 Volt
cm^{-1}	Unit of wavelength, 1 cm^{-1} = 0.00012 eV
Ry	Unit of energy in Rydbergs, 1 Ry = 13.68 eV
mol	Avogadro number $6{,}002\times10^{23}$ molecules in a mole
Joule	Unit of energy, 1 Joule = $6{,}242\times10^{18}$ eV
kJ mol^{-1}	Unit of energy per mole, 1 kJ mol^{-1} = 7.65e-04 Ry = 0.01 eV
P	Spontaneous polarisation
μC cm^{-2}	Unit of the spontaneous polarisation
V m^{-1}	Unit of Volts applied per meter
E_{mon}	Monomer energy
E_{cry}	Crystal energy
N_{mon}	Monomer number
N_{chain}	Chain number

E_{chain}	Chain energy
E_{coh}	Cohesive energy
Q	Electrostatics charge expressed as numerical fraction of electron charge
DFT	Density functional theory
MD	Molecular dynamics
OPLS	Optimised potential for liquid systems
B&S	Molecular dynamics force field
MSXX	Molecular dynamics force field
MSXX-noX	Molecular dynamics force field
FE	Ferroelectric
VDF	Vinyldenedifluoride
PVDF	Polyvinyldenedifluoride
T	Full trans backbone structure
TG^+TG^-	Backbone structure of trans and gauche$^{+/-}$ bonds
$T_3G^+T_3G^-$	Backbone structure of three trans and one gauche$^{+/-}$ bonds
DMF	*N*,*N*-dimethylformammide
NMP	*N*-methyl1-2-pyrrolidone
HMPA	hexamethylphosphor-ammide
DMAc	*N*,*N*-dimethylacetammide
Nap	Positive nucleating agent
OMS	Organically modified silicon
APA	Anodic porous alumina
GO	Graphene oxide
MFM	Metal ferroelectric metal

NP	Nanoparticle
IR	Infra-red
FTIR	Fast-Fourier transform infra-red
DSC	Differential scanning calorimetry
XRD	X-ray diffraction
SEM	Scanning electron microscopy
DC-EFM	Dynamic contact - electronic force microscopy
FE-SEM	Field emission - scanning electron microscopy
AFM	Atomic force microscopy
GIRAS	Grazing incident reflection absorption spectra
SAM	Self-assembly monolayers
vdW	van der Waals
PBE	Perdew-Burke-Ernzerhof
LDA	Local density approximation
LAMMPS	Large-scale Atomic/Molecular Massively Parallel
COMPASS	Condensed-phase Optimised Molecular Potentials Atomistic Simulation Studies
$\hat{H}$	Hamiltonian operator
KS	Kohn-Sham
MP	Møller-Plesset
NC	Norm conserving
PAW	Projector augmented wave
US	Ultrasoft
R_g	Radius of gyration
R_e	End to end distance

C_{xx}	X-axis conformation tensor
C_{yy}	Y-axis conformation tensor
C_{zz}	Z-axis conformation tensor
Exp.	Experiments
Std.	Standard deviation

Chapter 1

Introduction

The modern computers in use nowadays are based on the use of ferroelectric (FE) materials, as such materials have the ability to remember two opposed and distinguishable quantum states[34, 35] useful to represent the binary code[36] which constitutes the operational machine language of computers. The innovation of electronics devices to increase power efficiency, miniaturisation, speed, lightness and inexpensiveness, is the universal trend acting within these days on computer technology. A remarkable example of miniaturised FE units currently used in modern electronics (*e.g.* PCs, satellites) are the Metal-Ferroelectric-Metal (MFM)[37] and the Field-Effect-Transistor (FET)[38, 39] architectures that can accommodate a wide range of FE materials which are realised at the nanoscale to have the highest computational capacity in the smallest space. The architecture of modern electronic devices is constituted by multiple thin layered materials[34, 35] sandwiching a ferroelectric material, which can affect the FE layer operability and usually such additional layers of materials are chosen to enhance FE properties of the FE material used[35]. The interaction mechanism of a FE material with other materials in use in modern electronics is of crucial importance and such multi layers interactions can be seen as a surface interaction of such material with the FE material.

1.1 Fields of application of flexible ferroelectric devices

In the constant trend of evolving technologies, new fields of applications are emerging as such flexible electronics devices. At the current technological advancements, flexible devices are realised using rigid ferroelectric components adapted to thin film, which are flexible. However, as the ferroelectric materials are rigid, the flexible electronic devices realised nowadays are not real flexible devices, and several hardware failures are given by the bending stresses the ferroelectric materials receive. Such limitations on flexibility can not be surpassed by using traditional rigid ferroelectric materials, indeed, their commercialisation failed due to loss of operability after flexible electronic devices made with rigid ferroelectric materials suffered modest bending stresses.

To realise flexible devices, flexible ferroelectric materials able to tolerate bending stresses has still been missing. As the application fields of flexible electronic devices is at the beginning of its era and could be exponentially expanded, the search for good performing flexible ferroelectric materials is open. The current interest for flexible ferroelectric materials would already revolution, energy harvesting from sun[40], winds[41] and sea waves[41], wearable computers[42] and biometric spatial suits[43]. The technological expansion by having flexible ferroelectric materials is already considerable, the most important technological step to solve is the realisation of high quality grade of flexible ferroelectric materials. This thesis is concerned with the study of flexible ferroelectric materials, to fill the knowledge gap for realising flexible ferroelectric materials at high quality grade required by electronic devices standards.

1.2 Ferroelectricity

Ferroelectricity is a property of certain non-conducting crystals, or dielectrics, that exhibit spontaneous electric polarisation (separation of the centre of positive and negative electric charges that creates a non-neutral dipole moment) that can be reversed in direction by applying an appropriate electric potential (*e.g.* coercive field)[44, 45]. It is such a delicate quantum equilibrium that appears within the crystal and leaves its overall dipole tunable across two opposite directions (*e.g.* binary states as represented in Figures 1.2 and 1.3) by an electric potential, perpetuating the new induced state without an active stimulus acting on it[45]. Figure 1.1 shows the generic scheme of an hysteresis loop of a FE material with B representing the dipole moment magnitude and H the electric potential applied. The b and e coordinates represents the highest peaks of opposite magnitude of the dipole saturation reachable under an applied potential. The c and f coordinates represents the residual polarisation of the two opposite inducible quantum states and d and g represents the coercive field which is the magnitude of the electric potential necessary to induce the inversion of polarisation of the FE material. On top of the ferroelectric behaviour of a given material, the dipole moment magnitude of a FE material is another important property to consider. The dipole moment determines the magnitude of the spontaneous polarisation (P: μC cm^{-2}) where a P lower than 3 μC cm^{-2} would made the FE material useless[43, 35], hence, a FE material to be applied in modern electronics is required to have a spontaneous polarisation as high as possible.

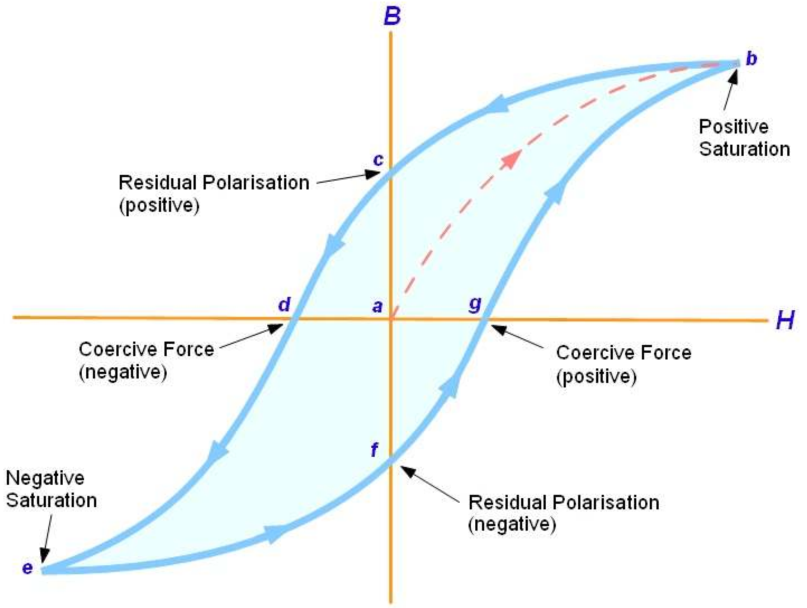
B
b
Positive
Saturation
c
Residual Polarisation
(positive)
d
a
g
H
Coercive Force
(negative)
Coercive Force
(positive)
f
Negative
Saturation
Residual Polarisation
(negative)
e

Fig. 1.1 Schematic diagram of a general hysteresis response of a ferroelectric material and all the properties the diagram can provide. B: Polarisation (μC cm^{-2}); H: Electric field (MV/m^{-2}); a: Starting neutral steady state where the medium has never been polarised or trespassed the Curie temperature; b/e: Maximum values of saturation of the dipole (μC cm^{-2}); c/f: Remnant polarisation after the applied electric potential vanished (μC cm^{-2}); d/g: Critical Coercive Field (MV/m^{-2}) able to induce a dipole inversion.

The reverse of the polarised state of a FE material can be obtained by applying an electric potential which trespass the coercive field[43] (expressed as MV m^{-1}) of the FE material, which for nanoscale devices is usually between 1-5 V[35] per ferroelectric unit (20-100 nm^2). The coercive field defines the magnitude of the voltage which needs to be applied to a material to reorient its dipole moment[35]. The Curie temperature (T$_c$) is another important parameter to be aware about FE materials, since trespassing that temperature will cause a loss of dipole order inside the FE crystal destroying the information of its current polar state (*e.g.* erasing the information of the FE unit)[35], hence, FE materials needs to have at least a T$_c$ of 400 K as a temperature limit high enough to satisfy the normal operational temperature range of computers[35]. Finally, the melting temperature (T$_m$) is the temperature at which a material becomes liquid, as analogy the T$_m$ is important as much as the T$_c$ which can be higher or equal to the T$_c$[35].

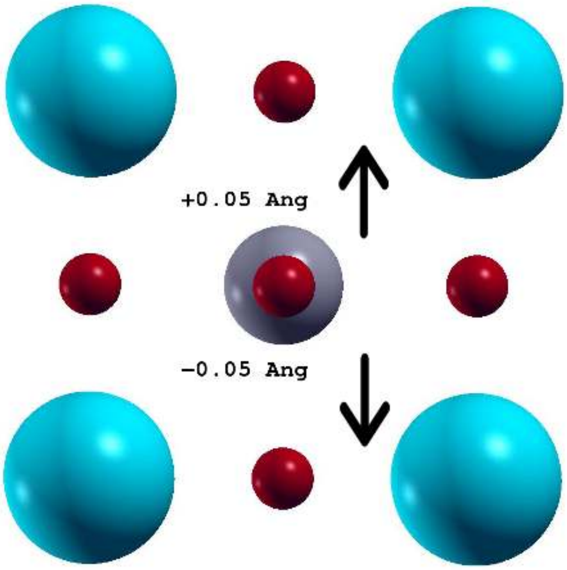

Fig. 1.2 Sketch of the ferroelectric $BaTiO_3$ perovskites crytal unit where the dipole reorients with a small Ti displacement of $\approx$0.05Å. Ba: light blue; O: dark red; Ti: grey.

1.3 FE materials

Ferroelectric perovskites such as $CaTiO_3$ are a very wide class of FE ceramics currently used in modern technology within a vast amount of compounds that forms ordered crystals having ferroelectric behaviour (*e.g.* $BaTiO_3$ as shown in figure 1.2, KNO_3, $Pb_5Ge_3O_{11}$, $Bi_4Ti_3O_{12}$ and $LiNbO_3$)[46, 47] and their performance in computing bits and reading/writing operations can reach very high performances up to 6.2×10^9 events per second[35]. Such FE ceramics rise high spontaneous polarisation (*e.g.* 50-150 μC cm^{-2})[35, 46] and can be made highly crystalline (*e.g.* 99.5%)[35, 46], remaining steady and chemically inert for long as microprocessors and memories made with FE ceramics last for decades. The dipole orientation in FE ceramics occurs along a central atom of the crystal which is perturbed of fractions of an Å as shown in Figure 1.2. The average T_c and T_m of FE ceramics are above 600 K and 800 K, respectively[35].

Along with the good features of FE ceramics there are also limitations as perovskites are rigid, heavy, brittle, polluting and expensive, furthermore, perovskites can not be flexible. As the emerging branch of technology based on flexible electronics devices is growing, perovskites can not stand for such versatility since ceramics are incompatible with flexibility. The needs of flexibility can be satisfied in using FE polymers since flexibility is native in polymers and their synthesis easier[48].

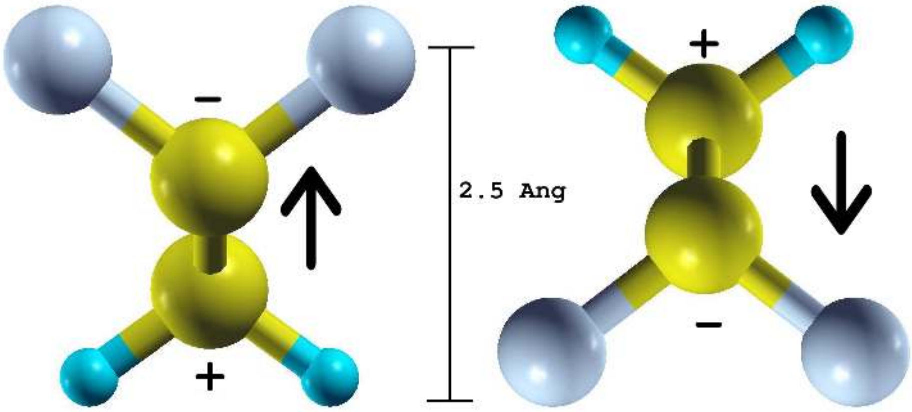

Fig. 1.3 Sketch of a PVDF ferroelectric crystal phase where at the chain dipole inversion correspond an entire chain flip of ≈2.5Å. In here, the two chains showed has to be intended as one chain drawn in both ferroelectric configurations. F: light grey; C: yellow; H: light blue.

1.4 Ferroelectric polymers

The wide area of polymers is restricted to those which manifest ferroelectric behaviour and along such restriction only FE polymers which satisfies all FE properties such as T_c, T_m, spontaneous polarisation and coercive field can be considered for being applied into electronics devices[40]. For example, polymers like -[C(CN)$_2$-CH$_2$]$_n$- (PVCCN)[40], -[CCl$_2$-CH$_2$]$_n$- (PVDC)[40], N_6 and N_9 nylons are excluded because of unsatisfying FE properties[40]. Beside FE properties also chemical stability is crucial as -[CB$_2$-CN$_2$]$_n$- (PVBN) possesses good FE properties but is not chemically stable[49, 50, 40], restricting the circle of reliable FE polymers to a single choice which is -[CF$_2$CH$_2$]$_n$- (PVDF)[40] that has good FE properties and chemical stability. The polarisation switch mechanism in PVDF is different than perovskites as in PVDF the whole chain reorient in space according to the direction of the applied potential as shown in Figure 1.3.

However, as PVDF is a high molecular weight polymer, to be grown crystalline at high percentage is difficult because of the entanglement of long polymeric chains[1, 43, 51, 52]. Such entanglement limits diffusivity and locally isolates chain conformations in clusters, where every cluster can possess very different degrees of freedom in the chains conformations which can assume different crystal structures or be blocked in amorphous states[53, 54, 51]. Ferroelectric materials exhibits ferroelectricity only within their ordered FE crystal structures and not in any amorphous region or non-FE crystals and in raw conditions PVDF is found to be partially amorphous and having a major population of non FE crystals along with a minority of FE crystals[1, 55, 56]. The crystalline grade of a PVDF sample is expected to be high and the best FE crystal of PVDF is the β-PVDF which is the crystal structure of main interest for flexible electronics applications for which many attempts to increase its crystalline percentage were made. Indeed, special processing techniques needs to be applied for enhancing PVDF crystallinity, however, processing polymers remains cheaper than FE ceramics.

The scientific research has been focused on suitable manufacturing approaches to increase the β-PVDF content in a sample eliminating other crystal structures whether FE or not and reducing to the minimum the amorphous regions. As mechanical stresses approaches turned to be too damaging for PVDF thin films[4], doping and surface deposition became the most modern and successful manufacturing procedures to increase PVDF FE crystals content[57, 7, 2, 6], however, with not great successes on high content of the β-PVDF as much as the γ-PVDF which has inferior ferroelectric properties. Doping and nanoconfinement conceptually reduces the size of a PVDF sample constricting the amount of material and degrees of freedom the polymeric chains of such sample will have in assuming random conformations, further stimulating the formation of FE crystals when the doping or surface effects are in synergy with such crystal structures.

In modern electronics, FE units are highly miniaturised and built as 2D functional units, hence, any FE material is formerly deposited on top of a surface chosen to enhance the FE behaviour. The choice of which material to use to assemble the FE unit must be done with the awareness of which properties the material is supposed to have to favour the operability of the FE material. Indeed, if a FE material is deposited on surface able to disrupt the FE behaviour or its crystallinity grade, the FE unit will result being not operational, therefore, it is necessary to understand the physical properties of the surface compatible with the FE material to ensure crystallinity and FE behaviour. In the case of PVDF, it is important to understand which surface properties favours the formation of the β-phase which is the most FE crystal of all PVDF polymorphs.

1.5 Aims

This thesis is concerned in understanding the surface effects which affects PVDF crystallinity and polymorphs formation. To be able to investigate such scientific question it is necessary to have reliable crystal models of PVDF characterised with a quantum mechanical (QM) calculations using DFT. The QM investigation of PVDF polymorphs allows to characterise all the metastable crystal structures of PVDF although such structures would be difficult to be observed experimentally. As DFT is a heavy computational methodology, the structural information gathered about PVDF crystals have been carried over molecular dynamics (MD) simulation to appreciate on a time consistent scale the particles evolution to understand how PVDF structural properties are affected by different environmental conditions such as temperature and presence of a surface. Indeed, such investigation performed on DFT would result to be hard to be performed because of very high computational demand. The study of surface/polymer interactions required to have a reliable classical model for studying PVDF dynamics under finite temperatures. The classical model which represents the force field (FF) resembling PVDF physical properties has been validated by the ability in predicting PVDF crystal structures in comparison with experimental and DFT observations and during the process of liquid phase equilibration which is the matter state at which the surface and polymer interactions have been appreciated. The surface study were focused in comparing the liquid properties of a bulk PVDF system with the liquid properties of PVDF in contact with a surface. The surface mechanisms investigated for their ability in affecting pVDF chains conformation were the surface confinement and electrostatics.

1.6 Thesis structure

Chapter 2 presents the literature review relevant to this research project introducing crystal phases of PVDF, physical properties, the main manufacturing processing techniques found in literature which aimed to increase FE crystalline domains in PVDF samplea, the relative manufacturing limitations and lacks of understanding which left open scientific questions addressed in the present thesis. Chapter 3 introduces the details of theories and methodologies applied during the present study such as introducing the quantum mechanical equations on which DFT has been based, the modern spontaneous polarisation theory, the phonons theory, the DFT basis set used in this study as well as the computational software chosen and an introduction to MD computations which are further integrated with FF set up along MD chapter results as appropriate. Chapter 4 presented the results gathered along the DFT study about PVDF polymorphs such as lattice structures, phase stability and energetics, spontaneous polarisation, electronic structures and vibrational frequencies. To follow, chapter 5 contained MD results for PVDF bulk properties from the crystal structure characterisation performed with different FFs, crystals energetics and the procedure developed to equilibrate a bulk liquid phase and system properties of the liquid phase equilibrium. Chapter 6 presented the liquid phase equilibrium surface properties of PVDF in contact with a surface investigating the effects of surface nanoconfinement and surface electrostatics effects on PVDF chains conformation. Chapter 7 summarised the conclusion of the research conducted in this thesis and the most appealing future research work to extend the study about PVDF over the present thesis. Along the whole thesis (including appendixes without appended papers) 81 figures and 44 tables are found to support the scientific investigation presented in this thesis.

Chapter 2

Literature review

Ferroelectric polymers are highly attractive materials for modern technological applications due to their low weight, flexibility, and chemical inertness coupled with substantial ferroelectric, piezoelectric and pyroelectric properties [58, 55, 59]. Such a fortunate combination of properties can be found only in PVDF and allows for a wide employment of such polymer in modern industry, with applications ranging from transistors[40, 35], sensors[40], actuators[1], transducers to ferroelectric optical memory, sonar equipment, and artificial muscles[55]. Along this chapter structural and physical properties of PVDF are exposed in detail together with the main attempt in post processing PVDF samples to increase the content of the ferroelectric crystals, especially the β-PVDF. As the main issue in PVDF is to achieve high yield of FE crystals the literature will follow from the background knowledge about PVDF to the most contemporary efforts in increasing FE behaviour of PVDF samples underlying what is still missing to be understood to concretely achieve a mature and scientifically meaningful control of the FE β-phase of PVDF.

2.1 Crystallinity and ferroelectric properties of PVDF

PVDF is a polymer synthesised by radical polymerisation, which is usually made to form concatenations from five hundred up to a thousand of thousands monomers (*e.g.* $\approx$0.5-1.0$\times 10^6$ Da[1, 60]), constituting high molecular weight chains. Polymers such as polyethylene, polypropylene as well as PVDF are semicrystalline, since such long polymeric chains tend to form ordered crystalline regions or crystalline domains along an interspersion of disordered chains. Disordered regions are so trapped due to the chains length which entangles[51] fraction of each PVDF chains in a disordered state. As PVDF is a linear polymer with no ramifications such compound is a thermoplastic which can be melted for repeated cycles and formed with different shapes. The transition glass (T_g) temperature of PVDF is 233 K[56] which makes a solid polymer sample of PVDF to spontaneously form ordered and disordered regions when the sample is found above the T_g temperature and below the melting temperature, which for PVDF is 438 K[56]. Such low T_g makes PVDF to benefit of its intrinsic flexibility useful for flexible electronics, but rises issues of controlling crystallinity[61].

Considering a generic preparation of a PVDF sample and cooled down to solid state, the majority of the sample will be found to form macroscopic structures called spherulites, which are constituted by thin crystalline lamellae disposed in circle from central point of origin forming a spherical bead with a contour of amorphous chains interspersed between the lamellae and around the sphere as shown in Figure 2.1-left[1]. In such sample ferroelectric behaviour is hardly found since it is generally assumed that when a PVDF sample forms spherulites the dominant crystal phase will the non-FE α-phase. Even thought, there could be a fraction of FE crystals in a spherulite, the spontaneous polarisation would radially dispersed along the circular structure not merging on the edge of the material. Looking at a lower level of detail as represented in Figure 2.1 on the right[2], it is possible to appreciate two main and distinct structural organisations within such sample, where the first with a brilliant spots in the middle are formerly identified as spherulites, while the needle-like[2] surrounding region contains a different crystal structures which are ferroelectric and mentioned later in the text as the most interesting PVDF crystal structure, however, this structural features are dependent by the sample manufacturing. The needle-like regions are assumed to be originated by PVDF chains exiting the spherulites body and finding other chains to form linearised ordered structures[2].

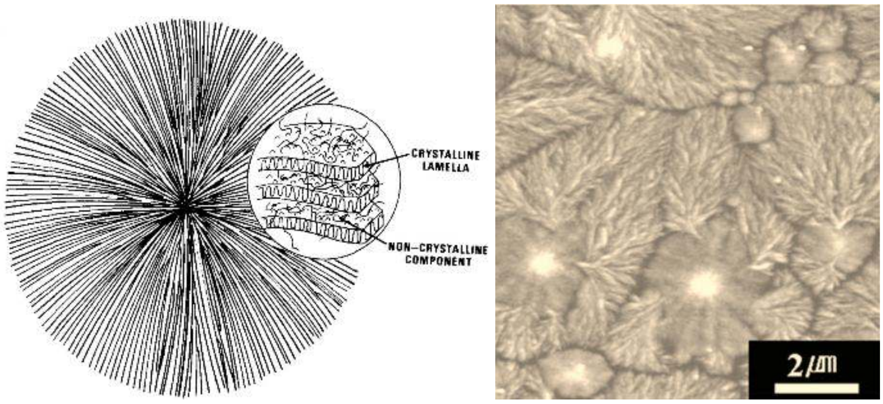

Fig. 2.1 Left: Schematic spherulite aggregation model of non-FE α-PVDF lamellae structures with chains fractions falling into disordered amorphous regions taken from Broadhurst[1] *et al*; Right: Atomic Force Microscopy of a PVDF spin cast and rapidly annealed on a coated gold surface taken from Kang[2] *et al*.

2.1.1 Crystal phases

The experimental determination of PVDF polymorphs started with a simple notation system made by Roman numbers that meant the discovery order of each crystal structure. The ferroelectric form I was the first, then non-FE form II was the second structure discovered, finally another ferroelectric phase was found and labelled as form III. The main distinguishing criteria between these three PVDF's forms at that early stage of knowledge was that every crystal structure possessed a different backbone orientation. The form I had an all trans bonds backbone T as Figure 2.2-a shows, the second form has been found to have a binary repetition of trans and gauche bonds as $TG^{+}TG^{-}$ ($\approx \pm 60^{o}$ for gauche bonds) where the trans bonds were always laying on the symmetry backbone plane as Figure 2.2-b shows. At last, the form III showed to have the most complex backbone organisation, where 3 trans bonds were interrupted by one gauche bond, then other 3 trans bonds were again interrupted by a gauche bond of opposite sign $T_3G^{+}T_3G^{-}$ ($\approx \pm 60^{o}$ for gauche bonds) as Figure 2.2-c shows.

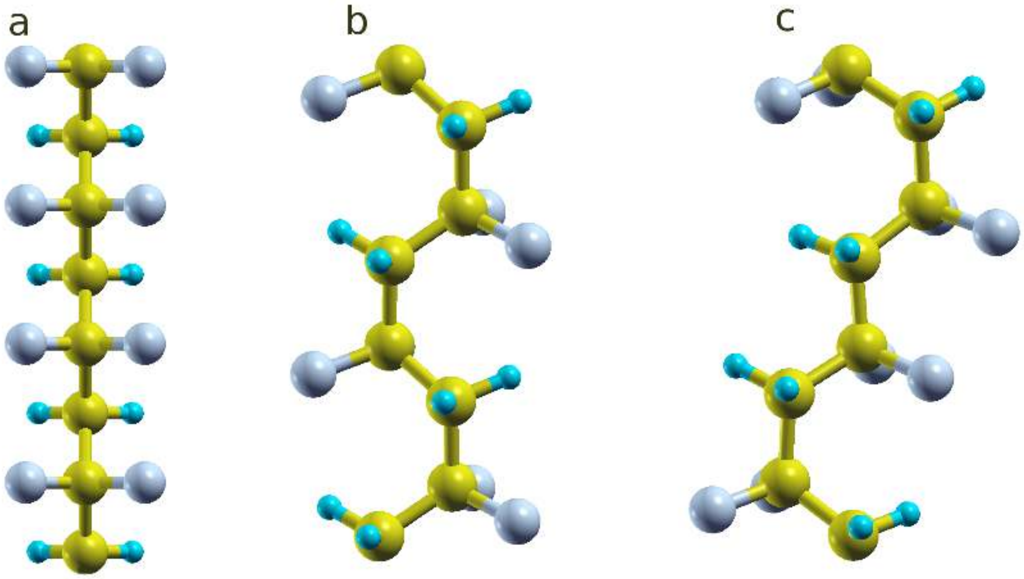

Fig. 2.2 The three backbone chains conformations of PVDF as full trans T (a), $TG^{+}TG^{-}$ (b) and $T_3G^{+}T_3G^{-}$ (c). F: light grey; C: yellow; H: light blue.

As the scientific interest on PVDF grown, further studies discovered more polymorphisms and made clear that the previous notation system with Roman was indeed obsolete. It became well known that PVDF did not only possessed a crystal structure per each backbone orientation, and when researcher observed that the form II existed in two different crystal structures of which one was ferroelectric while the other was not[1, 62] the number labelling became obsolete. Not much time later also the form III which was found to be ferroelectric was discovered to have a crystal non ferroelectric analogue[63, 64]. Different notations of PVDF crystal structures were used along the early stages of study about PVDF to recent days and Table 2.1 resume such notations used connected to the modern Greek alphabet labelling system which is still currently used and to increase clarity from this point and further only Greek letters will be used to refer to specific PVDF crystal polymorphs.

Furthermore, another structural variability of PVDF crystal structures containing gauche bonds (α, δ, γ and ε crystals) was found, as such backbone polymorphs could be represented with two different chains packing styles namely referred to as up-up and up-down, labelled to crystal phases as subscripts $_{uu}$ $_{ud}$. The α and δ phases resulted to have a strong preference of $\approx$97% in packing with the up-down configuration[21], hence, no ambiguity applies to α and δ crystals as only the up-down packing style is statistically representative. However, the packing style represented a major issue when considering the crystal structure of the γ and ε crystals and such polymorphs resulted to have the a statistical preference of packing up-up and up-down of $\approx$50%[63, 64], hence, γ and ε phases became structures more difficult to be studied because of such possibility of having both chains packing styles within different crystal units repetitions in the same PVDF sample. Further on, the γ and ε phases will be distinguished in their four variants as γ_{uu}, γ_{ud}, ε_{uu} and ε_{ud} phases as reported in Table 2.1.

Table 2.1 Labelling map from the old numbering system to the modern Greek alphabet and space groups list of all PVDF crystal structures. Space groups of the present predicted PVDF geometries were verified using FINDSYM online software[20]. N: number of symmetry operations; *: also mentioned as Form IV in the case of few contemporary papers[21] of the past; $_{uu}$: up-up chain packing; $_{ud}$: up-down chain packing.

PVDF		Space groups			
New label	Old label	Schoenflies	Hermann−Mauguin	N	Reference
α	Form II$_a$	C_{2h}^{5}	$P2_{1/c}$	14	[26, 65–67]
δ	Form II$_p$*	C_{2v}^{9}	P_{na2_1}	33	[26, 66]
β	Form I$_p$	C_{2v}^{14}	C_{m2m}	38	[26, 65, 66]
γ_{uu}	Form III$_{p-uu}$	C_{s}^{4}	C_c	9	[26, 63, 67]
γ_{ud}	Form III$_{p-ud}$	C_{2v}^{16}	$C2_{cm}$	40	[68, 26]
ε_{uu}	Form III$_{a-uu}$	C_{2v}^{5}	P_{ca2_1}	29	[26, 66]
ε_{ud}	Form III$_{a-ud}$	C_{2v}^{3}	$P2_{1/c}$	27	[26, 66]
ζ	-	D_{2h}^{5}	P_{mma}	51	Present

The polarisation mechanism of PVDF, recurs over chains dipole orientation and to change polarisation state of a FE PVDF crystal it is necessary to induce chains to reorient in space flipping upside-down hydrogen and fluorine atoms to invert the chains dipole direction[55, 35], which is achieved by applying an electric potential bigger than the coercive field of the sample[69]. Different samples manufactured in different ways can differ in the coercive field magnitude but generally for thin films of PVDF it is found to be ≈150 MV m^{-1}[69]. In a solid sample of PVDF, chains dipole may be found ordered pointing to the same direction as in FE crystals or alternatively pointing in opposite directions as in non-FE crystals, however, chains will be always polar and responsive to an applied electric potential[69]. As the T_c of PVDF has not been found below the T_m of 438 K[1, 70], the polarisation of a FE PVDF crystal persist until the sample melts. As all FE materials also PVDF is an insulator with a band gap experimentally measured to be ≈6 eV[18, 71].

The β-PVDF is the milestone of PVDF crystal phases and is FE with a spontaneous polarisation 19 μC cm^{-2}[57, 7], the highest registered of all PVDF FE phases, previous studies estimated a P for the β-PVDF of 13 μC cm^{-2}[29] and 7.6 μC cm^{-2}[72] showing how the refinement of PVDF manufacturing increased crystallinity and FE performance. The lattice structure of the β phase experimentally measured is orthorombic with the lattice being: a= 8.58 Å, b= 4.91 Å and c= 2.56 Å[65] and it is the most studied structure since it is the most compact crystal structure with the highest dipole order which can then rise the highest spontaneous polarisation possible[57, 7, 55], making the β phase the most appealing crystal for flexible electronics applications[8, 2, 73].

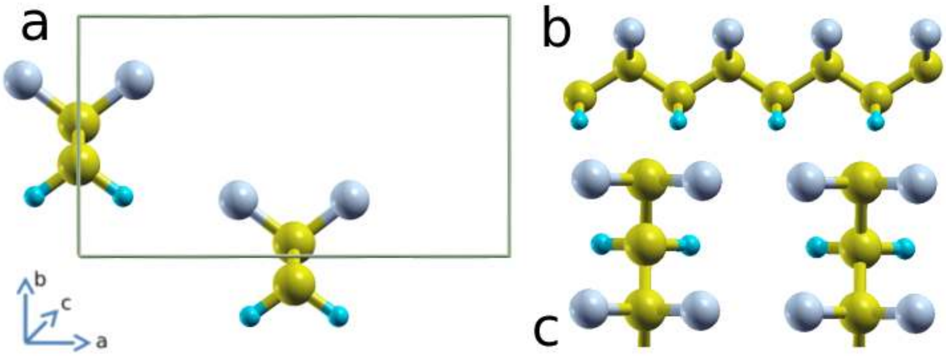

Fig. 2.3 A generic view of β-PVDF. a: front view including the crystal unit box; b: side view of one chain backbone trans bonds T; c: top view of the chains of the crystal unit box. F: light grey; C: yellow; H: light blue.

The Figure 2.3 shows the β crystal in front (a) and side (b) view in which is appreciable how chain backbones have full trans orientation and having all fluorine atoms closely aligned on one side of the backbone while hydrogen atoms are all found on the other side and the two chains represented in the crystal unit does not lay at the same height on the b-axis (bi-planar crystal).

The α-PVDF as earlier mentioned is a non ferroelectric crystal structure with TG$^+$TG$^-$ backbone which has the two chains of the crystal unit with dipole anti-parallel oriented as showed in Figure 2.4 on front (a) and side (b) view. It is the most abundant crystal structure present in a solid raw PVDF sample and for such reason it has been assumed to be the most stable, although, a study about thermodynamics phase stability has never been performed. It could be that the α-PVDF with the TG$^+$TG$^-$ backbone motif recurs more frequently because of the chain length entanglement effect[51] able to force the backbone structures to accommodate in a non ideal geometry because such geometry requires higher degrees of freedom which are forbidden by chain entanglement as recently observed in high definition atomic force microscopy (AFM) and X-ray diffraction (XRD) experiments[74]. As Figure 2.4 shows the lattice of the α-PVDF is monoclinic with a β^o angle of $\approx 90^o$ and the lattice: a= 4.96 Å, b= 9.64 Å and c= 4.62 Å[75].

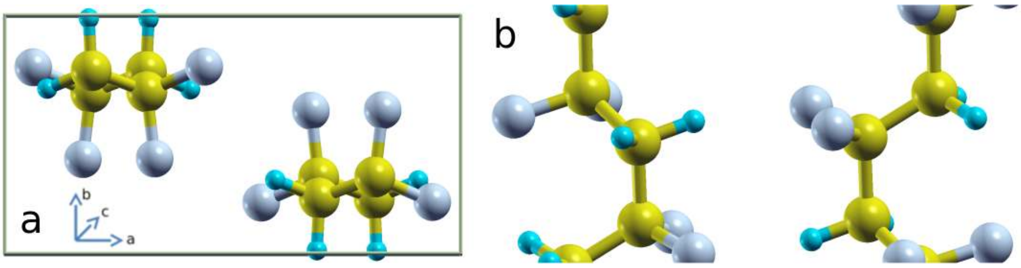

Fig. 2.4 A generic view of α-PVDF. a: front view including the crystal unit box; b: top view of two chains backbone trans bonds TG$^+$TG$^-$. F: light grey; C: yellow; H: light blue.

The δ-PVDF is the ferroelectric structure which also have the TG$^+$TG$^-$ backbone motif and as Figure 2.5 shows the front (a) and side (b) view, the only main difference from the α-PVDF is that the δ-PVDF has both chain dipoles oriented in parallel, hence it manifest ferroelectricity. The δ-PVDF structure appears to be similar to the non-FE analogue α-PVDF and still the lattice structure is given to be: a= 4.96 Å, b= 9.64 Å and c= 4.62 Å; but in the case of the δ-PVDF its lattice is orthorombic[21]. To support the fact that PVDF chains independently from their orientation can still respond to the threshold coercive field of ferroelectric transition, the δ-PVDF can be obtained by applying an external potential of $\approx$120-150 MV m^{-1} to an α-PVDF sample to induce the anti-parallel chains orientation to become parallel and forming the δ-PVDF[69]. However, for the reason given before the δ-PVDF can not withstand the spontaneous polarisation magnitude of β-PVDF, indeed, the highest measurement ever observed in experiments about the spontaneous polarisation of the δ phase was 7 μC cm^{-2}[69].

The more complex T$_3$G$^+$T$_3$G$^-$ backbone motif originates the γ-PVDF which is ferroelectric, although, its spontaneous polarisation has never been reported neither in experiments or

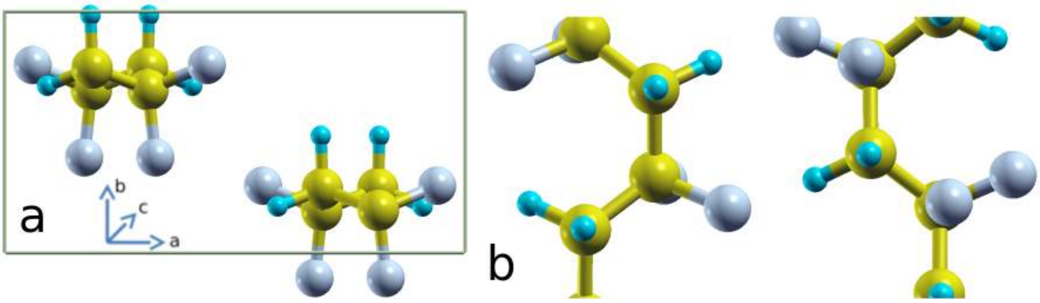

Fig. 2.5 A generic view of δ-PVDF. a: front view including the crystal unit box; b: top view of two chains backbone trans bonds $TG^{+}TG^{-}$. F: light grey; C: yellow; H: light blue.

computations. Furthermore, the γ-PVDF was found to exist as two different crystal structures such as one being monoclinic with β^{o} of 93^{o} with lattice: a= 4.96 Å, b= 9.67 Å and c= 9.20Å[64, 67], having the up-up chain packing as shown in Figure 2.6 (γ_{uu}-PVDF). The other crystal variants was found to be orthorombic with lattice: a= 4.97 Å, b= 9.66 Å and c= 9.18Å[63] with up-down chain packing as shown in Figure 2.7 (γ_{ud}-PVDF)[68]. However, the γ-PVDF crystal structure remained of less interest since the processing required to obtain high percentage yield of γ-PVDF is time and energy consuming and such crystal phase readily transforms back to the β crystal under weak mechanical stresses[63, 64].

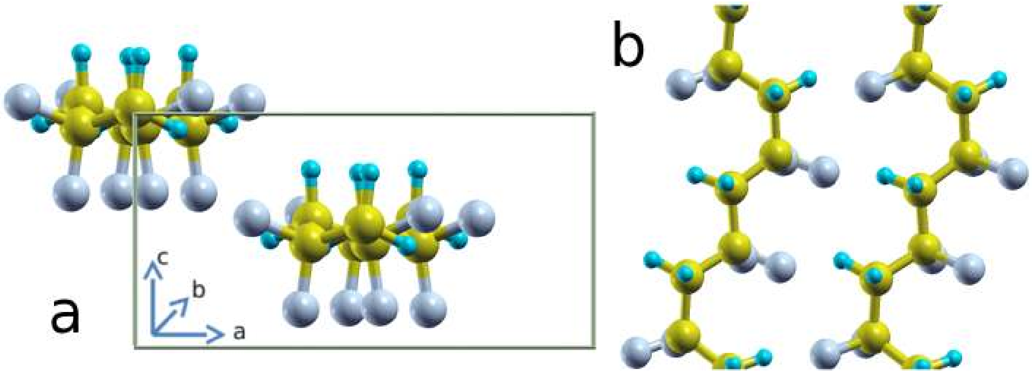

Fig. 2.6 A generic view of γ_{uu}-PVDF. a: front view including the crystal unit box; b: top view of two chains backbone trans bonds $T_3G^{+}T_3G^{-}$. F: light grey; C: yellow; H: light blue.

In the last decade the γ-PVDF became more notorious as the crystal structure able of the highest electric energy retention useful for energy storage devices such as batteries[76] where PVDF has been already applied extensively as well as in fuel cells technology[77] (in fuel cells the β-PVDF is assumed to be the most abundant crystal phase determined by IR spectra although PVDF functionality in fuel cells does not requires ferroelectricity). Despite other good insight about γ-PVDF it is unlikely to expect that such crystal structure will be applied in computing or memory devices, especially because any form of dipole disorder is anyway unwanted and both the FE δ and γ phases does not possess the same dipole alignment and P magnitude of the β-PVDF which remains, for the many reasons so far exposed the best FE candidate for PVDF enetring the flexible electronics applications.

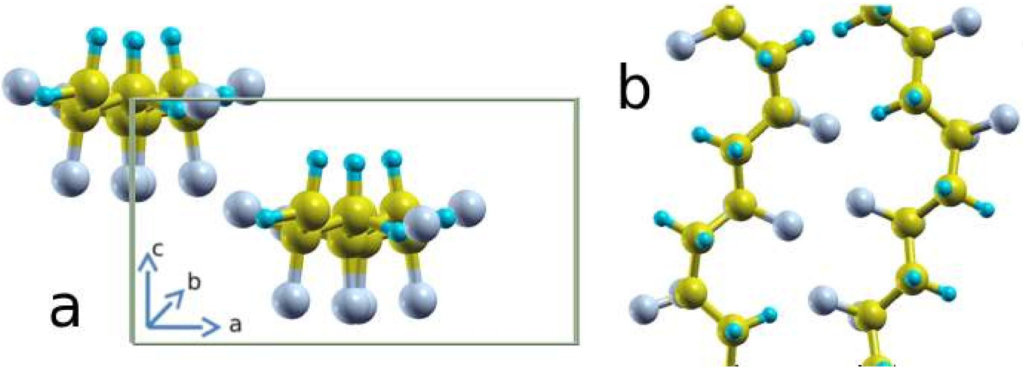

Fig. 2.7 A generic view of γ_{ud}-PVDF. a: front view including the crystal unit box; b: top view of two chains backbone trans bonds $T_3G^+T_3G^-$. F: light grey; C: yellow; H: light blue.

In literature a fifth crystal structure has been acknowledged but not intensively studied. Such structure is the ε-PVDF which is non ferroelectric and also shares has the $T_3G^+T_3G^-$ backbone motif[64]. With very few interest of investigating a non ferroelectric structure which still requires long time processing for obtaining it, the crystal structures merely ended with fibre diffraction experiments which demonstrated its existence as $T_3G^+T_3G^-$ backbone structure with a centrosymmetric inversion point which means it is a non ferroelectric structure[64] and without completing the study by experimentally observing its lattice structure. Its existence makes sense since it is expected that per each backbone motif there may be both ferroelectric and non ferroelectric polymorphs but its lattice remained experimentally undetermined. The ε-PVDF most probable crystal structure representation is shown in Figure 2.8 for the up-up chains packing (ε_{uu}-PVDF) and in Figure 2.9 for the up-down chains packing (ε_{ud}-PVDF) as computationally characterised by other authors[26, 66].

The conclusion of crystal phases description goes with the report of an undetermined crystal structure which has never been acknowledged in literature formerly as a possible crystal phase of PVDF. As other author reported it with the definition of the “non-poled β-PVDF”[78, 79], it has been observed a crystal phase which showed to have some of the characteristics of the FE β-PVDF but being non polar, hence, poling needed to be applied to induce FE out of this non-poled β-PVDF[30]. However, such crystal structure here computationally characterised would represent the sixth crystal polymorph of PVDF, formerly named as the ζ-PVDF (Table 2.1).

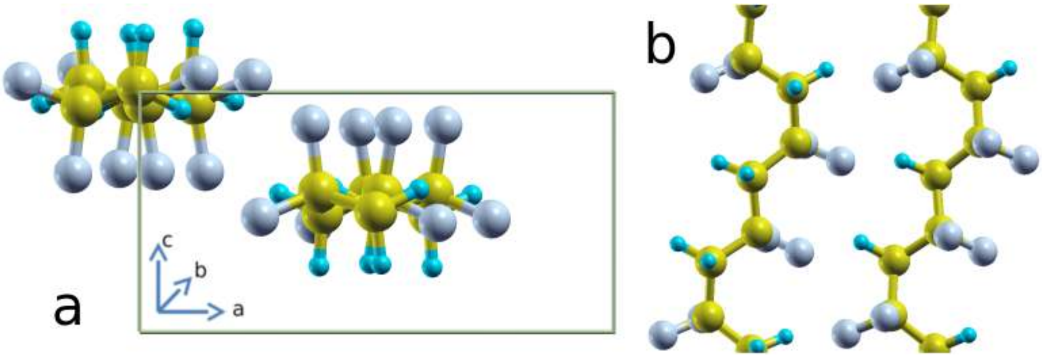

Fig. 2.8 A generic view of ε_{uu}-PVDF. a: front view including the crystal unit box; b: top view of two chains backbone trans bonds $T_3G^+T_3G^-$. F: light grey; C: yellow; H: light blue.

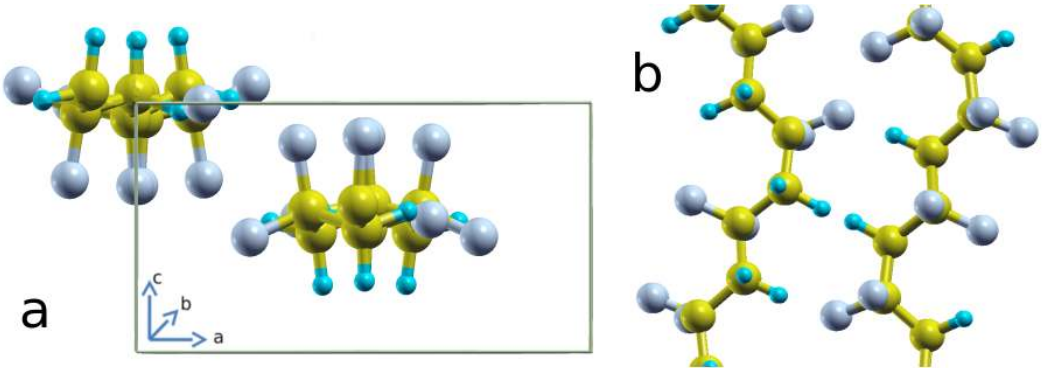

Fig. 2.9 A generic view of ε_{ud}-PVDF. a: front view including the crystal unit box; b: top view of two chains backbone trans bonds $T_3G^+T_3G^-$. F: light grey; C: yellow; H: light blue.

2.2 Polymorphs identification

The experimental determination of PVDF crystal structures can be done using X-Rays Diffraction (XRD) and Fourier Transform Infra-Red (FTIR) spectra which allows to gather structural information about the analysed sample. The XRD technique allows to know detailed information of atoms position and by detecting the repetitive pattern of atoms is possible to identify the minimal repetition of atoms which compose the crystal unit characteristic of each PVDF polymorph, which consequently allows to identify symmetry operators of the crystal lattice and its representative space group. As in principle this is also possible to be done with FTIR, practically, such task is more complex because FTIR is subject to more noise and wavelength interference. Usually FTIR is used for faster crystal structure identification than XRD thank to specific wavelength peaks absorption that every crystal unit possess that is characteristic of the space group and atom geometry of the crystal structure itself[80]. The XRD is a time consuming analysis that needs focus on the identification of every single crystal structure as different authors characterised crystal polymorphs of PVDF individually[68, 65, 63, 64, 66, 67]. The FTIR spectra analysis can quickly let known by looking to the spectra which crystal structures are present in the sample by their representative absorption peaks[80].

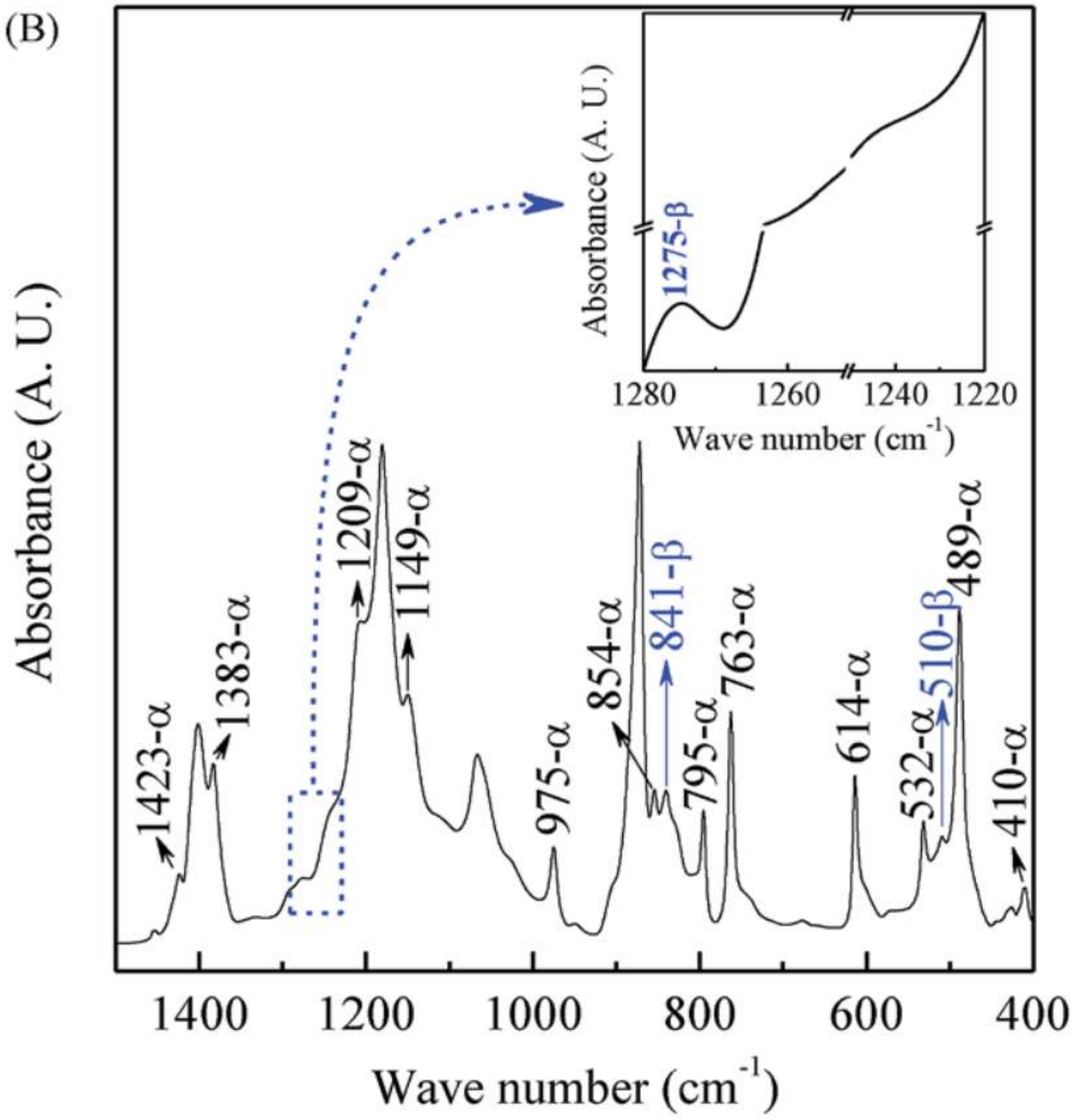

Fig. 2.10 FTIR spectra of a raw PVDF sample. Taken from Cai *et al*[3].

Figure 2.10 represents an IR spectra made by Cai *et al*[3] showing the contemporary presence of different PVDF polymorphs inside the same sample. The peaks 1423, 1383, 1290, 1149, 975, 854, 795, 763, 614, 532, 489 and 410 cm^{-1} are recognised as distinctive peaks of the α-phase as usually expected for raw PVDF sample to be rich in the α-phase, therefore, showing abundant α-phase absorption peaks. The peaks 1275, 841 and 510 cm^{-1} are attributed to the β-phase, which is usually a minority of crystalline seeds present in a raw sample of PVDF. The interesting work of Cai *et al*[3] put in evidence as other authors previously[30, 81, 82] did, the discrepancy it can be usually found between different experimental spectra determination of PVDF FTIR peaks. Cai *et al*[3] showed that often the same absorption peak found by different authors can deviate of $\approx$3-8 cm^{-1} between different studies. Furthermore, Cai *et al*[3] evidenced how different authors attributed a specific peak to different PVDF crystal phases by performing wrong peaks analysis. Such evidences made appreciable the complexity of comparing computational to experimental IR spectra due to the easy divergence experimental FTIR can present.

2.3 Crystallinity control

The most common approach to enhance PVDF crystallinity is to apply post synthesis manufacturing techniques which drives with different mechanisms of action the formation of specific crystalline phases. The priority is to form the β-phase avoiding to have the the α-phase which is widely the most common to appear in raw PVDF samples cooled from a melted state. However, to apply the FE crystals β-PVDF into electronics was still limited by crystallinity issues as nobody provided a complete explanation of the mechanisms that promotes the formation of the β-phase. Indeed, out of several post processing techniques which can increases crystalline yield of the β-PVDF based on physical stresses (e.g stretching and poling), it often happens that such treatments are not efficient enough to bring the sample at crystalline grades of 95% or more (standard crystalline grade for materials which feed electronics devices)[35] and also resulting to be manufacturing processes too aggressive that damages the treated sample that is not further applicable into electronics because of the high stress taken during the manufacturing process[4, 83].

These issues of low crystalline yields (*e.g.* 45-70%) and sample damages (*e.g.* high film roughness or film holes breakages) persisted along manufacturing techniques because as the mechanisms that promotes the β-phase formation is unknown, the successful approaches were found by try and error, essentially forcing the sample to be structured as desired without being aware of what could represent a more mild and effective way of enhancing the β-phase formation. This section introduces the main post processing approaches used to increase crystallinity of PVDF samples in favour of FE crystals. Table 2.2 shows a resuming list of the most common techniques mentioned in the present chapter vault to increase a PVDF sample crystallinity, comparing the efficacy of the β-phase increase, the major drawback of the techniques and its compatibility with the assembly of flexible electronic devices.

Table 2.2 Resuming table of different post processing techniques to increase the PVDF sample crystallinity showing pros and cons of each technique and its applicability in flexible electronics. Appl.: Applicability of the technique to flexible electronics.

Technique	β-phase gain	Defects	Appl.
Stretching	++	Film damages	No
Poling	+	Low polarisability	Yes
Spin coating	+	Sensible to solvents and temperatures	Yes
Thermal annealing	++	Dependent by solvents and surfaces	Yes
Shear stress	+/-	Not for pure PVDF	No
Ionic additives	+/+++	Strongly dependent by the additive	Yes
Zeolites	-	Selective for the γ-phase	No
Nanoclays	+++	Incompatibles for electronics	No
Perovskites	+++	Expensive	Yes
Silicon additives	+	Complex manufacturing	No
PdCl NPs	+++	Expensive	Yes
APAs memebranes	+++	Complex manufacturing	Yes
Surface deoposition	+/+++	Dependent by the surface	Yes

Table 2.3 Percentage of crystalline β-phase increase as function of elongation speed: cm min^{-1}; Taken from Mohammadi *et al*[22].

Stretching rate (cm min^{-1})	β-phase content, F(b) (%)	Accuracy (%)
10	77.6	0.3
20	80.8	0.8
30	81.6	0.7
40	82.5	0.9
45	86.5	1.1

2.3.1 Mechanical stretching

The first approach used to increase the β-phase richness of a sample was to induce the gauche bonds of the recurrent α-phase to become trans bonds, by simply applying a mechanical stretch on a melted PVDF mass during the cooling process, which forces PVDF chains to stretch avoiding the formation of spherulites as the stretching strength pulls chains along the strain opening the spherulites from the middle extending the chains until the next spherulite, which is consequently extended from its middle forming linearised structure characteristic of the β-phase[84]. The stretch makes the chains to become mostly linear towards the stretching direction with a high percentage of the β-phase[85, 22]. Table 2.3 reported the standardised stretching ratio of centimetres per minutes and how the β-phase increased under such stretching strength.

Mohammadi *et al*[22] showed that such technique significantly increases the β-phase content of a sample reaching a crystalline plateau around 86% which is far from the crystalline quality required for electronics devices (*e.g.* 95% or more)[35]. Furthermore, with this technique the thin film produced resulted to be significantly damaged depending on the stretching strength applied, the intensity and duration of the process[4]. Figure 2.11 taken from Caihong *et al*[4] showed that the thin film enriched with the β-phase through a progressive stretching speed suffer real damage and consequently increases the roughness at both film sides even opening cracks and holes within the thin film. Caihong *et al*[4] further proved that by repeating the stretching procedure while preparing a thin film of PVDF at the annealing temperature of 413 K the film damages were reduced of 40%. However, the β-phase percentage content when the sample was stretched and annealed was inferior to an average of 30% since the annealing treatment weakened the stretching efficacy in increasing the β-phase content of the sample which passed from 86%[22] in the simply stretched samples to 30%[4] in the stretched and annealed samples. This provided solid proof of how much such manufacturing technique can damage a FE thin film which makes it not feasible for electronics devices which requires reduced film roughness and homogeneity of the sample[35].

The work of Mohammadi[22] produced a higher crystalline quality of PVDF samples in comparison with the previous investigation of the stretching technique made by Salimi *et al*[86] which reached a 74% crystallinity with the same procedure Mohammadi used without pushing the stretching rate to 6.5 times the initial film length as Mohammadi did. Moreover, when the spontaneous polarisation of stretched thin film was measured by other authors which used the same methodology of Salimi *et al*[86], the polarisation magnitude of the stretched sample resulted to be $\approx$7 μC cm^{-2}[79] corresponding to a β-phase content in the thin film of $\approx$30-35%[4] which was unsatisfying. Stretching resulted to be a manufacturing process not effective in increasing crystalline and ferroelectric performance of PVDF.

In contrast to such evidences of Mohammadi[22] and Caihong[4], Ruan *et al*[84] showed the modest efficacy of the stretching strength to obtain high grade β crystalline samples. Indeed, Ruan *et al*[84] gave evidences of how the stretching strength is of secondary importance and the temperature at which to perform the stretching plays a more crucial role. Indeed, the disruption of spherulites rich in the α-phase occurs with modest stretching rates, while the temperature is crucial to allow chains to chain conformation and properly displace linearly forming β-phase crystalline domains. Indeed, the wrong temperature would lead to film breakages or discontinuities because of a too low or too high temperature applied during stretching, respectively. Such evidences of Ruan *et al*[84] showed how an optimised temperature and tensile strength could reduce films damages still forming β-crystals, underlying that the thermal contribution is more important than stretching itself.

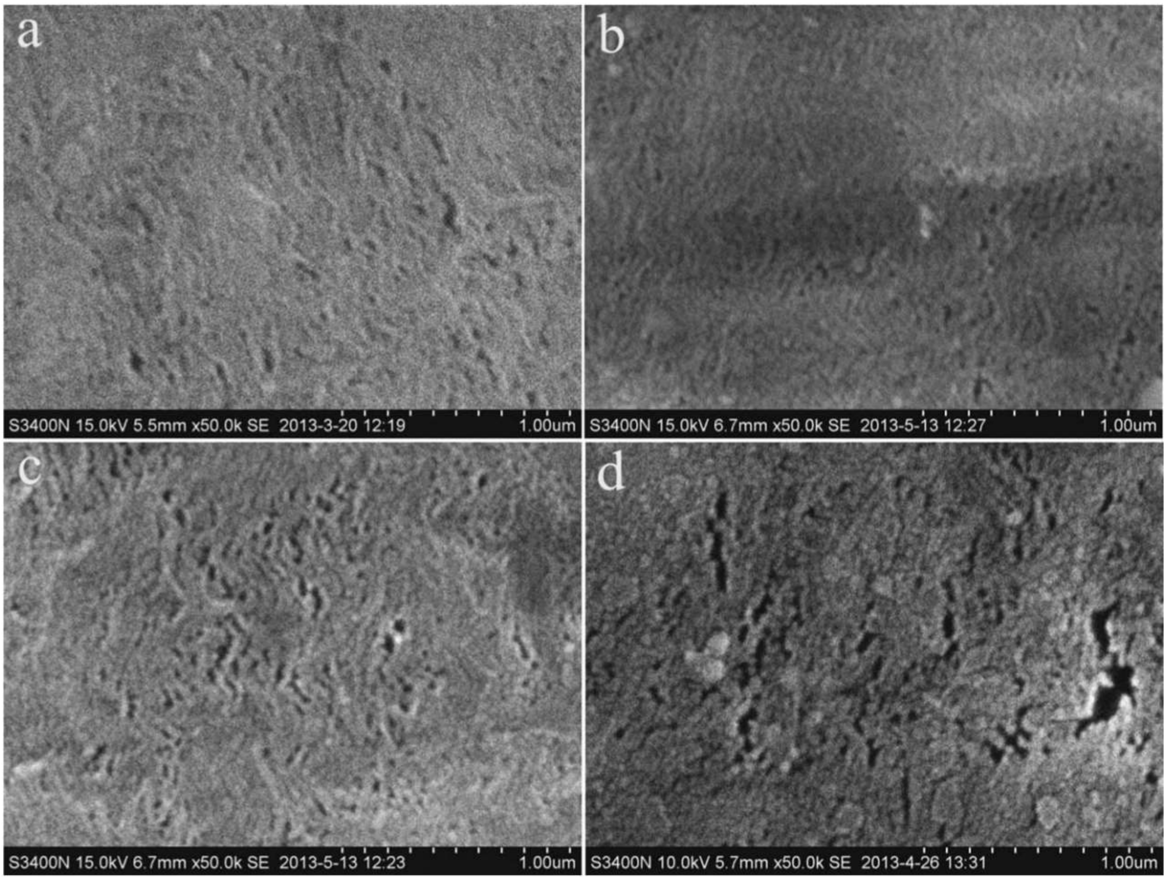
a
S3400N 15.0kV 5.5mm x50.0k SE 2013-3-20 12:19 1.00um
b
S3400N 15.0kV 6.7mm x50.0k SE 2013-5-13 12:27 1.00um
c
S3400N 15.0kV 6.7mm x50.0k SE 2013-5-13 12:23 1.00um
d
S3400N 10.0kV 5.7mm x50.0k SE 2013-4-26 13:31 1.00um

Fig. 2.11 Percentage of crystalline β-phase increase as function of Stretch ratio of a prepared thin film at different stretching speeds at room temperature. a: 0.18 cm min^{-1}; b: 0.6 cm min^{-1}; c: 1.02 cm min^{-1}; d: 2.04 cm min^{-1}. Taken from Caihong *et al*[4].

2.3.2 Poling

An alternative technique showed to be more suitable to increase the PVDF ferroelectric yield of PVDF samples. Such treatment was called poling and consisted in applying to a PVDF sample an electric potential higher than the coercive field of the sample to induce chains conformational changes without intensely stressing the sample. There are two main ways of using poling where in one case it is just the application of an electric potential on a PVDF sample effectively changing chains conformations and the other way if to use poling while heating the film. In the first approach it is possible to induce crystal phase changes of already existing crystalline regions while amorphous regions remains disordered, hence, not useful if the sample is highly amorphous. The second approach, using poling while the film is still under heat (*e.g.* 380-420 K) can influence a more wide chains reorganisation thank to the heat contribution which leaves PVDF chains with more degrees of freedom in reorienting inside the sample and such approach is called plasma poling as the heat is given my a warm plasma flux which surrounds the sample.

In the plasma poling, an applied electric potential to a PVDF thin film clamped between electrodes in a chamber filled with plasma stimulates the phase transition of the α-phase rich sample in favour of the β-phase by the external potential applied. With such approach the polarisation magnitude was proven to be consistent and repeatable but not more than 7.6μC cm^{-2}[72] since β-phase crystallinity never surpassed 40%. Also plasma poling showed to be an unsatisfactory approach to increase the β-phase crystalline content in a sample. Other authors attempted to use stretching and poling together during the film formation but again film damages were found and spontaneous polarisation resulted to be 9 μC cm^{-2}[87, 88], hence, crystallinity of the sample deputed to be around 40-45%, far from the quality standard for transistors and memory devices applications[35].

2.3.3 Solvent effects

The preparation of PVDF solutions[89, 90] became a versatile tool to prepare uniform thin films of PVDF. The basic approach was to dissolve PVDF into compatible solvents and processing such sample as a liquid material[90] at which some additives could be added as discussed further. The outcomes of the solution processing approach resulted to be encouraging in promoting β-phase formation. The most remarkable research papers on solvent effects were the ones of Gregorio Junior *et al*[89] and Salimi *et al*[90] which both prepared thin films of PVDF and analysing such film by FTIR and scanning electron microscopy (SEM) (only Gregorio investigated with SEM) to acquire images of the samples. Gregorio used four solvents such as N,N-dimethylformamide (DMF), N-methyl-2-pyrrolidone (NMP), acetone and hexamethylphosphor-amide (HMPA) while Salimi used N,N-dimethylacetamide (DMAc), and cyclohexanone.

The cyclohexanone showed to be ineffective (in both studies) in controlling any PVDF crystalline phase formation, while all other solvents played a role in that. Having different boiling points (*e.g.* acetone: 58° C, DMF: 110° C, NMP: 147° C, cyclohexanone: 155° C, DMAc: 165° and HMPA: 168° C), different solvents evaporated at different rates and the highest boiling point solvent offered the possibility to heat the sample for longer at higher temperature before the solvent evaporated entirely, factor that increased the formation of the β-phase, moreover, also the solvent polarity showed to matter in the crystalline yield of the β-phase[89, 90].

After film formation the solvent evaporation rate was promoted by keeping under constant heat the sample until all solvent was evaporated (verified by intelligent gravitometric essay[89, 90]). Both research work concluded that the solvent evaporation rate discriminates the formation of α, β and γ phases in the case of DMAc, while the solvents NMP, acetone, HMPA and DMF showed to be selective only between α and β phases[89, 90]. A slow evaporation rate while using NMP, acetone, HMPA and DMF promoted the β-phase formation while fast evaporation rates mainly formed the α-phase[89, 90]. What was common within these two studies of Salimi *et al*[90] and Gregorio *et al*[89] was the heating procedure and the agreement that solvent polarity and evaporation rates have major influences on the crystalline formation of crystal phases in the thin film of PVDF. Indeed, the evaporation speed defines the time frame in which PVDF chains can relax to form ordered crystals, depending on the solvent to favour the formation of the β-phase a different solvent evaporation speed must be selected.

2.3.4 Spin coating, thermal annealing and shear stress

The evolution of solution cast approaches brought to the state of the art of different techniques which opened the experimentation of coating surfaces with PVDF liquid samples. Spin coating is a technique which allow to deposit a defined volume of liquid PVDF as a drop at the centre of a substrate plate which is made to spin and the centripetal force makes the PVDF drop to span and coat the whole substrate plate[2, 91]. The spin coating strength define the amount of shear stress the PVDF drop will receive and this influence the formation of crystal structures of PVDF spin coated on the surface[43]. The thermal annealing is a heating treatment applied on a sample of PVDF which can be deposited on a surface with different approaches an thermally annealed during prior or after the deposition, then, the thermal annealing is used to remove solvents (if present) and favouring the formation of FE crystal phases of PVDF[2]. The annealing temperature and eventually the solvent used are as crucial as the substrate support on which PVDF is deposited on by shear stress (*e.g.* gold, alumina, glass, graphene). Spin coating and thermal annealing were here briefly presented since they were applied in many surface studies, hence, to avoid repetitions further in the text the concept of their mechanism has been here introduced and briefly mentioned further in the text when pertinent.

The shear stress is a standalone technique that exert a strain stimulus by immobilising a melted sample between to plates, and during the cooling when the sample reaches a specific temperature arbitrarily defined, the shear stress is applied by applying a constant deformation strength on one or both plate which are immobilising the cooled sample. Such technique has been used by several authors[92, 93] showing that shear stress increased the β-phase content within the sheared sample. However, in realising electronics components the use of shear is not allowed as it would not allow to precisely control the polymer deposition between different circumscribed FE units separated from each others by few nanometers. Moreover, PVDF is a thick polymer which does not respond well to shear and usually copolymers or polymer blends are used to make PVDF less thicker for shear stresses. For such reasons shear stress has been briefly cited but not considered of main interest for the present thesis.

2.4 Additives effects on PVDF

The use of additives became an effective approach to increase crystallinity of PVDF sample, although, some additives are not compatible with electronic devices manufacturing, such technique can make use of heterogeneous additives some of which remains compatible with flexible electronic devices. The main limitations of such post processing technique is to solve the diffusivity of the additives within the PVDF sample, as too big particles can not diffuse easily and too small particles would loose efficacy in enhancing the sample crystallinity. However, some additive has the potential to exalt the FE properties of PVDF, hence, such post processing approach inspired research interests as discussed in this section.

Indeed, it was also the case where other authors proved that using nanoparticles as additives which contained metals such as $BaTiO_3$ and Pd-Cl NPs the formation of the β-phase was still effective, and indeed, such NPs could provide both charge magnitudes (positive and negative) depending on the polarisation state[6, 5]. Hence, it would be more probable that despite the molecular charge present on an NPs side, charges could influence PVDF chains conformation thank to compatible charges interactions between PVDF side chain atoms and the charged molecules making PVDF chains to assume the best conformation that displays more homogeneously side atoms in contact with the charged molecules. As from literature a clear answer of what about charged molecules additives promotes the formation of FE crystals of PVDF, this question still remains to be answered.

2.4.1 Ionic molecules as additives to PVDF solutions

In addition to solvent effects, the use of additives is frequently used to enhance the the β-phase formation and Ying *et al*[94] studied different additives ionic species spacing from negative, neutral and positive charged molecules dissolved with PVDF and compatible solvents. Such molecules were added in small weight to volume ratio (*e.g.* $0.5 \div 3.0\%$) to a PVDF sample to elucidate which ionic class could act as the best nucleating enhancer for the β-phase. In such study, the abundance of the molecular specie added to PVDF, the effect on the melting temperature as well as the relative abundance of crystal structures present into the samples were evaluated in depth and it emerged that the best nucleating agent was effective in small percentage (*e.g.* 2 wt %) and it significantly increased the β and γ phases content of the sample[94].

Ying *et al*[94] observed with Differential Scanning Calorimetry (DSC) the PVDF crystallisation dynamics from a neat sample of PVDF and when ionic molecules were added, evidencing that the T_m of the solid thin film increased significantly upon addition of positive nucleation agents. The maximum increase in T_m of 8 and 9 K was observed with an addition of 2 wt % of positive nucleating agents (NAp$-$3, 5, 6, and 7 as described in the paper). The higher T_m of PVDF in the blends has been attributed to the presence of the β and γ phases of PVDF as these polymorphs are known to have higher melting temperatures[5]. Ying *et al*[94] verified the presence of crystalline phases of PVDF by collecting attenuated total reflectance IR spectrum.

The bands at 614, 763, 795, and 975 cm^{-1} were recognised as characteristic of the α-phase, clearly observed in neat PVDF and peaks at 1275 and 839 cm^{-1} were considerate indicative of the presence of the β-phase, and the peaks at 1231, 839, and 811 cm^{-1} were ascribed as the formation of the γ-phase[94]. Ying *et al*[94] that the α-phase almost disappeared in the samples containing 2 wt % of positive nucleation agents. At the same time, strong β-phase and γ-phase bands at 839, 1275 cm^{-1} and 839, 1231 cm^{-1} appeared, which meant for a change of chain's conformation. At the opposite, the α-phase remained steady in the samples containing negative and neutral nucleating agents[94] as absorption peaks of the α-phase at 975, 795, 763, and 614 cm^{-1} of a pure PVDF sample without any added molecule were conserved in sample with the addition of negative and neutral nucleating agents[94].

As the concentration of the NAp-3 increased from 0.05 wt % up to 8 wt %, the peaks associated with the α-phase decreased, replaced by the β bands at 1275 and 840 cm^{-1} as well as absorption bands attributed to the γ-phase PVDF at 1233 and 840 cm^{-1}, indeed, their intensity also increased as the concentration of NAp-3 augmented. Ying *et al*[94] concluded that α-PVDF with its chain conformation and anti-parallel dipoles alignment is disfavoured in interacting with nucleating agents[94]. In contrast, the conformations of the β or the γ phase resulted in a much greater interaction with the positive nucleation agents. Ying *et al*[94] proposed that the driving mechanism in forming the β and γ ferroelectric phases was due to the ion-dipole interaction that caused the polymer chain to align on the nucleation agent surface, favouring the preferential formation of β or γ structures of PVDF instead of the α-phase. However, such mechanisms of FE crystals formation was only proposed and not verified against other plausible mechanisms, hence, a conclusive hypothesis was not formulated and still missing form literature papers.

Another analogue study was performed by adding water and ionic hydrated salts to a PVDF sample by Song *et al*[95] which concluded that some positive hydrated salts at specific concentrations promoted the β-phase formation more than the α phase, however, such research paper has not been considered relevant since the use of water and hydrated salts bring a prominent problem that hygroscopic salts will strongly retain water or even rehydrate from a dried sample and this goes in strong conflict with the use of such prepared samples with electronics devices which tolerate very small percentage of humidity (*e.g.* 1-4%)[35].

2.4.2 Nanoclays, zeolites and perovskites as additives

The use of dopants was the most recent research branch applied to PVDF which saw heterogeneous molecules used as promoter agents of the ferroelectric crystal phases of PVDF such as the β and γ. Lopes *et al* found and effective way of enhancing the γ-phase yield by using a nanoclay made of montmorillonite[23] (other nano clays were tested and montmorillonite resulted to be best enhancer) and subsequently using NaY zeolites nanoparticles[24] as additives and in both studies Lopes verified the crystalline yield by using FTIR spectrum analysis.

Table 2.4 γ-phase content for PVDF with wt 0.5% of Montmorillonite nanocomposites obtained by recrystallisation after melting at different temperatures. It was reported that the samples crystallised after melting at 210 °C crystallised fully in the α-phase. The accuracy in estimating the β-phase content using FTIR has been evaluated to be ≈0.6%. Taken from Lopes *et al*[23].

Temperature (°C)	percentage of γ-phase (%)
170	97
180	98
190	96
200	95
210	0
220	0

In its first paper Lopes *et al*[23] tested the efficacy of montmorillonite nano clays that resulted to be effective to a montmorillonite wt of 0.5% and profiled the best temperature range at which to melt the clay with PVDF which was found to be between 170-190°C as reported in Table 2.4. Beyond 200°C as for melted samples at 210°C and 220°C the resulting crystal phase of the PVDF sample was found to be mainly the α-phase[23], hence, a temperature threshold was found where the nanoclay lost its crystalline enhancing efficacy on PVDF. In the second paper[24], Lopes used the optimal temperature range between 170-190 °C defined in the first paper[23] and used NaY zeolites showing that the optimal percentage content of NaY additive to peak the highest γ-phase content was to a wt of 24% of

NaY as reported in Table 2.5. The research of Lopes *et al*[24, 23] has been the first to uncover a feasible procedure to reach high crystalline yield of the γ-phase where both fillers such as montmorillonite and NaY zeolites reached a γ-phase crystalline content of 97% and 98% as reported in Tables 2.4 and 2.5, respectively.

Table 2.5 γ-phase content for the PVDF/NaY zeolite composites with different NaY content and crystallised after annealing at 190 °C and recrystallised. It was reported that the samples crystallised after annealing at 210 °C crystallised fully in the α-phase[23]. Taken from Lopes *et al*[24].

NaY (wt %)	Percentage of γ-phase (%)
4	89
16	96
24	98
32	97

Table 2.6 β-phase content for the PVDF/$BaTiO_3$ mixture made with different percentage content of $BaTiO_3$ and different average particle sizes. Taken from Mendes *et al*[5].

$BaTiO_3$ content (wt %)	β-Phase content (10 nm)	β-Phase content (500 nm)
5	82%	42%
10	70%	41%

Such research work by Lopes *et al*[24, 23] presented very interesting results which could be brought to a more deep analysis of the spontaneous polarisation of such highly crystalline γ-phase samples. Indeed, the experimental measurement of the spontaneous polarisation of the γ-phase has never been conducted for the difficulty in producing high grade γ crystalline domains and here a new fresh input of valuable insight of the γ-phase could be added analysing its ferroelectric behaviour, although, it would not be the FE crystal of choice for electronics devices as the β-phase has superior FE properties[40], to uncover the FE behaviour of the γ-phase would be still important for scientific knowledge.

Analogously, Mendes *et al*[5] studied the effect in the β crystalline yield by using the BaTiO3 perovskite as small nano particles of ceramic crystals as additive dispersed into PVDF samples dissolved into compatible solvents. The work of Mendes *et al*[5] remained focused on the crystalline increase of the β-phase using $BaTiO_3$ perovskite as additive and in such study Mendes emphasised the importance of the particle size of $BaTiO_3$ ceramics in the enhancing efficacy to nucleate the β-phase. Since different $BaTiO_3$ average particle size exerted significant differences in promoting FE crystals formation, Mendes *et al*[5] underlined such efficacy by verifying with FTIR the β crystalline yield within different samples that was more effective when the $BaTiO_3$ ceramic particles were rather small with a particle size distribution with average of $\approx$10 nm. Bigger particles size of $\approx$500 nm of $BaTiO_3$ showed to have small effect on the crystalline yield of the β-phase as reported in Table 2.6.

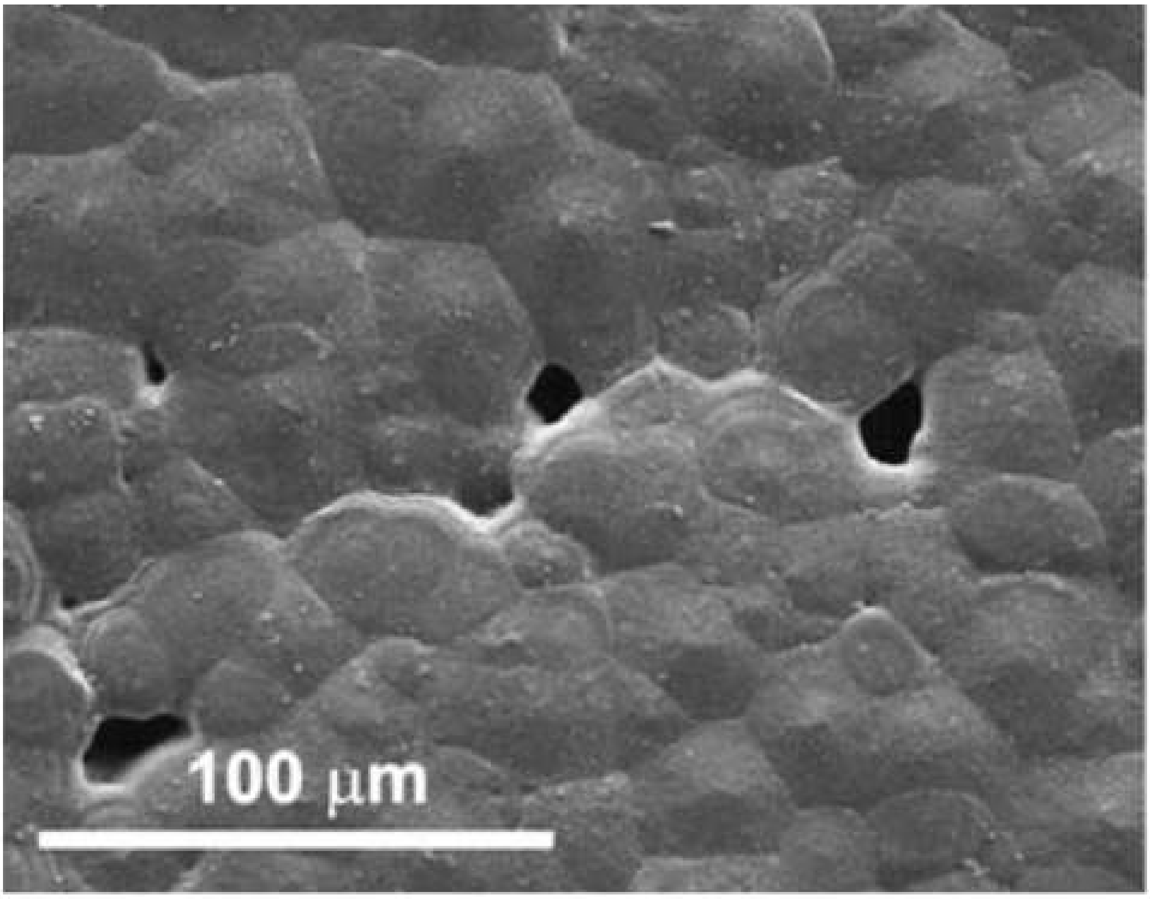

Fig. 2.12 Sample of PVDF/$BaTiO_3$ mixture rich in spherulite domains containing $BaTiO_3$ ceramic particles of average size of 500 nm. Taken from Mendes *et al*[5].

Conceptually the particle size should be of relative importance since the crystalline enhancement of the β-phase should also be achievable on a flat surface of $BaTiO_3$ if the interface interaction of the $BaTiO_3$ ceramics crystal is able to promote the nucleation growth of the β-phase, however, in term of additives, too big particles represented a diffusivity problem and Mendes uncovered that big particles of $BaTiO_3$ were not able to diffuse homogeneously in the sample for at least the preparation condition used in the research work conducted by his research group[5]. Furthermore, the particle size has been retained relevant for the surface area the particles can display to interact with PVDF chains promoting crystallinity with a gaussian distribution of particle size and efficacy in crystalline enhancement[5]. Figure 2.12

showed that average particle size of 500 nm left a macroscopic organisation of the PVDF sample with a considerable amount of spherulites which are known to be made mainly of α-phase crystalline layers disposed in spherical lamellae[1]. Again, Mendes *et al*[5] ignored the spontaneous polarisation of PVDF/$BaTiO_3$ composites samples and in such case, considering that $BaTiO_3$ is a ferroelectric ceramic which already possesses a high spontaneous polarisation of its own (*e.g.* 50 μC cm^{-2})[96], $BaTiO_3$ could represent a proactive additive which stimulates the β-phase formation and strengthen the spontaneous polarisation of PVDF thin films added with $BaTiO_3$.

2.4.3 Silicon nanoparticles as additives

The work of Ramasundaram *et al*[25] aimed to produce highly crystalline β-PVDF samples by making thin films added with organically modified silicon (OMS) nanocomposites derived from chemical modification of lucentite clay as PVDF/OMS. The preparation of PVDF/OMS samples was performed in batches from havin neat PVDF to PVDF/OMS from a wt from 0.05% up to 2% optimising the process by forming the film by melt quenching and annealing (MQ-AN) at 160°C. The PVDF samples doped with OMS and MQ-AN were found to have a correlation between the crystalline content of the β and γ phases in the samples as the OMS content increased due to the interaction of the dopant with PVDF chains favouring the β-phase formation proportionally with the increase of dopant. With the progressive increase of OMS content the α peaks disappeared and β and γ absorption peaks appeared as the OMS content increased and at 2.0 wt % only the β-phase was found[25]. Table 2.7 reported the crystal phases found at every wt % ration of OMS added into the PVDF thin film showing that to a 2% wt mainly the β-phase was found, although Ramasundaram did not estimated the percentage content of the β-PVDF no other crystal structures were found. Also in this study the measurement of the spontaneous polarisation that has not been performed would have represented an important property to appreciate the quality of the FE behaviour of such thin film of PVDF/OMS(wt 2%).

Table 2.7 PVDF crystal phases content with increasing wt % of OMS by MQ-AN the thin film samples. Work made by Ramasundaram *et al*[25].

OMS (wt %)	PVDF crystal phases found
0-0.5	α
0.5-1.5	γ, β
2.0	β

2.4.4 Palladium Chloride nanoparticles as additives

The research milestone performed in terms of a PVDF dopant in producing thin films of doped PVDF was conducted by Mandal *et al*[6] which applied a dopant to enhance the β-phase crystallinity which was spin coated on a clean glass surface to assemble a functional memory unit and subsequently testing the writing, reading and erasing of bits of information on such support by using dynamic contact electrostatic force microscopy (DC-EFM). In this case the dopant was palladium chloride nano particles (PdCl-NPs) with average diameter of 3 nm[6] trying two PdCl-NPs concentrations of 0.1 and 0.2 wt % added to the PVDF sampled melted with DMF. The crystalline yield was remarkable and Figure 2.13 showed the macroscopic conformation of α and β domains distribution differences between a neat PVDF sample and a PdCl-NPs doped PVDF sample.

Figure 2.13-a reported the field emission scanning electron microscopy (FE-SEM) of a neat PVDF sample evidencing the reduced amount of β-phase domains present in the absence of dopant and Figure 2.13-b reported the effect of the PdCl-NPs dopant on the PVDF doped sample which fully nucleated the β-phase in an equivalent surface area taken at FE-SEM. Such evidence was further strengthen by the effect of the PdCl-NP dopant in reducing the film roughness, indeed, the Atomic Force Microscopy (AFM) showed in Figure 2.13-c the imaged of neat PVDF and in Figure 2.13-d the film roughness at three different regions of the film. In contrast Figure 2.13-e-f showed the same image and roughness plot, respectively, for the PVDF/PdCl-NP doped thin film which showed a completely different topographic surface image (Figure 2.13-e) also with reduced roughness (Figure 2.13-f) of $\approx$60% less than neat PVDF.

The experimental evidences reported a remarkable increase of the β-phase formation in PdCl-NP doped PVDF thin films also reducing the film roughness. Furthermore, the research conducted by Mandal *et al*[6] investigated the mechanism or writing, reading and erasing bits of information on the PdCl-NP doped PVDF thin film. Figure 2.14 reported on the left panel the behaviour of neat PVDF (Figure 2.14-a-c) while on the right panel it was reported the behaviour of PdCl-NP doped PVDF (Figure 2.14-b-d). In Figure 2.14-a the neat PVDF sample has been written analogously to the inner square of Figure 2.14-b and erased on the outer square analogously as in Figure 2.14-b, but in Figure 2.14-a no squares were observed while in Figure 2.14-b the inner and outer squares were both present and distinctly visible with a light yellow colour different from the dark orange of the background sample not interested from the writing and erasing currents. The plots under Figure 2.14-a-b showed the electrostatic surface potential which is as background noise in Figure 2.14-a and well disciplined in Figure 2.14-b.

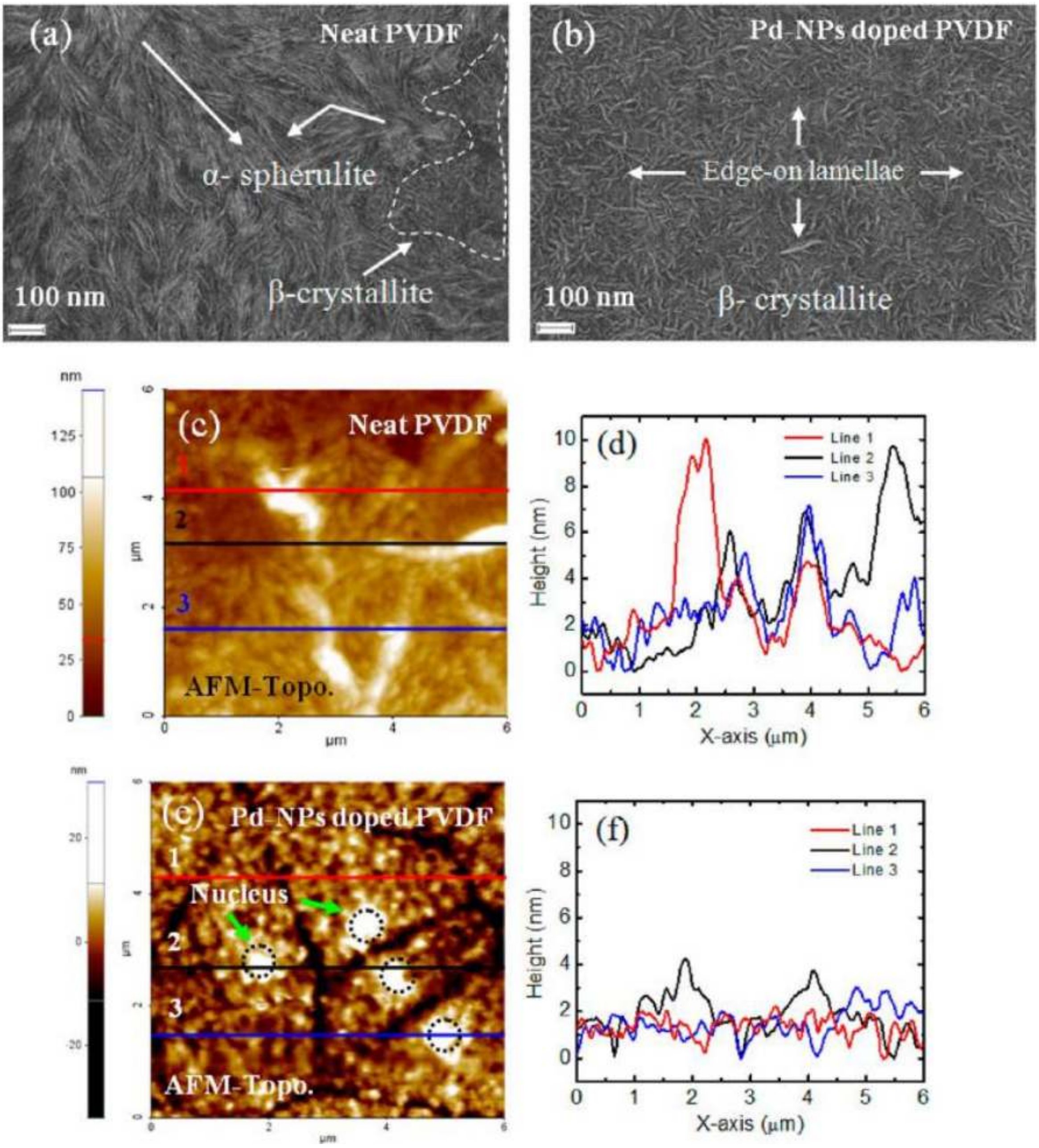

Fig. 2.13 FE-SEM images of (a) neat PVDF and (b) PdCl-NP-doped PVDF thin films. AFM topographic images (scan area 6 μm × 6 μm) of (c) neat PVDF and (d) corresponding line (roughness height at three different intersecting lines) profiles and (e) a PdCl-NP-doped PVDF thin film and (f) the corresponding line (roughness height at three different intersecting lines) profile. Taken from Mandal *et al*[6].

The phase shift induced by the writing and erasing currents in neat PVDF was reported in Figure 2.14-c as random, hence, not disciplined by the applied potentials, while Figure 2.14-d reported the distinct phase inversion of the inner and outer squares of PdCl-NP doped

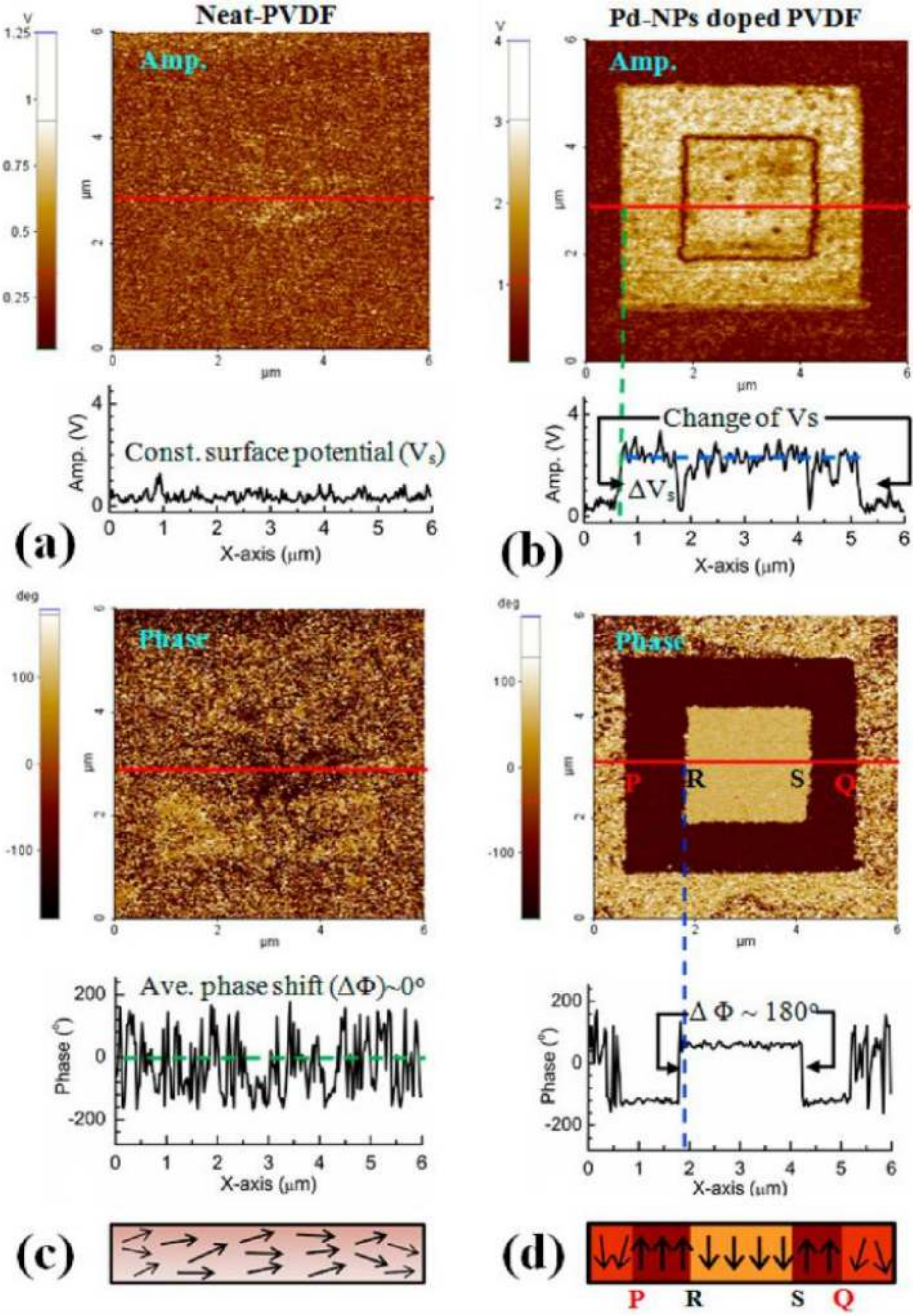

Fig. 2.14 DC-EFM images ((a, b) amplitude, (c, d) phase) of neat PVDF (left panel) and PdCl-NP-doped PVDF (right panel) thin films. Scan area: 6 μm × 6 μm. The corresponding line (marked with red lines) profiles are shown at the bottom (a, b) and in the middle (c, d) of the each image. (Bottom of c and d) Schematic illustrations of the orientation of the dipoles (cross-sectional view) along the marked lines shown in the DC-EFM images. Taken from Mandal *et al*[6].

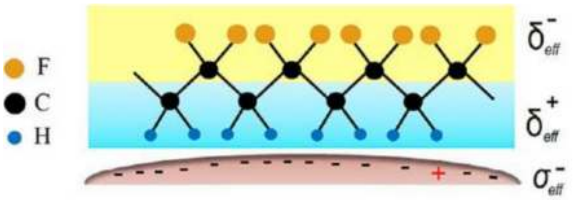

(a) CASE I : the effective surface charge density of the nanoparticle is negative.

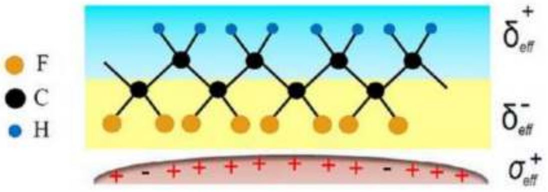

(b) CASE II : the effective surface charge density of the nanoparticle is positive.

Fig. 2.15 Schematic representation of the electrostatic interaction between the surface charges of nanoparticles and the CH_2/CF_2 dipoles of PVDF. Taken from Mandal *et al*[6].

PVDF which were written and erased by the applied current, respectively. The plots under the Figure 2.14-c-d reported the phase shift induce the currents applied to the sample which did not affected the neat PVDF sample of Figure 2.14-c as well as the dipole sketch below the plots and at the contrary the potentials applied to the PdCl-Np doped PVDF thin film affected phase order which as sketched below the plot of Figure 2.14-d it reminds the dipole orientation which oriented towards the potential applied.

Mandal *et al*[6] evidenced that the dipole momentum can be reversed in the PVDF sample doped with PdCl-Np and showed that the dipole switch can be red back and verified after writing as a permanent information written into the sample. In Figure 2.15, Mandal *et al*[6] conceptualise that the PdCl-Np could promote the β-phase formation by charges interactions of PVDF side chain atoms, a type of interaction which brings the PVDF chains backbone to linearise to maximise the side atom charges interactions. Obviously, in the case of PVDF the polarisation was referred to the spontaneous polarisation of the crystal phase, for the palladium atoms of PdCl-NPs the polarisation was referred to the soft polarisation of the palladium electrons influenced by the electric potential, hence, forming a stable complex of β conformers. Such conclusive study was the only case were a ferroelectric thin film of doped PVDF was formed and tested for writing, reading and erasing memory operations. In conclusion, the use of additives to enhance PVDF sample crystallinity in favour of FE phases such as the β and γ resulted in showing a trend where positively charged molecules as additives enhanced the content of β and γ phases as some authors proved that[24, 23, 25, 94].

2.5 PVDF on surfaces

The use of additives and solvents showed some interesting results in promoting the formation of FE crystals of PVDF with the possibility to discriminate between the formation of the β or γ phases, showing that is possible to find selective condition towards the nucleation of FE PVDF crystals. The mechanisms which promotes the FE phase formation remained not understood and considering that modern electronic devices are built at the nanoscale were a FE material is deposited on a surface substrate, the interests of the present thesis has been move towards studying the way a surface and its properties can positively affect the β-phase nucleation, as the following literature is presented and discussed. With the interest in getting nearer to the realisation of applicable electronics devices and to understand what is the promoting physical mechanisms which increases the β-phase formation, the study of PVDF deposited on different types of substrates took its steps into experimental observation towards different deposition techniques and surface materials.

A post processing technique developed to deposit mono atomic layers of material on a surface was the Langmuir−Blodgett deposition which assures the realisation of ultra thin ferroelectric films of PVDF deposited on a substrate. The technique consisted in immersing and retrieving a solid substrate from a liquid solution that contains the polymer melted into an appropriate solvent to deposit layer by layer the polymer chains on the substrate by repetitive bath cycles[97] (deposition of a single molecular layer per each bath cycle). This approach was the first of the kind which allowed to deposit PVDF layers in close contact with a substrate significantly reducing roughness at the interfaces which would increase greatly the final sample quality, however, such approach was mainly applied not on pure PVDF but on P(VDF[70%]-TrFE[30%]) copolymer samples[98, 99]. For this reason such technique has been only briefly mentioned and not discussed further.

Another approach to enhance PVDF ferroelectric properties was attempted in the nanoconfinement of PVDF into Anodic Porous Alumina (APA) matrices were Cauda *et al*[57, 7] characterised the efficacy of such approach from a macroscopic morphological point of view[7] and then proceeded to characterise piezoelectric and ferroelectric properties of fluorinated polymers of such nanoconfined assembly[57]. The schematic sketch of Figure 2.16 is to give an idea on how PVDF dissolved in solvent (*e.g.* NMP removed by heat) filled APA mesopores as the procedure was defined in the first research work conducted on PVDF/APA and SEM image of the PVDF nanofibres generated is reminded to Figure 1a, 1b and 1c of the Cauda *et al*[7] research paper.

The nanoconfinement that supposedly enhanced the formation of β-crystals in a long vertical pile with chains loops between stacked layers as showed by Cauda *et al*[57, 7] in Figure 2.16, the spontaneous polarisation remained accessible by direct measurement on

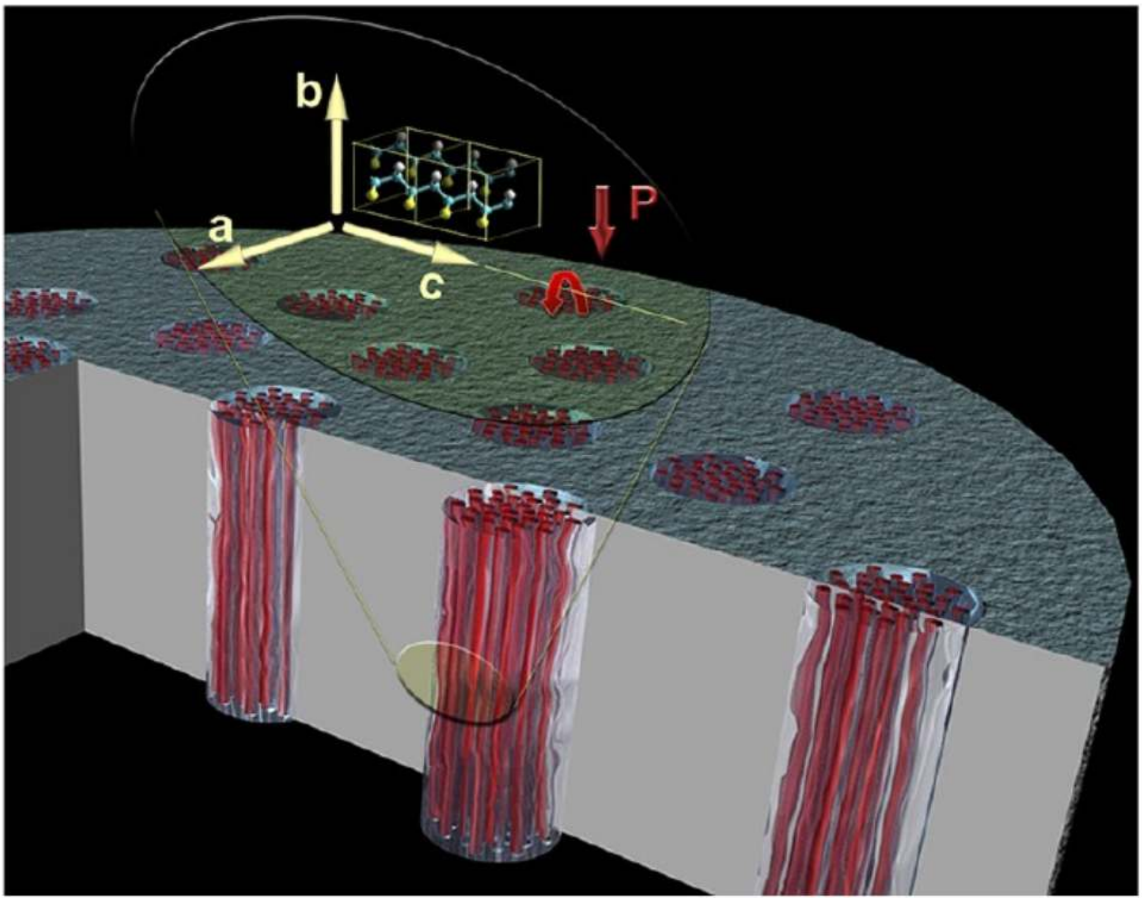

Fig. 2.16 Schematic sketch to make visible the β-PVDF chains orientation. Taken from Cauda *et al*[7].

the APAs edges. In this type of assembly, the PVDF thickness is dominate by the APA matrix height which could represent a problem because if the film is too thick it does lose spontaneous polarisation potential despite the crystalline grade considered[8]. Thus far, Cauda *et al*[57] applied the same nanoconfinment methodolofy for pure PVDF and copolymers of P(VDF-TrFE).

The spontaneous polarisation potential reported for P(VDF-TrFE) resulted to be almost a half of the spontaneous polarisation measured for pure PVDF. The spontaneous polarisation of nanoconfined P(VDF-TrFE) resulted to to be 9.6 μC cm^{-2} and 19 μC cm^{-2} for pure PVDF showing a neat superior performance of PVDF against its copolymer[57, 7]. In this investigation the spontaneous polarisation of pure PVDF resulted to be the highest ever reported[57, 7]. The crystallinity of the sample was verified by X-ray diffraction (XRD) as well as FTIR after spin coating the APA matrices with PVDF and P(VDF-TrFE).

As the use of graphene has attracted strong interest in a very wide range of material science applications, also PVDF has been approached with the addition of carbon materials, to verify the ability of carbon nanutubes and graphene sheets used as surfaces in enhancing the sample crystallinity in favour of the β-phase. El-Achaby*et al*[100] showed that the addition of GO nanosheets (GO$_n$) or multilayer GO sheets to a PVDF sample both dissolved in DMF and formed as thin films, increased the β-phase content verifying the trans bonds abundance by FTIR analysis. An interesting investigation dedicated to surface effects of graphene on PVDF assembling MFM devices was performed by Kang *et al*[8], although, Kang used the P(VDF-TrFE) copolymer, such studied remained of interest. A sandwich construct was made by using a field effect pentacene layer as an opening gate substrate on which on top of it, a layer of silicon as control substrate in one prototype, and a graphene sheet as higher promoting surface of the β-phase in the other prototype, were assembled. On both tops of the silicon surface and the graphene sheet, a copolymer made of P(VDF-TrFE) was spin coated and annealed at 200°C[8]. The two different sandwich prototypes were represented with a schematic sketch on top a SEM image in Figure 2.17-a and 2.17-b, respectively.

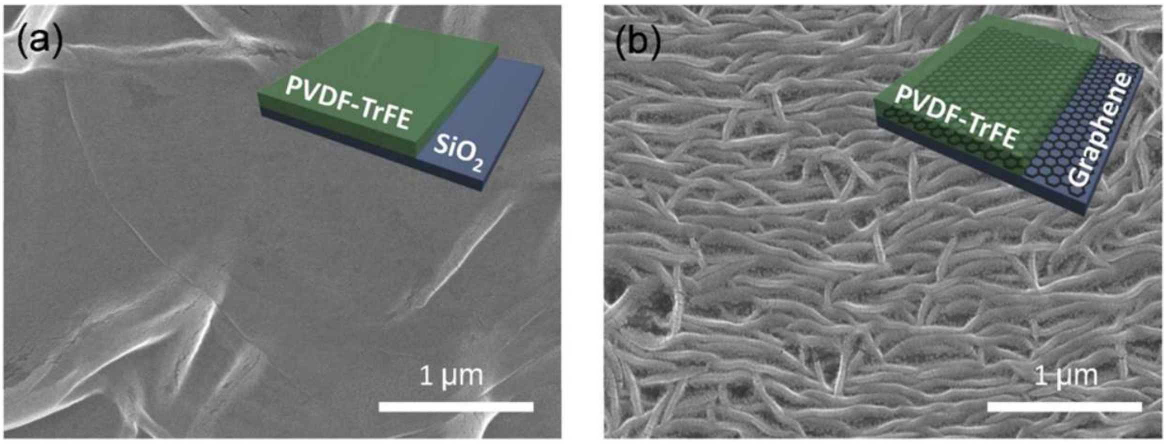

Fig. 2.17 SEM images of 3 wt % PVDF-TrFE on (a) SiO 2 and (b) CVD-graphene substrates thermally annealed at 200 °C for 30 min. The inset presented a schematic of the sample structures. Taken from Kang *et al*[8].

The MFM assembly copolymer/graphene resulted to have a significant superior spontaneous polarisation of $\approx 7\ \mu$C cm^{-2}[8] ($\approx 5\ \mu$C cm^{-2} for the MFM without graphene). Kang *et al*[8] investigated with molecular dynamics the copolymer backbone displacement of one PVDF chain on the graphene sheet observing that the carbon bonds of the graphene sheet were similar in length to the backbone carbon bonds of the copolymer chain which geometrically displayed in a zig-zag pattern along carbon rings edges, factor that should have been promoting the higher spontaneous polarisation found into the MFM assembly with graphene[8], although, the spontaneous polarisation of this MFM assembly remained significantly weaker than pure PVDF thin films deposited on other substrates (*e.g.* 19 μC cm^{-2}[7, 57]).

The case of study of a gold surface was faced with the use of spin coating to cover a gold plate and appreciate the effect of such metal in the formation of FE crystals of PVDF conducted by Kang *et al*[2]. To uncover the hypothesis that the surface itself does affect crystal growth Kang spin cast PVDF dissolved in DMF on a gold plate which was left as raw metal and also functionalised in thin stripes by self assembled monolayers (SAMs) able to chemically link on the gold surface an skirmish the gold properties offering to PVDF -COOH chemical groups. With this approach the gold surface was partially covered in SAMs and partially available as raw metal to the PVDF which was going to be spin cast on top of it.

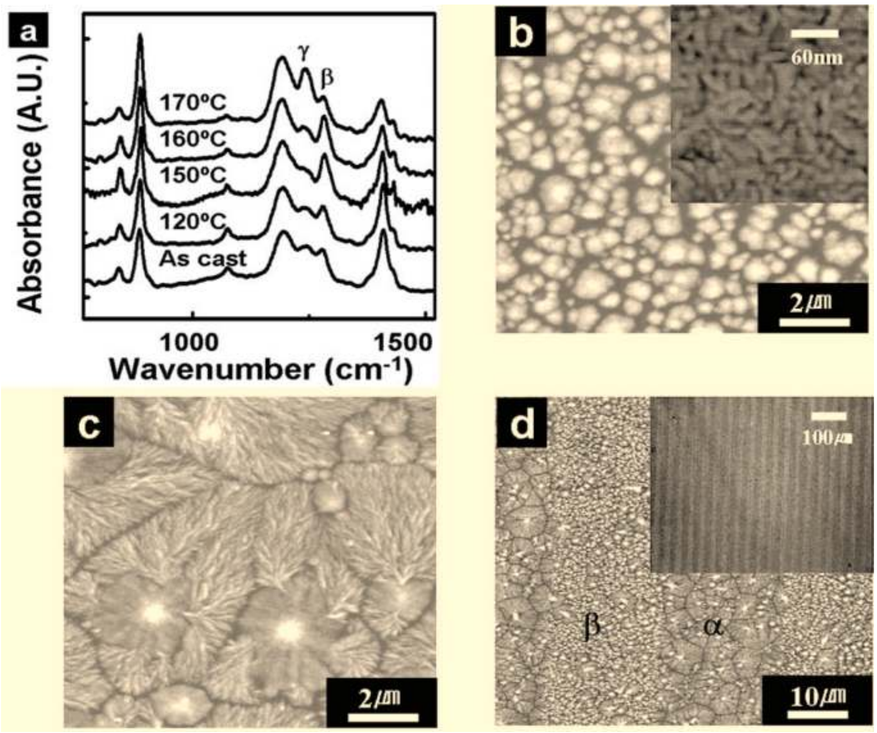

Fig. 2.18 (a) Grazing incidence reflection absorption (GIRAS) FTIR of the the inset of (b) displays a magnified image with the characteristic needlelike β crystals. (c) AFM images of a PVDF film spin cast and rapidly annealed on COOH-terminated SAMs treated Au substrate. AFM (d) and OM image show micropatterned β and α PVDF crystals. Taken from Kang *et al*[2].

Kang *et al*[2] provided solid evidences that depending on the surface substrate used, PVDF which is deposited on top of it, tends to form different crystal structures depending on the chemical properties of the surface itself. Different types of surfaces can indeed promote specific crystal phase formations, however, to find which surface does promote more efficiently the formation of the β-phase must deal with the understanding of which chemical interaction that has to occur between PVDF and the substrate to promote the β-PVDF crystallinity, otherwise, try and error experiments would become countless. The understanding of such chemical interaction has not been found yet, neither by Kang or other authors.

The raw gold metal resulted to favour the β-phase formation with a not excellent efficiency since the crystalline yield was measured to be 40%[2] and the spontaneous polarisation to be 7 μC cm^{-2} in agreement with spontaneous polarisation of plasma poled PVDF thin film which reached a crystalline percentage of the β-phase of ≈40%[72]. As visibile from Figure 2.18-a the Grazing-incident reflection absorption spectra (GIRAS) reported that when the DMF dissolved PVDF sample was spin cast and annealed between 150°C and 160°C the peak at 840 and 1280 cm^{-1} reached the maximum intensity which confirmed the presence of the β-phase estimated to be 40% of the sample region where the β-phase formed on the raw gold surface[2].

Figure 2.18-b showed and AFM image of region of space where the raw gold plate mainly presented β crystal domains, while Figure 2.18-c a region of space where the gold plate covered with SAMs mainly formed the α-phase visible by the spherulites domains it forms macroscopically[1] and Figure 2.18-d show a magnification of a larger area of the gold surface where was visible the confines of the gold strip covered with SAMs and raw gold regions by the alternation of β seeds and α seeds in stripes as the SAMs were deposited[2]. The experimental conditions produced in the study of Kang *et al*[2] reached averaged performance in promoting the β-phase formation.

2.5.1 Evaporated oligomers on glass substrates

Noda *et al*[29] characterised the remnant polarisation of evaporated olygomers under vacuum cryogenic evaporation at -160°C forming 500 nm thin films which in the MFM assembly resulted to be a working ferroelectric unit having a remnant polarisation of 13.0 μC cm^{-2}[29]. Also the ferroelectric (testing pyroelectric currents) reliability as function of temperature was examined as at 75°C the VDF olygomers film switched from being ferroelectric to be paraelectric[9] as reported in Figure 2.20-left, although, the best fitness temperature of VDF FE units was found at 61°C which was surprising to see that the optimal operating temperature was that near to the paraelectric switch temperature. Furthermore, the crystallinity of the VDF olygomer film was verified by XRD crystallography as Figure 2.20-right reported that a neat majority of β-phase (≈86% crystallinity) was formed in the VDF evaporated film. Such evidences well matched with the observation than with a β-phase crystallinity of 40%, a spontaneous polarisation of 7 μC cm^{-2} was observed by previous authors[2, 72] and here with around double the crystallinity (≈86%) the spontaneous polarisation was almost the double as reported by Noda to be 13.0 μC cm^{-2}[29].

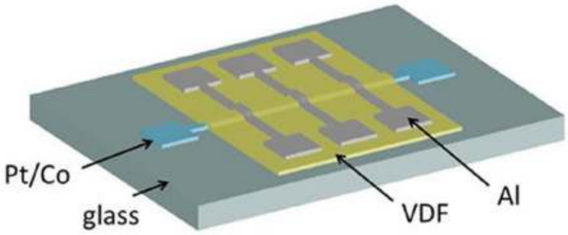

Fig. 2.19 Schematic sketch of the ferroelectric device assembly. Pt/Co: Platinum Cobalt bottom electrode; VDF: VDF olygomers; Al: Aluminium top electrode; glass: glass support of the chip. Taken from Foreman *et al*[9].

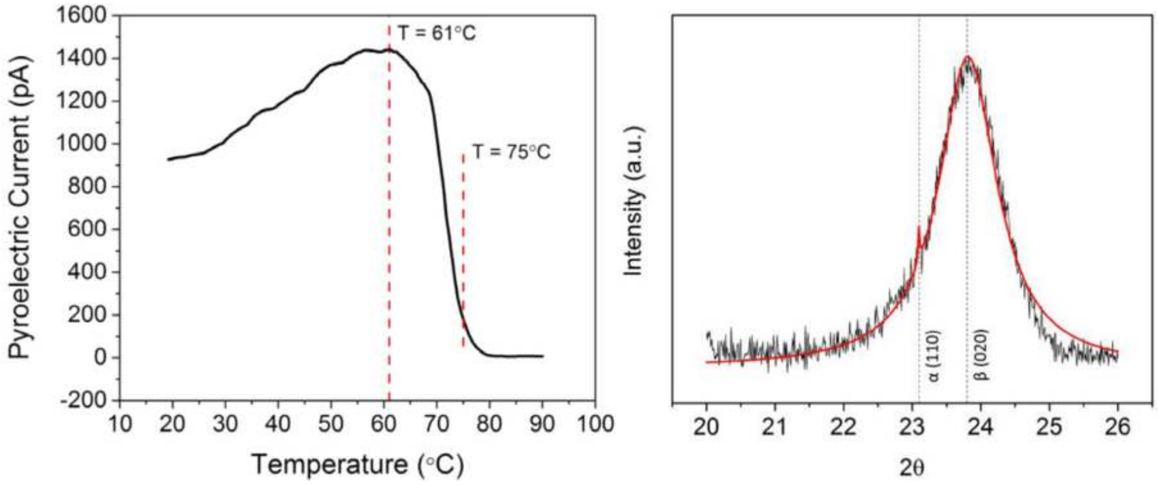

Fig. 2.20 Left: Pyroelectric current of a dynamic heating of the chip sample showing the paraelectric phase transition at 75°C. Taken from Foreman *et al*[9] Right: XRD data for the as-grown VDF oligomer thin film. Taken from Foreman *et al*[9].

2.6 PVDF computational studies

Computational studies of PVDF have been mainly limited to the investigation of bulk properties using density functional theory and molecular dynamics. Computational modelling offers easy access to molecular structures, atomic coordinates and other nanoscale details difficult to achieve in experiments. With computational modelling is possible to virtually reproduce any experimental condition although there are limitations on the size of the system modelled which is limited by the computational power needed to solve large or complex heterogeneous systems. However, as much as computational research allow to model defects, damages and dopant additions, such investigation have been almost unexplored in computational research, as such aspects requires big atomistic system computationally expensive. Moreover, the complementation of MD with DFT and vice versa to solve with high detail the electronic structures of PVDF crystals and feeding such structural information into MD, was again investigated rarely.

2.6.1 Crystal structures

As the main interest about crystal phases of PVDF were the α and β phases, especially to understand properties of such crystals to find a solution in obtaining high crystalline grade samples of β-PVDF, several authors dedicated research efforts only to those two crystal structures as Akira *et al*[101], Ramer *et al*[81, 82, 102] and Nakhmanson *et al*[103]. Pei *et al*[66] and Su *et al*[104] studied more widely PVDF crystal structures covering from the α-phase to the ε-phase. However, weaknesses found across all these DFT studies were the convergence threshold cutoffs, which were not properly converged giving improper crystal structures and lattice dimensions, which were not representative of the XC-f used for their studies which were PBE[66, 81, 82, 102–104], PBE0[101] (hybridisation of PBE with Hartree-Fock energy terms functional) and PBE+D2[66] (PBE functional with vdW correction scheme not based on first principle).

Moreover, nobody ever used first principle vdW forces corrections to estimate the effects on crystal lattice structures and for soft matter as polymer are, an accurate evaluation of vdW forces contribution on crystal structures is indeed crucial and missing from literature papers about PVDF. Especially crystal structures characterised with DFT using PBE showed good agreement with experimental observations, although low convergence parameters improved by chance computational predictions fitting experimental observations, most remarkably on the β-phase more than any other crystal structure. As Pei *et al*[66] used DFT to characterise the ε_{uu} and ε_{ud} phases (Karasawa was earlier than Pei but using MD), the non polar β-phase remained uncharacterised until this present thesis, indeed, the study of PVDF using DFT could not be considered exhaustive before the present thesis.

2.6.2 Crystal properties

Su *et al*[104] which characterised PVDF crystal structures also investigated phase energies and cohesive energies finding that the α and δ phases are two crystal structures with similar phase energies and cohesive energies and showing that all PVDF crystal structures are distinguished by small energy differences which remains in magnitude within a range of less than 3 kJ mol^{-1}. Other authors such as Nakhmanson *et al*[32, 103] characterised the spontaneous polarisation and vibrational spectra of the β-phase, Ramer *et al*[81, 82, 102] characterised the vibrational spectra of the α and β phases, Kobayashi*et al*[65, 105] investigated the vibrational spectra of the α, β and γ phases, Tashiro *et al*[106] focused on the vibrational spectra of the γ-phase and Takahashi *et al*[67, 107] characterised the vibrational spectra of the β and γ phases. The same weaknesses mentioned for the crystal structure characterisation persisted here, although, the vibrational spectra characterisation is less sensible to the functional used, convergence parameters are even more important, while for the spontaneous polarisation a not converged set of energy cutoffs altered the PBE prediction in Nakhmanson's work.

The vibrational spectra characterisation of the α and β phases was also performed by Wang *et al*[108] but instead of characterising the absorption peaks of the crystal unit of these two crystals, the study was focused on the structural defects of PVDF such as inverted monomers which are often present in synthesised PVDF chains and influences the IR spectra broadening absorption peaks. With such study Wang showed that structural defects of PVDF chains concretely affects IR spectra quality[108]. Moreover, Wang *et al*[108] also estimated the dipole magnitude growth relation with PVDF chain length showing that the dipole magnitude reached a plateau when the polymeric chain length was between 16-20 monomers, showing that despite polymer length the dipole magnitude saturates to a state where the addition of other monomers is invariant on the dipole moment magnitude of the chain.

The vibrational spectra characterisation of Nakhmanson *et al*[32] was not a vibrational spectra investigation of the standard and well known β-phase crystal unit but performed on a two structural variants called planar zig-zag deflected structures with the aim of finding bands structure and vibrational spectra differences between such structures which were deputed to be stable crystal variants of the β-phase at room temperature conditions[32]. Both Wang and Nakhmanson studies aimed to enrich the understanding of vibrational spectra broadening effects about PVDF considering structural chains defects and crystal variants, indeed, when it comes to experiments many interfering agents spreads peaks absorption making spectra interpretation more difficult and computational studies as Wang[108] and Nakhmanson[32] performed helped to understand such heterogeneous phenomena.

The studies afore mentioned showed that a definitive DFT set up to be use to study PVDF polymorphs properties was not achieved from literature evidences as different authors used different functionals with different energy cutoffs which made results divergent and sometimes confusing as in the case of Nakhmanson[103], which underlined the uncertainty of the β-phase crystal structures as such crystal could have to structural variants such as the planar zig-zag and full trans, respectively, but using higher cutoffs it was showed that only the full trans structure was indeed metastable[108].

2.6.3 Phase transformation mechanisms

The study of Wang *et al*[108] diverged from the phase energy magnitude found by Su *et al*[104] since Wang reported that the energy phase difference between the α and β phases was of

8 kJ mol^{-1} while Su saw that all PVDF polymorphs ranged within an energy difference of 3 kJ mol^{-1}. Furthermore, Wang *et al*[108] investigated the phase transformation mechanisms finding an energy barrier of 16 kJ mol^{-1} which separated the backbone of the α-phase while transitioning to the β-phase backbone and vice versa. This energy magnitude in phase energies can be explained by methodologies differences in energy convergence thresholds as in both studies (Wang and Su) not converged parameters were used. Another study which investigated the phase transformation from the α-phase and δ-phase to the β-phase was performed by Kim *et al*[109] which computed with molecular dynamics (using the COMPASS force field) the effects of stretching and poling on the phase transformation mechanism under finite temperatures. Kim *et al*[109] showed that the phase transition was effective obtaining the β-phase from both α and δ crystal conformations.

However, in computation the stretching and poling were applied in a perfect manner as all chains were subject to a uniform stretching strength and the electric potential of the poling also applied perfectly uniform, while in real experiments the stretching and poling treatments resulted to have a limited efficacy[72] and stretching resulted to damage the treated sample[4, 22]. In this case, computations showed that stretching and poling could be an effective manufacturing approaches with the assumption that the sample treated would be uniformly interested by the process and omitting the potential damages observed in experiments. The interesting evidence supported by both papers was that phase transition is a mechanisms which can occur without encountering prohibitive energy barriers, although, in real experiments there are factors to account for which were not considered in Kim's research[109], while Wang[108] performed the study at the ground state energy of crystal structures of α and β phases at 0 K using DFT.

2.6.4 Solid and liquid bulk properties

In molecular dynamics few authors approached the study of PVDF where Karasawa *et al*[110, 26] developed a force field called MSXX for the purpose of characterising the phase properties of solid bulk PVDF crystals. Within literature papers about the force field made by Karasawa, a wide physical properties characterisation was performed along PVDF polymorphs also studying physical properties of liquid bulk PVDF. Remarkably, Karasawa *et al*[110, 26] group was the first to computationally characterise the crystal structure of the ε_{uu} and ε_{uu} phases. As the MSXX force field was especially made to fit experimental solid properties of PVDF crystals, such FF was not describing accordingly to experimental observations liquid phase dynamics as the melting mechanisms and liquid bulk properties as chains conformations into the liquid phase. To such extent Byutner *et al*[27] developed a FF (Byutner and Smith B&S) focused in fitting the melting mechanisms of PVDF and liquid phase properties of disordered and amorphous PVDF chains where Erdtman *et al*[111] kept using such force field to extend the match of computed properties compared to experimental observations.

However, both MSXX and B&S force fields were developed and demonstrated to fit experimental observations for what such force fields were built for without moving the PVDF computational study any further. Indeed, computational studies about PVDF appeared to be rather limited and confined to basic investigations which did not exploit the full potential of calculation on both DFT and molecular dynamics sides. It is still unknown which DFT functional is best in describing physical properties of PVDF crystal structures and in molecular dynamics there is not such a force field accepted for its ability to describe accordingly to experimental observations PVDF dynamics at finite temperature, which could be used to further unveil physical interactions of PVDF chains with other materials to understand surface effects on the crystalline formation mechanisms which could favour high percentage presence of the β-phase.

2.6.5 Surface studies

As the study of liquid bulk properties was found limited in computations, the study of surface was even less approached, indeed, to present days only the investigation of Guryel *et al*[28, 112] was known. Guryel *et al*[28, 112] investigated with DFT the interaction of PVDF short chains and other polymers on graphene to appreciate with the details of electronics structures the energy interaction mechanisms between polymers and graphene. Then, Guryel *et al*[28, 112] used the standard optimised potential for liquid systems (OPLS) force field to investigate PVDF interaction with a graphene surface. The DFT and molecular dynamics studies were not related as the DFT data were not used to fit force field parameters as the standard OPLS FF was used in molecular dynamics. Weaknesses of such study were the missed FF validation with experimental observations and no investigations of PVDF bulk properties described with OPLS in comparison with the surface system as only the surface model set up and finite temperature dynamics were described making conclusions weaker and potentially uncertain.

2.7 Summary

The post processing techniques methodologically evolved trying to enhance FE properties of PVDF to make reliable and well performing flexible electronic devices. From the literature review it emerged that some solvents, additives and surfaces can promote the formation of the PVDF FE crystal phases such as the β and γ. A gold surface resulted to modestly promote the β-phase crystallinity ($\approx$40%) and graphene allows to prepare working MFM devices with 40-48% of crystallinity. Investigated solvents effects it was found that some solvents are selective in favour of the β-phase, the same results has been obtained using positive ionic small molecules. Using NPs as additives also resulted to be effective in promoting ferroelectric PVDF crystal phases formation where clays and zeolites NPs promoted the γ-phase and $BaTiO_3$ and PdCl NPs promoted the β-phase formation.

A remarkable evolution of the methodology saw the ability in controlling crystal phases and crystalline yield reaching the state of the art with the preparation of a ferroelectric PVDF sample nanoconfined in APA membranes that reached a spontaneous polarisation at the peak of what quantum mechanics can predict. However, as different authors provided different manufacturing approaches to increase crystalline and ferroelectricity of PVDF samples, no authors concluded to explain what is the common physical mechanisms which makes some approaches successful and other unsuccessful. Indeed, the concrete mechanisms which drives the formation of FE crystals of PVDF was supposed by some authors but such hypothesis was never demonstrated experimentally nor computationally by proof of concepts.

The computational investigation about PVDF has been found to a primordial stage of fundamental properties investigation using both DFT and MD, furthermore, the characterisation of PVDF physical properties has never been brought to the state of the art by defining the best computational set up to investigate PVDF for both DFT and MD approaches. The present computational project aimed to move forward the computational analysis of PVDF properties performing an exhaustive DFT investigation of PVDF crystals, as in literature there was not enough exhaustive work about PVDF polymorphs. The contribution of vdW forces implemented in DFT using first principle functionals has never been investigated, as well as previous authors used not converged energy cutoffs which brought different authors to different structural properties prediction of the PVDF crystals so far investigated. In MD simulations no authors dedicated attention in benchmarking different force fields in their accuracy in predicting PVDF structural properties. The main efforts in MD were dedicated to validate a specific force field against experimental observations and some force fields used for studying PVDF were not even validated against experimental evidences.

2.8 Objectives

As from literature appeared that PVDF crystal structures investigation never reached a complete satisfactory disclosure both in experiments than computations, in the present computational thesis a full investigation of crystal phase properties of PVDF has been conducted using DFT to characterise lattice structure, phase stability (*e.g.* cohesive energies and phase energy ordering), spontaneous polarisation and vibrational frequencies. These properties would represent a precious data collection useful to future investigations to recognise more easily different crystal polymorphs of PVDF and addressing more clearly the related properties of every crystal. Along the DFT study an extensive benchmark of DFT functionals has been performed to define which functional would better describe PVDF physical properties in agreement with experimental observations, also considering the inclusion of first principle vdW forces[113–115] into DFT.

The present study aimed to provide more clarity about the less studied crystal structures such as the γ and ε phases which were acknowledged to exist in two different structural conformations which have the same statistical probability of existing of about 50% per each conformation[68, 63, 64, 67] labelled as γ_{uu}, γ_{ud}, ε_{uu} and ε_{ud} reflecting the up-up chains conformation and the up-down chains conformation, respectively. As their metastability has never been determined using DFT and it was unknown the energy ordering of such crystals sharing the $T_3G^+T_3G^-$ backbone shape in respect of the other known crystal structures of PVDF, in the present study such questions have been addressed. Furthermore, the so called "unoriented β-phase"[30] or "non-poled β-phase"[78, 81, 79, 105] which conceptually meant for a probable non polar crystal structure which has the same full T backbone shape of the β-phase, has never been investigated and characterised as a possible metastable non-FE crystal structure of PVDF, hence, such undetermined crystal phase has been investigated.

On the MD computational side, less author's contribution lead to a more extensive work in benchmarking and validating the most appropriate force field able to describe PVDF molecular dynamics at finite temperatures, making such question part of the present research project. The benchmark was concerned with the lattice structure properties prediction of different force fields compared with the crystal lattice structures determined with present DFT results and experimental observations from literature.

The FFs chosen for the present study were further validated in their consistency by performing liquid phase equilibration tests as the investigation of the liquid phase properties of PVDF has been an investigation of interest in the present study. Finally, the most important research question of the project has been conducted to understand which polymer to surface interaction mechanism would promote the formation of FE crystalline phases of PVDF such as the β-PVDF. Indeed, along the literature review has been possible to appreciate that different authors provided more or less effective preparations methodologies to obtain FE crystals of PVDF without explaining which was the mechanism that promoted such crystal formation. As some authors results successes could conceptually go against other author's findings, a comprehensive understanding of the ferroelectric crystalline formation mechanisms was indeed missing and here investigated.

Chapter 3

Methodology

The computational software used in this study were the quantum mechanics code based on DFT Quantum ESPRESSO and the Large-scale Atomic/Molecular Massively Parallel Simulator (LAMMPS) code based on classical molecular dynamics. The present research project has been conducted on a computational modelling basis to study PVDF physical properties at the ground state using DFT and the dynamical behaviour of particles in classical molecular dynamics to further investigate how PVDF polymers interact with a surface with the scope of understanding which is the physical interaction that controls the crystalline phase formation of PVDF crystals. The use of two distinct software became necessary since DFT is a quantum mechanical theory computationally too heavy to account for finite temperature computations as well as for the number of electrons that a quantum model can contain, which limits the system size to a maximum of 400 electrons[116]. To investigate bigger models which contains thousands of atoms and calculate the dynamical properties of the system, the use of MD is strictly necessary for a scalability issue (*e.g.* thousands of atoms in MD is a very fast computation)[16].

These two aforesaid computational approaches have been widely adopted in the scientific community[117, 116, 12, 118, 119], furthermore, it is often seen that research conducted with QM codes complements research made with MD codes and vice versa to complete the understanding of a modelled system and also QM theory can be used to gather data which feed an MD force field (FF) to perform accurate molecular dynamics computations[16] with parameters derived from QM studies. In this study, DFT has been used to unveil the physical properties of PVDF crystals and to use structural information such as the crystal lattice and atoms geometries to cross compare and benchmark MD simulations. Furthermore, MD moved the study forward in calculating the dynamical properties of PVDF bulk and surface models, a task not feasible on DFT. In this chapter the methodologies applied in the present study PVDF were presented to make clear the computational set up used for reproducibility purposes.

3.1 Density functional theory

The physical properties study of a system using quantum mechanics presents a highly complex task because every atom of the system is a composition of subatomic particles that have to be accounted per every single atom of the system, which quickly makes even a small system a complex networks of interacting particles. In practical terms, to be able to describe the physical properties of a model at the quantum level it is necessary to solve its ground state energy minimum, referred as the Hamiltonian ($\hat{H} = \hat{T} + \hat{V}$)[120, 121] operator of the system, which is the operator that includes the total energy of the system and a complex to solve energy interaction term for all the particles of the system. To solve the Hamiltonian of an atomistic model in quantum mechanics, it is necessary to evaluate the energy state of every particle and its interaction with every other particle of the system, making the amount of iteration to evaluate all energy interactions considerably high even for small systems and difficult to solve since as particles interact to each others they also perturb each others in their energy states, which requires to evaluate again all their energetics until a convergent solution is found.

As the $\hat{H}$ is a complex operator, along quantum mechanics developments different approaches to solve it were made, which were more or less approximative. Indeed, one convenient way to reduce the complexity of quantum mechanics equations is to approximate particle interactions to obtain equations of easier solution. There are different equations, which deal to solve the $\hat{H}$ of a system approaching its complexity with different types of approximations and despite their formalisms such equations are generally grouped as belonging to the many body theory which is the branch of Hamiltonian solvers, which deal with many bodies systems.

An exact quantum mechanics equation able solve the Hamiltonian of a system was the Schrödinger equation, that represented the starting point for developing modern quantum mechanics $\hat{H}$ operator solvers, that dealt the complexity of the Schrödinger equation to obtain operators easier to be solved. Indeed, the complexity of the Schrödinger equation is so high that normally it is not used to solve bigger systems than one or two hydrogen atoms[122]. An example of a many body theory equation, which transformed the Schrödinger equation to an easier $\hat{H}$ solver was the Møller-Plesset[123, 124] (MP) equation that attempted to maintain the accuracy of the original Schrödinger equation minimising the approximations. However, such equation was still complex to solve and its application limited to systems made of few atoms. To expand the scalability the MP equation was further developed with exponential orders coined as MP-2 and MP-3[125] which made the original MP equation more scalable (2-33 atoms) but still computationally heavy.

Density functional theory was another approach to solve the $\hat{H}$ operator using an approximation on particles interactions, based on the scientific demonstration that at the ground state energy of a system, the wavefunction of the system can be written as the functional of its energy density, from which all other physical properties can be derived[11, 126, 10]. The density functional theory allowed to simplify the Schrödinger equation reducing significantly the complexity of the many body problem and the computational cost of solving the $\hat{H}$ operator, which made DFT a notorious and widely applied methodology[10, 127] scalable even to few hundreds of atoms (*e.g.* 100-200). The equation derived from DFT is referred under the main authors surnames Kohn and Sham which coined the Kohn-Sham (KS) equation[10, 127]. Conceptually, how DFT formalised the many body problem with the functional of the energy density can be expressed in the sketch of Figure 3.1 which shows the generalisation of many interacting particles on an ion as their energy density functional still shaped by interacting with the ion.

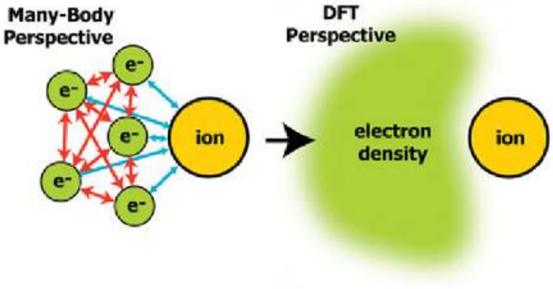

Fig. 3.1 Conceptualisation of a many body system seen in the DFT formalisms as the functional of the energy density of the system. Sketch inspired from [10].

3.1.1 Born-Openheimer approximation, core particles as pseudopotentials, Bloch's theorem and unit cell

As the hamiltonian of a quantum system is originally a complex equation to solve, a crucial discrimination to reduce its computational weight was to give a weight to the particles possessed by each atom included in the system. Conceptually, if some subatomic particles energetic states behave almost as constants despite the quantum model their part of, they can be easily excluded from the $\hat{H}$ operator as their presence would not significantly alter the final solution of the equation as their energy contribution could be assumed to be always the same.

To such extent the particles of atom nuclei such as proton and neutrons can be enclosed in one constant wavefunction with a constant energy density value. Such approximation has been developed by Born and Openheimer[128, 129], which made possible to exclude nuclei particles that possess constant energy states into a fixed potential. Every atom type would possess a specific potential derived by the number of protons and neutrons in their nuclei[128, 129] used to reduce the number of interacting particles of the quantum system.

Moreover, not just the nuclei particles were found to have a constant energy density along different quantum systems, but also the inner core electrons not involved in forming chemical bonds were found to have a repetitive energy density along different quantum system investigated. Therefore, also the core electrons were included into the core particles group with their characteristic energy density value. This core particles inclusion took the name of pseudopotential, which divide the wavefunction of a quantum systems into parts, where one part contains all core particles which can be approximated by their energy density constant into one pseudopotential expressed in a pseudo-wavefunction of the inner core particles of the quantum system. The second part of the wavefunction of the system is the one that needs to be solved by the KS equation to achieve the final energy density of the system which varies depending on the bonds formed by the valence electrons. The KS eqution became an equation that solves the electron density of the valence electrons contained into a system. In this way, it has been possible to sensibly reduce the amount of particles that a quantum system would contain, lightening the computational effort needed to solve the KS equation.

As the pseudopotential contains the pseudo-wavefunction of the inner core particles of an atom, such wavefunction can be expressed with different mathematical formalisms which have the same physical meaning not changing the energy density of the system, but serves for different interests in calculating specific properties of materials. The mathematical formalisms are so called normconserving (NC)[130], ultrasoft (US)[131] and projector augmented wave (PAW)[132]. The NC pseudopotential has been made to conserve the norm of the core particles pseudo-wavefunction not altering the computational cost of solving the quantum system, US makes the core particles pseudo-wavefunction smoother decreasing the computational cost of the quantum system as lower energy cutoff are required to solve the energy states of the system wavefunction, while PAW pseudopotential is used to augment the complexity of the pseudo-wavefunction requiring more projected planes to solve the wavefunction of the quantum system requiring higher energy cutoffs and higher computational costs. In some cases a specific pseudopotential is preferred among others, but nowadays for most uses the US pseudopotential are the preferred pseudopotentials. The introduction of such general approximation makes clear that the KS equation is intended to be an hamiltonian solver of the electron density of the system of valence shell electrons not included into pseudopotentials and intergrated with the costant values of the pseudo-wavefunction of the pseudopotentials used for a specific quantum systems. The description of the KS equation further in the text will be explicit only for electrons.

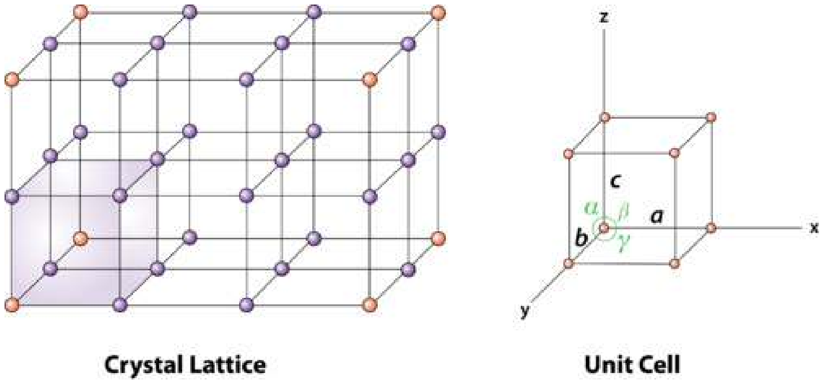

Fig. 3.2 Graphical representation of a unit cell with a, b and c are the lattice vector and α, β and γ are the angles between the lattice vectors. Sketch made from Ashcroft's book [11].

Furthermore, dividing core particles from outer shell electrons, is not enough to make the $\hat{H}$ of a quantum system an easy to solve equation. Indeed, even by considering only the valence shell electrons of every atom of a system, there is still the infinity problem that would include the infinite amount electrons present into a solid. Therefore, since the quantum system is expressed as a wavefunction, the periodicity of wavefunctions can be exploited to assume that by defining a unit cell, which is the region of space containing the minimum amount of atoms representing a solid as shown in Figure 3.2, such unit cell would represent the minimal repetitive unit able to represent the entire solid if repeated indefinitely in space. With such assumption it is possible to calculate only the electron density of the particles inside the unit cell and assuming that every other periodic repetition of the unit cell will contains the same periodic wavefunction with the same properties found in the first unit cell. This is the Bloch's theorem[133, 122] which can confine the computational cost of an hamiltoninan operator within the atoms explicitly given in the unit cell model. Equation 3.1 resumes the Bloch's theorem[133, 122], with $\psi_{j,k}(r)$ representing the wavefunction period associated with the unit cell imposed to be equal to every other periodic repetition $\nu_j(r)e^{ikr}$ of the initial unit cell.

$$\psi_{j,k}(r) = \nu_j(r)e^{ikr} \tag{3.1}$$

These premises allow to make the discussion of the KS equation lighter as such equation is focused on solving the $\hat{H}$ operator of the wavefunction of the system constituted by the former valence shell electrons that each atom possess as explicitly given in the initial periodic unit cell.

3.1.2 The Kohn-Sham equation

The mathematical demonstration made by Kohn, that a system found at the energy minimum of its ground state, its associated wavefunction can be written as the functional of its energy density, from which is possible to derive any other physical property of the system, made possible to reinterpret the Schrödinger equation as one-electron equation of a system of particles that do not interact and that has the same density of a system of interacting particles. The Kohn-Sham equation dealt with the complexity of many interacting particles with an elegant solution that allowed to decouple the complexity of their interaction into a more simple term of the equation, called exchange-correlation functional (XC-f) that made the KS equation scalable to much bigger systems than any other many body theory equation. At the creation of KS equation, such XC-f was to some extents a bit coarse since the complexity of long range force interactions was almost neglected assuming that the non interacting particles were immersed in a uniform averaged field of electron density, but depending on the type of matter studied such as metals, that gross approximation revealed to behave better than expected[120], and mostly, it allowed the KS equation to be practically solvable. To follow, many different modifications of the first XC-f were made and the vast amount of DFT flavours present nowadays enriched DFT versatility and completeness (treated further in next section).

$$E = T + E_{ext} + E_{ee} + E_{II} \tag{3.2}$$

$$E[n(r)] = T_s + E_{ext} + E_H + E_{xc} + E_{II} \tag{3.3}$$

$$E_{xc} = (T - T_s) + (E_{ee} - E_H) \tag{3.4}$$

$$E[n] = \sum_a f_a \langle \psi_a | \left(-\frac{1}{2}\nabla^2 + V_{ext} + \frac{1}{2}\int \frac{n(\mathbf{r'})d^3r'}{|\mathbf{r'} - \mathbf{r}|} \right) | \psi_a \rangle + E_{xc}[n] + E_{II} \tag{3.5}$$

The equation 3.2[121] shows how the total energy of a system with many interacting particles is divided in specific energy interaction terms each of which describing part of the total energy of the system. In such formalism, the equation 3.2 remains constrained by the many body complexity problem where T is the kinetic energy of the particles, E_{ext} is the external energy interaction which included the electron-ion interaction, E_{ee} is the electron-electron interaction which represents the complexity of the $\hat{H}$[120, 121] and E_{II} is the ion-ion interaction energy term. The KS equation 3.3[121] decouples the E_{ee} term into two variables which are the Hartree-Fock energy term E_H and the exchange correlation energy term E_{xc}. With this decomposition, the KS equation decouples the electron-electron energy interaction and solve energy terms of particles as a system of non-interacting electrons. To allow this decomposition also the kinetic energy is reduced to the kinetic energy of non interacting particles T_s[121].

Then the exchange-correlation term E_{xc} of equation 3.4 takes care of the many body complexity calculating the energy contribution of interacting particles[121] after that the energy interaction terms of non interacting particles are already defined. The residual kinetic energy $(T - T_s)$ and electron-electron energy $(E_{ee} - E_H)$ of interacting particles is accounted with a different and simpler to solve formalism[121]. More explicitly the the KS equation 3.3 can be represented as written in 3.5[121] where the f_a Fermi-function is the occupation of a single-particle state ψ_a which has to be evaluated per every possible particle state of ψ_a. The Laplace operator (∇^2) represent the kinetic energy term, V_{ext} the potential energy and the next term is the coulomb interaction potential.

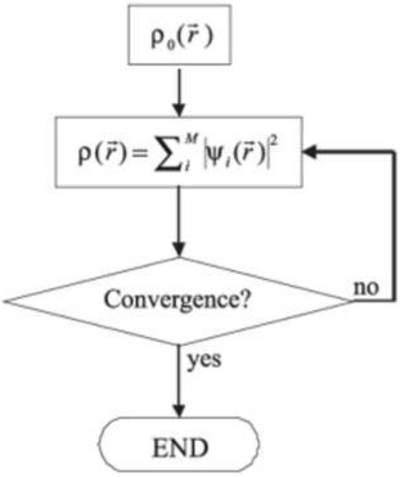

Fig. 3.3 Typical self-consistent iterator to solve the KS equation. Taken from [10].

Equation 3.5 helps to understand better how the XC-f formulated into the E_{xc} energy term makes the equation easier to solve, indeed, without the XC-f decomposition, the energy contribution of particle interactions would be inside the Fermi-function, making such function iteration considerably heavier. In this way, the KS equation became easier to solve which expanded its use significantly, by moving out of the Fermi function f_a the residual energy of interacting particles. The limitation of the KS equation is that since the energy contribution of interacting particles is retained by the E_{xc} term, it is still unknown the correct formalism to solve exactly the energy term E_{xc} and so far such term is solved by guessing its mathematical formalisms which leads to an approximative solution. Conceptually, if there will be a way of solving the E_{xc} exactly without guessing, DFT will become exact as much as the Schrödinger equation. So far, the XC-f has been refined to more complex formalisms which also includes non bonded long range interactions such as the van der Waals forces with the attempt to go nearer to the final exact solution of the E_{xc} energy term.

To achieve a conclusive solution of the KS equation, it is necessary to iterate the solution process more times until the final energy density result converges within a tolerance threshold (*e.g.* 1.0e-06 Ry). Indeed, as the KS equation can not be solved if not having the electron density of the system and being the energy density of the system the end value of the solution, the first time the equation is iterated, an energy density value $\rho_0(\vec{r})$ is guessed and given to the equation to initiate the solution process. Per every time the equation is solved a new energy density value $\rho(\vec{r})$ of the system is achieved and used as a new starting value of energy density for the next iteration. When the previous energy density value is similar to the present value obtained with the last iteration within the tolerance threshold, the solution of the KS equation is considered converged and the iterative process interrupted. The initial electron density given during the first KS iteration has a relative weight since the final electron density value must be refined until the initial density value reaches the convergence threshold. Figure 3.3 shows how the iterative loop of the KS equation to refine the final energy density $\rho(\vec{r})$ of a quantum system to reach the accuracy of the tolerance threshold desired. However, the convergence of the KS equation is not certain to be reached per every quantum system investigated, indeed, if the system set up results to be physically inconsistent (*e.g.* treating a metal as a non metal) the convergence will never be reached despite the amount of iterations performed.

3.1.3 The Exchange-Correlation functional

The XC-f in the KS equation 3.5 is what makes DFT approximative and computationally affordable at the same time, the approximative nature of the XC-f resides in the fact that there is no known way of solving such energy term exactly as the XC-f guesses the mathematical formalism that rules the energy contribution of interacting electrons. The first XC-f made was based on the local density approximation (LDA)[10, 134], which consisted in assuming that all electrons of the system were distributed across a uniform electron density field, hence, electron's energy was given only by their position in the system, representing a significant gross approximation. However, LDA surprised in describing physical properties of hard matter such as metals since in such materials atoms are tightly bound to each other and shell electrons resemble such dispersed uniform electron density field (*e.g.* typical condition of conductors). The LDA XC-f is an example of local DFT functional.

As DFT became more widely used, other XC-fs were developed in order to make the XC-f less approximative. The General Gradient Approximation (GGA) of which a notorious implementation was made by Perdew-Burke-Ernzerhof[135, 136], consisted in introducing a gradient of electron density around each electron which should be able to account for longer range of energy interactions accounting for a variable electron density gradient along the unit cell dependent on the position that every electron has in the unit cell. As LDA is a local functional notorious for overbinding electron-electron interactions, GGA is a semi-local functional which became notorious for underbinding electron-electron interactions[136, 137], as such functional made the electron density gradient to expand too much resulting in weaker particles cohesion.

Since both LDA and PBE are XC-f that neglected long range forces interactions, to account for such long range forces, it was chosen to add to the semi-local PBE functional a corrections which would account for long range forces such as van der Waals. These corrections were essentially added into the E_{xc} energy term and two notorious examples were made by Grimme *et al*[138] and Tkatchenko *et al*[139]. These two approaches saw some technical restriction as the Grimme vdW correction essentially needed to be tuned specifically per different materials type and fitted to experimental evidences, while the Tkatchenko vdW correction was less applicable to different atomic species.

A more modern approach to solve DFT approximations was to make non-local first principle functionals which accounted for vdW forces and two remarkable examples were the vdW-DF[113, 114] and vdW-DF2[115]. However, such first principle vdW implementation does not represent concretely new XC-fs, but is more correct to say that the vdW-DF and vdW-DF2 are first principle vdW forces implementations obtained by the use of a kernel which sums the vdW energy contribution found into a system to other XC-f functional such as PBE. Such XC-fs requires indeed the use of a functional like PBE and overrides on it the vdW implementation, concretely making the hybrid XC-f vdW-DF and vdW-DF2, non local XC-fs. Comparing the energy profiling of interaction energy profile between PBE, vdW-DF and vdW-DF2 as shown in Figure 3.4, it is possible to appreciate the difference between the energy interaction profile as function of space of the semi-local functional PBE in contrast with vdW-DF and vdW-DF2. Furthermore, there is also a difference between vdW-DF and vdW-DF2 in how the energy profile as function of space is estimated by these two functionals, hence, the needs for testing both vdW implementation to verify the most consistent functional in predicting the physical properties of PVDF crystals in comparison with experimental evidences.

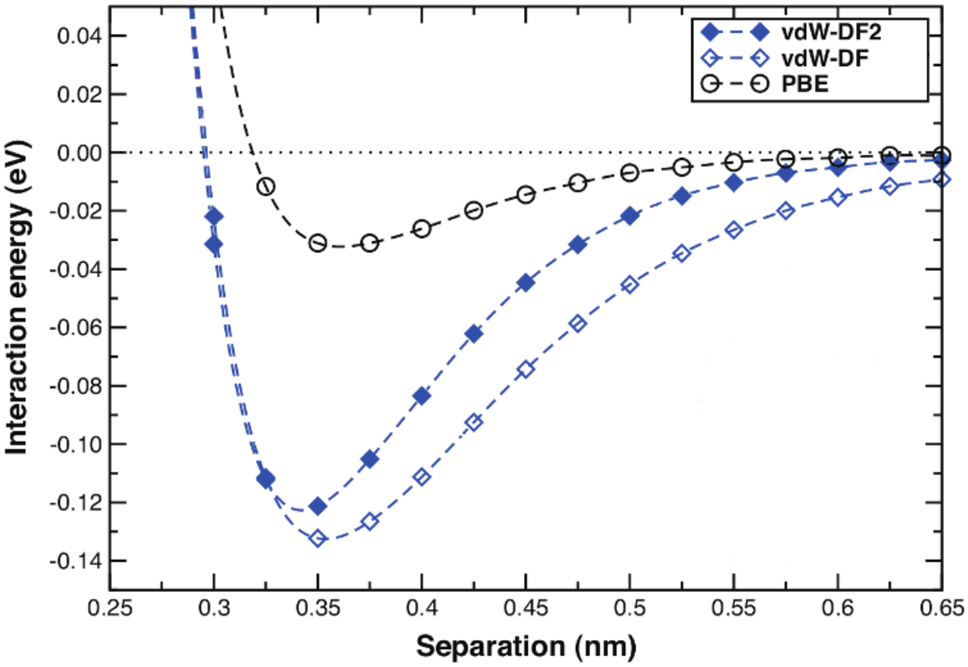

Fig. 3.4 Energy profile of van der Waals forces estimation as function of space comparing three different functionals such as PBE, vdW-DF and vdW-DF2 taken from Giannozzi[12].

However, the vdW-DF and vdW-DF2 XC-fs are still relatively young implementations not widely adopted by the scientific community, especially because of the higher computational demand that including vdW forces into DFT represents. Indeed, the inclusion of vdW forces restrict the scalability of DFT forbidding the simulation of clusters and big system made of few hundreds of atoms, to a maximum amount of atom of approximately a hundred of atoms with the current computational power technology can offer.

3.1.4 Reciprocal lattice, k-point sampling and energy cutoff

The reciprocal lattice and k-point sampling are other two formalisms needed to solve the KS equation as such concepts apply mathematical transformation of the quantum system useful for solving the KS equation. The unit cell model built in real space containing all the particles of a quantum system to be solved with the KS equation, first needs to be transformed into its reciprocal lattice. The reciprocal lattice is a Fourier transform of the original lattice built in real space, the real space lattice and the reciprocal lattice are complementary and by Fourier transforming again a reciprocal lattice, the original real space lattice would be restored. To make an analogy, taken a cubic lattice, as all lattice vectors are equal, its reciprocal lattice would stay unaltered, while for an orthorhombic lattice the smallest lattice vector would become the biggest and vice versa.

In reciprocal space also known as K-space, it is possible to discretise the lattice structure of a quantum system as a discrete quantum momentum and the energy density of the system descretised in reciprocal space can be integrated in discrete points called k-points. The k-point sampling allows to solve the energy density of the system by integrating the energy of the system in a finite number of discrete k-points, making the calculation lighter as to know the energy density of the system is enough to solve the energy density of the explicit k-points given at the beginning of the calculus. The number of k-points is subject to convergence as depending on the inverse of the system size over a certain amount of k-points the energy density of the system remains unaltered. Adding more k-points over the convergence threshold, would results in heavier computational effort without refining the energy density more than the energy convergence threshold defined at the beginning of the calculation. Hence, for a given quantum system, it is necessary to do a convergence test to quantify the amount of k-points needed to converge the energy density of the quantum system, optimising the computational cost of the system.

Similarly to the number of k-points, which helps to converge the energy density of a quantum system, also the kinetic energy cutoffs needs to have a threshold at which higher energy states will be ignored, as by considering the lower energy states below a fixed kinetic energy cutoff, it is enough to have a fine converged energy density value for a specific quantum system. Also in this case it is necessary to do a convergence test for any quantum model to verify the energy cutoff that makes the KS equation to converge. To minimise the computational cost of the calculation it is necessary to select the lowest energy cutoff which satisfy good convergence parameters at the limit of resolution of DFT which is 1 mRy per every atom present in the quantum model. The kinetic energy cutoff are two, one for the kinetic energy of the wavefunction and one for the kinetic energy of the charge density. Together, k-points and kinetic energy cutoffs can refine the accuracy the KS equation can have. The overestimation of such parameters is not beneficial for the accuracy and only increases the computational cost of the KS equation. Referring back to pseudopotentials, the main differences that can be found between the use of specific types of pseudopotentials and kinetic energy cutoffs is that, NC pseudopotentials generally requires a ration of charge density cutoff 4 times the wavefunction cutoff, while PAW pseudopotentials require 8 times such ratio and US pseudopotentials requires 10 times the ratio between the charge density versus the wavefunction cutoff. Other parameters may be important for the energy density convergence and accuracy, but it does depends on the type of atoms involved into the quantum model, hence, such parameters has not been discussed if not directly needed for the quantum model built in the present research project.

3.1.5 The Brillouin zone, gamma point and bands structure

In reciprocal space the Brillouin zone is defined as the region of space that is possible to reach without crossing any reticulum plane of the Bragg law. Every lattice type or Bravais lattice has different geometry, that shapes differently the Brillouin zone in the reciprocal space. The k-point sampling is mapped per each Brillouin zone of each Bravais lattice, and by selecting the k-point numbers and their crystal coordinates it is possible to integrate the energy density of the system to such specific spatial points. The gamma point is a k-point that by definition is found at the centre of the Brillouin zone being the highest symmetry point of the Brillouin zone. In the interest of studying the electronic bands structure of a quantum model, the k-point sampling is mapped going out and in the gamma point to observe the electronic states of the system at specific high symmetry points, which allow to know the perturbation states of electrons at such specific coordinates. These information are very important for retrieving important physical properties of a material such as its conductive, optical and acoustic properties. Figure 3.5 shows on the left the typical Brillouin zone of the face centred cubic (FCC) lattice with its representative maps of k-points, while on the right of Figure 3.5 is visible how sampling a specific k-path in the FCC Brillouoin zone, the electronic states can be plotted to visualise the electronic bands structure as function of energy found at the k-points coordinates given.

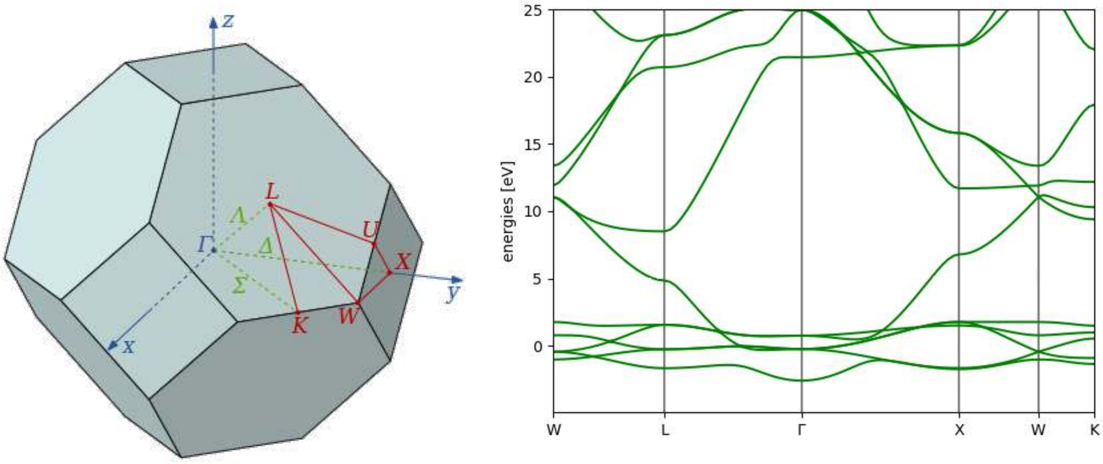

Fig. 3.5 Left: Face Centred Cubic brillouin zone and k-path taken from Setyawan[13]. Right: Bands structures of the FCC gold geometry taken from Setyawan[13].

3.2 The Berry's geometry polarisation phase theory

The characterisation of the spontaneous polarisation P of a system which is characterised at the quantum level is a task which encounters important technical difficulties, as the quantum model is built within a simulation box, by the bloch's theorem is assumed to be infinitely repeated in any spatial direction, evading the surface termination problem that a real solid would have. Although, the spontaneous polarisation of a material is measured at the surface edges and its P is expressed as μC cm^{-2}, the spontaneous polarisation of a FE material is not a surface property. The surface edges represents the region of space at which the spontaneous polarisation is measured, but the polarisation phenomena span across the entire solid, where negative and positive charges separation rises the dipole that can be measure by a potential applied on both edges of a material[14].

In quantum modelling, the model is infinitely repeated by the Bloch's theorem and periodic boundaries conditions, however, being the spontaneous polarisation a phenomena occurring along the whole solid, its estimation using quantum mechanics is indeed possible. Anyhow, the theoretical possibility of estimating the spontaneous polarisation of a material still represents a challenge by its mathematical complexity. The P of a material is a multidimensional phenomena which makes a calculation significantly more complex because it must be considered along all dimensional axes[14]. The Berry's geometry polarisation phase theory came to solve the P estimation with some simplifications of the problem. The first simplification was that the multidimensionality of the P of a material was broken into a mono-dimensional problem making the equation able to concern the P magnitude on one axis per time[14].

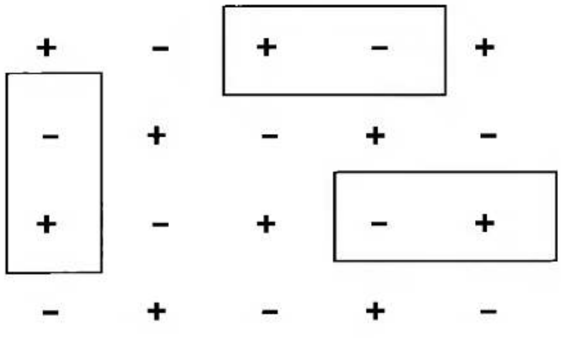

Fig. 3.6 Positive an negative charges coupling of many unit cells repeated in space. Taken from Martin[14].

Furthermore, it has to be considered that the spontaneous polarisation magnitude of a material is proportional to the dipole moment generated by the positive and negative charge separation and to estimates the P it is necessary to find such two extremes of charge separation[140]. Moreover, it is crucial that the spontaneous polarisation calculation will consider to find the maximum dipole momentum present in the axis considered, invariantly from the atomic coordinates given[140]. Indeed, the same crystalline solid can be represented with different and equivalent geometries, and the estimation of the dipole moment of a material should be found to be always the same despite the atomic geometries built within the unit cell[140]. Moreover, considering a repetition of many unit cell, each unit cell will contain the highest positive and negative charges entities, as shown in Figure 3.6, the spontaneous polarisation magnitude should result to be the same despite the charge couples take into consideration. The Berry's geometry polarisation phase theory achieves such results by analysing the unit cell of the quantum model by slicing the unit cell in many finite segments calculating the charge density of each slide, and the conclusive dipole momentum calculated as the quantum modulus of the difference between the highest positive and highest negative charges found along the whole axis[140].

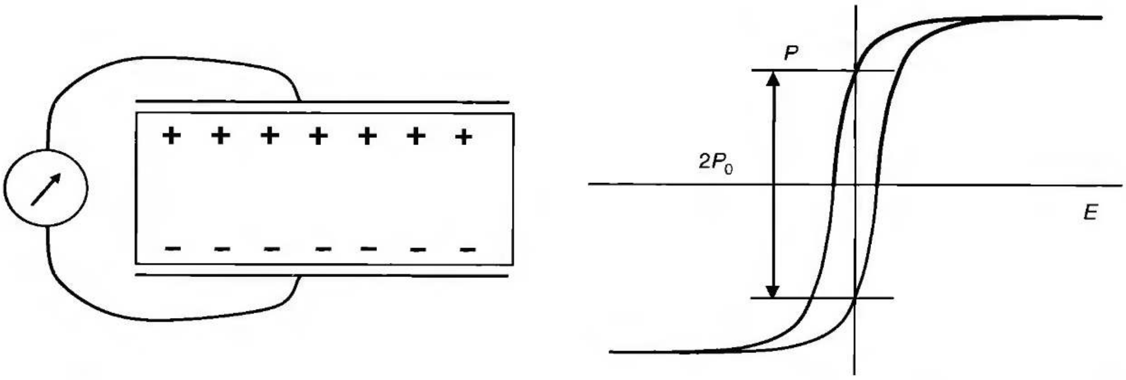

Fig. 3.7 Left: Experimental measurement of the spontaneous polarisation of a medium. Right: Hysteresis loop retrievable from the experimental measurement of P which correspond to the double of the real P magnitude of the solid. Taken from Martin[14].

However, the outcome of a Berry's phase calculation does not tell directly the spontaneous polarisation of a solid, but it only tells the quantum modulus of its maximum dipole momentum[14, 140] expressed in μC cm^{-2}. To know the real spontaneous polarisation value it is necessary to perform at least two calculations, where one is performed on an optimised geometry of a crystal, which will have a characteristic quantum dipole momentum P_1 oriented on one axis direction, while the other calculation is performed on the adiabatic transformation of such crystal made to point the dipole of the crystal in the opposite direction, which will tell the other extreme value of its quantum dipole momentum[14, 140] P_2. Having these two extreme values of the dipole momentum P_1 and P_2 of a crystal, respectively, the spontaneous polarisation of such crystal will be half of the difference between P_1 and P_2[14, 140] as described in equation 3.6. Figure 3.7 shows how the phenomena exists also experimentally, as while attempting to measure the spontaneous polarisation of a material the hysteresis diagram reports double the value of the real P as the hysteresis response gives the sum of dipole momentum inversion between one polarised state to the other, which is why theoretically it necessary to estimate the dipole momentum of both condition of a crystal to retrieve the same answer as it would be for experiments.

$$P = \frac{\Delta \mathbf{P}}{2} = |P_1 - P_2| \tag{3.6}$$

$$P = \frac{d}{V} \tag{3.7}$$

A conclusive remark about using the Berry's phase theory to estimate the spontaneous polarisation of a crystal is that in general terms the spontaneous polarisation magnitude is influence by the ration of dipole momentum a crystal has by the volume of the unit cell of such crystal. However, in DFT, depending on the functional used to perform the Berry's calculation, the volume of the crystal will be affected as well as the polarisable state. Indeed, depending on the XC-f used, the charge density of the system will be estimated differently, which will cause a minor alteration of the dipole moment estimation, altering the spontaneous polarisation magnitude. This is to say that despite equation 3.7 describes the relation of P by the dipole momentum of the crystal model and its volume, such relation it is not to be expected perfectly linear when expressing the spontaneous polarisation as function of volume since any DFT XC-f could have minor effects on the prior estimation of the dipole momentum of a given crystal.

3.3 Vibrational frequencies

As the prediction with DFT of structural properties of PVDF polymorphs is a computational approach which does not guarantee that the predicted structures will necessarily be stable neither exist experimentally, it is possible to perform additional calculations which can verify the phase stability of a crystal[15]. The phonons calculation allows to verify such stability, furthermore, from phonons calculation it possible to extrapolate the vibrational frequencies of a crystal of further help for validating with experimental IR spectra the consistency of the calculation performed in merit of every single PVDF crystal structure[15]. When calculating the phonons of a crystal, the vibrational modes associated to the phonon modes are expected to have positive wavelengths if the crystal structure is at its energetic ground state[15]. Therefore, phonons can be used to verify if the predicted geometries could be stable, hence, expected to be observable in experiments.

The foundation of phonons resides in the concept of interatomic vibrations, as being near to 0 K the atoms will have some small vibrations, and depending on the nature of atomic species of a crystal with their peculiar chemical relation with other atoms, groups of atoms will vibrate at specific frequencies, which is directly correlated to a vibrational frequency wavelength[15]. Negative wavelengths can not exit, hence, finding negative frequencies would mean that the crystal structure investigated is not found at the energy minimum of its ground state[15].

Phonons constitute an important information for understanding acoustical and optical properties of a material which determine the technological field of application of a material. Phonons describes the physical behaviour of a material interacting with mechanical waves (acoustics) and electromagnetic waves (optics) in a convenient concept made with the perturbation theory[15]. Indeed, to describe how atoms react with energy and how such energy is exchanged among different atoms of different species sharing different chemical bonds within a crystal structure, is mathematically impossible if considering every atom as a unique entity exchanging energy towards interatomic interactions (e.g collisions, vibrations, bonded orbitals)[15]. The perturbation theory was made to solve such complex matter interaction considering atoms and molecules up to the entire system considered as a wavefunction which can be perturbed by energy[15]. The harmonic approximation has been applied to the perturbation theory to formalise the phonon mode of a couple of atoms as an harmonic oscillator which is deformable under a mechanical of optical wave. The deformation magnitude of such spring can be determined by the mass of each atom and the spring deformation constant reflecting the nature of the chemical bond between such atoms. The deformation of such spring is interpreted as energetic phenomena, which can be translated to a wavelength, the phonon mode. The phonon mode can also be translated to a vibrational frequency, which is what it is observable by IR and Raman spectroscopy. Figure 3.8 shows a simple harmonic oscillator which can be used to described a phonon mode occurring between two atoms both having mass M with an initial spring constant g connecting atoms centres with a length a and a deformation length of d=(a-u) dependent by the atoms mass and the deformation constant of the spring.

Describing the phonon modes as harmonic oscillators simplified the problem of describing the speed of interatomic energy interactions, which can significantly vary even between different crystal made by the same atoms which arrange spatially with different chemical bonds, such as graphite and diamond which has significantly different heat conduction capacity. With the perturbation theory every material can be easily adapted to fit its real physical behaviour within a simple formalism. The speed of interatomic energy interaction does change on the properties of the system by accessing its associated wavefunction properties. Also between heterogeneous materials such as metals and rubbers, the propagation speed of energy can be adjusted to the system under study[15].

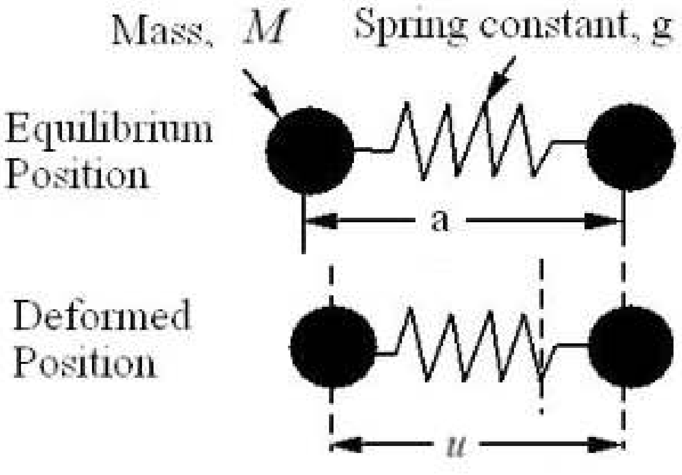

Fig. 3.8 Harmonic oscillator sketch. Taken from Ziman[15].

The vibrational frequencies of a system can be retrieved from the phonon calculation. Every vibrational mode represents the population of atoms within a crystal, which reacts to a specific energy stimulus[15]. Into a vibrational mode, one or more oscillation types can occur (e.g stretching, rocking, twisting, waking and at the far red peaks there are also traslations, librations and docking) between the atoms active in such mode. Such oscillations represent the way atoms reacts to acoustic or optical wavelengths and are associated to specific vibrational frequencies which define absorption, reflection or emission of energy in the case of electromagnetic waves (IR and Raman modes), while acoustic waves more generically represent an homogeneous waving motion of mechanical nature of all atoms along the crystal structure[15].

The phonon modes are generally expressed in hertz, while the vibrational frequencies extrapolated from phonon modes are expressed in cm^{-1} and associated with the respective peak intensity. To calculate the phonons of a crystal it is necessary to first solve the $\hat{H}$ of the quantum model to have the wavefunction of the system, then apply the perturbation theory to calculate the phonon mode from the optimised wavefunction. Every crystal structure has a space group operator which defines the amount of phonons modes to be expected from such structure, hence, also the amount of vibrational frequencies is fixed. The phonon modes number are three times the number of atoms minus three null modes as equation 3.8 and the vibrational frequencies are have six null modes as equation 3.9.

$$f_{hz} = 3N - 3 \tag{3.8}$$

$$f_{cm^{-1}} = 3N - 6 \tag{3.9}$$

3.4 Quantum ESPRESSO

Quantum ESPRESSO is the computational tool used to apply DFT theory on predicting the physical properties of the polymorphs found for PVDF, more precisely it consists of a collection of distinct software able to work in synergy where applicable, useful to achieve deep physics analysis of atomic models of interest. The DFT code of the Quantum ESPRESSO package is implemented with the planewaves basis set, which describes the wavefunction of a quantum system as a group of projected planewaves that together represents the wavefunction energy states up to a fixed kinetic energy cutoffs for the wavefunction, which is generally defined at the beginning of a calculation. The software present in the Quantum ESPRESSO package has not been developed to only perform DFT calculations but it also compute other theoretical approaches (*e.g.* car-parrinello[12]). Here, the Quantum ESPRESSO software package has been uniquely used for the interest in DFT and related post process analysis.

3.4.1 Methods applied to DFT calculations

The DFT study of PVDF crystal structures was performed with a work flow which allowed to have converged structures from which to characterise the physical properties of every crystal. Structures were firstly built and convergence tests performed to verify the right DFT parameters set up, then optimised with a variable cell relaxation (vc-relax) relaxing ions and the lattice using the Broyden–Fletcher–Goldfarb–Shanno (BFGS) algorithm embedded into Quantum ESPRESSO and the relaxed structures used to perform further studies. Table 3.1 reported the main thresholds parameters used along the whole DFT study of PVDF crystal structures equal for all XC-fs used. Table 3.2 reported the description of different types of calculations performed along the DFT study with the relative codes work flow to obtain the results of interest, and Table 3.3 reported the specific parameters that calculations like band structures, DOS, Berry phase and phonons required for performing such calculations with converged parameters. Convergence tests were reported in Figures A.1, A.2 and A.3 concerning the T, TG^+TG^- and $T_3G^+T_3G^-$ crystal geometries, respectively, Table A.1 reported conversion constants and formulae in Appendix.

Table 3.1 Table of general parameters used to conduct calculations always used if not differently specified. wfc: Kinetic energy cutoff of the wavefunction; rho: Kinetic energy cutoff of the charge density; forces: Convergence threshold of forces acting on ions; tot. eng.: Total energy convergence threshold of the total energy of ions minimisation; Tot.Eng.: Total energy convergence threshold of the scf calculation; Mesh: k-points mesh of the Brillouin zone along x,y,and z axes, respectively; N$_K$: Number of k-points in the Brillouin zone.

PVDF	Basic						
	wfc (Ry)	rho (Ry)	forces (a.u.)	tot. eng (a.u.)	Tot.Eng. (Ry)	Mesh	N$_K$
α	80	800	1×10^{-3}	1×10^{-4}	1×10^{-8}	3-2-4	14
β	80	800	1×10^{-3}	1×10^{-4}	1×10^{-8}	2-3-4	12
δ	80	800	1×10^{-3}	1×10^{-4}	1×10^{-8}	3-2-4	14
γ	80	800	1×10^{-3}	1×10^{-4}	1×10^{-8}	3-1-2	4
ε	80	800	1×10^{-3}	1×10^{-4}	1×10^{-8}	3-1-2	4
ζ	80	800	1×10^{-3}	1×10^{-4}	1×10^{-8}	2-3-4	12

Table 3.2 Procedure description of calculation types. Calc. Type: Calculation Types.

Calc. Type	Calculation Procedure
scf	self-consistent-function calculation with basic parameters
nscf	scf + non-scf (nscf) with basic parameters
relax	fixed cell relaxation of ions coordinates with basic parameters
vc-relax	iterative variable cell relax and lattice shape with basic parameters
Bands	scf + nscf + bands (increasing the K-mesh on all axes) + extraction
Berry	scf + nscf (more bands and higher the K-mesh along the polarisation axis)
Phonon	scf + phonon (higher Tot.Eng) + extraction

Table 3.3 Table of parameters used to conduct specific types of calculations. N$_a$: Number of atoms; N$_b$: number of kohn-Sham states (bands). N$_{K+}$: Number of K-points added to any axis in the K-mesh for band and DOS; N$_{K+axis}$: number of K-points added to the polarisation axis for Berry phase calculation; tot.eng.: Total energy convergence threshold of the total energy in scf calculation; Tot.Eng.: Total energy convergence threshold for ions relaxation.

PVDF		Bands & DOS		Berry		Phonon	
	N$_a$	N$_b$	N$_{K+}$	N$_b$	N$_{K+axis}$	tot.eng (a.u.)	Tot.Eng. (Ry)
α	24	54	+7	120	+9	1×10^{-8}	1×10^{-16}
β	12	30	+7	120	+9	1×10^{-8}	1×10^{-16}
δ	24	54	+7	120	+9	1×10^{-8}	1×10^{-16}
γ	48	102	+7	120	+9	1×10^{-8}	1×10^{-16}
ε	48	102	+7	120	+9	1×10^{-8}	1×10^{-16}
ζ	12	30	+7	120	+9	1×10^{-8}	1×10^{-16}

3.5 Molecular dynamics

The study PVDF under finite temperature dynamics has been done using classical molecular dynamics, which is an affordable computational method to simulate large systems of thousands of atoms, furthermore, MD is a time consistent methodology that allow to calculate dynamical properties of particles, the main interest of this research project. In the present project it was of interest to observe the time scale of dynamical properties evolution, hence, the use of MD was the preferred classical mechanics approach. In MD, each atom is treated as a single particle neglecting the subatomic particles which are averaged as generic particle properties with specific parameters such as bonds, angles, dihedral and charges. MD simulations are performed by calculating the trajectories of moving atoms which are ruled by matter interactions[16].

In MD the Newtonian's laws of motion are solved to rule how particles moves under applied forces[16]. The first and third Newtonian's laws of motion defines the condition of energy conservation of the system, as in the first law as equation 3.10 an object (in MD an object is represented by a particle) will preserve its stationary or motion status if the total sum of all vectorial forces acting on it are zero. The second Newtonian's law of motion is of particular interest for MD simulations since it defines that the motion momentum of an object is proportional the force applied as equation 3.11. The third Newtonian's law of motion defines that at any object that applies a force F_a to a second object will receive a reciprocal and opposed force $-F_b$ from such object as equation 3.12.

$$\sum F = 0 \tag{3.10}$$

$$\vec{F} = m \times a \tag{3.11}$$

$$\vec{F}_a = -\vec{F}_b \tag{3.12}$$

The prediction of how particles and molecules of an atomistic system behave under certain condition of motion, are defined by the FF used in the in simulation and the specific parameters that defines how different particles interact with bonded and non bonded interactions. The equations of a FF that rules the particles interactions are known as potentials. Every potential describes the energy interaction relation of different particles and depending on the potential, to describe the behaviour of a particular particle, specific parameters must be given to tune the potential efficacy in shaping the interaction of such particle with bonded and non bonded particles. Every particle represents an atom, and its specific parameters per each potential of the FF must be derived from quantum mechanics simulations or from experimental observation to make the potential able to mimic a specific atom type behaviour as observed in experiments[16].

3.5.1 Molecular dynamics general settings

As molecular dynamics simulates the dynamics evolution along time of physical properties of materials simulated under the environmental conditions desired, to observe how the system properties change across time steps, there are settings of the model to simulate that are specific of the force field (parameters to feed FF potentials), where the FF used influences such settings, and other settings which remains necessary and independent from the FF used in the simulation. This section does treat the independent settings of MD which are necessary to configure to start simulating from initial atomic coordinates set.

In MD, particles motion are describe by the dynamic evolution of their properties in function of time satisfying the Newtonian's laws of motion. The equation of motion express the particles potential and kinetic energy evolution in function of time depending on the external forces applied. This particle motion is independent from the FF selected, however, the FF describes the energetic boundaries relations of particles from bonds, angles, dihedral and long range forces. To make MD able to describe the dynamics evolution of particles properties as function of time, the time step evolution must fall in the time scale of chemical bond vibrations, which is in the time length of one femtosecond. At such time scale atoms vibrates and move in space and to simulate consistent particles behaviour as observed in experiments, the time scale of the simulation must be based at such time step of one femtosecond. Using longer time step would make the dynamic properties evolution inconsistent as the chemical bond vibrations of atoms would be neglected, hence, the properties of the system would evolve inconsistently.

As MD simulates moving particles along time, moving particles presents the problem where particles would move out of the initial simulation box built for the computation of interest, indeed, to avoid that atoms would go over the simulation box boundaries if allowed to move is simply impossible. At the same time, as an MD simulation is built within a simulation box size, the conditions of the simulation apply inside such box, hence, particles that leave the simulation box would be lost and released from the properties within the box. As the Newtonian's laws of motion are valid only in the case of constant mass systems, no particles can leave the simulation box getting distant from the rest of the particles of the system. To conserve the system mass and number of particles, periodic boundaries conditions are applied to make the particles which crosses the box boundaries to re-enter the simulation box. The periodic boundaries restriction project particles that are exiting the box boundaries to the other side of the axes edges. More practically, a particles which is going over the bottom boundary of the a-axis of a simulation box, would be projected as re-entering in the simulation box from the top of the a-axis, such periodic boundaries applies along all axes.

The environmental conditions of an MD simulation box includes temperature and pressure, which influence the energetic and aggregation states of the simulated system. The thermostat is deputed to control the evolution of temperature along the simulation time steps and the barostat takes care of the pressure evolution of the system along time. Moreover, other properties of the system can be accounted to stay constant or vary along the time step evolution, in general, when setting an MD simulation a specific properties ensemble is chosen to set the more adapt simulation conditions to observe the dynamics behaviour of interest. Two MD notorious ensembles are the "nvt" and "npt", where nvt takes care of keeping fixed the number of particles of the system and the volume of the simulation box and npt keeps the number of particles and the pressure within the simulation box fixed. Both nvt and npt ensembles uses the Nose-Hoover thermostatting and manage the temperature of the simulation box to start with the initial temperature and to terminate the simulation with the final temperature. The initial, final and temperature ramps are given to the Nose-Hoover thermostat at the beginning of the simulation. The present MD simulations has been carried over entirely with the npt ensemble keeping the pressure of the simulation box fixed at one atmosphere using the Nose-Hoover barostat.

3.5.2 Force field definition

A force field contains all the classical mechanics equations which rules atoms behaviour based on the parametrised properties of bonds, angles, dihedrals and long range forces, any physical phenomena neglected in the FF, is neglected in the whole simulation[16]. The FF potentials can be generalised in two categories, the first category is made by bonded potentials, which defines energy contributions such as bonds, angle and dihedrals of atoms that are physically connected as a couple or groups of three and four atoms, respectively. The other category is made by non bonded potentials of which coulomb electrostatics and vdW forces are the most representative non bonded energy contribution generally used in MD simulations. Figure 3.9 shows on the left the a classic vdW energy potential profile and on the right a classic coulomb energy potential profile. Structural properties dynamic evolution of the system along simulation time steps, are given by the whole energy contributions of all bonded and non bonded potentials of the FF[16].

The bonded potentials are usually not heavy to compute as such potentials only consider the energy contribution of atoms in tight contact. The long range forces potentials such as coulomb and vdW forces becomes more heavy to be computed as per each particle in the simulation box, its energetic state is dependent by all the other particles which are within the simulation box, increasing exponentially the amount of particles interactions to account for solving the non bonded potentials[16]. In some non bonded potentials, to reduce the computational cost of the energy contribution of non bonded interactions an explicit distance cutoff is given to exclude all particles which are found over such distance cutoff from a specific particle. This reduces the amount of non bonded interactions in the simulation box without significantly affecting the energy contribution of the non bonded interactions if the distance cutoff is large enough to neglect particles so distant from a reference particle to not significantly affect the energy interaction contribution, as more distant are two particle and weaker will be their energy interaction[16].

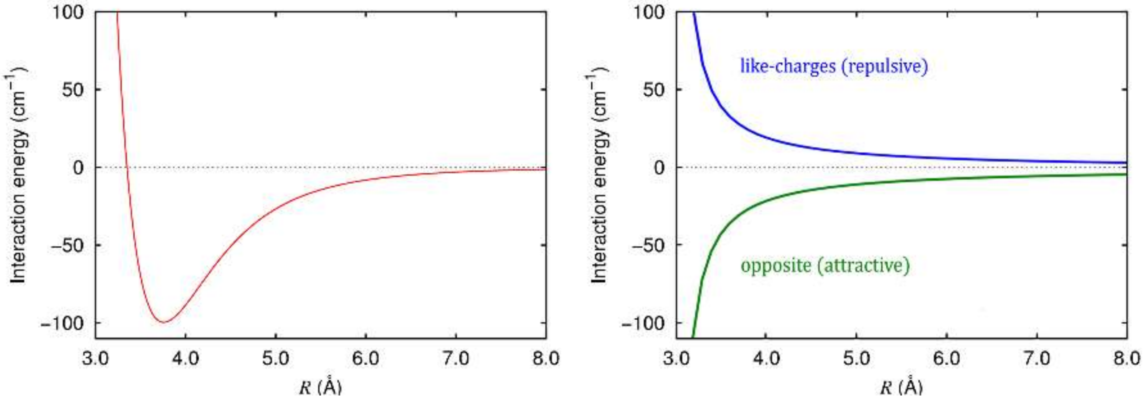

Fig. 3.9 Left: The van der Waals energy interaction contribution of non bonded particles as function of space. Taken from Martin [14]. Right: The Coulomb energy interaction contribution of non bonded particles as function of space. Taken from Martin [14].

As non bonded potentials increases the computational demand of solving many particles interactions, to reduce the computational cost is not only done by applying a distance cutoff, but also by choosing different methodologies to perform the summation of energy contributions of non bonded potentials. A specific case which is fast and accurate, hence, used in the present MD simulations set up is the Ewald summation[16]. The Ewald summation allow to perform a summation of particles energy contribution separating interacting particles with a cutoff. In this case, the cutoff of the Ewald summation does not excludes particles but, defines short and lond range particles based on their distance from a reference particle. The short range non bonded energy interactions ψ_{sr} are summed directly as occurring in real space, while the long range non bonded interactions ψ_{lr} are summed by a Furrier transformation of the long range space[16] as equation 3.13. This distinction allows to consider in the short range the energy contribution of near particles that have higher impact on the energy contribution, and to consider as marginal distant particles as a whole group of energy contribution which is weaker, hence, change only marginally the energetic contribution of a reference particle interacting with non bonded distant particles. The Ewald methodology compromises accuracy and speed, therefore, is a widely used summation technique applied in calculating the energy contribution of long range potentials[16].

$$\psi(r) = \psi_{sr}(r) + \psi_{lr}(r) \tag{3.13}$$

Sometimes, FFs can have special potential which usually are added in the bonded potential class which are used to tune the FF potentials, the ability of describing specific structural features of a material, such potentials are generally referred as cross terms as they mix energy interactions of the same bonded potential or different types of bonded potentials to make the FF able to describe more consistently the structural features desired[16]. However, this practice of using cross terms has been in the last decade left behind as an old MD simulation practice since cross terms are very specific potentials, often non standard and usually difficult to find their implementation in modern MD codes.

3.6 Literature force fields

3.6.1 MSXX

Karasawa *et al*[26] developed the MSXX force field which was mainly meant to describe crystalline and physical properties of bulk PVDF such as elasticity, young modulus, piezo-, pyro- and ferroelectric related properties. The MSXX parametrisation was based on experimentally observed physical properties. Later on, Karasawa *et al*[110] and Su *et al*[104] used MSXX for finite temperature dynamics studies. The force field is described using the following equations where energy constants were expressed in kJ mol^{-1}. The bond potential E_b if of the morse form with D as a constant energy variable specific per every bond type, α as a unit of space in Å, r the real bond length and r_0 the optimal bond length type distance both expressed in Å.

The angle potential E_a is of the cosine^2 form which has an energy constant $\frac{C}{2}$ specific per every angle type, multiplying the squared value of the cosine of the real angle type versus the cosine of the optimal angle type. The torsional potential E_t is of a custom form made by Karasawa *et al*[110] to adapt to PVDF polymer chains with C_m as an energy constant specific per every torsional type multiplying the real dihedral type value together with the constant factor m. The van der Waals potential E_{vdW} has the Buckingham form with A_{ij} and C_{ij} as energy constant specific per every atomic specie and the expression $-\alpha(\frac{-r}{\rho})$ as function of distance over energy per every atomic species combination. The electrostatics potential E_{coul}

has the Coulomb form with C_{coul} as energy constant which multiply couples of electrostatics charges q_i and q_j over the ratio of energy ε expressed kJ mol^{-1} multiplying the charges distance r expressed in Å.

$$
\begin{aligned}
E_b &= D[1-e^{-\alpha(r-r_0)}]^2 && (3.14)\\
E_a &= \frac{C}{2}(cos\ \theta - cos\ \theta_0)^2 && (3.15)\\
E_t &= \sum_{m=0}^{6} C_m cos\ m\phi && (3.16)\\
E_{vdW} &= A_{ij}e^{-r/\rho} - \frac{C_{ij}}{r^6} && (3.17)\\
E_{coul} &= \frac{C_{coul}q_iq_j}{\varepsilon r} && (3.18)\\
E_{tot} &= E_b + E_a + E_t + E_{vdW} + E_{coul} + E_x && (3.19)
\end{aligned}
$$

In Table 3.4 all parameters assigned to each force field potential were reported and equations 3.14, 3.15, 3.16, 3.17 and 3.18 described the potentials for bonds, angles, dihedrals, vdW forces and coulomb interactions, respectively. Equation 3.16 is a dihedral potential developed as summation of seven factors and per each factor has a specific constant $C_{0,6}$ given in Table 3.4. Equation 3.17 is the Buckingham potential that defines the repulsive $(-\frac{C_{ij}}{r^6})$ and attractive $(A_{ij}e^{-\frac{r}{p}})$ van der Waals force, where A_{ij}, C_{ij} and p constants, which defines the repulsive, attractive and energy units constants, respectively, are given in Table 3.4. Equation 3.19 shows the energy terms summation of all potentials including the energy terms of the four non standard cross terms E_x, decomposed in equation 3.20 which describe the energy terms summation of the four cross terms implemented in MSXX.

$$
\begin{aligned}
E_x &= E_{ab} + E_{bb} + E_{1aa} + E_{2aa} && (3.20)\\
E_{ab} &= D(cos\ \Theta - cos\ \Theta_0)(R-R_0) && (3.21)\\
E_{bb} &= k_{RR}(R-R_e)(R'-R'_e) && (3.22)\\
E_{1aa} &= G_{ij:kl}(cos\ \Theta - cos\ \Theta_0)(cos\ \Theta' - cos\ \Theta'_0) && (3.23)\\
E_{2aa} &= F_{i:jk:l}(cos\ \Theta)(cos\ \Theta - cos\ \Theta_0)(cos\ \Theta' - cos\ \Theta'_0) && (3.24)
\end{aligned}
$$

Equation 3.21 is an angle-stretch cross term that correlates bond energy with angle energy normalised by the constant D which is specific per every angle and bond types of different groups of atoms. Equation 3.22 is a stretch-stretch cross terms which correlates the stretching

Table 3.4 MSXX force field parameters made by Karasawa *et al*[26]. X: Cross term values of cross term potentials. *: Values adjusted in the present study to simulate finite chains length. The units of K,D, k_R,k_θ,A_{ij},C_{ij} are in kJ mol^{-1}. The units of R$_b$,ρ are in Å. The units of Θ_a D$_{C0}$, D$_{F0}$, D$_{H0}$ and D$_{RR}$ are in degrees. The units of Charge are in elementary charge (e).

Units						
Electrostatics						
	C_{H2}	C_{H3}*	H	C_{F2}	C_{F3}*	F
Charge	-0.54	-0.54	0.18	+0.70	0.78	-0.26

van der Waals				Bond Stretch		
	A_{ij}	ρ	C_{ij}		k_R	R$_b$
F-(F,C,H)	470692.3	0.22112	277.0	C-C	2854.3	1.5242
C-(F,C,H)	57473.5	0.32364	2423.5	C-H	3051.4	1.0789
H-(F,C,H)	9228.0	0.27097	145.6	C-F	3481.4	1.3457

Angle Bend			Dihedral		One-Center $\Theta-\Theta$ X	
	k_θ	θ_a		K		K
H-C-H	220.8	116.4161	C$_{m0}$	3.33	$G_{CC:HC}$	10.33
C-C-H	271.0	116.0913	C$_{m1}$	-1.93	$G_{CC:HH}$	-6.88
C$_F$C-C$_F$	746.8	116.3318	C$_{m2}$	-1.82	$G_{CH:CC}$	86.77
C-C$_F$-C	650.8	119.3277	C$_{m3}$	3.19	$G_{CH:CH}$	3.59
F-C-C	582.4	114.8591	C$_{m4}$	-0.16	$G_{CC:FC}$	10.32
F-C-F	772.9	109.5665	C$_{m5}$	-0.53	$G_{CC:FF}$	114.47
			C$_{m6}$	-0.69	$G_{CF:CF}$	-24.42

Two-Center $\Theta-\Theta$ X		Angle-Stretch X			
	K	D$_{C0}$	D$_{F0}$	D$_{H0}$	K$_{RR}$
$F_{C:CC:H}$	119.41			-86.14	22.33
$F_{C:CC:C}$	-44.43	-109.18		-92.37	4.15
$F_{F:CC:H}$	1.01	-84.14			77.95
$F_{F:CC:C}$	122.58	-113.47			52.72
		-204.95	-263.40		464.97
				-317.92	608.34

energy of two groups of two atoms which shares a common atom, this energy is normalised by the constant k_{RR}. Equation 3.23 is one centre angle-angle cross terms which correlates the angle energy of two group of three atoms which shares one common atom and normalised by the constant $G_{ij:kl}$. Equation 3.24 is a two centre angle-angle cross terms which correlates the angle energy of two group of three atoms which shares two common atoms and normalised by the constant $F_{i:jk:l}$. Typically, cross terms are used to adjust structural features of specific materials[16], and apart from the complexity, such cross terms were not standard cross terms implemented in modern MD codes such as LAMMPS or GROMACS. Therefore, being impossible to reproduce such cross terms into the modern MD code used for this study (*e.g.* LAMMPS) and to avoid ambiguity, the present incomplete force field reproduction was labelled as MSXX-nocross (MSXX-noX) to distinguish it from the original MSXX force field.

3.6.2 Byutner and Smith

Byutner *et al*[27] developed a FF which has been based on *abinitio* QM data. In such force field, Byutner *et al*[27] parametrised carbon, fluorine and hydrogen atoms properties to describe PVDF properties in bulk system to study the melting mechanisms of PVDF at finite temperatures[27, 111]. Table 3.5 shows the characteristic parameters of B&S force field assigned to each potential. The equations 3.25, 3.26 and 3.27 describe the potentials which rule bonds, angles and dihedrals energetics, respectively. The long range forces such as vdW and Coulomb are in common with MSXX as equations 3.17 and 3.18 reported, respectively.

$$E_b = K_b(r - r_0)^2 \tag{3.25}$$

$$E_a = K_a(\theta - \theta_0)^2 \tag{3.26}$$

$$E_t = \sum_{m=1}^{m} K_i[1 + cos(n_i\phi - 180)] \tag{3.27}$$

$$\tag{3.28}$$

Equation 3.25 which is he bond potential with harmonic form has the squared value of the difference of the real bond length r versus the optimal bond length r_0 per every bond type multiplied by the energy constant K_b specific per every bond type. The angle potential of equation 3.26 with the harmonic form has the squared value of the difference of the real angle value Θ versus the optimal angle value Θ_0 multiplied by the energy constant K_a specific per every angle type. Equation 3.27 is the torsional potential with Furrier form with K_i as energy constant (*e.g.* K1, K2, K3, K4, K5 and K6 of Table 3.5) which changes up to six times per every summation step that multiply the cosine value of the dihedral angle adjusted per every summation step with the variable n_i which is an integer that changes at every summation step (*e.g.* from 1 up to 6) and the dihedral angle phase reversed of 180^{o}.

3.6.3 OPLS

A FF for more general uses such as the OPLS[141] has been recently used to conduct studies in how polymers behave in contact with a surface substrate such as PG, PVDF was one of the polymers studied by Guryel *et al*[28]. The OPLS force field shared with the B&S set up

Table 3.5 Byutner & Smith force field parameters made by Byutner *et al*[27]. a: B&S original. b: Erdtman original. The units of K1, K2, K3, K4, K5, K6, A_{ij},C_{ij} are in kJ mol^{-1} and K_b, K_a in kJ mol^{-2}. The units of r_0 and ρ are in Å. The units of $\Theta_0$is in degrees. The units of Charge are in elementary charge (e).

Units					
Electrostatics		van der Waals			
	Charge		A_{ij}	ρ	C_{ij}
C_{H2}	-0.57222	F-F	568111.9	0.219969	444.0
H	0.19877	H-F	188673.3	0.261910	1091.1
C_{F2}	0.67320	C-F	51436.2	0.241365	225.4
F	-0.24926	C-C	62659.6	0.323625	2681.1
C_{H3}	-0.68365	C-H	18074.9	0.292826	578.4
C_{F3}	0.83512	H-H	11085.9	0.267380	114.5

Bond Stretch			Angle Bend		
	K_b	r_0		K_a	θ_0
C-C	2584.9	1.534	C-C-C	672.0	118.24
C-H	2741.4	1.085	F-C-C	753.1	107.74
C-F	4178.1	1.357	F-C-F	1004.2	105.27
			C-C-H	359.0	108.45
			H-C-H	322.2	109.27

Dihedral						
	K1	K2	K3	K4	K5	K6
CCCC^a	3.31	6.02	-3.18	-1.72	3.56	-0.21
Others^a	2.97	2.89	-3.18	1.18	1.21	-0.21
CCCC^b	1.65	3.01	-1.59	-0.86	1.78	-0.10
Others^b	1.49	1.44	-1.59	0.59	0.61	-0.10

the bonds and angles harmonic potentials reported in equations 3.25 and 3.26, respectively, as well as the Coulomb potential which was in common between all three force fields used in this study as defined in equation 3.18. The dihedrals potential was different as reported in equation 3.29 and also the vdW long range forces potential in the case of OPLS it was chosen to be the standard Lennard-Jones (LJ) potential as in equation 3.30 with a long range cutoff of 11 Å as used by Guryel *et al*[28].

$$E_t = \frac{1}{2}K_1[1+cos\phi]+\frac{1}{2}K_2[1-cos2\phi]+\frac{1}{2}K_3[1+cos3\phi]+\frac{1}{2}K_4[1-cos4\phi] \tag{3.29}$$

$$E_{vdW} = 4\varepsilon\left[\left(\frac{\sigma}{r}\right)^{12} - \left(\frac{\sigma}{r}\right)^{6}\right] \tag{3.30}$$

Equation 3.29 for the torsional potential with OPLS form has the cosine of the dihedral value adjusted as a summation of four terms of the same value multiplied by a growing integer number (*e.g.* from 1 up to 4) at which is summed or subtracted the value of 1 depending on the summation step, also multiplied by half of the energy constant specific per every summation term (*e.g.* K1, K2, K3 and K4). Equation 3.30 is the vdW potential with the Lennard-Jones form of σ 12 and 6 for the repulsive and attractive terms, respectively, where σ is the optimal distance where repulsion and attraction cancel out and r is the real distance of the two particles multiplied by four times the energy terms ε. Table 3.6 reported all parameters used in the OPLS potentials and to be noted is that in Guryel's paper[28] the σ distance parameters of the LJ potential were given in Table as σ Å^{-1} but it was evident from the magnitude of σ values that such parameters were indeed given as σ nm^{-1}, hence, corrected and here given in Table 3.6 with the correct parameters magnitude of σ Å^{-1}.

Table 3.6 OPLS force field parameters used by Guryel *et al*[28]. The units of K_a, K_b andε are given in kJ mol^{-1}. The units of r_0 and σ are given in Å. The units of Θ_0 are given in degrees. The units of Charge are in elementary charge (e).

Units							
Electrostatics		van der Waals			Bond Stretch		
	Charge		ε	σ		K_b	r$_0$
C_{H2}	-0.0148	C-C	0.4393	3.75	C-C	1121.3	1.529
C_{H3}	-0.02220	C-H	0.2347	3.06	C-H	1422.6	1.090
H	0.0074	C-F	0.3347	3.42	C-F	1535.5	1.332
C_{F2}	0.24	H-H	0.1255	2.50			
C_{F3}	0.36	F-F	0.2552	3.12			
F	-0.12	F-H	0.1799	2.79			

Angle Bend			Dihedral				
	K_a	θ_0		K1	K2	K3	K4
H-C-H	146.4	109.0	CCCC	27.6	4.0	-5.8	-8.9
C-C-H	146.4	113.0	FCCC	-10.5	0.0	10.5	0.0
C-C-C	244.1	112.70	FCCH	0.0	0.0	1.7	0.0
F-C-C	209.2	109.50	HCCC	-3.2	-1.2	2.8	0.0
F-C-F	322.2	109.1					

3.7 Molecular dynamics data analysis techniques

The main interest of using MD simulations in this project was to calculate the dynamic properties of the system, and this section treats the data analysis used to evaluate how the dynamic properties of the simulated systems changes across time. With such data analysis it becomes possible to evaluate the structural properties of PVDF chains at certain simulation conditions such as crystalline solid phase, liquid phase and how the presence of a surface and depending on the surface properties, how the structural properties of PVDF chains are affected. Data as energetics and lattice dimension are direct simulation output, hence, no data analysis is required and data of chapter 5 in section 5.1 the lattice are normalised by the minimal repetitive unit cell and energies are simply normalised by PVDF unit block, which the CF_2-CH_2 monomer.

The liquid properties of PVDF models studied further in the thesis, required data collection and analysis to evaluate the evolution of the system dynamic properties. Data as density, radius of gyration (R_g), end to end distance (R_e), dihedrals distribution and conformation tensor were used to evaluate the structural features of PVDF chains in different simulation condition such as bulk models and surface models. The density of the system allows to understand the aggregation state of the system as from passing from solid to liquid the system density changes significantly and per each material a specific density of the solid and the liquid is experimentally known. Monitoring the density evolution as function of time allows to know when the system phase changes from solid to liquid, and when the density changes across time even out to a fixed value (if fixed temperature applies), it represent a clue that the system is encountering a steady state where the density is not significantly changing any more.

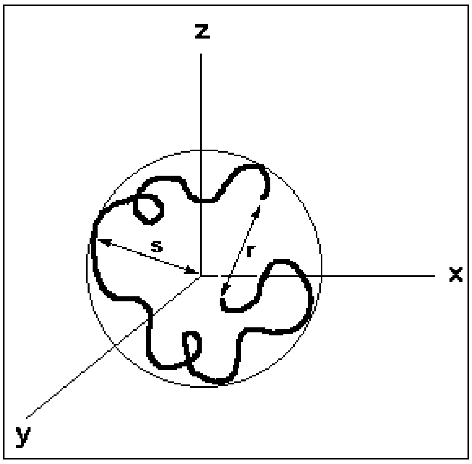

Fig. 3.10 Schematic sketch of R_g (s) and R_e (r) identification. Taken from Rapaport[16].

The R_g is a properties of molecules which represents the averaged distance that every atom of a molecule has from its centre of mass, if a molecule is planar, its R_g will be higher than when a molecule is folded on itself. In the case of polymers, linear chains has higher R_g averages than coiled chains, by distinguishing the average value of R_g of linear chains, its decrease would mean that the molecules are coiling on themselves, a general indication that molecules are getting more disordered. The R_e represent the distance of the two more distant atoms of the molecule, again, higher the value indicates a molecule which is expanded in space, and lower values of R_e indicates the molecules are getting coiled on themselves. Figure 3.10 shows a schematic sketch to easily identify the properties of a long linear polymer as s represents the R_g averaged value of the polymer and r represents the R_e value. In this thesis, the density, R_g, R_e properties of the simulated system are visualised with graphs and table, in which the standard deviation of such properties was also reported.

The dihedral distribution of backbone chain atoms is another important structural information which relates to R_g and R_e, although, the dihedrals are more informative on the structural features of polymeric chains as they specific the orientation of four chemically bonded backbone atoms. In polymers, a linear chain is expected to have all dihedrals at 180^o, deviation from such values indicates that the polymer backbone is deformed to assume less ordered structures. The dihedral distribution of backbone atoms allow to understand the linear state of polymer chains with high structural detail, which allow also to understand how lateral atoms attached to the backbone atoms are displaced as direct consequence of backbone atoms dihedral orientation. Figure 3.11 shows the potential energy of dihedral backbones of polyisobutylene, depending on the dihedral a group of four carbon atoms assumes, the relative methyl group is twisted around the backbone chains. Equations 3.31 and 3.32 shows how the R_g and R_e properties are calculated.

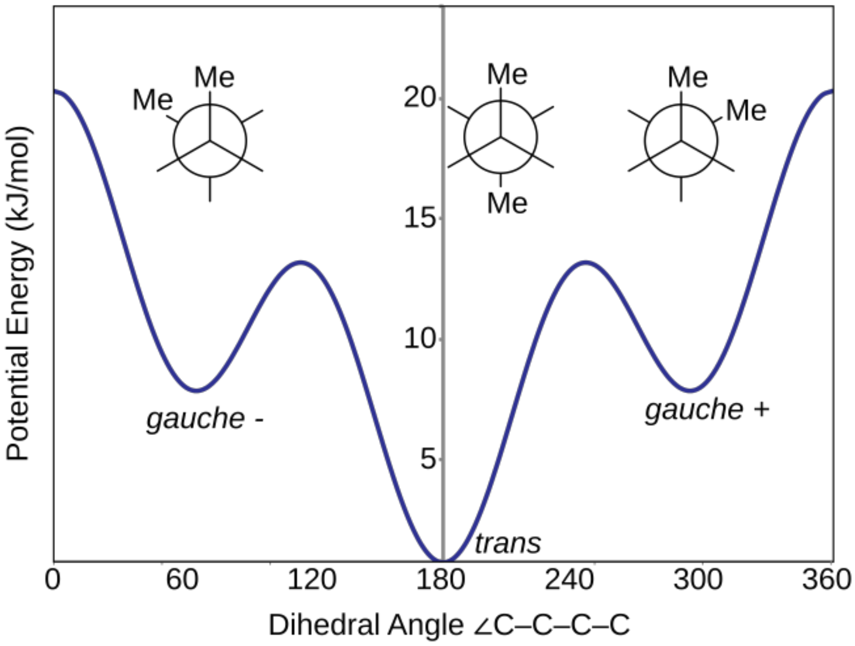

Fig. 3.11 Dihedral distribution sketch of a polyisobutylene chain. Taken from Hari[17].

The distribution of atoms along the simulation box can represent another interesting property to be calculated as it makes possible to appreciate between different simulation conditions, how atomic species distribute along the simulation box. Conceptually, when all atomic species of a material are equally dispersed in the simulation box, it makes evident that in any place of the simulation box specific conditions apply to influence the spatial distribution of atoms, making the system homogeneous. In the case where by observing the atoms distribution of different species present in the simulated atomistic model, different atoms are dispersed at different concentrations in space, it means that some local properties of the system are influencing atomic species distribution. Comparing homogeneous systems with non homogeneous systems and knowing the differences applied between different simulation conditions, is possible to deduce that the differences between the simulations are altering the atomic species distribution. Such informations are crucial to understand which conditions are needed to make a stochastically disordered system of homogeneously dispersed atoms, to become a system which presents degree of order in the atomic species distribution.

Finally, an important information which can tell when the particles included into a simulation box have reached a steady state equilibrium of homogeneous disorder, is the conformation tensor. The conformation tensor calculates the atomic displacements of all particles from their original starting point at a given initial time step, to a final time step. The spatial coordinates of all particles at all recorded time steps occurred between the starting and final points are used to calculated the conformation tensor of the system. If particles moves around enough that all particles at the final time step are found to be far from the original starting point and stochastically distributed, the conformation tensor will make it evident. Indeed, the conformation tensor is a vectorisation of particle movements in three dimensional as equation 3.33, and the diagonal of such vectorised matrix of three by three (for three dimensional systems) represents the sum of all atomic displacement occurred in the a, b and c axes, respectively. In the case of a fully disordered system where all particles have enough time to move far from their original place, the diagonal of the conformation tensor will converge to one as presented in Table 3.7. By following the density dynamics as function of time and the conformation tensor convergence to one, it is possible to determine when the material modelled in the simulation box melts, becoming liquid, and its stochastically disordered state where all particles moved significantly from their point of origin, indicating that system reached an equilibrium where the system properties becomes independent from time, hence, being the system liquid as verified by the density and conformation tensor convergent to one, the system can be assumed to be at its liquid phase equilibrium.

$$R_g = \langle \sum_{0}^{j} \frac{|r_j - \sum_0^j \frac{r_j m j}{n}|}{j} \rangle_{x,y,z} \tag{3.31}$$

$$R_e = euclidean \; |(x_{ja}, y_{ja}, z_{ja}), (x_{jb}, y_{jb}, z_{jb})| \tag{3.32}$$

$$C_{tensor} = \langle \frac{3RR}{\langle R_e^2 \rangle} \rangle \tag{3.33}$$

$$\tag{3.34}$$

Table 3.7 Examples of the conformation tensor of a system where all atoms moved stochastically far from their original place, showing the diagonal matrix is converged to one. Taken from Hari[17]. [a]: conformation tensor of x-axis C_{xx}; [b]: conformation tensor of y-axis C_{yy}; [c]: conformation tensor of z-axis C_{zz}.

Conformation tensor		
1.000[a]	0.000	0.000
0.000	1.000[b]	0.000
0.000	0.000	1.000[c]

Chapter 4

DFT study of bulk crystalline PVDF

The use of density functional theory to compute physical properties of PVDF represented the first investigation step with the aims of finding the best XC-f able to predict PVDF physical properties accordingly to experiments, and using such XC-f to complete an exhaustive investigation of the structural properties of PVDF crystals. Within this chapter, the crystal properties such as lattice structures, phase and lattice energies, bands structures, spontaneous polarisation and vibrational frequencies were investigated to define the best DFT functional that better described physical properties of PVDF in comparison with experiments and to answer key questions related to PVDF polymorphisms. Indeed, as much PVDF was studied in the past, some crystal structures of PVDF and some modern XC-fs of DFT were never investigated. Such missing pieces of research represented an important study focus for this thesis since it was necessary to complete the knowledge about PVDF crystal properties together with the individuation of the most consistent DFT functional. As DFT is an approximative quantum methodology to solve the electron density of a quantum system, its limit of accuracy is generally acknowledged to be of 1 mRy (0.14 eV) per atom in the model, and depending on the XC-f further accuracy limitations can be present in predicting specific physical properties of a material such as lattice structures, phase and lattice energies, bands structures and band gap, spontaneous polarisation and vibrational frequencies[142]. For such reasons, the individuation of the most suitable XC-f has been taken into account for the present research project.

Table 4.1 Lattice constants, angle β^{o}, and volume V, for the α-phase for different functionals compared to DFT and experimental results available in the literature. *: Estimated lattice accuracy from present convergence tests, see Tables A.1, A.2, A.3.

Method	XC	a (Å)	b (Å)	c (Å)	β^{o}	V(Å^3)	Reference	Accuracy (Å)
Exp.	-	9.64	4.96	4.62	90.0	220.9	[75]	0.01
DFT	LDA	8.95	4.65	4.58	90.9	190.3	Present	1.0e-05
DFT	PBE	10.0	5.21	4.68	90.7	243.7	Present	1.0e-05
DFT	vdW-DF	9.57	4.99	4.69	90.6	224.0	Present	1.0e-05
DFT	vdW-DF2	9.39	4.85	4.69	90.7	213.6	Present	1.0e-05
DFT	PBE-D2	9.27	4.80	4.65	90.8	206.9	Present	1.0e-05
DFT	PBE	10.3	5.18	4.70	91	250.7	[82]	0.09*
DFT	PBE	9.77	5.02	4.67	90	229.0	[66]	0.09*
DFT	PBE-D2	9.24	4.75	4.64	90	203.7	[66]	0.09*
DFT	PBE0 hybrid	9.98	5.03	4.65	90.4	233.4	[101]	0.09*

4.1 Lattice structures

α PVDF

The α-phase is monoclinic with space group $P2_{1/c}$[65, 66, 75, 107] and has a TG^{+}TG^{-} chain structure with the dipoles aligned antiparallel resulting in a non-polar centrosymmetric structure as shown in Figure 2.4. The lattice parameters for the α-phase for various functionals are shown alongside previous calculations and experimental values from literature in Table 4.1. The c lattice parameter is along the chain and the a and b parameters are along inter chains directions (where not chemical bonds connects distinct PVDF chains). The LDA was seen to underestimate the a and b lattice constants by 6-7% but is in good agreement with the c lattice constant.

In contrast, PBE significantly overestimates the a and b lattice constants by 4-5% but again is in reasonable agreement with the c lattice constant, which is in good agreement with previous PBE results[66, 82] as well. The lattice constant in the c direction is determined by the carbon backbone and this length is less sensitive to the functional. However, the polymer chains are held together by van der Waals forces which are wrongly approximated in LDA and GGA. As expected, the a and b lattice constants were underestimated by LDA that overbinds electrons, whereas the GGA underbinds electrons overestimating a and b lattice constants[143].

All calculations with vdW functionals or corrections give lattice constants that are closer to experimental results. The vdW-DF2 and PBE-D2 calculations underestimate the experimental values by 2-4% for a and b lattice constants and 1% along c axis. The vdW-DF

Table 4.2 Lattice constants and volume V, for the δ-phase for different functionals compared to DFT and experimental results available in the literature. *: Estimated lattice accuracy from present convergence tests, see Tables A.1, A.2, A.3.

Method	XC	a (Å)	b (Å)	c (Å)	V(Å^3)	Reference	Accuracy (Å)
Exp.	-	9.64	4.96	4.62	220.9	[21]	0.01
DFT	LDA	8.92	4.62	4.58	188.6	Present	1.0e-05
DFT	PBE	10.09	5.17	4.69	244.4	Present	1.0e-05
DFT	vdW-DF	9.53	4.98	4.70	223.2	Present	1.0e-05
DFT	vdW-DF2	9.32	4.85	4.69	211.9	Present	1.0e-05
DFT	PBE-D2	9.21	4.80	4.65	205.6	Present	1.0e-05
DFT	PBE	9.71	5.02	4.67	227.6	[66]	0.09*
DFT	PBE-D2	9.10	4.79	4.65	202.7	[66]	0.09*
DFT	PBE0 hybrid	10.0	5.01	4.65	233.0	[101]	0.09*

agrees with the experimental values to within 1% for a and b lattice constants and 1.5% along c axis. Our results for PBE-D2 are in close agreement to previously authors results[66]. The type of pseudopotential used only has a small effect on the lattice constants (PAW, US and NC were tested and only US PPS were included in the thesis) compared to the effect of the XC-f, with PAW giving slightly larger volumes than US. The monoclinic space group of the α-PVDF has α and γ angles fixed to 90° but the β-angle is not constrained to be 90°[82]. Our results for all functionals show a small deviation from 90°, similar to previous DFT calculations[101, 82]. This is a small deviation that is within the DFT limits of accuracy, however, experimentally the β angle of the α-phase was found to be 91°, hence, consistent with the present computations.

δ PVDF

The α-phase can be transformed into the δ-phase by application of a strong electric field[21, 69]. The δ-phase is similar to the α-phase except that the dipoles are aligned so that there is a net spontaneous dipole moment, as shown in Figure 2.5. The crystal structure of the δ-phase is orthorhombic with space group $P_{na}2_1$ (or equivalently $P2_{1cn}$)[21, 69], which corresponds to a parallel chain orientation[66] which permits spontaneous polarisation to rise. The lattice parameters for the δ-phase are presented in Table 4.2. All angles in this space group are equal to 90°. The lattice parameters of the δ-phase are similar to those of the α-phase. The trends shown by the various functionals lattice prediction seen for the α-phase were similar to the trends observed for the δ-phase.

Table 4.3 Lattice constants and volume V, for the β-phase for different functionals compared to DFT and experimental results available in the literature. *: Estimated lattice accuracy from present convergence tests, see Tables A.1, A.2, A.3.

Method	XC	a (Å)	b (Å)	c (Å)	V(Å^3)	Reference	Accuracy (Å)
Exp.	-	8.58	4.91	2.56	107.8	[65]	0.01
DFT	LDA	7.97	4.46	2.54	90.2	Present	1.0e-05
DFT	PBE	8.95	5.00	2.59	115.7	Present	1.0e-05
DFT	vdW-DF	8.62	4.80	2.60	107.5	Present	1.0e-05
DFT	vdW-DF2	8.40	4.66	2.60	101.8	Present	1.0e-05
DFT	PBE-D2	8.27	4.55	2.58	97.0	Present	1.0e-05
DFT	PBE	8.55	4.83	2.58	106.5	[32]	0.09*
DFT	PBE	8.69	4.85	2.58	108.7	[66]	0.09*
DFT	PBE-D2	8.22	4.51	2.58	95.6	[66]	0.09*
DFT	PBE0 hybrid	8.69	4.89	2.57	109.2	[101]	0.09*

β PVDF

The β-PVDF structure is the crystal form with the highest spontaneous polarisation and therefore the most studied structure. The chain has an all-trans structure and the dipoles are in parallel alignment, as shown in Fig. 2. The lattice constants for the β-phase are shown in Table 4.3. First, we note that in the interchain directions, LDA overbinds by 7% and 9% for a and b, respectively, and PBE underbinds by 4% and 2% for a and b respectively. Our PBE calculation results in a considerably larger value for a = 8.95 Å than the PBE values reported previously, which gave a = 8.69 Å[66] and a = 8.55 Å[32]. We attribute this to methodological differences, such as lower plane wave energy cutoffs of ≈38 Ry (500 eV)[66] and 30 Ry[32]. We tested this by decreasing the plane wave cutoff from 80 Ry to 40 Ry and this resulted in a decrease in the a lattice parameter from 8.95 Å to 8.57 Å and a decrease in the volume from 115.7 Å^3 to 106.6 Å^3 which then agreed with previous authors, showing anyway that previous calculations were not performed to converged cutoff parameters. The vdW calculations lie between the two extremes of the LDA and GGA. Our results for the PBE-D2 calculations are in close agreement with the previous D2 calculations of Pei *et al*[66]. About the vdW functionals, vdW-DF gave the best overall agreement with experimental values, with a volume of 107.5 Å^3, compared to the experimental volume of 107.8 Å^3[65].

ζ PVDF

The characterisation of the non polar ζ PVDF crystal structure experimentally suggested by Costa *et al*[78] and Sencadas *et al*[79] (referenced as non-poled β-phase), was here presented.

Comparing the lattices of the β-phase with the ζ-phase, is possible to see a distinctive homogeneity of lattices and especially volume prediction when comparing ζ and β predicted by the same functional.

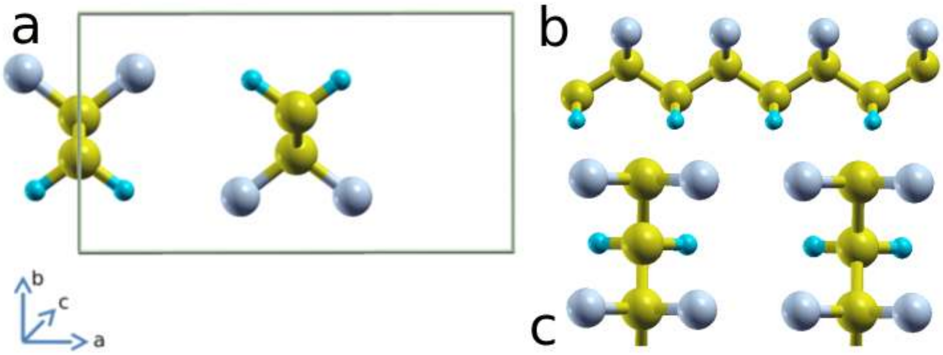

Fig. 4.1 A generic view of ζ-PVDF. a: front view including the crystal unit box; b: side view of one chain backbone trans bonds T; c: top view of the chains of the crystal unit box. F: light grey; C: yellow; H: light blue.

However, this only evidence a potential consistency with the overall lattice and volume prediction between ζ and β phases (recurrent for α and δ comparison in Tables 4.1 and 4.2 respectively). Thought, an experimental space group characterisation for the ζ phase is still missing, the theoretical characterisation has been performed and showed in Table 4.4. The ζ PVDF resulted to be an othorombic and coplanar crystal as shown in Figure 4.1, the symmetry operator that describe its crystal structure is the 51st space group P_{mma}. Without any experimental comparison it was not possible to evaluate the prediction reliability of each functional for the ζ-phase, presumably, being volumes of β and ζ phases quite consistent across same functionals as shown in Tables 4.3 and 4.4 for the β and ζ phases, respectively, the functionals were assumed to behave as described for the β crystal.

Kim *et al*[144, 109] observed in molecular dynamic calculations the ζ-phase formation during the backbone transition from TG^+TG^- to T. However, their observation was referred to the possibility of having this intermediate phase while passing from α or δ phases to the β-phase and concluding that the ζ structure could readily undergoes to form the β-phase[144, 109].

γ PVDF

The γ-PVDF crystal has a more complex backbone motif with its repeats of $T_3G^+T_3G^-$ with parallel chains aligned in a monoclinic lattice structure[63], presents ferroelectric behaviour[60, 56] and it has been the most debated crystal polymorph[1, 65, 63]. Indeed, across

Table 4.4 Lattice constants and volume V, for the ζ-phase for different DFT functionals.

Method	XC	a (Å)	b (Å)	c (Å)	V(Å^3)	Reference	Accuracy (Å)
DFT	LDA	7.96	4.45	2.54	89.9	Present	1.0e-05
DFT	PBE	8.99	5.00	2.59	116.2	Present	1.0e-05
DFT	vdW-DF	8.65	4.77	2.60	107.1	Present	1.0e-05
DFT	vdW-DF2	8.42	4.64	2.60	101.5	Present	1.0e-05
DFT	PBE-D2	8.26	4.56	2.58	97.0	Present	1.0e-05

Table 4.5 Lattice constants and volume V, for the γ_{uu}-phase for different functionals compared to DFT and experimental results available in the literature. *: Estimated lattice accuracy from present convergence tests, see Tables A.1, A.2, A.3.

Method	XC	a (Å)	b (Å)	c (Å)	V(Å^3) (°)	β (°)	Reference	Accuracy (Å)
Exp.	-	9.67	9.20	4.96	440.7	93.0	[63, 67]	0.01
DFT	LDA	9.09	9.08	4.59	378.3	93.1	Present	1.0e-05
DFT	PBE	10.18	9.28	5.18	488.8	92.7	Present	1.0e-05
DFT	vdW-DF	9.71	9.32	4.95	446.6	94.4	Present	1.0e-05
DFT	vdW-DF2	9.41	9.31	5.85	510.9	94.5	Present	1.0e-05
DFT	PBE-D2	9.38	9.23	4.78	413.2	93.3	Present	1.0e-05
DFT	PBE	9.69	9.34	5.00	452.4	91.5	[66]	0.09*
DFT	PBE-D2	9.26	9.25	4.76	407.1	93.1	[66]	0.09*

years of study several authors revisited the γ-phase with more rigorous structural analysis to clarifiy the initial ambiguity where some authors observed the γ-phase being orthorombic while others authors reported the γ-phase being monoclinic. At the end, it was evidenced that both crystal structure have the same probability to exist[1, 65, 63, 67]. These two structural variants were labelled as γ_{uu} and γ_{ud} (as discussed in literature chapter) and represented in Figures 2.6 and 2.7 respectively. The crystal structures characterisation of the γ_{uu} and γ_{ud} phases were reported in Tables 4.5 and 4.6, respectively.

Results from LDA and PBE+D2 functionals showed to underestimate lattice and volumes of the γ_{uu}-phase (expected from LDA) and of opposite trend PBE overestimated lattice and volume (expected). Current results for PBE gave slightly larger a and c lattice constants compared to previous results, which was attributed to methodological differences. Pei *et al* [66] used low wavefunction cutoff ($\approx$ 38-40Ry), while in this study a much higher cutoffs was applied as described in method section (*e.g.* 80 Ry). The vdW-DF and vdW-DF2 functionals were expected to behave in a more balanced way nearer to experiments by including first principle vdW forces, however, the vdW-DF very well agreed with experiments[63] and vdW-DF2 did not in the characterisation of γ_{uu}-phase.

Table 4.6 Lattice constants and volume V, for the γ_{ud}-phase for different functionals compared to DFT and experimental results available in the literature. *: Estimated lattice accuracy from present convergence tests, see Tables A.1, A.2, A.3.

Method	XC	a (Å)	b (Å)	c (Å)	V(Å^3)	β (^{o})	Reference	Accuracy (Å)
Exp.	-	9.66	9.18	4.97	440.7	90.0	[68]	0.01
DFT	LDA	9.21	8.79	4.81	389.4	90.0	Present	1.0e-0.5
DFT	PBE	10.78	9.38	5.29	534.7	91.7	Present	1.0e-0.5
DFT	vdW-DF	9.45	9.38	5.15	456.5	90.0	Present	1.0e-0.5
DFT	vdW-DF2	9.45	9.12	5.04	434.4	89.8	Present	1.0e-0.5
DFT	PBE-D2	9.32	9.09	4.96	420.2	89.9	Present	1.0e-0.5
DFT	PBE	9.75	9.39	5.17	473.3	90.0	[66]	0.09*

The structural prediction of the γ_{ud}-phase showed a rather similar functionals prediction scheme as described for the γ_{uu}-phase. Indeed, also for the crystal structure of the γ_{ud}-phase LDA and PBE+D2 underestimated lattice and volume of such crystal, PBE overestimated the lattice and volume while vdW-DF and vdW-DF2 functional predicted more faithfully to experiments the crystal lattice and volume of the γ_{ud}-phase.

Lovinger *et al*[63] experimentally determined the γ_{uu}-PVDF being a monoclinic structure with C_c[73, 67] space group matching the present γ_{uu}-phase characterisation and both the computational work of Pei *et al*[66] and Karasawa *et al*[26]. Apart the space group agreement, the lattice structure prediction of Pei *et al*[66] and Karasawa *et al*[26] showed moderate diversion from the present results since for Pei's work the PBE prediction has been performed using low cutoff threshold using DFT as previously stated and in the case of Karasawa's work the prediction has been done dy using classical molecular dynamics, motif for which Karasawa's results are reported in next chapter and here considered only for a more generic discussion of the γ-PVDF structures.

The space groups of the γ_{ud}-PVDF here characterised and reported as in Table 4.6 was firstly calculated from its raw coordinates and native lattice vectors resulting to be a monoclinic crystal with space group C_c, however, such crystal structure only deviates slightly from being orthorhombic by a crystal unit factor of 0.001. Hence, recalculating the space group accounting for such small tolerance factor showed that the γ_{ud}-PVDF resulted to be orthorhombic having the space group $Pna2_1$, which well agreed with the computational work performed by Karasawa *et al*[26] and Pei *et al*[66] as well as with the experimental observation of Lovinger *et al*[63] as reported in Table 2.1. It was deduced that such small crystal symmetry deviation between the present computations with the previous found in literature was caused because Quantum ESPRESSO did not constrain atomic model coordinates to space groups symmetries.

Table 4.7 Lattice constants and volume V, for the ε_{uu}-phase for different functionals compared to DFT results available in the literature. *: Estimated lattice accuracy from present convergence tests, see Tables A.1, A.2, A.3.

Method	XC	a (Å)	b (Å)	c (Å)	V(Å^3)	β (^{o})	Reference	Accuracy (Å)
DFT	LDA	9.16	9.08	4.61	383.4	89.8	Present	1.0e-05
DFT	PBE	10.09	9.30	5.18	486.1	89.9	Present	1.0e-05
DFT	vdW-DF	9.79	9.32	4.95	451.7	90.0	Present	1.0e-05
DFT	vdW-DF2	9.55	9.32	4.83	429.9	90.0	Present	1.0e-05
DFT	PBE-D2	9.52	9.23	4.75	417.4	89.9	Present	1.0e-05
DFT	PBE	9.78	9.33	5.08	463.5	90.0	[66]	0.09*

In the lattice and volume prediction of the γ_{ud}-phase there was discrepancy between the present computational prediction of the lattice structure compare to the work of Karasawa *et al*[26] and Pei *et al*[66] because of the less accurate methodology they applied in their studies (*e.g.* low convergence cutoff[66], classical mechanics[26]). For the space group symmetry, considering the same crystal geometry discrepancy of 0.001 (crystal units) for the γ_{uu}-phase, the γ_{ud}-phase space group agreed to be $C2_{cm}$, equivalent to previous computations and experimental observations[66, 68] as reported in Table 2.1.

ε PVDF

The ε-PVDF also has the $T_3G^+T_3G^-$ backbone motif but antiparallel oriented chains, therefore, is non-ferroelectric and again both up-up and up-down structures were expected[63, 64]. However, ε-PVDF's existence has only been acknowledge by fiber and X-Ray diffraction experiments[64] as well as with IR[145] spectra but a crystal structure and its space group symmetry has never been proposed for ε_{uu} or ε_{ud} variants. This made any further results presentation, comparison and discussion more difficult to be justified and defended, therefore, only a critical presentation of results has been concerned.

The Figures 2.8 and 2.9 shows the structures of ε_{uu} and ε_{ud} phases, respectively and Tables 4.7 and 4.8 reported the structural prediction of the ε_{uu} and ε_{ud} phases, respectively. The different DFT functionals used showed the same trends described in previous crystal structures characterisation of PVDF where LDA underestimated lattice and volume, PBE overestimated lattive and volume and the vdW corrected functionals, presumably behaved more consistently.

The ε_{uu}-phase presented a modest deviation of the β angle from 90^o, a deviance within the negligible DFT margin of error. The ε_{ud}-phase presented a consistent deviation of the β angle from 90^o, while depending on the functional used, the α and γ angles slightly deviates from 90°, again these differences were indeed negligible by the margin of accuracy of DFT. The raw structure of both ε_{uu} and ε_{ud} phases did not present any symmetry group operator (*e.g.* space group $P1$), however, within a small tolerance factor of 0.001 (crystal units), the ε_{uu}-phase showed to have the P_{ca2_1} space group and the ε_{ud}-phase showed to have the $P2_{1/c}$ space group, both in agreement with previous computations[26, 66]. The comparison with other computational work such as Pei *et al*[66] represented the only DFT reference about the ε-phase lattice characterisation for both variants. However, Pei *et al*[66] did use lower cutoff which made their lattice and volume prediction to disagree with the present characterisation.

Table 4.8 Lattice constants and volume V, for the ε_{ud}-phase for different functionals compared to DFT and experimental results available in the literature. *: Estimated lattice accuracy from present convergence tests, see Tables A.1, A.2, A.3.

Method	XC	a (Å)	b (Å)	c (Å)	V(Å^3)	α (^{o})	β (^{o})	γ (^{o})	Reference	Accuracy (Å)
DFT	LDA	8.87	9.17	4.84	393.8	90.0	93.0	90.1	Present	1.0e-05
DFT	PBE	10.71	9.34	5.38	538.5	90.1	95.2	90.0	Present	1.0e-05
DFT	vdW-DF	9.46	9.41	5.18	460.4	90.0	93.0	90.0	Present	1.0e-05
DFT	vdW-DF2	9.18	9.41	5.07	438.0	90.0	93.3	90.0	Present	1.0e-05
DFT	PBE-D2	9.21	9.30	4.95	424.2	90.2	91.2	90.1	Present	1.0e-05
DFT	PBE	9.68	9.38	6.17	560.2	90.0	121.9	89.9	[66]	0.09*

On top of that, the work of Pei and Karasawa underlined the ε_{ud}-phase having a β^{o} of $\approx 120^{o}$ which did not appeared to be such in the present study as visible in Tables 4.7 and 4.8. Indeed, replicating the exact ε_{ud} crystal structure from Pei *et al*[66] (earlier reported from Karasawa *et al*[26]), lead to a structure ≈500 kJ mol^{-1} less stable than the present α-PVDF crystal structure. With such premises, the comparison of the present research work did not found a satisfactory agreement with the previous work of Pei[66] and Karasawa[26] in terms of lattice structure and volume because of methodological differences. Finally, strong of diligence and accurate convergence tests performed for the present work, it was assumed that the present research work does represent a good reference for further studies on ε_{uu} and ε_{ud} PVDF crystal phases.

4.2 Cohesive energies

The cohesive energies of the three PVDF backbone variants (*e.g.* T, TG^{+}TG^{-} and T$_3$G^{+}T$_3$G^{-}) and per every crystal structure has been calculated using various DFT functionals and presented as energy per monomer as equation 4.1. The inclusion of vdW interactions were expected to have a significant effect on the cohesive energy of the polymorphs, shown in Tables 4.9 and 4.10. As the limit of accuracy of DFT is 1 mRy per atom, the limit of accuracy of the crystal energetics is of 1.3 kJ mol^{-1}.

$$E_{coh} = \frac{E_{cry} - N_{chain}E_{chain}}{N_{mon}N_{chain}} \tag{4.1}$$

In equation 4.1 E_{cry} is the total energy of the crystal, E_{chain} is the total energy of one relaxed chain in vacuum, N_{chain} is the number of chains in the unit cell and N_{mon} is the number of monomers per chain of the crystal model. The isolated chains were relaxed in a box with a = b = 19 Å (enough vacuum to vanish long range forces interactions) and with the c lattice parameter fixed to respect the backbone periodicity where the all trans backbone typical of the β-phase has been taken as relative zero. The cohesive energy of the T$_3$G^{+}T$_3$G^{-} backbone resulted to be ≈14 kJ mol^{-1} weaker than the full trans T backbone and the cohesive energy of the TG^{+}TG^{-} backbone ≈19 kJ mol^{-1} weaker than the full trans backbone, indicating that the PVDF crystal with the full trans backbone possesses the highest cohesive energies. The energies of isolated chains reported in Table 4.9, were similar for all functionals, which was expected since this is due to bonded interactions rather than van der Waals interactions. Su *et al*[104] also found the TG^{+}TG^{-} chain structure to be 19.9 kJ mol^{-1} weaker than the full trans backbone reaching good agreement with the present

Table 4.9 Cohesive energies of PVDF backbones, $\Delta_{TG^{+/-}}$ and $\Delta_{TTTG^{+/-}}$ isolated chains energies referred to the full trans chain energy Δ_T used as reference and compared to DFT results available in literature; Δ: kJ mol^{-1}. Acc.: The accuracy is normalised per chain's monomer, averaged for all chains types of the same functional and expressed in kJ mol^{-1}. XC: Exchange correlation functional.

XC	$\Delta_{TG^{+/-}}$	$\Delta_{TTTG^{+/-}}$	Reference	Acc.
LDA	-18.3	-13.4	Present	0.11
PBE	-16.0	-12.6	Present	0.16
vdW-DF	-17.6	-12.5	Present	0.09
vdW-DF2	-18.5	-12.4	Present	0.12
PBE-D2	-18.2	-14.1	Present	0.13
PBE	-19.9		[104]	-

study. Table 4.10 reported the cohesive energy of every PVDF crystal structure showing how all functionals saw the all trans T structures having the strongest cohesion energy, also in agreement with previous PBE's results of Su *et al*[104] for β, γ_{uu} and ε_{uu} structures and not agreeing for α and δ phases that resulted in Su's work having almost a fourth of the cohesive energies found here.

The PBE functional predicted the smallest cohesive energies, which is not surprising as PBE is known to underbind electron interactions. The vdW methods resulted to predict stronger cohesive energies than LDA. The three vdW corrected functionals gave very similar results, with vdW-DF giving the strongest cohesion between the three and PBE-D2 giving the weakest cohesion as similar as the LDA profile. There is no experimental data on the cohesive energy for PVDF, however, present results were qualitatively compared with a similar study on polyethylene[114]. GGAs gave cohesive energies of less than 1 kJ mol^{-1} per CH_2 , LDA gave ≈11 kJ mol^{-1} per CH_2 and vdW-DF gave a result of ≈10 kJ mol^{-1} per CH_2, which is slightly smaller than the LDA and in best agreement with the experimental value of 7.8 kJ mol^{-1} per CH_2[146].

4.3 Phase energies

The phase energies of different PVDF polymorphs has been calculated using various DFT functionals and presented as energy per monomer as equation 4.2 where E_{mon} is the energy per monomer, E_{cry} is the energy of the crystal and N_{mon} is the number of monomers present in unit cell.

Table 4.10 Cohesive energies of all PVDF polymorphs compared to DFT results available in literature. Energy ranges are expressed in kJ mol^{-1}. Acc.: The accuracy is normalised per chain's monomer, averaged per all crystals of the same functional and expressed in kJ mol^{-1}. XC: Exchange correlation functional. Ref.: Reference.

XC	α	δ	γ_{uu}	ε_{uu}	β	ζ	γ_{ud}	ε_{ud}	Ref.	Acc.
LDA	-25.5	-26.0	-32.8	-28.7	-41.7	-41.8	-23.1	-23.2	Present	0.18
PBE	-8.1	-8.1	-10.6	-10.4	-17.5	-17.3	-7.0	-6.9	Present	0.25
vdW-DF	-33.7	-34.0	-38.6	-37.9	-47.5	-47.4	-32.9	-32.8	Present	0.16
vdW-DF2	-30.9	-31.3	-36.8	-35.8	-46.8	-46.7	-29.8	-29.8	Present	0.19
PBE-D2	-27.0	-27.2	-30.3	-29.8	-41.6	-41.7	-25.5	-25.6	Present	0.21
PBE	-2.6	-2.8	-10.0	-8.6	-17.6	-	-	-	[104]	0.48
PBE-D2	-0.7	0.6	-1.7	-0.8	-2.0	-	-	-	[66]	-

$$E_{mon} = \frac{E_{cry}}{N_{mon}} \tag{4.2}$$

The energy differences relative to the α-phase were presented in Fig. 4.2 and it is notable that all functionals predict the δ-phase to be the lowest energy polymorph although for a negletible energy difference below the energy accuracy of DFT. However, LDA predicted that the γ_{uu}-phase to be more stable than the α-phase, with an energy difference of $\approx$2.2 kJ mol^{-1}, hence LDA deviated from the phase energetics prediction of the other functionals for the α, δ and γ_{uu} crystals. Apart from LDA all other functionals see the γ_{uu}-phase $\approx$1 kJ mol^{-1} less stable than α and ε_{uu}-phase $\approx$2 kJ mol^{-1} less stable than α. To follow the β-phase and ζ-phase showed to be higher in energy within $\approx$4 kJ mol^{-1} across all functional except for PBE that see these two structures $\approx$7 kJ mol^{-1} less stable than the α-phase. Finally, the γ_{ud} and ε_{ud} phases vary depending on the functional by $\approx$7 kJ mol^{-1} from the α-phase. The overview of Figure 4.2 depicts a clear phase energy similarity to an extent of less than 8 kJ mol^{-1} from the most stable structure to the least. This scenario explain at least partially why is difficult to form a single PVDF polymorph.

The present results agree with previous PBE results[104], which found the δ-phase to be marginally stable, and a very small energy range of less than 5 kJ mol^{-1} which included all the studied polymorphs[104]. Another DFT study calculated the energy difference between the α and β-phases and found the α-phase to be 4.4 kJ mol^{-1} per monomer lower than the β-phase[147]. Another PBE study found that the α-phase is 2.6 kJ mol^{-1} per monomer lower in energy than the β-phase[82]. A study using the PBE0 functional found that the α, β, δ-phases differ in energy by less than 3 kJ mol^{-1}, with the α-phase being only marginally lower in

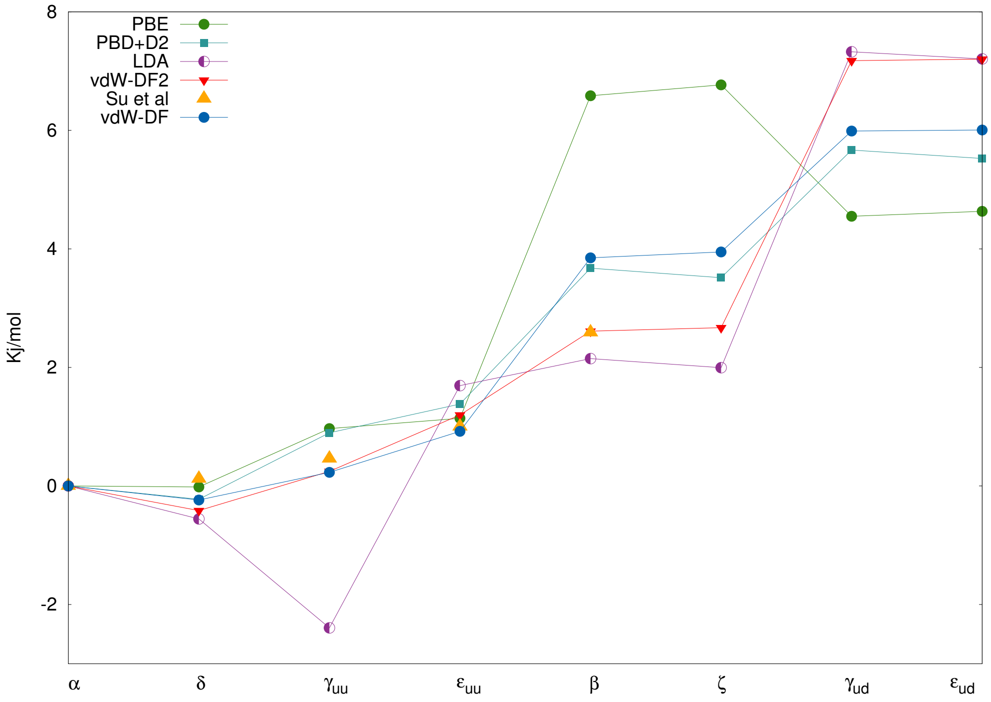

Fig. 4.2 Phase energies of all PVDF polymorphs compared to literature DFT results.

energy than δ[101]. A study into the possible routes from α to β-phase transformations found the α and δ-phases to be almost equi-energetic, and the β-phase to have a higher energy of 3.4 kJ mol^{-1}[144, 109].

Without a comparison with experimental observation it was hard to say which functional would be the most consistent with experiments. On the experimental side, the α-phase is assumed to be the ground state crystal structure since it is most frequently formed and found in PVDF samples, however, without the thermodynamics study of its stability, this assumption could not be considered true or false.

4.4 Spontaneous polarisation

The spontaneous polarisation of all three ferroelectric PVDF crystals such as β, δ and γ has been calculated using various DFT functionals and here presented together with all the literature results available. The methodological approach exerted from Spaldin *et al*[140] in how to perform and adiabatic spontaneous polarisation calculation using the modern approach of the Berry's geometrical polarisation theory (explained in methods section), was the current approach used to predict the spontaneous polarisation of PVDF using DFT.

Figure 4.3 reported the spontaneous polarisation obtained from different DFT functionals relating to the unit cell volume normalised by the number of monomers present in every crystal model of the FE β, δ, γ_{uu} and γ_{ud} phases with the spontaneous polarisation of every crystal structure. The relation between the dipole and lattice volume is not expected to be perfectly linear since its true that the volume exert a major effect on the spontaneous polarisation as stated in the equation 3.7, but is also true that each functional predicts differently the electron density of the system, hence, estimating differently the system dipole moment from which derives in connection with the lattice volume its total spontaneous polarisation.

The LDA functional scored the highest spontaneous polarisation, PBE the lowest and the vdW corrections predicted a spontaneous polarisation between the LDA and PBE extremes resembling the usual XC-fs trend observed during phase lattice prediction in which the overbinding functional LDA overestimated the spontaneous polarisation and the underbinding functional PBE underestimates the spontaneous polarisation, while vdW corrected functionals predicted a spontaneous polarisation within the LDA and PBE trends. The β-phase resulted ot be the crystal structure that rise the highest spontaneous polarisation, true across all functionals, while the δ and both γ variants appeared to be almost equivalent in term of the achievable spontaneous polarisation (the γ_{ud} modestly more polarisable than the γ_{uu}), motif for which the β-phase remained the most appealing crystal phase for electronics applications. The spontaneous polarisation reported by other computations in literature did not deviated sensibly from the present PBE prediction. However, these literature estimations reported in Table 4.11 were made by using low energy cutoff which is strongly discouraged when attempting to calculate the spontaneous polarisation of a material since the energy cutoff affects directly the quality prediction of the bands structure of the material, affecting the prediction of the spontaneous polarisation.

Table 4.11 reported the spontaneous polarisation of all FE forms of PVDF predicted with DFT in the present study compared with all the experimental and computational reference from literature. Regarding the β-phase several experimental measurements and DFT prediction of its spontaneous polarisation were performed and it was possible to evince the diversity occurring between experiments and computations approaches (also present between the δ-phase spontaneous polarisation divergence between the experimental reference to the present calculation). These differences can be explained by some factors that apply to the real world of experiments which are absent in computations as reported in Table 4.11.

The fact that computational modelling builds perfect defect free systems not accounting for thermal energy contribution and being that in experiments finite samples are studied at non-zero temperatures with the presence of defects at the microscopic scale (*e.g.* monomers

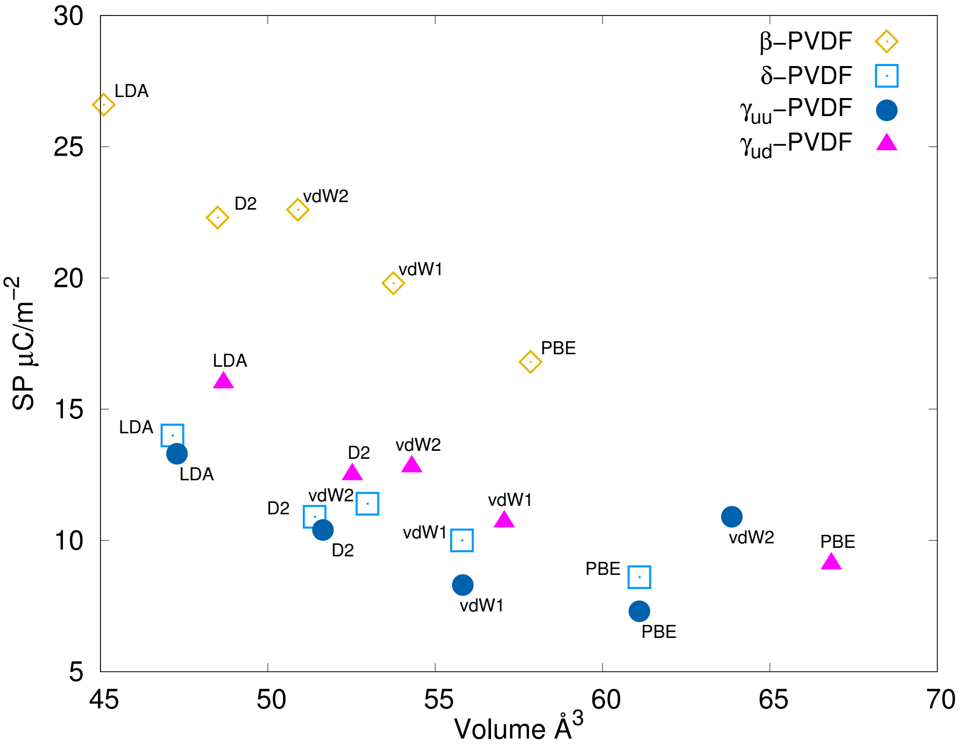

Fig. 4.3 Spontaneous Polarisation of all FE PVDF crystals predicted with the current DFT study. Volume has been normalised by the number of monomers present within each modelled crystal structure.

inversion defects, unwanted chemical reactions, denaturation, pollutants neutralising the dipole charge) as well as at the macroscopic scale (*e.g.* amorphous regions, simultaneous polymorphisms, holes, breakages, surface roughness)[148] does make the computational prediction to deviate from an experimental observation. All experimental defects mainly depend on prior material synthesis, conditioning, preparation and the environment in which the study of the sample is conducted (*e.g.* vacuum, ambient atmosphere, apparatuses used)[148].

The circuital architecture and the switching potential applied to a FE sample also influences its hysteresis response magnitude, therefore, many factors comes in play during an experimental determination of the effective spontaneous polarisation of a FE material[148], hence, deviations between computational and experimental spontaneous polarisation measurements are expected as much as a real sample deviates from the perfect conditions set of the computed model. It is possible to deduce that divergence from computed to experimental spontaneous polarisation does not necessary have a bad meaning and that computations offers the best estimation possible of a material's spontaneous polarisation, while experiments report the achievable spontaneous polarisation in a sample within such specified experimental

Table 4.11 Spontaneous polarisation of the β, δ, γ_{uu} and γ_{ud} phases compared with different DFT functionals and experiment from literature (where applicable). *: Evaporation of $[VDF]_{12/16}$ oligomers in vacuum for deposition on electrode substrate[29]. Acc.: The accuracy is normalised by the crystal unit, averaged for all crystals of the same functionals and expressed in μC cm^{-2}.

P (μC cm^{-2})				Method	Reference	Acc.
β	δ	γ_{uu}	γ_{ud}			
26.6	14.0	13.3	16.0	DFT LDA	Present	0.27
16.8	8.6	7.3	9.1	DFT PBE	Present	0.42
19.8	10.0	8.3	10.7	DFT vdW-DF	Present	0.15
22.6	11.4	10.9	12.8	DFT vdW-DF2	Present	0.31
22.3	10.9	10.4	12.5	DFT PBE-D2	Present	0.14
	7.0			Poling	[69]	-
7.6				Plasma poling	[72]	-
10.0				Extrusion	[149]	-
13.0				Evaporated*	[29]	-
19.0				APA confinement	[57]	-
18.1				DFT PBE	[102]	-
17.8				DFT PBE	[103]	-
17.6				DFT PBE0 hybrid	[101]	-

conditions, which may be improved to a higher state of art to further refine the sample preparation.

For example, there are many experimental studies focused on improving the crystallinity and purity of the β-phase. For example, Noda *et al*[29] formed thin films of β-like VDF evaporated oligomers and measured a spontaneous polarisation of 13 μC cm^{-2} which is almost double the previous determination of 7.6 μC cm^{-2} attributed to be the highest possible for the β-phase several decades ago by Mc Kinney *et al*[72]. Finally, another remarkable and recent experimental study made by Cauda *et al*[7, 57] reported that nanoconfined PVDF samples in APA membranes does form high percentage contents of β-PVDF with a spontaneous polarisation which reached 19 μC cm^{-2} which is almost at the theoretical limit of the spontaneous polarisation of the β-PVDF reported in Table 4.11 by using the DFT vdW-DF functional. The study of Cauda *et al*[7, 57] did showed how experiments and theory can converge when the experimental sample crystallinity is brought to a very high crystalline quality which almost resemble the computed model perfection, making the present investigation sensibly consistent and the DFT vdW-DF functional the most appropriate DFT functional for predicting the spontaneous polarisation of PVDF determining the most appropriate ratio of volume and dipole moment.

4.5 Electronic structures

The band structure and DOS provides information about the energy levels (eV) and electronic structure of a material. The electronic states which matter most are the valence bands (highest occupied levels). In the case of PVDF which is a well known insulator, the band structure and DOS calculation have been performed to verify that the optimised geometries obtained so far were consistent with real physical properties of PVDF which resulted to be described with DFT as an insulator (as observed experimentally)[1, 70]. The present results were compared with Duan *et al*[18] which computed (with DFT using the PBE functional) the bands structures and DOS states of the β-phase. To make direct comparison with Duan, the present bands and DOS computations were performed using PBE and the vdW-DF functional referred into appendix A.3.2 (all Figures of that section) as no significant differences were found in bands and DOS using different functionals, indeed, such functionals results were considered rather similar. Duan *et al*[18] built the β-phase model into a face centred orthorombic lattice where the Brillouin zone and k-path are shown in Figure 4.4. The present β model was built in a classic orthorombic lattice as such was the experimentally determined geometry for the β-phase[65] and represented in Figure 4.5 with its Brillouin zone. For such differences in how the crystal model was built the bands structure shapes were expected to be significantly different as visible between the Duan's computation[13] in Figure 4.4 and the present computed bands and DOS reported in Figure 4.6.

Figure 4.6 showed the bands and DOS of the β-phase of the present study, where the red line represents the Highest Occupied Molecular Orbital (HOMO) and the green line represents the Lowest Unoccupied Molecular Orbital (LUMO). The k-path was chosen on the literature paper of Setyawan *et al*[13] which provided a solid methodology for high throughput electronic structures study of materials with DFT. Black dotted error bars were added along the $\Gamma(.0,\ .0,\ .0) \rightarrow Z(.0,\ .0,\ .5)$ k-path to easily refer at the experimental bands characterisation of the β-phase made by Berge *et al*[19] (the dotted bars were rigidly shifted in the energy range to fit the bands shape of the present characterisation as DFT underestimates the band gap). Despite different bands shapes, the DOS computed by Duan *et al*[18] and present DOS were found to be in good agreement as in the present computation the band gap resulted to be 6 eV as also predicted by Duan *et al*[18]. The experimental PVDF band gap was observed to be 6.5 eV[150], remarkably, an experimental sample would be most probably represented by a mixture of PVDF polymorphs and amorphous regions which could alter the band gap value retrieved experimentally, unless the analysed sample would be highly crystalline in favour of the β-phase which is known to be extremely difficult to obtain.

The present bands and DOS characterisation of the β-phase made with PBE has been reported here in Figure 4.6 and to appendix in section A.3.1 the partial DOS characterisation

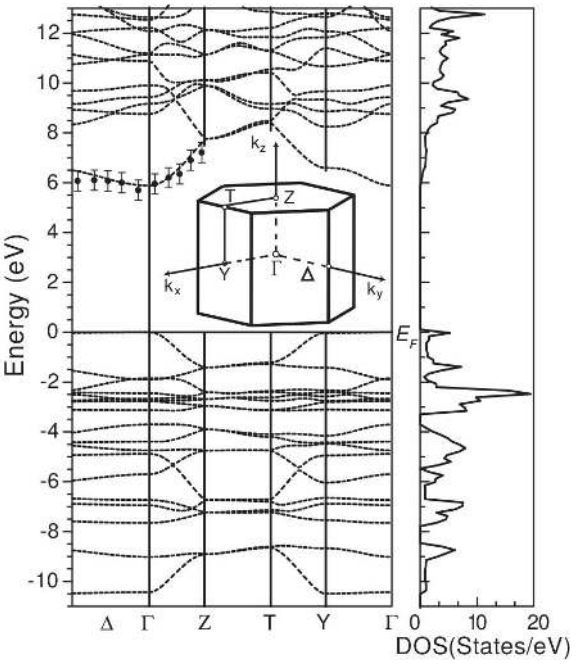

Fig. 4.4 Bands structure and DOS states of β-PVDF comparing DFT and experimental results taken from Duan *et al*[18]. Duan's k-path: $\Delta(.5,\ .3,\ -.2) \rightarrow \Gamma(.0,\ .0,\ .0) \rightarrow Z(.5,\ .5,\ .0)$. Black dotted bars express the comparison of theoretical with experimental bands structure determination[19, 18] mapped into a Face-Centred Orthorombic lattice.

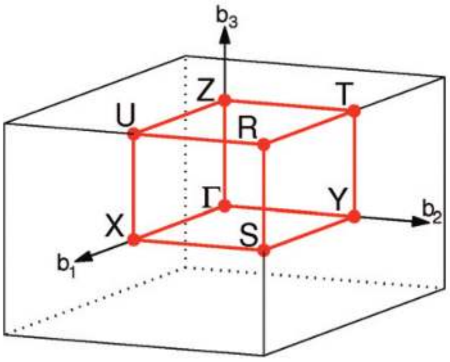

Fig. 4.5 Orthorombic lattice structure and Brillouin zone of the β-phase. Taken from Setyawan *et al*[13].

that allowed to determine the identities of the electronic states of the crystal models (projected DOS were calculated also for the ζ and α phases). From the present characterisation it emerged that the flat bands of the β-phase within the energy range of -25 eV up to -23 eV were s and p electrons of carbon and fluorine atoms exclusively as shown in Figure A.4. The electronic states between -15 eV up to -10 eV were mainly s electrons of carbon atoms (carbon to carbon bonds) with minor contributions of hydrogen and fluorine atoms (both s

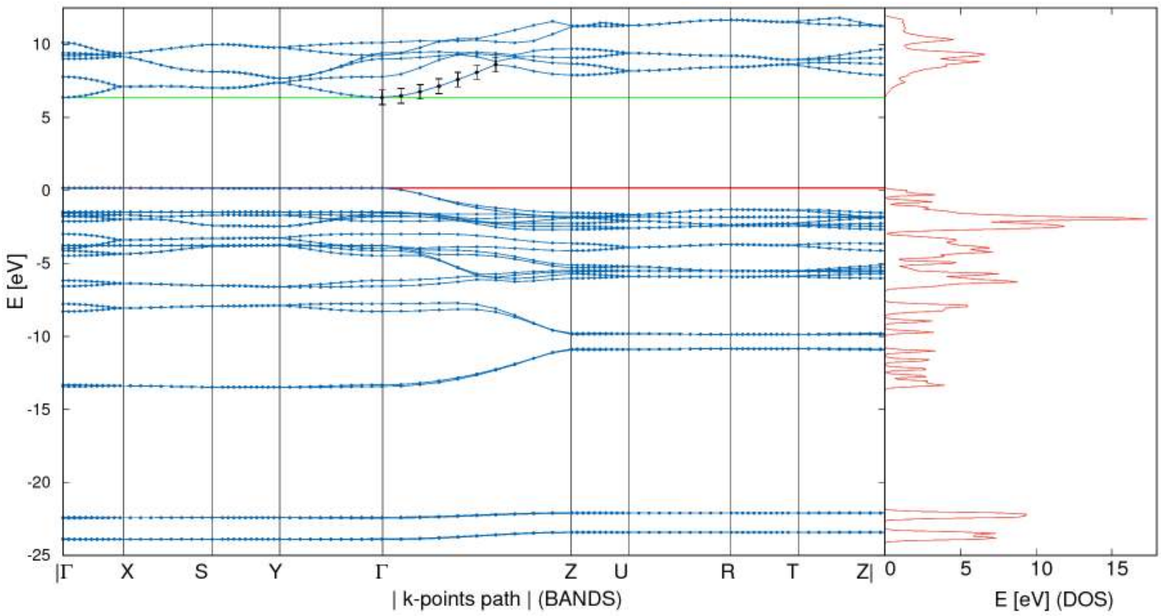

Fig. 4.6 Bands structure and DOS states of β-PVDF predicted with the current DFT study using PBE. Red line: HOMO; Green line: LUMO.

and p electrons) and between -10 eV up to 0 eV s and p electrons of carbon, fluorine and hydrogen atoms were more hybridised and the major DOS contribution within -5 eV and 0 eV was given by p electrons of fluorine atoms as shown in Figure A.5. The full bands structure and DOS of the β-phase were represented in Figure 4.6 and the present observations of the electronic states are in line with Duan *et al*[18].

The ζ-phase is a newly proposed crystal structure with limited experimental data available. However, with bands and DOS calculation it is interesting to compare the ζ-phase with the β-phase. The bands and DOS of the ζ-phase showed in Figure 4.7 are similar to the bands and DOS of the β-phase showed in Figure 4.6 and also the partial DOS projection showed in Figure A.6 and A.7 representing the s and p electron states of the ζ-phase, respectively, well agreed with the partial DOS projections of the β-phase. The ζ-phase band gap resulted to be 6 eV as for the β-phase. The differences in bands shape between the ζ-phase and the β-phase (Figures 4.7 and 4.6 respectively), were attributed to the different crystal geometries as the atoms of these two crystal structures are displaced differently in the Brillouine zone.

The bands, DOS and mostly the partial DOS projections performed on the α-phase structure resulted to be almost identical to the electronic states found for the β and ζ phases which was expected as electronic states are related to the chemistry of electron bonds and atoms properties which are the same in all PVDF polymorphs. The partial DOS projection was reported in Figures A.8 and A.9 for s and p electrons, respectively, and resulted to be rather identical to the electronic states of the β-phase (Figures A.4 and A.5). The bands

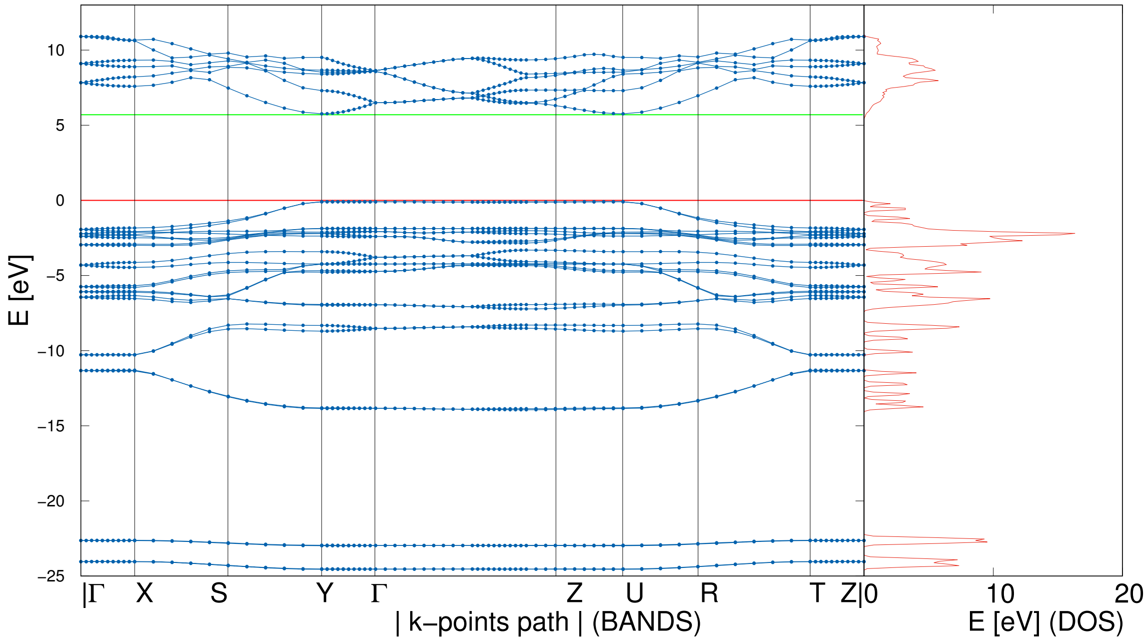

Fig. 4.7 Bands structure and DOS states of ζ-PVDF predicted with the current DFT study using PBE. Red line: HOMO; Green line: LUMO.

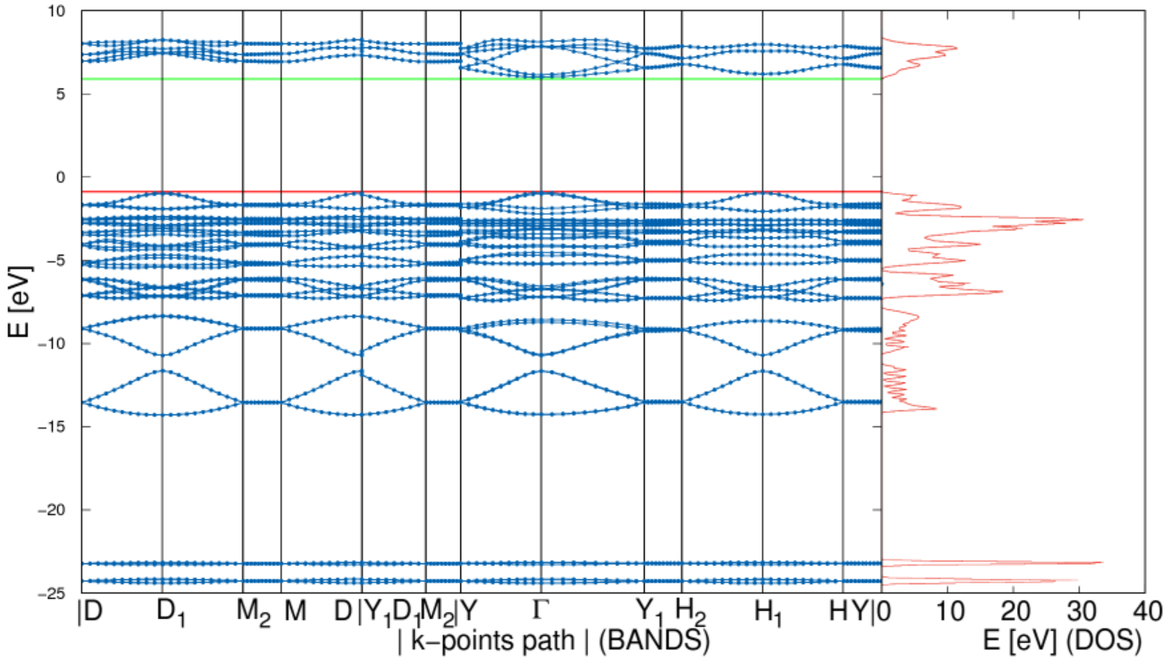

Fig. 4.8 Bands structure and DOS states of α-PVDF predicted with the current DFT study using PBE. Red line: HOMO; Green line: LUMO.

and DOS of the α-phase showed in Figure 4.8 are different than the bands and DOS of the β-phase as expected since these crystals have different lattice structures, number of atoms, geometries and Brillouine zones. The band gap resulted to be 6.2 eV nearer to the experimental value of 6.5 ev[150]. The bands and DOS of other crystals were omitted because of the high similarity of electronic states between different PVDF crystals and the fact that no experimental literature for comparison was indeed available, the discussion of other crystals bands and DOS would indeed resulted redundant and poor of literature comparison.

4.6 Vibrational frequencies

Many investigations have been conducted to provide data that can be used to determine which PVDF crystal structures are present in PVDF sample prepared with different methodologies. By already having experimental spectra for α[82], β[81] and γ[30] phases the vibrational frequencies computed here were directly compared to literature, furthermore, vibrational spectra were collected also for δ, ε and ζ phases which enriched the vibrational frequencies knowledge about PVDF crystal strucures. Although, for the δ, ε and ζ crystals there were limited information available for comparison, the computation were performed with the same rigour of the other PVDF crystal structures to ensure the reliability of the current prediction.

The vibrational frequencies of the ferroelectric crystals of PVDF have been determined within the representative primitive cell which half the number of atoms and consequently half the number of vibrational modes present in the model reducing peaks redundancy. In the case of the γ-phase the evaluation of vibrational frequencies of its primitive cell vanished the distinction between the γ_{uu} and γ_{ud} variants. Furthermore, the present PVDF spectra were computationally predicted with DFT using the PBE functional as the vdW-DF functional resulted to be too computationally expensive. Unless differently specified the computed vibrational frequencies of other authors were performed with DFT using the PBE functional. The vibrational frequencies and phonons frequencies of a defined model are expected to be an exact number which is 3 times the number of atoms present in the computed model and in the case of vibrational frequencies 6 modes are excepted to be zero while for phonons modes 3 are indeed zero (along this section only non zero modes will be counted and presented). The accuracy of vibrational frequencies predicted by the present computation using the converged parameters given in chapter 3 is given per crystal model within the table which presents the computed peaks compared with experiments and other author's computations.

4.6.1 Vibrational frequencies of the β-phase

The vibrational frequencies of the primitive cell of the β-phase (6 atoms model) having 12 modes were reported in Table 4.12 together with previous computation and experimental frequencies observations (the β-phase space group being C_{m2m}). Ramer *et al*[81], Karasawa *et al*[26] (using MD) and Nakhmanson *et al*[32] computed the phonons modes for the β-phase primitive cell, Bormashenko reported other few β frequencies from experimental observations[30] while Kobayashi compared computational phonons modes with experimental IR spectra of the β-phase[65, 105, 151] along multiple studies. Here, all non zero modes for the primitive cell of the β crystal were reported in Table 4.12 and present results agreed with previous calculations[32, 81] also agreeing with experimental frequencies[30, 151] observations reported for the β crystal.

It was noticed that the highest discrepancy of peaks comparison was found with the work of Nakhmanson *et al*[32] as in his study the phonons modes were calculated instead of vibrational frequencies as in the present study. Furthermore, Nakhmanson investigated two crystal variants of the β-phase model and the most stable crystal structure was here compared with the present vibrational frequencies of the β-phase (primitive cell). The discrepancy was attributed to the scaling factor Nakhmanson used (1.0427 in the low-frequency region under 2000 cm^{-1} and 0.9879 for the high-frequency) to fit the phonons modes to the experimental frequencies, moreover, Nakhmanson reported only 12 phonons modes (15 expected). The present vibrational frequencies were scaled using the same factors used by Nakhmanson to show putative differences as reported in Table 4.12. Also the vibrational spectra computed using MD by Karasawa *et al*[26] showed some discrepancies with more consistent match with previous authors[32] calculations than the present computation.

The 511 cm^{-1} peak[30] experimentally described as a characteristic bending mode of the CF_2 group of the β-phase was found to correspond in the current characterisation as the peak at 476 cm^{-1} which was not surprising since also in the computational work of Ramer *et al*[81] was found that such peak appeared shifted at 482 cm^{-1} instead of 511 cm^{-1}[30]or 508 cm^{-1}[73, 105, 151] as other authors reported from experiments, therefore, such peaks were attributed to be equivalent. Few other peaks determined by both Ramer *et al*[81] and Bormashenko *et al*[30] were found within the range 600-900 cm^{-1} as distinctive of the β-phase peaks again with shifted wavelengths when compared to the computed frequencies as showed in table 4.12. The 600 cm^{-1} peak has been referred by Bormashenko *et al*[30] and Boccaccio *et al*[31] to belong to the β crystal and found here at 623 cm^{-1}. Indeed, such peak at 600 cm^{-1} was discussed by Bormashenko *et al*[30] and Boccaccio *et al*[31] as a distinctive peak of the β-phase never reported previously by experimental literature.

Table 4.12 Vibrational frequencies of the β-PVDF primitive cell compared to previous calculated and observed values. The accuracy of peaks prediction of the present computation has been estimated to be 0.32 cm^{-1} for the β crystal. ^{a}: observed by other authors[30, 31] as the experimental peak at 600 cm^{-1}; ^{b}: Observed experimentally by Bormashenko *et al*[30] as the experimental peak at 511 cm^{-1}; ^{c}: Present vibrational frequencies scaled with the empirical factors used by Nakhmanson[32] to show how peaks would be like if scaled; IR: present IR peaks relative intensity. ν: stretching (a: symmetric, s: asymmetric); r: rocking; w: wagging; t: twisting; δ: bending; τ: torsional; L: librational.

Vibrational frequencies (cm^{-1})							Modes		IR
DFT	DFT	DFT			MD	Exp.			
Present	Scaled^{c}	[81]	[105]	[32]	[26]	[65]	[81]	Present	
3075	3038	3069	3024	3024	3017	3022	$\nu_a(CH_2)$	$\nu_a(CH_2)$	0.03
3009	2973	3015	2975	2971	2983	2980	$\nu_s(CH_2)$	$\nu_s(CH_2)$	0.08
1553	1619	1424	1434	1467	1429	1428	$\delta(CH_2)$	$\delta(CH_2)$	1.29
1396	1456	1325	1408	1414	1397	1398	$w(CH_2)-\nu_a(CC)$	$\delta(CH_2)$	0.81
1251	1304	1213	1283	1270	1276	1273	$\nu_s(CF_2)-\nu_s(CC)$	$\nu_s(CF_2)-\nu_s(CC)+\delta(CCC)$	1.36
1194	1245	1159	1177	1139	1165	1176	$\nu_a(CF_2)-r(CF_2)$	$\nu_a(CF_2)-r(CF_2)$	3.67
954	995	1139	1074	1088	1072	1071	$t(CH_2)$	$\delta(CCC)-r(CH_2)$	3.80
928	968	1022	980	870	980	-	$r(CH_2)-\nu_a(CF_2)$	$r(CH_2)-\nu_a(CF_2)$	5.90
655	683	856	883	-	887	884	$r(CH_2)-\nu_a(CF_2)$	$w(CF_2)-\delta(CH_2)+\delta(CCC)$	0.93
-	-	810	844	842	841	840	$\nu_s(CF_2)-\nu_s(CC)$	-	-
623^{a}	650	-	-	-	-	-	-	$t(CH_2)-\nu_a(CF_2)$	0.30
476^{b}	496	482^{b}	508^{b}	493^{b}	511^{b}	508^{b}	$\delta(CF_2)$	$\delta(CF_2)$	0.33
-		482	471	-	480	468	$w(CF_2)$	-	-
405	422	419	444	445	447	442	$r(CF_2)+r(CH_2)$	$r(CF_2)+r(CH_2)$	0.01
-		258	265	-	267	-	$t(CF_2)$	-	-
-		81	72	77	17	70	Librational	-	-

However, other author's computations[26, 65, 32, 81, 105] did not found such peak at 600 cm^{-1} in their analysis as reported in Table 4.12. To that concern it must be noticed that other authors computed phonons frequencies instead of vibrational frequencies and some authors such as Nakhmanson[32] used scaling factors to fit phonons modes to vibrational frequencies. In the present study rigorous convergence threshold tests were performed while other authors which used DFT applied lower thresholds in relaxing the initial model (*e.g.* 40 Ry while in the present study a cut off of 80 Ry was used with other more stringent thresholds as discussed in section 3) which could have been altered the frequencies prediction fitness.

The peak at 928 cm^{-1} of the present characterisation in Table 4.12 appeared to have a high intensity and shifted of 40-80 cm^{-1} in respect to other literature references of both computational and experimental observations studies, but the vibrational mode appeared to be the same for all the studies compared to the present peak at 928 cm^{-1}. Two rather strong and distinctive peaks of the β crystal at 954 and 655 cm^{-1} as reported in Table 4.12, were observed in the present study at such wavelengths, although, previous studies found for such vibrational modes significantly different wavelengths and vibrational modes deputed to the fact that other authors computed phonons instead of vibrational frequencies and in experiments such peaks (mapped to the correspondent 954 and 655 cm^{-1} peaks) were mapped out from computed phonons[65, 106]. Indeed, purely experimental observations[31, 30] of the β-phase spectra never reported β peaks around 1000 cm^{-1} and 880 cm^{-1}. Moreover Milani *et al*[73] reported experimentally the peak region within 880-860 cm^{-1} as a peak range were same peaks and relative intensity were found for multiple PVDF crystal structures such as β and α phases. Only Bormashenko reported a β peak at 840 cm^{-1} which could be referred to the computed peaks around 880 cm^{-1} of other computations[26, 65, 32, 81, 105]. However, considering the impurity of crystal phases in experimental samples and the experimental observations of Milani *et al*[73] about the ambiguity of peaks within 880-860 cm^{-1} the peaks reported by other authors[26, 65, 32, 81, 105] around 880 cm^{-1} could be not specific of the β-phase.

Other frequencies characterised in the present study which matched well with other computational papers as shown in Table 4.12 were not experimentally recognised (sometimes not even observed in experiments) as characteristic of the β-phase crystal. In previous research papers the 1279 cm^{-1} peak was deputed to be a distinctive peak of the non-poled β-phase[73] and reported by Bormashenko *et al*[30] as an out of plane deformation characteristic of non-poled samples rich in β crystals domains and such peak was found in the present study at 1251 cm^{-1}. The correlation of the present and previous computed β-phase frequencies with the experimental frequencies was calculated and all computed studies resulted to correlate well with the experimental observation as showed in Figure A.19.

4.6.2 Vibrational frequencies of the ζ-phase

Interestingly, as Table 4.13 reported the vibrational frequencies of the ζ-phase having 30 vibrational modes (12 atoms model with the P_{mma} space group), a peak at 1280 cm^{-1} has been found. Such peak could represent a putative evidence of the ζ-phase as this mode would appear only for the ζ-phase at 1280 cm^{-1} since in experimental observations Costa[78] and Bormashenko[30] described that the peak at 1279 cm^{-1} is a distinctive peak of the non-poled β-phase. Costa *et al*[78] showed that such peak disappears if the sample rich in the non-poled β-phase was successively poled and the IR spectra sampled again. To such extent it could be seen that the 1280 cm^{-1} peak found for the ζ-phase would shift to 1251 cm^{-1} for the β-phase also with a significant lower peak intensity which in the β-phase is about 3 times weaker than the ζ-phase. Despite the possibility that in experimental IR spectra such peak would not be appreciated in such small wavelength shift between the ζ and β phases, its intensity should still be a distinguishable factor between the two crystal phases.

Indeed, the first time it has been found in literature the use of terms such as "unoriented β-phase"[30] and "non-poled β-phase"[78, 81, 79, 105] was across vibrational frequencies studies. It was observed that a sample deputed to be rich in the β-phase content was recognised to show modest but distinguishable differences in some IR peaks governed by the role of poling, which is a post processing technique often applied on a PVDF sample. Non-poled β-phase rich samples showed to have few weak peaks which were assumed to belong to the β-phase which was non-poled[30, 65], such peaks would disappear if the sample was successively poled slightly changing the IR spectra profile appreciable by observing together the spectra of poled and non-poled samples[78, 79] and the peak at 1279 cm^{-1} was the most evident peak to disappear in poled samples. In such case this was the first time where different authors agreed on a non-polar β-phase like structure found in some non-poled β-phase rich samples[78, 79]. To this reference, such "non-poled β-phase"[78, 81, 79, 105] resulted to be more concretely as the ζ-phase (characterised in the present study), the non ferroelectric analogue of the β-phase.

When not considering the existence of the ζ-phase, the richness of trans bonds of a PVDF sample by FTIR spectra analysis has been retained as a valid meter of the abundance ratio of the β-phase. Considering that the ζ crystal has never been officially recognised before this study, it may be plausible that the ζ-phase existence remained hidden in samples reach in trans bonds, especially in non-poled samples[78, 79] where more probably chains may remain antiparallel aligned[1, 109] keeping the full trans backbone configuration. The 1279 cm^{-1} peak could have been historically confused to belong to the β-phase just because nobody never accounted for the existence of the ζ-phase. As no other evidences about the vibrational frequencies of the putative ζ-phase were available the ζ spectra analysis was found limited

Table 4.13 Vibrational frequencies of the ζ-PVDF. IR: present IR peaks relative intensity. The accuracy of peaks prediction of the present computation has been estimated to be 0.24 cm^{-1} for the ζ crystal. ν: stretching (a: symmetric, s: asymmetric); r: rocking; w: wagging; t: twisting; δ: bending; τ: torsional; L: librational.

Vibrational frequencies (cm^{-1}) Present ζ	Modes	IR
3132	$\nu_a(CH_2)$	0.32
3071	$\nu_a(CH_2)$	0.07
3031	$\nu_s(CH_2)$	0.05
2668	$\nu_s(CH_2)$	0.74
1544	$\delta(CH_2)$	2.32
1445	$\delta(CH_2)$	0.99
1363	$\delta(CH_2)$	1.14
1339	$w(CH_2)+w(CF_2)$	8.54
1280	$\delta(CH_2)+\delta(CF_2)$	5.47
1211	$\delta(CCC)$	2.39
1159	$t(CH_2)$	1.12
1157	$t(CH_2)$	2.08
1141	$t(CH_2)+\delta(CCC)$	0.19
1076	$w(CH_2)+\nu_a(CC)$	5.67
989	$t(CH_2)+\nu_s(CC)$	5.13
871	$t(CH_2)$	0.56
860	$t(CH_2)+t(CF_2)$	2.43
820	$\delta(CCC)$	0.36
624	$t(CH_2)-\delta(CF_2)$	0.78
556	$\nu_a(CC)-\delta(CF_2)$	0.52
517	$\delta(CH_2)+\delta(CF_2)$	0.12
472	$\delta(CC)-\delta(CF_2)$	0.32
433	$t(CH_2)$	0.08
359	$r(CH_2)+r(CF_2)-\delta(CF_2)$	0.30
261	$t(CH_2)-t(CF_2)$	0.00
247	$w(CF_2)-w(CH_2)$	0.00
157	$L(R_c^0)$	0.00
73	τ_s	0.00
51	$L(T_a)$	0.01
39	τ_a	0.08

in comparison. The peak at 1544 cm^{-1} in Table 4.13 was found to be a common peak that the ζ-phase shared with the β-phase found at 1553 cm^{-1} (Table 4.12) with the same vibrational mode. The strong peaks at 1339, 1071, 989 and 860 cm^{-1} appeared to have rather strong intensities and being distinctive of the ζ-phase, although, no experimental evidences were available about the ζ-phase to support such analysis.

4.6.3 Vibrational frequencies of the α-phase

The α-phase, by possessing the $P2_{1/c}$ space group lead to a crystal unit with a minimal of 24 atoms which accounts for 66 vibrational frequencies as reported in Table 4.14. In Table 4.14 is possible to appreciate the redundancy of several peaks which is expected as more atoms are present in the model with a simple chemistry as PVDF and more vibrational frequencies will resemble one vibrational mode degenerated in more peaks. The α-phase peaks match consistently the Ramer *et al*[82] computational study with 80% of frequencies matching within less than 1.2% of error, while another 20% of the frequencies match within 2.5% of error[82]. The computational and experimental vibrational frequencies study made by Kobayashi *et al*[65] was found in line with the present prediction with peaks matching within a 1.8% of error and also in agreement with the computational study of Ramer *et al*[82]. The only significant discrepancy between the study of Kobayashi *et al*[65] was the present peak found at 1740 cm^{-1} which corresponded in Kobayashi study to the peak at 1477 cm^{-1}.

Experimentally, Bormashenko *et al*[30] linked some frequencies as determinant of the α-phase as the peaks at 489, 530, 615, 766, 795, 855 and 976 cm^{-1} which were also observed by other authors[30, 152, 82] to be distinctive of the α-phase. The present vibrational frequencies calculations matched consistently with experimental observations apart for the missing peak at 766 cm^{-1}. The correlation of the present and previous computed α-phase frequencies with the experimental frequencies was calculated and all computed studies resulted to correlate well with the experimental observation as showed in Figure A.20.

Table 4.14 Vibrational frequencies of the α-PVDF. Frequencies are compared to previous calculated and observed values. The accuracy of peaks prediction of the present computation has been estimated to be 0.44 cm^{-1} for the α crystal. IR: present IR peaks relative intensity. ν: stretching (a: symmetric, s: asymmetric); r: rocking; w: wagging; t: twisting; δ: bending; τ: torsional; L: librational.

Vibrational frequencies (cm^{-1})						
Present	Previous				Modes	IR
	Calc.			Exp.		
α	[82]	[65]	[26]	[65]		
3116	3068	3042	3035	3030	$\nu_a(CH_2)$	0.04
3107	3068	3042	3034	3017	$\nu_a(CH_2)$	0.00
3087	3071	3040	3032	3017	$\nu_a(CH_2)$	0.04

3076	3072	3040	3031	2990	$\nu_a(CH_2)$	0.40
3034	3016	2977	2992	2980	$\nu_s(CH_2)$	0.16
3029	3016	2977	2992	2977	$\nu_s(CH_2)$	0.04
3024	3011	2975	2991	2977	$\nu_a(CH_2)$	0.28
3022	3010	2975	2989	2970	$\nu_s(CH_2)$	0.19
1740	-	1477	1418	1442	$\delta(CH_2) - w(CH_2) + w(CF_2)$	0.60
1436	1402	1477	1400	1430	$\delta(CH_2) - w(CH_2)$	0.16
1423	1407	1456	1382	1420	$\delta(CH_2 - w(CH_2))$	0.40
1400	1401	1455	1380	1406	$\delta(CH_2) - w(CH_2) + w(CF_2)$	0.35
1381	1354	1392	1351	1402	$\delta(CH_2) + w(CH_2) - \nu_a(CC)$	0.47
1357	1353	1392	1351	1399	$\delta(CH_2) + w(CH_2) - \nu_a(CC)$	8.22
1357	1342	1360	1302	1384	$\nu_s(CH_2) + w(CH_2)$	0.02
1342	1337	1359	1290	1383	$\nu_s(CC) + w(CH_2)$	1.74
1291	1253	1279	1219	1200	$w(CH_2) + \nu_s(CC) + \delta(CH_2) - \nu(CH_2)$	0.01
1255	1254	1278	1218	1209	$\nu_a(CF_2) + w(CH_2)$	0.99
1251	1296	1241	1208	1294	$w(CH_2) + w(CF_2) - \nu_s(CC)$	0.00
1234	1291	1241	1205	1290	$r(CH_2) + \nu_s(CC) - \nu_a(CF_2)$	0.28
1160	1130	1199	1182	1190	$\nu_a(CC) - \nu_s(CF_2)$	17.1
1152	1161	1198	1180	1182	$\nu_s(CF_2) + t(CH_2)$	0.06
1137	1149	1159	1145	1150	$\nu_a(CC) + t(CH_2) - w(CH_2)$	7.00
1119	-	1158	1143	1149	$\nu_s(CC) - w(CF_2)$	5.08
1113	-	1083	1129	-	$w(CH_2) + \nu_s(CC)$	0.05
1108	-	1083	1128	-	$t(CH_2) + w(CH_2)$	4.24
1080	1116	1069	1092	1064	$\nu_s(CC)$	1.55
1067	1117	1069	1091	1067	$\nu_s(CC)$	0.12
1012	1077	975	1011	1056	$\nu_s(CF_2) + w(CH_2)$	4.06
1003	1014	973	1010	976	$t(CH_2)$	0.00
914	913	935	1010	976	$t(CH_2) - \nu_a(CF_2)$	1.13
901	913	934	1010	940	$t(CH_2) - \nu_a(CF_2)$	0.45
882	-	880	934	885	$t(CH_2) + \nu_s(CC) + \nu_s(CF_2)$	0.74
854	854	877	934	878	$t(CH_2) - \nu_a(CC)\nu_s + (CF_2)$	0.11
834	769	818	849	800	$r(CH_2) + \nu_s(CC) + t(CH_2) - \nu_a(CF_2)$	0.62
829	849	815	849	878	$t(CH_2) + \nu_a(CF_2)$	2.18
828	829	835	881	841	$t(CH_2) + \nu_a(CF_2)$	5.47
782	-	834	879	795	$r(CH_2) - \nu_a(CF_2)$	1.80
748	-	776	844	766	$r(CH_2) + w(CF_2) - \nu_a(CF_2)$	0.82

725	-	775	842	-	$r(CH_2)+\nu_a(CF_2)$	0.15
717	733	621	725	766	$t(CH_2)+\nu_a(CF_2)$	2.73
608	-	617	723	612	$t(CH_2)+\nu_a(CF_2)-\delta(CF_2)$	0.22
587	584	529	632	612	$\delta(CF_2)-\delta(CCC)$	2.33
586	-	528	632	-	$\delta(CF_2)-\delta'(CCC)$	0.04
508	510	513	533	536	$\delta(CF_2)+\delta(CH_2)-w(CH_2)$	0.47
475	508	509	529	531	$r(CH_2)+t(CH_2)-\delta(CF_2)$	0.11
463	464	434	510	489	$\delta(CF_2)+w(CF_2)+t(CH_2)$	2.16
438	-	423	509	488	$\delta(CF_2)+\delta'(CCC)$	0.00
408	-	407	436	414	$t(CH_2)+t(CF_2)-\nu_s(CF_2)$	0.11
380	-	372	433	410	$t(CH_2)+t(CF_2)$	0.16
368	392	371	419	389	$t(CH_2)+w(CF_2)$	0.02
350	-	309	417	357	$t(CH_2)+t(CF_2)$	0.08
329	339	304	368	355	$t(CH_2)+t(CF_2)$	0.03
282	275	283	367	215	$\delta(CCC)+\delta'(CCC)+r(CF_2)$	0.00
276	276	283	298	216	$\delta(CCC)+w(CF_2)+r(CH_2)$	0.00
272	-	247	295	288	$r(CF_2)+r(CH_2)$	0.08
262	279	231	281	287	$t(CF_2)+w(CF_2)$	0.01
210	200	247	279	208	$t(CF_2)-\delta(CCC)+\delta'(CCC)$	0.24
195	-		267	206	$r(CF_2)+r(CH_2)$	0.03
186	-	130	260	176	$t(CH_2)+t(CF_2)$	0.01
159	-	120	208	176	$t(CH_2)+t(CF_2)$	0.00
127	174	120	207	100	τ_a	0.05
91	-	94	108	99	$t(CH_2)+t(CF_2)$	0.21
87	105	84	107	75	$\tau_a+\tau_s+\delta(CCC)+r(CF_2)$	0.06
34	64	62	39	-	$L(R_c^0)$	0.00
33	55	59	-	53	$L(R_c^\pi)$	0.00
-	-	11	-	52	$L(T_b)$	-
-	-	-	-	29	$L(T_c)$	-

4.6.4 Vibrational frequencies of the δ-phase

The δ-phase is ferroelectric having the space group P_{na2_1}, hence, the frequencies characterised on its primitive cell were expected to be the half[153] of the α-phase. Table 4.15 reported the non zero modes of the primitive cell of the δ-phase. About the δ spectra only Mengyuan *et al*[154] reported an experimental spectra together with the α-phase spectra with the purpose of underlining the very high similarity of such couple of spectra and the intrinsic difficulty of discriminating such crystal structures experimentally[154] with FTIR experiments. The δ-phase frequencies calculated, widely overlap with the α-phase frequencies as expected and observed in experiments[154].

The relative intensity of 1357 and 1160 cm^{-1} peaks represents the few α to δ discrimination peaks[154] where in the α-phase such peaks can be found at such wavelengths while in the δ-phase such modes both appeared to be down shifted of $\approx$40 cm^{-1} as noted experimentally[154] corresponding to the δ-phase peaks at 1301 and 1142 cm^{-1}, respectively. In experiments to further distinguish the α-phase against the δ-phase, also the determination of the ferroelectric behaviour is usually required, which is present only in the δ crystal[69]. In favour of the δ-phase, no other frequencies were explicitly assigned by other authors since the experimental spectroscopic distinction of the α-phase versus the δ-phase remained intrinsically difficult and generally authors focused more on distinguishing the α-phase from the β-phase.

4.6.5 Vibrational frequencies of the γ-phase

The vibrational spectra of the γ-phase was reported in Table 4.16 and its space group C_c is represented in its primitive cell by 24 atoms having 66 modes and also in this case peaks redundancy was found. Karasawa *et al*[26] contributed with and MD computational prediction of the vibrational spectra of the γ-phase and Kobayashi *et al*[65] and Tashiro *et al*[106] joined experimental and computational studies of the γ-phase spectra. The studies of Karasawa[26], Kobayashi[65] and Tashiro[106] well agreed with the present γ peaks prediction with peaks matching within a margin of error lower than $\approx$2%.

Experimentally, some of the γ-PVDF modes were observed by Bormashenko *et al*[30] which found the 483, 812, 831, 834, 837, 840, 880 and 1234 cm^{-1} peaks and by Gregorio *et al*[155] which recognised the 778 and 855 cm^{-1} peaks, all being distinctive of the γ-PVDF. Such peaks were all found in the present study of the γ-phase within a margin of error of $\approx$2%. The majority of peaks were found to have weak intensities most likely not detectable in experimental spectra analysis (without fitting computed frequencies) and the high intensity peaks were found to be seventeen of which the distinctive γ-PVDF peaks were previously referenced to experimental literature. The correlation of the present and previous computed γ-phase frequencies with the experimental frequencies was calculated and all computed studies resulted to correlate well with the experimental observation as showed in Figure A.21.

Table 4.15 Vibrational frequencies of the δ-PVDF primitive cell. IR: present IR peaks relative intensity. The accuracy of peaks prediction of the present computation has been estimated to be 0.45 cm^{-1} for the δ crystal. ν: stretching (a: symmetric, s: asymmetric); r: rocking; w: wagging; t: twisting; δ: bending; τ: torsional; L: librational.

Vibrational frequencies (cm^{-1}) Present δ	Modes	IR
3099	$\nu_a(CH_2)$	0.28
3079	$\nu_a(CH_2)$	0.19
3036	$\nu_s(CH_2)$	0.29
3021	$\nu_s(CH_2)$	0.10
1465	$\nu_s(CH_2) - w(CH_2)$	0.43
1442	$\nu_s(CH_2) + w(CH_2)$	1.09
1385	$\delta(CH_2)$	1.47
1314	$w(CH_2)$	2.11
1301	$w(CH_2) - \delta(CCC)$	0.28
1225	$\nu_s(CC)$	1.08
1173	$\delta(CCC)$	5.41
1142	$\nu_s(CC) - \delta(CCC)$	6.08
1088	$\nu_s(CC)$	1.99
1052	$w(CH_2) + \delta(CCC)$	3.30
974	$w(CH_2) + \delta(CCC)$	3.46
908	$t(CH_2) + \delta(CCC)$	0.78
865	$t(CH_2)$	1.70
840	$r(CH_2) + \nu_s(CF_2)$	1.13
787	$w(CH_2) + \nu_a(CF_2)$	3.29
745	$w(CH_2) + \delta(CCC) - r(CH_2)$	0.18
650	$\delta(CCC)$	0.50
543	$\delta(CF_2) + r(CH_2)$	1.11
494	$\delta(CF_2)$	0.58
486	$t(CH_2)$	0.51
419	$w(CH_2) + \delta(CF_2)$	0.53
395	$t(CH_2)$	0.08
302	$w(CF_2)$	0.03
246	$w(CF_2) - \delta(CCC)$	0.03
236	$w(CF_2) - \delta(CCC)$	0.02
98	$L(T_c)$	0.17

Table 4.16 Vibrational frequencies of the γ-PVDF primitive cell. The accuracy of peaks prediction of the present computation has been estimated to be 0.81 cm^{-1} for the γ crystal. ν: stretching (a: symmetric, s: asymmetric); r: rocking; w: wagging; t: twisting; δ: bending; τ: torsional; L: librational.

Vibrational frequencies (cm^{-1})						
	Calc.			Obs.		
Present	[26]	[65]	[106]	[106]	Modes	IR
γ						
3086	3022	-	3027	3032	$\nu_a(CH_2)$	0.12
3072	3021	-	3027	3032	$\nu_a(CH_2)$	0.25
3065	3015	-	3027	3022	$\nu_a(CH_2)$	0.05
3069	3015	-	3026	3015	$\nu_a(CH_2)$	0.05
3026	2984	3036	2987	2990	$\nu_s(CH_2)$	0.09
3019	2984	2984	2988	2990	$\nu_s(CH_2)$	0.12
3013	2976	-	2987	2985	$\nu_s(CH_2)$	0.08
3010	2976	-	2986	2985	$\nu_s(CH_2)$	0.04
1473	1420	-	1424	1427	$\delta(CH_2)$	0.24
1420	1411	1430	1404	1400	$\delta(CH_2)$	0.48
1406	1383	-	1385	1385	$\delta(CH_2)$	0.35
1397	1379	1396	1380	1385	$\delta(CH_2)$	0.30
1373	1319	-	1370	1365	$\delta(CH_2)$	2.97
1363	1250	-	1363	1320	$\delta(CH_2)$	0.54
1355	1251	-	1325	1274	$\delta(CH_2)$	5.01
1343	1233	-	1320	1250	$w(CH_2)$	0.92
1302	1194	-	1254	1234	$w(CH_2)$	0.18
1288	1185	1287	1246	1205	$\nu_a(CF_2)$	0.21
1249	1170	-	1245	-	$\nu_a(CF_2)$	0.28
1207	1164	-	1243	-	$\nu_s(CF_2)$	2.78
1180	1159	1182	1198	1190	$\nu_s(CF_2)$	8.35
1167	1157	-	1188	1175	$\nu_a(CF_2)$	2.02
1165	1147	-	1169	1134	$\nu_s(CF_2)$	8.02
1129	1101	-	1142	1115	$\nu_s(CC)$	10.02
1086	1097	-	1119	-	$\nu_s(CF_2)$	1.09
1088	1093	-	1095	1075	$\nu_s(CF_2)$	1.64
1062	1011	1065	1065	1052	$\nu_s(CC)+w(CH_2)$	4.43
1042	1005	-	1062	-	$\nu_s(CC)+w(CH_2)$	0.97
1019	991	-	964	-	$\nu_s(CC)$	1.03
1023	978	-	950	-	$\nu_s(CC)$	2.90
970	947	982	945	964	$t(CH_2)$	0.20

904	896	-	932	878	$t(CH_2)$	0.56
885	891	880	879	874	$\nu_s(CC)$	0.79
852	869	-	872	858	$\nu_s(CC)$	0.86
845	864	-	839	842	$\nu_s(CF_2)$	2.26
837	857	-	839	835	$\nu_s(CF_2)$	0.36
822	854	825	797	811	$r(CH_2) - \nu_s(CF_2)$	6.54
805	843	-	792	791	$\nu_s(CF_2) + r(CH_2)$	1.76
780	737	-	775	748	$t(CH_2)$	0.84
754	700	-	764	723	$r(CH_2)$	1.20
720	618	-	737	700	$r(CH_2)$	0.63
633	553	-	652	656	$\delta(CH_2)$	0.11
586	548	-	561	614	$\delta(CF_2)$	0.62
520	534	-	548	539	$\delta(CF_2)$	0.05
516	511	510	534	512	$\delta(CF_2)$	0.57
505	507	-	499	500	$\delta(CF_2)$	0.07
486	454	473	490	484	$\delta(CF_2) - w(CH_2)$	0.64
461	448	-	432	442	$\delta(CF_2) - w(CH_2)$	1.89
414	437	458	430	432	$r(CF_2 - r(CH_2)$	0.62
407	411	-	417	404	$r(CF_2 - r(CH_2)$	0.03
392	375	-	399	370	$t(CF_2)$	0.20
383	345	-	377	350	$t(CF_2)$	0.01
340	333	-	346	304	$\delta(CF_2)$	0.02
305	313	-	303	299	$\delta(CF_2)$	0.05
294	277	-	301	286	$t(CF_2)$	0.07
275	274	262	276	267	$t(CF_2)$	0.06
250	265	-	273	-	$t(CH_2)$	0.00
246	246	-	168	-	$t(CH_2)$	0.00
215	226	-	164	-	$r(CH_2)$	0.00
205	185	-	-	172	$r(CH_2)$	0.02
174	160	-	129	172	$\delta(CCC)$	0.06
111	135	-	84	130	$\delta(CCC)$	0.04
104	135	-	79	98	$\delta(CCC)$	0.02
76	102	-	63	84	$\delta(CCC)$	0.31
78	65	-	32	64	$\delta(CCC)$	0.01
37	65	106	32	-	τ_s	0.06

4.6.6 Vibrational frequencies of the ε-phase

In concern to the ε_{uu} and ε_{ud} phases as no experimental evidences about FTIR spectra were available as well as neither the crystal structure nor the space group of such crystals were never characterised experimentally. Hence, the Tables referring to the vibrational frequencies of the ε_{uu} and ε_{ud} phases were left to appendix in section A.3.4. Such computational study about the ε_{uu} (Table A.2) and ε_{ud} (Table A.3) phases vibrational frequencies could not be analytically discussed because of the complete lack of literature evidence about such PVDF polymorphs.

4.7 Summary

The quantum mechanics study showed that the inclusion of first principle vdW long range forces implementation represents the best DFT set up to describe PVDF physical properties, getting nearer as ever to the real experimental correct geometry and showing to consistently describe any other PVDF physical property as discussed earlier in this chapter. Furthermore, the crystal structures of the ε-PVDF (with $_{uu}$ and $_{ud}$ variants) proposed in past computational works[26, 66] has been here confirmed although with small geometry deviation due to the fact that the software used here did not perform the geometry optimisation by applying space group symmetry constraints to the crystal model as previously performed by other authors which first proposed such crystal structures[26, 66].

The ζ-PVDF emerged to be a putative metastable PVDF crystal structure and as already indirectly mentioned in many other experimental works[30, 81, 78, 79], such structure represents the non ferroelectric counterpart of the most studied β-PVDF crystal. Its existence would make necessary to reinterpret the crystalline quality of PVDF samples rich in trans bonds which manifest low ferroelectric behaviour. As the ζ-phase has a full trans backbone, it would make to result a sample rich in trans bonds, to have weak ferroelectric properties, and generally the estimation of the magnitude of the spontaneous polarisation of a PVDF sample has been interpreted as a direct indicator of the sample crystallinity. With the existence of the ζ-phase would become incoherent. The positive consequence of having found the ζ-phase, is that the crystallinity of a PVDF sample in favour of crystal rich in trans bonds would be at least partially solve since even if a sample is rich in the ζ-phase, the application of a potential trespassing the coercive field of the sample, would make the ζ-phase to become the β-phase.

A plausible reason that explains why the ζ-phase has never been characterised before is that the ζ-phase resulted to be a coplanar structure, and as all other PVDF crystals are biplanar, even though such crystal may be appeared in crystallography studies, it could be assumed that such coplanar would not be a representative crystal structure of PVDF.

Moreover, as the majority of PVDF studies found in literature did not study PVDF crystals using X-ray crystallography, the experimental individuation of the ζ-phase would results almost impossible as shown in chapter 4 where the vibrational frequencies of the β and ζ phases resulted to be similar, and with the limit of accuracy of experimental IR spectra[3], to recognise the ζ-phase from the β-phase without any structural information, would be impractical. Furthermore, the ζ-phase is non FE and the scientific research about PVDF has always been focused in refining the sample quality of the β-phase crystal. Such work enriched the PVDF crystal structure knowledge by not only determining PVDF crystal structures with the inclusion of vdW forces in DFT but also verifying the metastability of all PVDF polymorphs including the ε and ζ phases. Also the γ_{uu}, γ_{ud}, ε_{uu} and ε_{ud} phases were acknowledged as metastable crystal variants of PVDF showing the energetic ordering of such structures in comparison with the other PVDF polymorphs.

On top of the structural study reported in this chapter, it has also been seen that other physical properties such as the electronics structures, spontaneous polarisation and vibrational frequencies of PVDF have been described accordingly to other computational and experimental works. For such physical properties of PVDF crystals the present study confirmed solid matches with experiments where available and enriching the knowledge about less studied PVDF crystals such as the ε_{uu}, ε_{ud} and ζ phases.

Chapter 5

Force fields performance on bulk PVDF

The completion of physical properties and structural information about all PVDF crystals allowed to move the investigation to the next step. Indeed, having a reliable set of information on structural features of PVDF polymorphs, it has been possible to scale some PVDF geometries predicted with DFT into molecular dynamics simulations. It was chosen MD over other methodologies since MD provides a consistent time step evolution of the simulated system, to appreciate the dynamic interaction of particles within different simulated conditions such as temperature, bulk and surface conditions. A time consistent simulation methodology allow to appreciate the time frame in which phase transition and structural chains switches events occurs, which represent an advantage to understand how much an event is likely to happen. Furthermore, a time consistent simulation methodology allows to calculate dynamic properties evolution, to appreciate how structural properties of PVDF chains changes during time under certain conditions, which a key question to understand how a surface affects PVDF chains conformation. In other methodologies such as montecarlo, the simulation of the system randomly switches atomic configuration, although, such simulations provides the statistical probability of such event, it does not provides the time scale on which such event is likely to happen.

The structural studies of PVDF were simulated using classical molecular dynamics and three different force fields were compared. FFs performance depends strongly on the model and parameters and a force fields need extensive tests to ensure reliability. In this thesis project the force fields considered, were the few which other authors developed specifically for PVDF. The FFs used were the Byutner and Smith (B&S)[27, 111], the optimised potential for liquid systems (OPLS)[28] and MSXX[110, 26, 104], where B&S was mainly made for studying the melting mechanism of PVDF, OPLS for studying the liquid phase behaviour of PVDF while interacting with surfaces and MSXX for determining geometries and physical bulk properties of PVDF.

The MD study started with the determination of the crystal geometry properties of PVDF for the three force fields found in literature as pertinent to study PVDF. This chapter's work was mainly focused to benchmark DFT versus MD and appreciate the ability of different FFs to predict the properties of PVDF. The optimised lattice structure of all PVDF's crystal phases together with phase and lattice energies were the only properties collected from frozen MD systems, any further investigation gathered data from proper molecular dynamic computations at finite temperatures. Furthermore, this chapter also shows the finite temperature computations approaches performed to reach equilibration of a liquid bulk system and the properties of the equilibrium state.

The liquid phase properties of PVDF are important because the liquid state allows to appreciate molecular interactions to a faster time scale than a solid phase, a liquid phase can be formerly considered to reach a steady state where all molecules posses the same average properties and because it makes more evident how specific matter interactions can alter such equilibrium forming new steady states with different averaged properties independent by time and dependent on the new simulation conditions computed.

5.1 Crystal structures & energetics

Within this chapter the MD work has been dedicated predicting the crystal structures properties such as geometries, crystal energies and cohesive energies, furthermore, in such chapter also the liquid phase equilibration has been presented. For such purposes different initial models were built. In predicting the crystal geometries and energetics small simulation boxes were made as the exact same PVDF polymorphs geometries predicted with DFT. For this part of study the MD simulation boxes of every PVDF crystal is reminded to Figures 2.4, 2.5, 2.3, 2.6, 2.8 and 4.1 which showed the simulation boxes used in DFT and MD of the α, δ, β, γ, ε and ζ periodic crystals, respectively. For the liquid phase equilibration instead of considering small periodic crystals, the simulation box has been expanded keeping periodic boundaries conditions but having PVDF finite chains. The initial configuration of the simulation box for the liquid phase equilibration was made building an orthorhombic box of a= 52 Å, b= 16 Å, c= 34 Å containing 36 linear PVDF chains in a 6×6 frame respecting the spatial geometry of the β-phase (see Figure 2.3), each chain made by twelve monomers terminated on one side with a CH_3 group and a CF_3 on the other side. Such initial configuration is shown in Figure 5.3.

Table 5.1 DFT and MD lattice comparison of PVDF polymorphs compared with DFT_{vdW} results and literature. DFT_{vdW}: DFT results from XC-f vdW-DF.

Phase	a(Å)	b(Å)	c(Å)	Vol.(Å^3)	$\beta°$	Ref.	Method
β	8.58	4.91	2.56	107.8	90	[75]	Exp.
β	8.61	4.72	2.56	104.0	90	[26]	MSXX
β	8.62	4.80	2.60	107.5	90	Present	DFT_{vdW}
β	8.41	4.62	2.63	102.2	90	Present	B&S
β	8.51	4.75	2.72	109.9	90	Present	OPLS
β	8.53	4.78	2.60	106.1	90	Present	MSXX-noX
ζ	8.65	4.77	2.60	107.1	90	Present	DFT_{vdW}
ζ	8.43	4.53	2.64	100.8	90	Present	B&S
ζ	8.44	4.62	2.79	108.8	90	Present	OPLS
ζ	8.52	4.74	2.61	105.4	90	Present	MSXX-noX
α	4.96	9.64	4.62	220.9	90	[75]	Exp.
α	5.07	9.47	4.59	220.4	92	[26]	MSXX
α	4.42	9.51	4.69	224.0	90.6	Present	DFT_{vdW}
α	4.92	9.43	4.72	219.0	90	Present	B&S
α	4.92	9.52	4.58	214.5	90	Present	OPLS
α	5.01	9.59	4.80	230.6	90	Present	MSXX-noX
δ	4.96	9.64	4.62	220.9	90	[21]	Exp.
δ	5.08	9.32	4.58	216.8	90.1	[26]	MSXX
δ	4.98	9.53	4.70	223.2	90	Present	DFT_{vdW}
δ	4.91	9.40	4.67	215.5	90	Present	B&S
δ	4.97	9.52	4.70	222.4	90	Present	OPLS
δ	5.00	9.52	4.80	228.5	90	Present	MSXX-noX
γ_{uu}	4.97	9.66	9.18	440.7	90	[68]	Exp.
γ_{uu}	5.02	9.53	9.14	437.3	97.7	[26]	MSXX
γ_{uu}	4.95	9.71	9.32	419.6	90	Present	DFT_{vdW}
γ_{uu}	4.76	9.47	9.17	413.4	90	Present	B&S
γ_{uu}	4.47	9.70	9.48	411.0	90	Present	OPLS
γ_{uu}	5.06	9.65	9.16	447.3	90	Present	MSXX-noX
ε_{uu}	4.68	9.68	9.13	413.6	90	[26]	MSXX
ε_{uu}	4.95	9.79	9.32	451.8	90	Present	DFT_{vdW}
ε_{uu}	4.89	9.73	9.29	442.0	90	Present	B&S
ε_{uu}	4.95	9.79	9.32	451.7	90	Present	OPLS
ε_{uu}	4.77	9.70	9.46	442.2	90	Present	MSXX-noX

5.1.1 Crystal structures

The geometry prediction ability of the MSXX, MSXX-noX, B&S and OPLS force fields was compared with the DFT results obtained with the vdW-DF functional which were presented in the previous chapter, and in Table 5.1, the results of experimental references, DFT vdW-DF and MSXX, MSXX-noX, B&S and OPLS FFs were presented and compared. For brevity in the geometry optimisation performed with LAMMPS using the three force fields MSXX, MSXX-noX, B&S and OPLS FFs, the up-up and up-down variants for γ and ε phases were omitted.

Table 5.1 showed that the original MSXX[26] force field predicted PVDF crystal structures consistently with a deviation of less than 1% from experimental lattice and volumes. The MSXX-noX reproduction did not deviate much more than that, indeed, the lattice and volume predicted deviated from experiments less than 1.5%, hence, the cross terms did not influence significantly the crystal structure prediction ability of the MSXX-noX force field. The B&S[27] geometries showed in Table 5.1 appeared to have a good agreement with experiments with small deviations again within the order of less than 1.2%. No significant structure prediction anomalies were found within any of α, δ, β, γ, ε and ζ phases predicted by B&S. The OPLS force field also predicted geometries within 1% of deviation from experimental data. In terms of volume estimation, MSXX-noX overestimates the volumes of PVDF crystal structures in respect of the original MSXX of less than 0.05%, B&S underestimates volumes in respect of experimental observations of less than 0.04%, while OPLS did not presented a neat trend in volume estimation in respect of experimental values.

The overall collection from experimental, DFT and MD optimised geometries in Table 5.1 shows clearly that between different force fields there were no significant differences in the ability of defining the minimal energy of frozen PVDF crystal structures. Even in the case of ε and ζ phases where there were no experimentally determined crystal structures, the geometries predicted by the MSXX, MSXX-noX, B&S and OPLS force fields remained consistent with the DFT vdW-DF functional. Surprisingly it was found that the geometry prediction performed with DFT, resulted in more divergent results between functionals (*e.g.* LDA, PBE, PBE+D2, vdW-DF and vdW-DF2) than the geometries predicted with MD between different force fields (*e.g.* MSXX, MSXX-noX, B&S and OPLS). Such fact was not surprising for MSXX and MSXX-noX since such FF was made for describing solid crystals mainly, but it was surprising for B&S and OPLS since the scope of these two FFs were to describe the melting mechanism and the liquid phase properties, respectively.

5.1.2 Cohesive and relative crystal energies

The optimised geometries obtained with the MSXX, MSXX-noX, B&S and OPLS force fields were used to calculate phase energy orderings relative to the α-PVDF. The isolated chains energies of Table 5.2 showed that between MSXX-noX, B&S and OPLS there is a significant difference in how such force fields described energetics of isolated chains. In

Table 5.2 Isolated chain energies of PVDF backbones in vacuum of $\Delta_{TG^{+/-}}$ and $\Delta_{TTTG^{+/-}}$ chains with isolated chain energy of Δ_T as relative zero. The unit of Δ is kJ mol^{-1}.

Functional	$\Delta_{TG^{+/-}}$	$\Delta_{TTTG^{+/-}}$	Reference
B&S	-22.09	-18.07	Present
OPLS	-53.43	-57.19	Present
MSXX-noX	-0.92	1.04	Present
vdW-DF	-17.6	-12.5	Present

Table 5.3 Cohesive energies of all PVDF polymorphs compared to MD results available in literature. Energies are expressed in kJ mol^{-1}.

Functional	α	δ	γ_{uu}	ε_{uu}	β	ζ	Reference
B&S	-37.67	-24.35	-27.95	-27.24	-48.95	-51.63	Present
OPLS	-30.42	-42.80	-67.90	-43.72	-50.21	-62.34	Present
MSXX-noX	-16.74	-14.94	-15.65	-64.02	-39.54	-37.32	Present
vdW-DF	-33.7	-34.0	-38.6	-37.9	-47.5	-47.4	Present
MSXX	-20.08	-20.50	-33.30	-26.28	-25.94	-	[26, 104]

particular, the MSXX-noX FF appeared to not discriminate cohesive chains energies between different conformers since all three backbones (*e.g.* T, TG^+TG^- and $T_3G^+T_3G^-$) showed to have negligible energy difference of 1 kJ mol^{-1} and the $T_3G^+T_3G^-$ backbone to be the most stable conformer as reported in Table 5.2. The OPLS FF did not deviate much from the prediction of MSXX-noX and the TG^+TG^- backbone resulted to be more stable than the $T_3G^+T_3G^-$ of 4 kJ mol^{-1}. The B&S at the contrary predicted the cohesive energy in agreement with the computed results of the DFT vdW-DF functional predicting the TG^+TG^- to be the less stable backbone conformer and the $T_3G^+T_3G^-$ stability to be between the full trans backbone (the most stable backbone) and the TG^+TG^- backbone.

Figure 5.1 reported the phase energies of all MSXX, MSXX-noX, B&S and OPLS force fields together with the Table 5.3 which reported such results for more precise reading. The energy ordering made with vdW-DF (DFT), the original prediction with MSXX[26, 104] and B&S force fields reported in Figure 5.1 remained consistently in a narrow range of energy of less than 14 kJ mol^{-1}. However while vdW-DF and B&S found the α-phase as the stable structure, the original MSXX found the β-phase to be stable (Figure 5.1).

The OPLS prediction reported in Figure 5.1 showed to be less consistent as the α, δ, γ_{uu} and ε_{uu} phases were energetically grouped within 11-16 kJ mol^{-1} as similarly to the prediction of the B&S force field, but the β and ζ phases appeared to be significantly less stable than the α-phase by more than 45 kJ mol^{-1}. On the contrary, the MSXX-noX

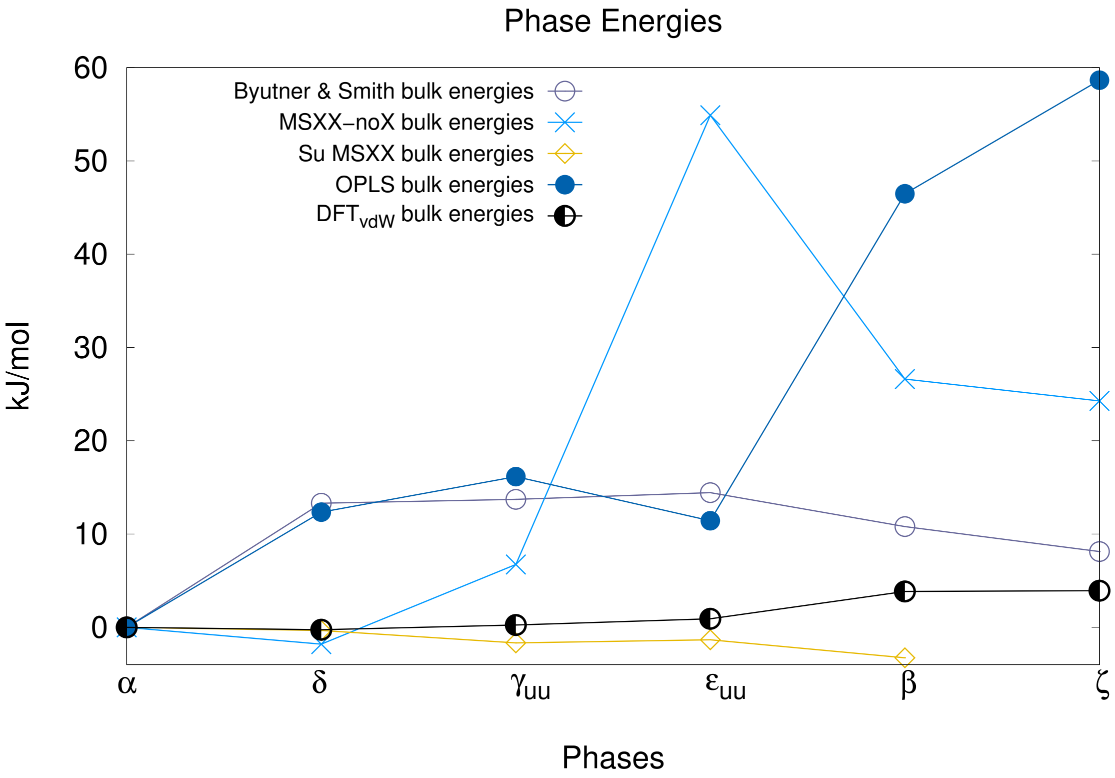

Fig. 5.1 Phase energy plot of all PVDF structures characterised using the three FFs and with literature comparison, the α-PVDF is the reference structure from which the zero has been set. Results are in comparison with DFT$_{vdW}$. DFT$_{vdW}$: DFT results from XC-f vdW-DF. The energy minimisation threshold was fixed to 4.18e-09 kJ mol^{-1}.

force field to the contrary, appears to be less consistent than MSXX, indeed, the δ-phase appeared to be the stable structure while the γ_{uu}, ε_{uu}, β and ζ were ordered differently and the ε_{uu}-phase being the less stable of all crystal structures of PVDF.

Table 5.3 and Figure 5.2 report the data of cohesive energies between the different crystal structures of PVDF and as visible the original MSXX and MSXX-noX force field did differ significantly also in predicting cohesive energies as MSXX ordered cohesive energies between -(20-32) kJ mol^{-1} while MSXX-noX saw the α, δ and γ_{uu} phases within -(16-19) kJ mol^{-1} and the other phases having significantly stronger cohesive energies. In particular as the ε_{uu} phase which was seen as the least stable crystal structure by MSXX-noX its cohesive energy resulted to be the highest. Considering both phase ordering and cohesive energies predicted by MSXX-noX is has been possible to assess that the missing cross terms played a crucial role in crystal structure energetics.

Furthermore, in Table 5.3 and Figure 5.2 the vdW-DF, B&S and OPLS predictions appeared to be more consistent with each other and with an almost uniform trend in seeing

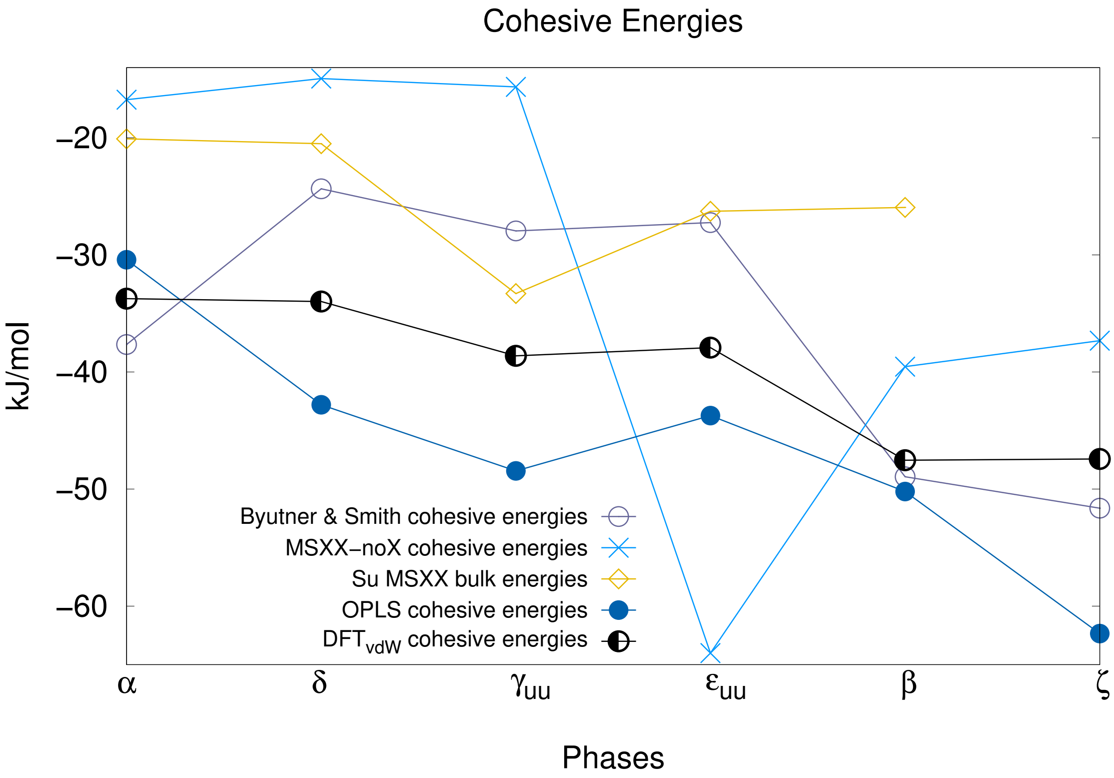

Fig. 5.2 Cohesive energies of PVDF polymorphs per each FFs compared to DFT$_{vdW}$ results. Each backbone type (*e.g.* $T_3G^+T_3G^-$, TG^+TG^- and T) represent the relative reference from which to calculate the individual cohesive energies of each crystal phase grouped per backbone type. DFT$_{vdW}$: DFT results from XC-f vdW-DF. The energy minimisation threshold was fixed to 4.18e-09 kJ mol^{-1}.

the α-phase as the crystal structure with the weakest cohesive energy and the β and ζ phases having the highest and similar cohesive energies, although, OPLS predicted the ζ-phase to have a cohesive energy 10 kJ mol^{-1} stronger than the β-phase. About these evidences, the B&S force field showed to be the most consistent set up in describing the energetics of PVDF crystal structures when compared to the prediction performed using the DFT vdW-DF functional (Figures 5.1 and 5.2).

5.2 Liquid phase properties

This section is concerned with the physical properties of PVDF in liquid phase using MD simulations because the effects of external conditions such as presence and absence of a surface and electrostatics charges on a surface are appreciable at the nanoscale which is usually the feasible time scale for MD simulations[54, 156, 51, 16]. A liquid phase is characterised by randomly oriented molecules with no long range structural order. With the study of polymers the liquid phase becomes complicated to simulate because the high molecular weight of polymers requires very long time to enter the liquid phase as polymer chains have many degrees of freedom in chains motion and conformation that takes a time which is usually beyond the MD time scale. Along the full length of a polymer chain several forces will differently shape the chain conformation making difficult that the full chain will possess an homogeneous conformation of its former atoms from start to end of the chain[53].

Therefore, it is important to find a procedure which is able to melt polymer chains to the liquid state and keep such conditions long enough to make sure that all chains will have enough time to assume random and uniform molecular conformations. A main factor for the amount of time needed for every chain to assume random and uniform conformations is the polymer chain length as the entanglement is what limits polymer chains diffusivity most[156, 51]. To reach an equilibrated liquid phase with MD simulations is not only a matter of procedure, but it is also a matter of the FF used as indeed is not certain that with any force field a specific equilibration procedure will always work.

The evaluation of the liquid phase equilibrium state must rely on key properties which can help to assess if the polymeric chains reached random and uniform molecular conformations. These properties will allows to know when the liquid phase equilibrium has been reached and properties such as radius of gyration (R_g) and end to end distance (R_e) tells the coiled state of polymeric chains and the conformation tensor gives information about polymeric chains conformers. In particular the conformation tensor is a way to quantify the atomic movements of a molecule from its point of origin at a given initial time which monitor movements until a final time. When atoms are displaced enough to ensure that each atom of each molecule will be found to a point distant from the initial coordinates of the initial time, the conformation tensor value will tend to be near to one and when the X (C_{xx}), Y (C_{yy}) and Z (C_{zz}) axes diagonal conformers values will tend all to one and the molecules of the system are considered to have reached a disordered random state characteristic of a liquid phase[53].

Furthermore, the averaged properties of a liquid phase equilibrium are time independent since the system reaches the steady state and such averaged liquid phase properties can be reached independently from the initial configuration of the system and the density is a useful property to consider for determining when the system becomes liquid and its properties independent by time. By comparing experimentally measured liquid phase properties to the simulated liquid phase properties of PVDF under different conditions makes possible to understand which are the effects of such different conditions on the liquid phase properties of PVDF. This comparison is useful in understanding which conditions promote the formation of specific PVDF crystal structures starting from a random and uniformly disordered liquid phase, which is the main goal of this thesis. In this chapter the procedure used to complete the liquid phase equilibration of bulk PVDF has been presented together with the averaged properties of the liquid phase equilibrium.

5.2.1 Equilibration procedure

In the study by Kremer *et al*[51] it was demonstrated that the chain length of polymers represents a major issue in reaching the liquid phase equilibrium and Erdtman *et al*[111] demonstrated that short PVDF oligomers such as 12 monomers per chain represents a good chain length for studying PVDF melting mechanism matching computed liquid phase properties to experimental properties and in this study the number of monomers per chain was kept the same as in the Erdtman's study. The FFs used for testing the equilibration procedure were MSXX-noX[110, 26], B&S[27] and OPLS[28] which were previously introduced in section 3.6, applying to the whole liquid phase study the NpT ensemble (*e.g.* fixed number of atoms, pressure and temperature).

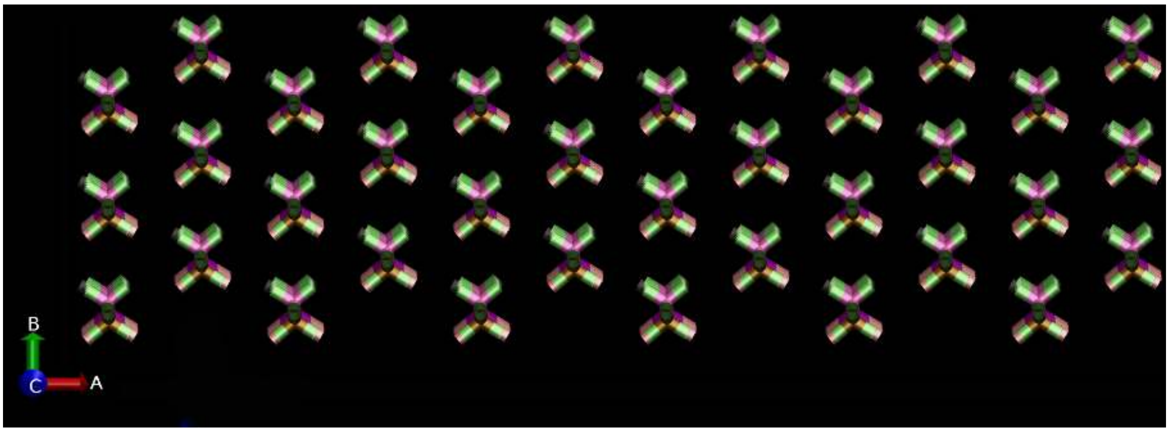

Fig. 5.3 Initial structure of the bulk model. A: *a*-axis; B: *b*-axis; C: *c*-axis. Green: Hydrogen; Purple, Cyan: Carbon; Pink: Fluorine.

The whole equilibration procedure was followed monitoring system properties mentioned before such as the density, R_g, R_e and conformation tensor using the B&S FF to perform the most extensive equilibration tests since such FF was designed for studying the liquid phase of PVDF. The liquid phase equilibration procedure can be generally divided in three phases where the first is the annealing phase for which several temperatures were tested annealing the model in parallel from 500 K up to 900 K jumping 100 K per test and running each annealing test per 40 ns. As usually other authors[27, 111] used short annealing time such as 5 ns or less, with the concern of being prudent, 40 ns was an annealing time considered sufficient to reach the liquid phase and leaving enough time to the system to assume a disordered steady state

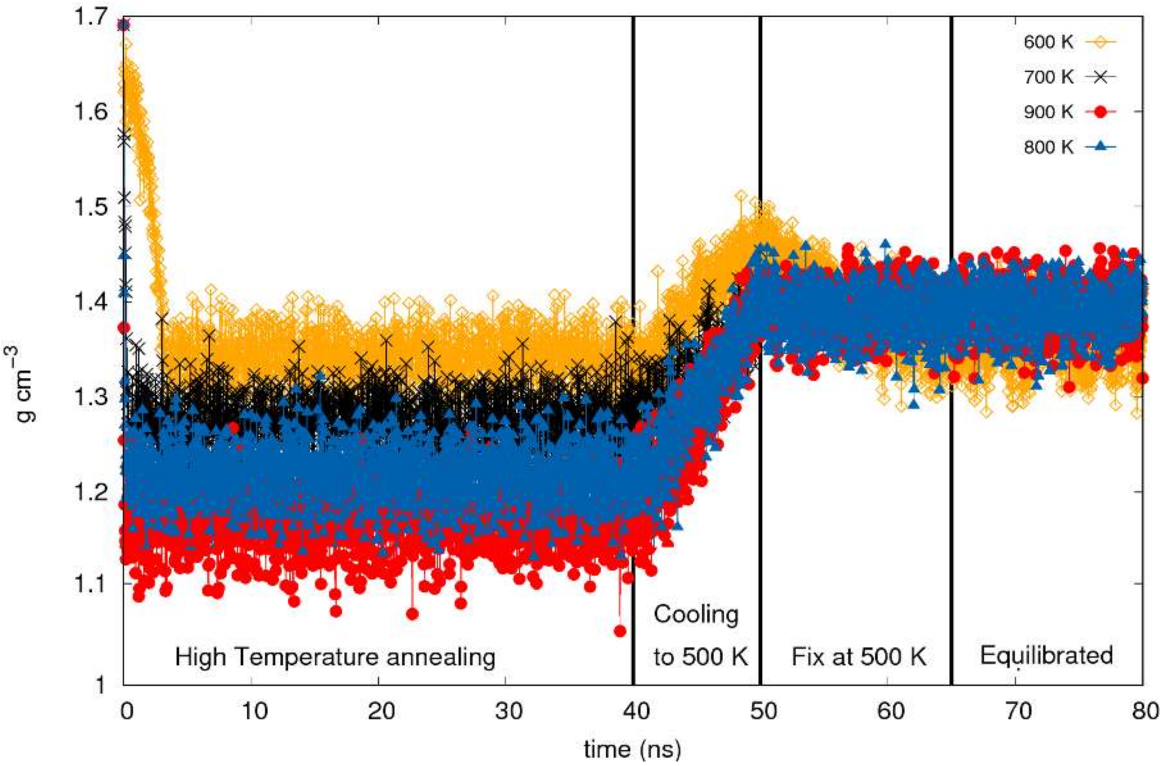

Fig. 5.4 Density versus time of bulk β-PDVF short chains during all heating approaches tested together with the complete liquid phase equilibration procedure using the B&S FF. High temperature annealing: constant thermal treatment to melt the chains; Cooling: cooling process to bring the system to 500 K; Fix at 500 K: steady dynamic run at the fixed temperature of 500 K; Equilibrium: Equilibrium of the liquid phase.

far from the original system conformation. Figure 5.4 showed the density as function of time of the annealing tests and the annealing temperatures from 600 K up to 900 K using the B&S FF were effective in melting the system although the annealing phase performed at 600 K took 3 ns to reach a density average characteristic of the liquid phase and after the cooling phase it was also evidenced that the annealing at 600 K made the density as function of time to overshoot in the first 3 ns of the steady state at 500 K making clear that higher annealing temperatures should be chosen to equilibrate the system. The density profile showed to have significant fluctuations since the npt ensemble keeps the pressure of the simulation constant and leaves the volume to adjust consequently to keep the pressure constant (one atmosphere), hence, being the density of the of a system tightly dependent by its volume expansion and contractions, such large density fluctuations were expected.

In Figure 5.4, from 700 K up to 900 K the system average density quickly changed and remained steady for the whole annealing time where the only difference was that with different annealing temperatures the density average changed accordingly to the heat applied on the system. Figure 5.4 also showed the density as function of time along the cooling phase performed in 10 ns and the steady state at 500 K reached from different annealing temperatures and from 700 K up to 900 K the density as function of time of the 500 K steady temperature resulted to even out on the same density average across the last 30 ns of simulation time. Table 5.4 reported the averaged properties of the last 15 ns of the annealing temperatures tested from 500 K up to 900 K showing that the 500 K annealing did not melted in 40 ns the initially crystalline model as density, R_g, R_e and conformation tensor retained characteristics properties of a solid, while from 600 K up to 900 K the density, R_g and R_e properties changed significantly describing coiled chains with density and conformation tensor properties which were typical of the liquid phase[27, 111].

Table 5.4 Averaged properties of the B&S FF MD runs for different annealing temperatures from 500 K up to 900 K performed for 40 ns. T_{ann}: Annealing temperature. Std.: Standard deviation.

B&S					
T_{ann} (K)	900	800	700	600	500
Density (g cm^{-3})	1.17	1.22	1.28	1.36	1.75
Density Std. (g cm^{-3})	0.03	0.03	0.03	0.06	0.02
R_e (Å)	16.25	16.23	16.45	16.42	27.64
R_e Std. (Å)	0.84	0.91	1.09	1.23	0.22
R_g (Å)	6.34	6.33	6.37	6.36	8.90
R_g Std. (Å)	0.15	0.17	0.21	0.24	0.03
Conformation tensor by diagonal elements					
C_{xx}	1.079	1.056	1.075	1.102	0.066
C_{yy}	1.085	1.090	1.073	1.160	0.412
C_{zz}	1.083	1.097	1.100	0.949	2.524

The second phase was to cool the system down to a temperature still able to keep the system in the liquid phase avoiding to perform the most important part of the study under a thermal energy too high which could disrupt energy matter interaction. To such extent the cooling rates tested were 60, 30 and 22.5 K ns^{-1} and the cooling rate of 30 K ns^{-1} (the cooling speed is referred to the system annealed at 800 K) resulted to be equivalent to the others in term of averaged properties along the cooling procedure as showed in Figures 5.5, 5.6 and A.22 showing the density, R_g and R_e of the cooling rates tested, respectively. Table 5.5 reported the averaged properties of the three cooling rates as density, R_g, R_e and conformation tensor showing that the averaged properties of the system cooled at three different rates were rather equivalent.

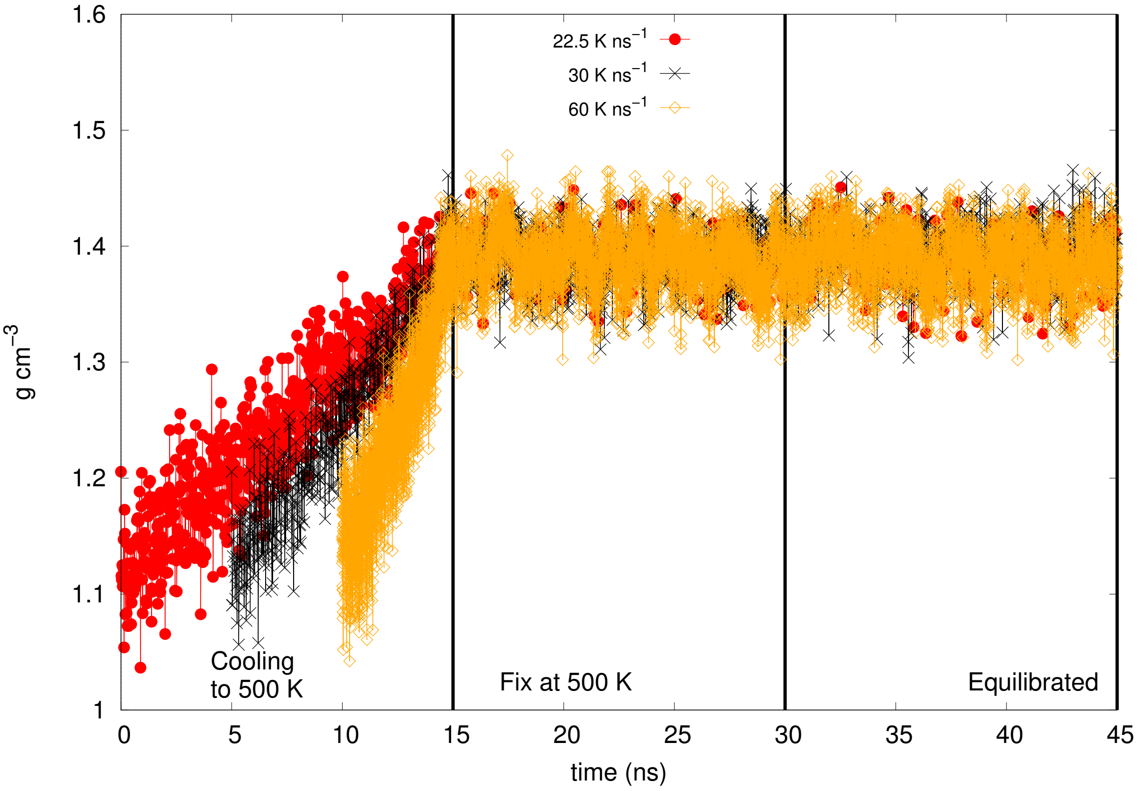

Fig. 5.5 Density as function of time of bulk PDVF annealed at 800 K and cooled to to 500 K using 3 different cooling rates using the B&S FF.

Hence, the cooling rate of 30 K ns^{-1} was chosen since it was the intermediate cooling rate between the three speeds tested. Furthermore, the other annealing temperatures such as 700 K and 900 K which were cooled arbitrarily in 10 ns showed to reach the same average density during the steady state at 500 K than the system annealed at 800 K, showing that 10 ns cooling time was an effective time to make the system correctly transiting in a new homogeneous properties average state as showed in Figure 5.4. After completing the cooling process, the fixed temperature at which the model was kept liquid (when melted during the annealing phase) was chosen to be 500 K as it represent a temperature over the experimental melting point of PVDF (*e.g.* 438 K) where the thermal energy is not too high to significantly cancel out long range forces. At such temperature the system was made to run for 30 ns with the intent of checking over a long period of time that the system properties were not changing during the fixed temperature dynamics at 500 K. The last 15 ns of the fixed temperature at 500 K were taken as the representative statistics of the liquid phase equilibrium and further in this chapter the properties of the liquid phase will be discussed.

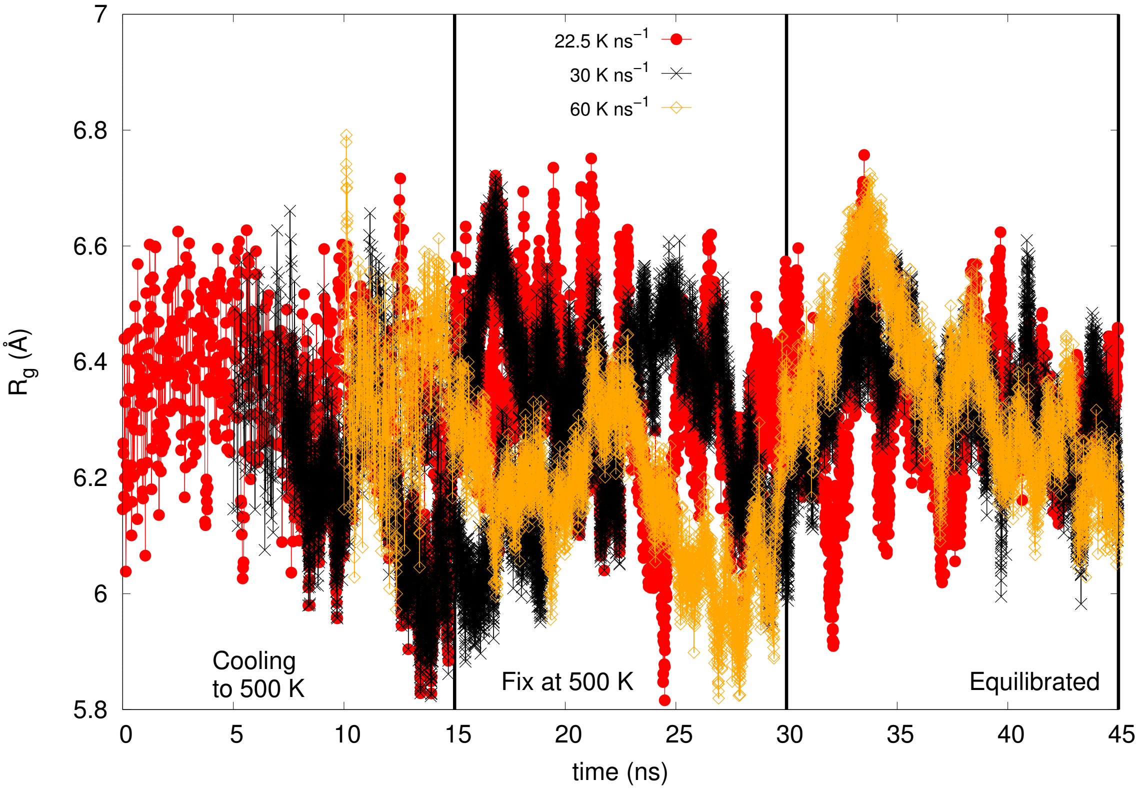

Fig. 5.6 R_g as function of time of bulk PDVF annealed at 800 K and cooled to to 500 K using 3 different cooling rates using the B&S FF.

As Figure 5.4, 5.7 and A.23 showed that the annealing temperatures from 700 K up to 900 K were equivalent in term of density, $R_g$and R_e along the annealing, cooling and steady state at 500 K. Then, the annealing phase performed at 800 K with a cooling rate of 30 K ns^{-1} which brought the system from 800 K to 500 K in 10 ns and kept it steady for 30 ns was the liquid phase equilibration procedure chosen as the standard procedure to reach the representative liquid phase equilibrium averaged properties discussed further.

A quick reference was here made to the PVDF model computed using the B&S FF before the annealing procedure was started to show the physical properties of the purely crystalline model used as a starting point of a solid crystal. Table 5.6 showed the averaged properties of the fully crystalline model used as initial configuration which has been brought to the liquid state. The density, R_g, R_e and conformation tensor of Table 5.6 will be cited when appropriate to underline analogies with the properties of the initially crystalline model.

Considering the liquid phase equilibration procedure described thus far, the same approach has been adopted to run the equilibration using the MSXX-noX and OPLS FFs reporting results to discuss efficacy of these force fields in achieving the liquid phase equi-

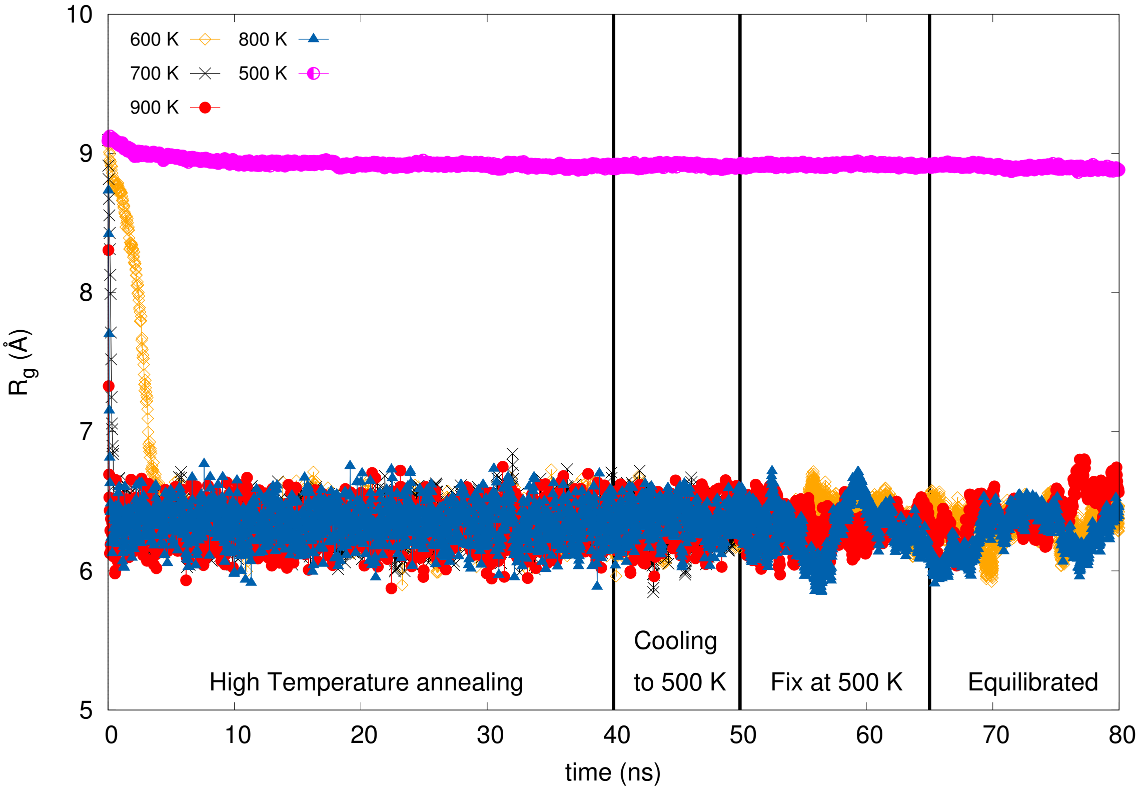

Fig. 5.7 R_g as function of time of the annealing temperatures from 500 K up to 900 K using the B&S FF.

Table 5.5 Averaged properties of the B&S FF MD runs of different cooling rates from 800 K to 500 K. Std.: Standard deviation.

	B&S cooling rates		
t (*ns*)	15	10	5
Density (g cm^{-3})	1.25	1.25	1.25
Density Std. (g cm^{-3})	0.08	0.08	0.08
R_e (Å)	16.15	16.36	17.23
R_e Std. (Å)	0.69	0.77	0.72
R_g (Å)	6.27	6.32	6.41
R_g Std. (Å)	0.11	0.13	0.12
Conformation tensor dy diagonal elements			
C_{xx}	1.076	1.033	1.059
C_{yy}	1.080	1.149	1.121
C_{zz}	1.082	1.070	1.059

librium. Table 5.7 reported the density, R_g, R_e and conformation tensor properties of the equilibration performed with MSXX-noX and OPLS. Remarkably, for neither the MSXX-

Table 5.6 B&S FF physical properties averages of the geometrically optimised β crystalline system and its conformation tensor. Geom. opt.: Data of the optimised geometry of β-PVDF 100% crystalline at 0 K before annealing started; Conformations tensor has been calculated on the optimised geometry at 0 K before annealing started.

	Geom. opt.
Density (g cm^{-3})	2.08
R$_e$ (Å)	29.78
R$_g$ (Å)	9.05
Conformation tensor by diagonal elements	
C$_{xx}$	0.00
C$_{yy}$	0.00
C$_{zz}$	3.00

noX nor the OPLS FFs the annealing temperature of 800 K was not able to melt the initially crystal structure as reported in Table 5.7 which showed the density, R$_g$, R$_e$ and conformation tensor properties along the annealing and cooling process (the annealing temperatures of 900 K and 1000 K were tried but resulted to be incompatible with the MSXX-noX and OPLS FFs). Using both FFs the β chains never reached coiled states as the R$_g$ and R$_e$ values were representative of linearised chains and the conformation tensor of Table 5.7 were rather similar to the conformation tensor of the initially crystalline model reported in Table 5.6. The density as function of time was described differently by MSXX-noX and OPLS than the B&S FF but this was essentially up to the force field set up. The averaged properties of the liquid phase equilibrium while using the MSXX-noX and OPLS were omitted since the liquid phase was never reached using such FFs.

As the MSXX-noX FF showed to describe inconsistently crystal and cohesive energies deviating from the original MSXX implementation, DFT vdW-DF and experimental results, as well the liquid phase equilibrium was not achieved with the equilibration procedure defined with B&S, the MSXX-noX force field was no longer considered for further liquid properties studies. However, since the OPLS FF was used for studying surface effects of graphene on PVDF and other polymers[28], another equilibration attempt was tried for OPLS in order to verify if the initial configuration from where the simulation started could be a limitation factor for achieving the liquid phase equilibrium.

The last trajectories snapshot of the amorphous liquid phase obtained with B&S FF at the annealing temperature of 600 K (trajectories of higher annealing temperatures were incompatible to be restarted with OPLS) were moved into OPLS set up, cooled down to 500 K in 10 ns and kept steady per 30 ns, but again, inconsistent results by using the OPLS force field emerged. Indeed, as Figure A.24 reported the density as function of time, a big

Table 5.7 MSXX-noX FF runs averaged properties of the full equilibration attempt. Cooling: cooling rates of 30 K ns^{-1}. Std.: Standard deviation.

	MSXX-noX		OPLS	
t (*ns*)	40	10	40	10
T (K)	800	Cooling	800	cooling
Density (g cm^{-3})	1.43	1.49	1.13	1.23
Density Std. (g cm^{-3})	0.03	0.04	0.03	0.06
R_e (Å)	29.39	29.39	28.93	28.74
R_e Std. (Å)	0.08	0.07	0.24	0.30
R_g (Å)	8.84	8.84	9.27	9.38
R_g Std. (Å)	0.01	0.01	0.03	0.03
Conformation tensor by diagonal elements				
C_{xx}	0.059	0.067	0.121	0.008
C_{yy}	0.200	0.172	0.216	0.052
C_{zz}	2.742	2.761	2.667	2.941

density drop was suffered while passing the liquid phase obtained with B&S to the OPLS force field. The density drop reported in Figure A.24 was followed by a quick density recover which indicated an anomalous behaviour of OPLS which was prolonged during the cooling process, where the B&S (Figure 5.4) force field saw the density increasing linearly with the temperature decrease. In Figure A.24 the OPLS force field kept the system density steady until the cooling process terminated and only within the first 5 ns at the steady temperature of 500 K the density decreased to a new even value remained stable for the rest of the simulation time. The strange density behaviour was accompanied by the R_g and R_e properties which quickly moved to values representative of PVDF chains almost completely linear as reported in Figures A.25 and A.26, respectively. The same trend was confirmed by the conformation tensor of Table A.5 which showed how passing from the B&S to the OPLS FF, PVDF chains progressively loss diffusivity and random conformations of atoms diminished.

Furthermore, visualising the trajectories of the simulation dynamics showed that the system's chains visibly reverted to a linear condition where chains were found bended with a smiling profile but with a linearised backbone. As shown in Figure 5.8, is possible to appreciate how across the simulation time the chains passed from being coiled and disordered within the simulation box (B&S annealing phase at T0), in recovering linearity. From T0 to T5 of Figure 5.8 the system chains progressively restored the linearity, from T1 where chains already were starting to becoming linear until T4 where was particularly visible the smiling bended profile of the chains which in T5 became very clear how the chains went back to be

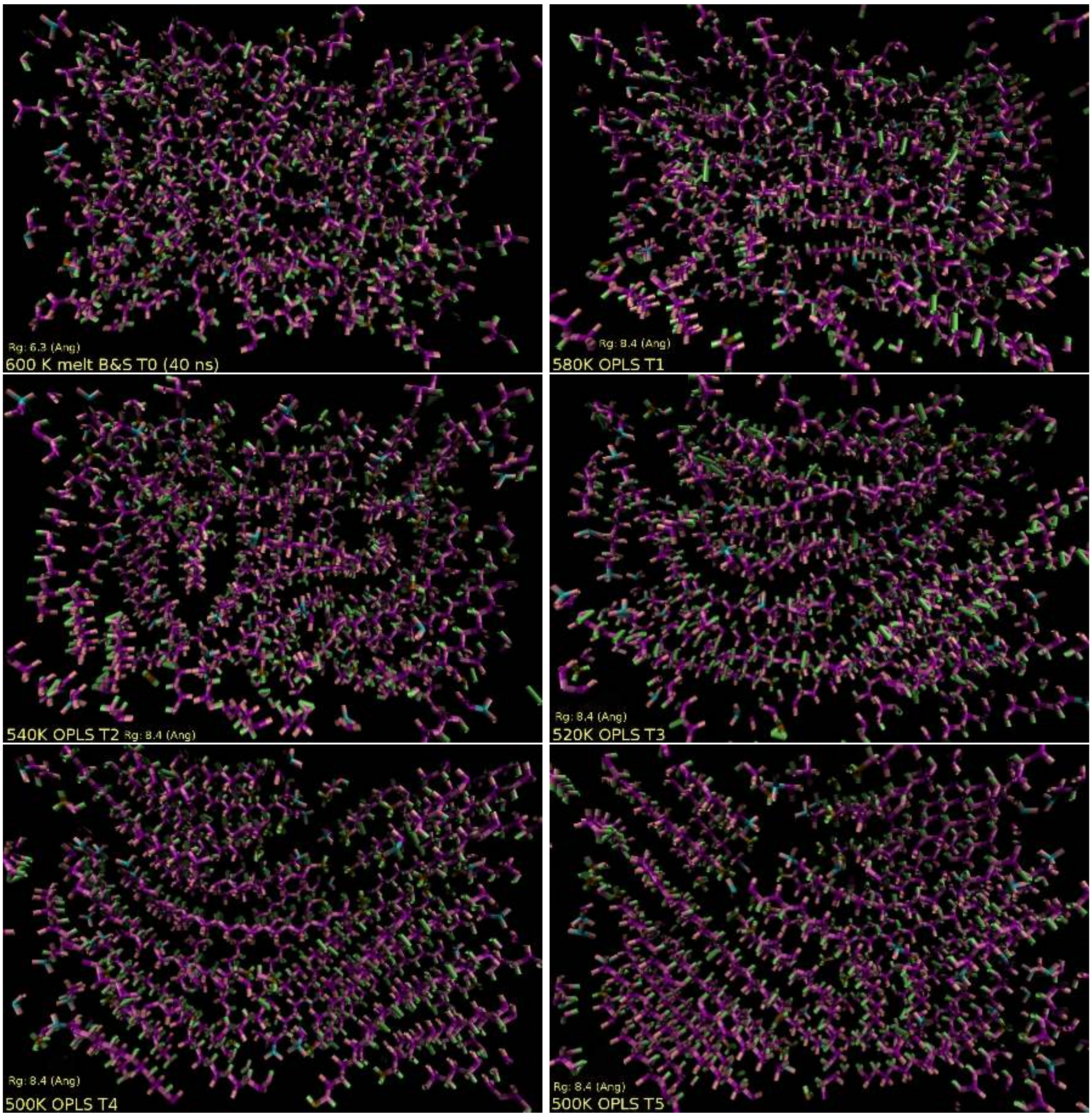
Rg: 6.3 (Ang)
600 K melt B&S T0 (40 ns)
Rg: 8.4 (Ang)
580K OPLS T1
540K OPLS T2
Rg: 8.4 (Ang)
Rg: 8.4 (Ang)
520K OPLS T3
Rg: 8.4 (Ang)
500K OPLS T4
Rg: 8.4 (Ang)
500K OPLS T5

Fig. 5.8 Pictures of the initial melted PVDF system at 600 K using the B&S force field which has been switched after 40 ns of heating to the OPLS force field, then cooled down to 500 K in 10 ns and kept at such temperature per 30 ns. To follow the picture from the restart moment swithing B&S with OPLS until the OPLS steady state at 500 K. T0: initial zero time step of the system melted at 600 K for 40 ns with B&S restarted with OPLS (initial disorder of B&S); T1: system cooled at 580 K in 2 ns; T2: system cooled at 540 K in 6 ns; T3: system cooled at 520 K in 8 ns; T4: system constantly resting at 500 K per 15 ns; T5: final steady state after 30 ns constantly at 500 K. Green: Hydrogen; Purple, Cyan: Carbon; Pink: Fluorine.

completely linear and even partially restoring layer's stratification from the bottom left of the T5 snapshot of Figure 5.8.

With the following evidences, it became very clear how the OPLS set up was able to produce crystalline artifacts, indeed, in Guryel's paper[28] it was showed that the polymers chains after being annealed at 600 K and cooled down to 500 K, the surface contact helped PVDF chains to recover linearity and crystallinity while the system was kept at 500 K. Here, it became evident that even in the absence of the surface the OPLS force field brought PVDF chains back to be linear and stratified as far as the temperature was reduced from 600 K to 500 K, although, the initial structure was liquid and amorphous. Such evidences brought to the conclusion that the OPLS force field was not a good force field on which to perform bulk nor surface studies since it produced crystalline artifacts which would completely vanish any analytical conclusion since any surface modelled would end up showing a beneficial effect on PVDF crystallinity. Remarkably, it was possible to recognise that only the B&S force field showed to be a reliable FF to count on for reaching an equilibrated liquid phase.

5.2.2 Physical properties distribution of PVDF liquid bulk

In this section, the averaged properties of the liquid phase equilibrium obtained with the B&S force field together with data gathered along the liquid phase equilibration tests were presented to underline the differences between the liquid and the solid phase of bulk PVDF. Table 5.8 reported the averaged properties of the liquid phase equilibrium obtained using the B&S FF annealing the initial model at 800 K per 40 ns, cooling to 500 K in 10 ns and keeping the system per 30 ns at 500 K, showing the averaged properties of last 15 ns of the steady state at 500 K as representative of the liquid phase equilibrium. As reported in Table 5.8 the average density of the PVDF liquid bulk model was found to be 1.39 g cm^{-1} which agree well with the experimental density of 1.30 g cm^{-1} (extrapolated with engauge from Byutner paper[27]) considering that the experimental amorphous density was retrieved from a sample with long polymeric chains (*e.g.* 10000 monomers), the density of the computed amorphous bulk model in the present study was assumed to be higher as finite short chains were used, hence, a reduced chains entanglement let PVDF chains free to pack more tightly. The R_g being 6.3 Å, the R_e being 16.1 Å, describing the states of coiled chains and C_{xx}, C_{yy} and C_{zz} diagonal conformers near to the value of one. Those data in Table 5.8 represents the standard reference of the liquid phase properties of the present PVDF bulk model computed with B&S FF.

Another way to appreciate the averaged chains conformations of the PVDF chains modelled in this study, are the dihedrals backbone distribution. Backbone dihedrals provide information of how the chemical bonds of the PVDF carbon chain are displaced in each chain, which is directly connected to the crystalline phase since the β-phase has a backbone of only trans bonds (*e.g.* 180°) and the α and δ phases have a ratio of trans and gauche

Table 5.8 Liquid phase equilibrium at 500 K of the PVDF bulk model using the B&S FF. Std.: Standard deviation.

Liquid phase equilibrium	
Density (g cm^{-3})	1.39
Density Std. (g cm^{-3})	0.02
R_e (Å)	16.10
R_e Std. (Å)	0.80
R_g (Å)	6.30
R_g Std. (Å)	0.14

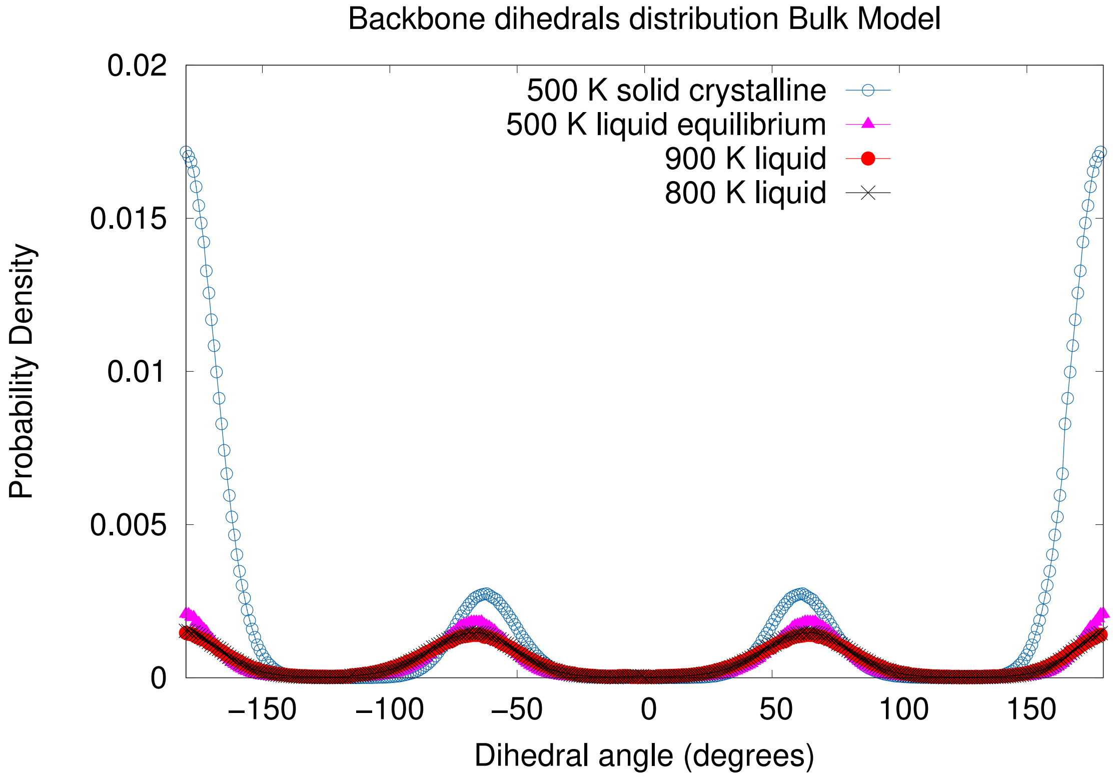

Fig. 5.9 Dihedrals backbone distribution of the bulk PVDF model of the annealing attempts of 500 K (solid), 800 K and 900 K (last 15 ns of annealing time) and the last 15 ns of the liquid phase equilibrated at 500 K (liquid) using the B&S FF.

bonds of 2:1:1 (*e.g.* 180°:+60°:-60°)[111]. Hence, by knowing the average distribution of all backbone dihedrals allows to know which crystal backbone of which crystal phase the chains preferentially have, although, the dihedral backbone distribution can not tell for sure if the chains are effectively crystalline, it still provide precious information on the preferred backbone conformation within the computed conditions.

Figure 5.9 reported the dihedrals backbone distribution of the last 15 ns for the model initially annealed at 900 K, 800 K and 500 K and the last 15 ns of the liquid phase equilibrium kept steady at 500 K. The liquid phase annealed at 900 K, 800 K and the liquid phase equilibrium at 500 K in Figure 5.9 presented a broad dihedral backbone distribution as indicative that the backbone dihedrals of a liquid phase are dispersed along the optimal values of gauche and trans bonds, $\pm 60^{o}$ and 180^{o}, respectively. However, the liquid models in Figure 5.9 presented a peak of gauche bonds distribution at $\pm 65^{o}$ and this was attributed to the fact that the thermal energy which melted and coiled PVDF oligomers, moved the optimal gauche dihedrals equilibrium which is $\pm 60^{o}$ to $\pm 65^{o}$.

Again in Figure 5.9, the dihedral backbone distribution of the model annealed at 500 K which was not melted, presenting a significant peak at 180^{o} which corresponded to a high content of trans bonds and minor peaks at $\pm 60^{o}$ which corresponded to a minor population of gauche bonds as meaning that the annealing at 500 K contributed to few degrees of disorder of the initial crystalline model without really disrupting the backbone conformation of the β chains. Such results agreed well with the similar study of Satyanarayana *et al*[157], where it was showed that a PVDF system heated at not more than 500 K was not melted, keeping a distinctive trans bonds population characteristic of the β-phase. The present dihedral distribution of Figure 5.9 also compared well with the original work of Erdtman *et al*[111] which reported a progressive loss of trans bonds that over 750 K became rather equivalent to the present dihedral distribution of the liquid bulk at 800 K and 900 K.

In conclusion, by observing the dihedral backbone distribution is possible to evidence the structural backbone trend assumed by PVDF oligomers at any particular computed conditions which is important to understand the effects of such conditions in the formation of ordered or disordered PVDF backbones. The liquid phase equilibration procedure allowed to reach a disordered state which did not preserved any conformational features of the initially crystalline model.

5.3 Summary

The present chapter presented all the work performed using MD to test three force fields such as B&S, MSXX-noX and OPLS. The main outcomes were that the prediction of crystal structures by performing geometry optimisation under the three different force fields set up, showed that all force fields similarly predicted the lattice structures in good agreement with DFT vdW-DF results and experimental evidences. The MSXX-noX, B&S and OPLS FFs showed more divergence in predicting structure energetics ordering and crystal's cohesive energies than DFT results using different functionals. Only the B&S set up described the phase energies profiling similarly to the present DFT results, while MSXX-noX and OPLS deviated with inconsistent energy peaks. The cohesive energies ordering of OPLS and B&S FFs remained in line with the DFT vdW-DF functional prediction while MSXX-noX was found to be inconsistent with the original MSXX implementation and DFT results.

Furthermore, the OPLS and MSXX-noX FFs were not successful during the liquid phase equilibration procedure where both FFs set ups forbid the PVDF crystalline model to melt and become liquid under the conditions tested. The OPLS force field resulted in reverting to crystalline state an amorphous liquid bulk melt of PVDF oligomers in conditions which should not promote crystalline structures formation. Only the B&S force field succeeded in such sense becoming the most consistent and reliable FF set up in equilibrating the bulk liquid phase PVDF model which could be further used for studying surface's effects (next chapter). The observation of physical properties such as the density, R_g, R_e, conformation tensor and the backbone dihedrals distribution showed to be key properties which provide important information about structural features of the computed models of PVDF in the present study.

Chapter 6

Surface study of PVDF oligomers

The investigation of surface effects on PVDF oligomers is presented in this chapter, where the B&S force field has been used to study PVDF oligomer on graphene. The choice of which surface to use was between gold[158, 2], alumina[57, 7, 158], silver[158], palladium[6] and graphene[8, 157, 159, 160] for which some authors provided experimental observations. However, since graphene is one of the most studied surfaces on which literature was found both on computational and experimental studies for specific case study of graphene/PVDF systems, the graphene surface was chosen as it was possible to cross compare directly with literature references. The aim was to understand the effect that graphene exerts on PVDF oligomers by confining a thin film of PVDF finite chains between a graphene sheet (periodic boundaries make the sandwich effective) and to verify if simply the vdW forces of an uncharged graphene sheet of the electrostatics charges play a role in PVDF oligomers conformations as the imposition of charges on the surface would mimic a mean electric field similar to the post processing technique of poling PVDF to increased the FE yield of the sample. Indeed, different authors proposed nanoconfinement[57, 7] and charge screening[6, 94] as two different approaches to promote the β-phase crystallinity, however, the nature of the physical polymer interaction with ions or surfaces which affects PVDF backbone conformation remained not understood and here investigated.

6.1 Surface model

The previous chapter presented the liquid phase bulk properties of a PVDF model made of 36 oligomers (12 monomers per chain) in a 6×6 frame. The same amount of chains and the same frame disposition has been used as well in the present chapter, which was focused on the surface study to understand the surface properties able to influence the structural conformation of PVDF in favour of the ferroelectric β-phase. To investigate the effect of confinement and electrostatics the system has been modelled as a PVDF thin film sandwiched between charged and uncharged graphene layers. The graphene surface was treated as a frozen sheet where all carbon atoms of the sheet were not allowed to move, hence, the graphene sheet was not parametrised to have bonds, angles and dihedrals as the sheet would not move. The simulation box was set to have lattice dimensions as a = 56 Å b = 23 Å c = 35 Å where a and c axes were fixed and b axis left free to change under the NpT ensemble with periodic boundaries. Figure 6.1 showed the initial model build with 36 β-phase chains on the top of a graphene layer which sit on the bottom of the b-axis.

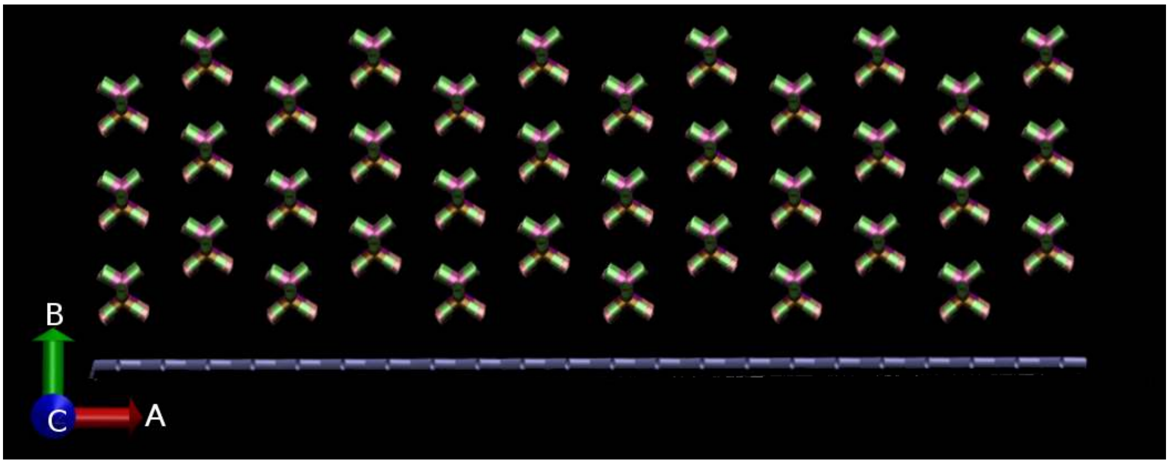

Fig. 6.1 Initial structure of the surface model. A: a-axis; B: b-axis; C: c-axis. Green: Hydrogen; Purple, Cyan: Carbon; Pink: Fluorine.

In the uncharged surface model, carbon atoms were neutral as neutral atoms without charges, and in the charged models different charges were selected to appreciate the trend on PVDF chains conformation with increasing charges. To maintain the overall system neutral in the case of charged graphene, a second layer of graphene was added with opposite charges magnitude increasing of 7 Å the b axis to accommodate the second layer and also a negative control with two uncharged graphene layers (the negative control) was computed to verify that the addition of the second graphene layer would not affect PVDF chains conformation significantly apart from adding electrostatics. The graphene charges chosen were three as Q: 0.025, 0.05 and 0.1 (elementary charge e) and deductively the second graphene sheet added to keep the overall system neutral brought charges of opposite magnitude (*e.g.* Q: -0.025, -0.05 and -0.1 of elementary charge e), these charge magnitudes were referred to the individual charge that every carbon atom of a graphene sheet possessed[161].

The magnitude of charges applied to the graphene sheet were based on the first principle study of gasses adsorption on a graphene sheet made by Leenaerts *et al*[161], since it was showed that charge screening increased significantly in magnitude on the graphene sheet as the polarity of the adsorbed gas was higher. As Leenaerts *et al*[161] correlated the gas molecule dipole to the charge screening magnitude occurring between the molecule and the graphene sheet and having PVDF a dipole of $\approx 6.672{\cdot}10^{-30}$ C m^{-1}[40] the three charges were chosen from fitting a low dipole moment of weak dipole molecules (*e.g.* CO_2 $0.734{\cdot}10^{-30}$ C m^{-1}) until covering the water polarity of $6{,}17{\cdot}10^{-30}$ C m^{-1} Debye which possesses a similar dipole than PVDF, although, this assumption is not strictly consistent it was assumed as fair for estimating the charges magnitude to apply to the graphene surface in the present study.

The vdW potential of PVDF chains interacting to each other has been kept as the original B&S FF using the Buckingham potential of equation 3.17 and the vdW potential for the PVDF/graphene interaction has been chosen to be the LJ potential of equation 3.30. The parameters for the mixed rules of the LJ potential were taken by the OPLS FF which was the only force field that used the LJ potential to account for vdW forces[28]. The LJ vdW potential is a very known and standardised potential for which well defined mixing rules[162, 28] allow to define mixed atomic species interactions for σ and ε parameters as showed in equations 6.1 and 6.2, respectively, which were used from Guryel *et al*[28]. Table 6.1 reported the mixed vdW parameters used for the LJ potential.

$$\sigma_{ij} = \sqrt{\sigma_{ii}\ \sigma_{jj}} \tag{6.1}$$

$$\varepsilon_{ij} = \sqrt{\varepsilon_{ii}\ \varepsilon_{jj}} \tag{6.2}$$

Table 6.1 OPLS Force Field vdW mixed parameters obtained using the mixing rules 6.1 and 6.2 to implement the LJ potential in the B&S FF. ε: kJ mol^{-1}; σ: Å;.

van der Waals		
Species	ε_v	σ
C_{F_2}-C_{sp^2}	0.3586	3.65
C_{F_3}-C_{sp^2}	0.3586	3.65
C_{H_2}-C_{sp^2}	0.3586	3.65
C_{H_3}-C_{sp^2}	0.3586	3.65
F-C_{sp^2}	0.2732	3.33
H-C_{sp^2}	0.1916	2.98
C_{sp^2}-C_{sp^2}	0.2929	3.55

The liquid phase equilibration was followed as detailed during the bulk study and with the awareness that surfaces generally slow down atoms kinetics and the liquid phase equilibration process[163, 51], the annealing temperature was chosen to be 1200 K and kept for 75 ns, then the cooling procedure with a temperature drop rate of 30 K ns^{-1} which brought the liquid phase at 500 K in 24 ns was applied and the system kept for 50 ns at the fixed temperature of

500 K, where the last 15 ns represented the liquid phase equilibrium of which the averaged properties were presented in this chapter. The initial crystalline model of PVDF oligomers sitting on a graphene sheet is represented in Figure 6.1.

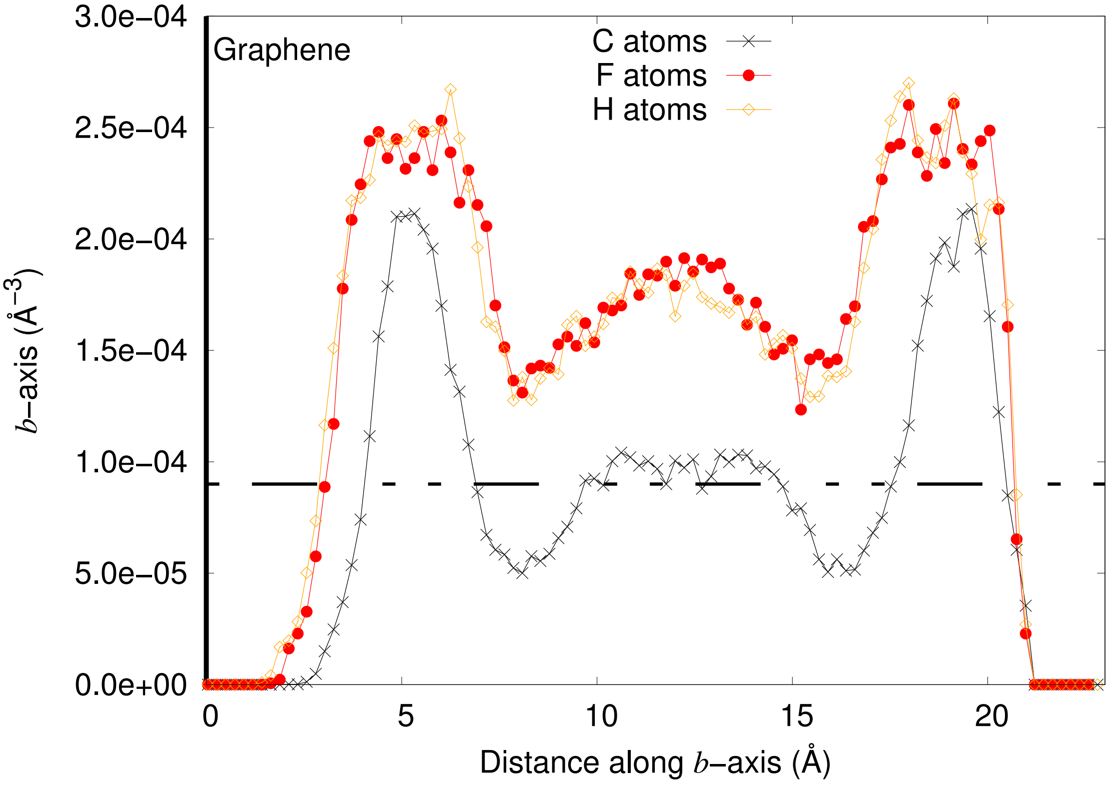

Fig. 6.2 Average atoms number distribution as function of space along the b-axis of the liquid phase at 500 K using the B&S FF. Surface: Graphene Surface Layer; 6.4 Å: regions of space where the surface augment the atom number concentration due to surface-polymer attraction. The dashed line represents the averaged atoms distribution sum of carbon, fluorine and hydrogen atoms of the liquid phase equilibrium of the bulk model at 500 K.

6.2 Surface nanoconfinement effect on β-phase formation with uncharged graphene

The liquid phase equilibrium of the surface model resulted to have a thickness of 23 Å along the surface b-axis (Std.: 0.64). The addition of the graphene sheet modestly increased system density as the liquid bulk model density was 1.4 g cm^{-3} while the liquid surface model reached a density of 1.5 g cm^{-3} (Std.: 0.05). Figure 6.2 reported the atoms density distribution of carbon, fluorine and hydrogen atoms at the liquid phase equilibrium of the surface model showing that atoms were strongly attracted within a range of 6.4 Å on both sides of the surface and the atom density distributions was symmetric along the *b*-axis as expected. The dashed line of Figure 6.2 represents the averaged atoms distribution of the bulk liquid phase where atoms dispersed homogeneously along the whole simulation box. All atom species of the surface model reported in Figure 6.2 distributed homogeneously along the *b*-axis which meant that the uncharged graphene sheet had no preference in attracting an atom species more than others.

Figures 6.3 and 6.4 reported the R_g and R_e properties (R_g: 6.2 Å Std.: 0.14 Å, R_e: 15.5 Å, Std.: 0.84 Å), respectively. The homogeneous PVDF oligomers coiled state showed in Figures 6.3 and 6.4, made clear that an uncharged graphene sheet was not influencing atoms and chains conformations if not for the stronger attraction within 6.4 Å on both surface sides which was anyway not selective on the atom species and between the liquid bulk model and the surface model with one uncharged graphene sheets the R_g and R_e properties showed to be rather equivalent.

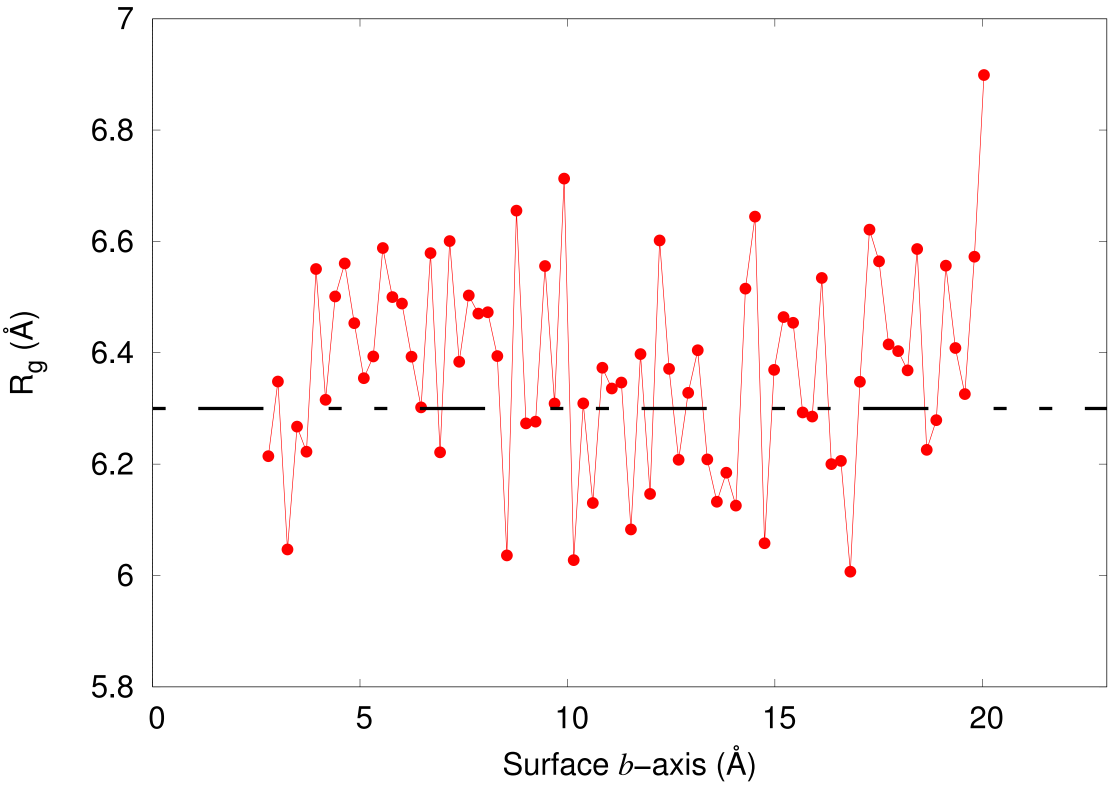

Fig. 6.3 PVDF chains averaged R_g distribution as function of space corresponding to the centre of mass of molecules calculated perpendicularly to the surface *b*-axis at 500 K using the B&S FF. The dashed line is the average R_g of the liquid bulk model at 500 K of Table 5.8.

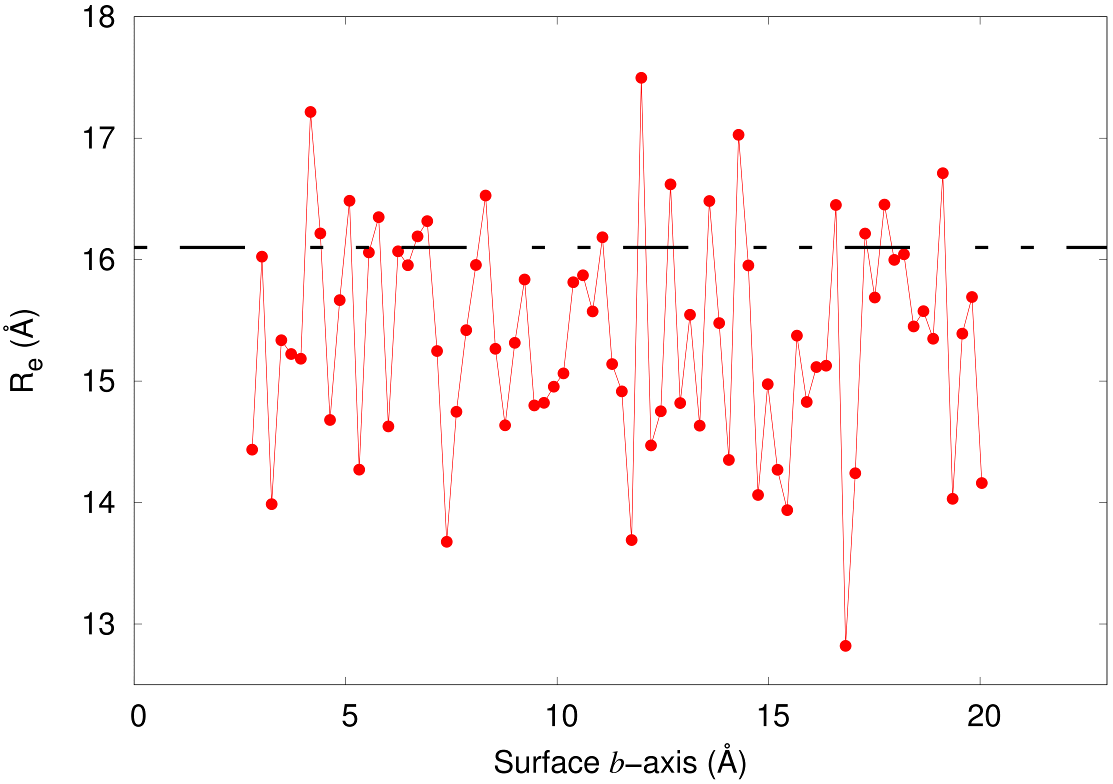

Fig. 6.4 PVDF chains averaged R_e distribution as function of space corresponding to the centre of mass of molecules calculated perpendicularly to the surface b-axis at 500 K using the B&S FF. The dashed line is the average R_e of the liquid bulk model at 500 K of Table 5.8.

The conformation tensor was in this case expressed as function of space slicing the simulation box in 5.75 Å layers along the b-axis as Table 6.2 reported. Table 6.2 showed that the C_{xx} and C_{zz} conformers were similar and diffusivity was not compromised by the surface since the graphene was positioned on the bottom of the b-axis. However, the C_{yy} conformer of Table 6.2 reported that along the b-axis atoms diffusivity was limited within the ≈2 nm of the modelled surface film as expected since the surface itself altered atoms conformations as generally observed by other authors[163, 51].

Table 6.2 Conformation tensor by diagonal elements as function of space from bottom to top of the b-axis for the liquid phase equilibrium of the PVDF surface model using the B&S FF.

	Layers (Å)			
	0-5.75	5.75-11.5	11.5-17.5	17.5-23
C_{xx}	1.472	1.599	1.693	1.399
C_{yy}	0.342	0.314	0.304	0.347
C_{zz}	1.440	1.287	1.210	1.482

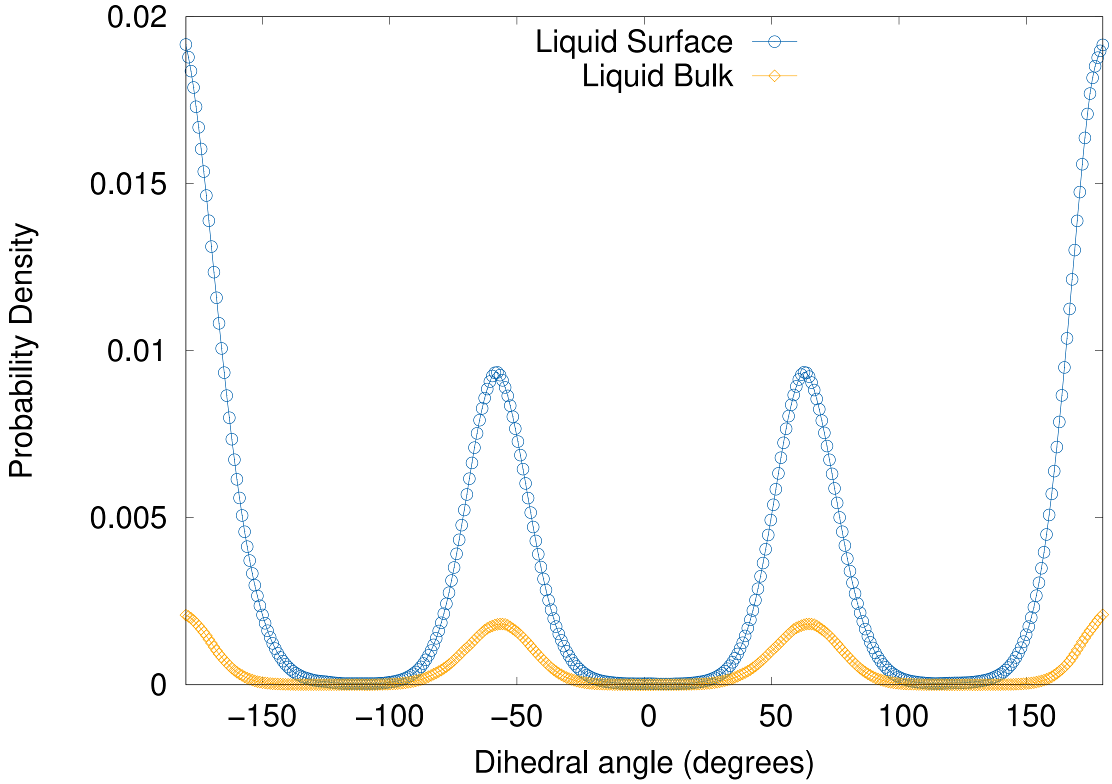

Fig. 6.5 Averaged dihedrals backbone distribution of the liquid PVDF surface model sandwiched in graphene sheets at 500 K using the B&S FF in comparison with the liquid bulk model at 500 K computed using B&S FF.

A conclusive evidence of the liquid phase properties of the uncharged graphene surface was the backbone dihedrals distribution which allowed to know the backbone chains conformations of PVDF oligomers assumed during the the finite temperatures dynamics of the thin film of PVDF between a graphene layer. As saw in the previous chapter for the bulk model reported in Figure 5.9, as far as the liquid phase was achieved the dihedral backbone distribution of PVDF chains became widely dispersed along 180° and ±60° meaning that no particular backbone conformations typical of any specific crystal structure persisted. In Figure 6.5 the dihedrals backbone distribution of the surface model in the final liquid phase equilibrium was reported and it was possible to appreciate that less broader peaks around 180° and ±60°, sign that indicated the surface changed the conformational degrees of freedom of PVDF backbone oligomers when the system was kept steady at 500 K.

The backbone dihedral distribution of the liquid phase equilibrium reported in Figure 6.5 showed that the ratio of 180° and ±60° was 2:1:1 as indicative of the α-phase backbone[111]. However, this was not verified by looking the trajectory image of Figure 6.6 which showed that PVDF oligomers were randomly dispersed without any structural similarity with the

α-phase and the R_g and R_e clearly evidenced that chains were coiled, hence, with no linear propagation of chains it is not possible to expect any crystal structure of PVDF. The current section of this result's chapter was concluded with the clear evidence that a plain uncharged graphene sheet which confined PVDF oligomers within 2 nanometers was not a promoting factor to enhance any crystalline phase formation.

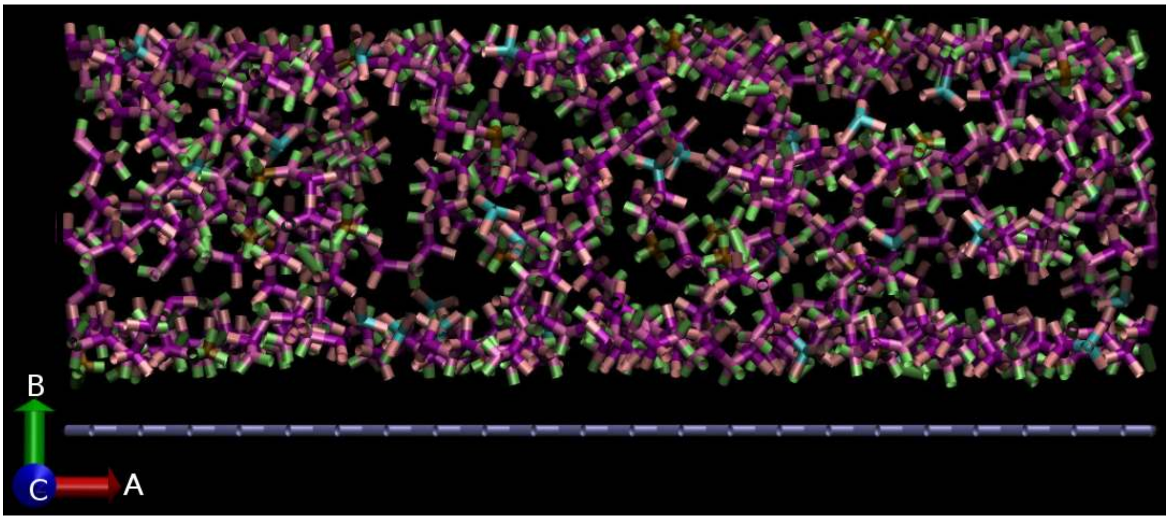

Fig. 6.6 Snapshot of the liquid phase at 500 K of the PVDF film on an uncharged graphene sheet using the B&S FF. Green: Hydrogen; Purple, Cyan: Carbon; Pink: Fluorine.

6.3 Surface electrostatics effects on β-phase formation

The evidence discussed showed that nanoconfinement was not a condition which promoted crystalline phase formation of PVDF, hence, the next hypothesis to be verified was the electrostatics surface effects on PVDF oligomers conformation. The electrostatics modelled in this study can be conceptually imagined as the poling procedure used to increase the ferroelectric crystals content in a PVDF sample. As an applied electric potential induces charge separation on the two edges of an insulator, resident electrostatics can to some extent mimic such polar state on a surface which would affect PVDF side chain atoms conformation. The study of electrostatics surface effects on PVDF oligomers represented the conclusive stage of this thesis.

The procedure was not started from scratch as the liquid phase equilibrium of the surface model was already reached with the study of the uncharged graphene sheet discussed in section 6.2. The atomic coordinates of the last trajectory snapshot of the uncharged surface model were taken and the graphene sheet charges were modified also adding the second graphene layer in the simulation box with opposite charges in respect to the first layer. This section shows the results from the four computed replicas with two graphene layers which in one case there were no charges on both graphene sheets (the negative control), while in the other three cases three different charges were applied as discussed in the surface model section 6.1 and resumed in Table 6.3. The negative control is formerly similar to the surface model with one uncharged graphene sheet, however, it has been considered to estimate if a second uncharged graphene sheet could already alter PVDF chains conformations, although, no charges were applied to both graphene sheet, hence, the definition of negative control.

Table 6.3 Statistics of the computed surface model using B&S FF, which have been perpetuated after the liquid phase equilibrium with the modification of charges from having two neutrally charged graphene sheets up to two graphene sheets with opposite charges magnitude to preserve system neutrality. A: Neutrally charged graphene sheets; B: Q=±0.025 charged graphene sheets; C: Q=±0.05 charged graphene sheets; D: Q=±0.1 charged graphene sheets; Std.: Standard deviation.

	A	B	C	D
Charge (*e*)	0.0	±0.025	±0.05	±0.1
b-axis thickness (initial) (Å)	30.0	30.0	30.0	30.0
b-axis thickness (equilibrium) (Å)	28.0	23.0	20.5	19.3
b-axis thickness (equilibrium) Std.	0.24	0.19	0.14	0.13
Density ($g\ cm^{-3}$)	1.58	1.73	1.89	2.01
Density Std. ($g\ cm^{-3}$)	0.02	0.01	0.01	0.01
R_e (Å)	17.14	24.01	32.12	31.43
R_e Std.	0.51	0.44	0.12	0.06
R_g (Å)	6.53	7.90	10.69	11.21
R_g Std.	0.13	0.08	0.01	0.01
Conformation tensor by diagonal elements				
C_{xx}	1.457	0.257	0.002	0.002
C_{yy}	0.198	0.020	0.123	0.228
C_{zz}	1.611	2.769	2.876	2.772

Table 6.3 reported that the film thickness on the *b*-axis was reduced with the increase of charges on the two graphene sheets with a reduction of ≈9 Å from the negative control to the highest charges applied on the two graphene sheets. The density increase in function of higher charges on the graphene sheets was found to correlate with the *b*-axis length reduction as reported in Table 6.3. In the negative control the density was 1.6 g cm^{-3} which remained similar to the density of the surface model with one uncharged graphene sheet which was 1.5 g cm^{-3}, while with the graphene sheets charged at Q of 0.1 (*e*) the density was found to be 2.01 g cm^{-3} which was near to the bulk density of the optimised geometry at 0 K of the β

crystal which was 2.08 g cm^{-3} as reported in Table 5.6. Such density increase indicated a strong effect of charges in attracting PVDF oligomers.

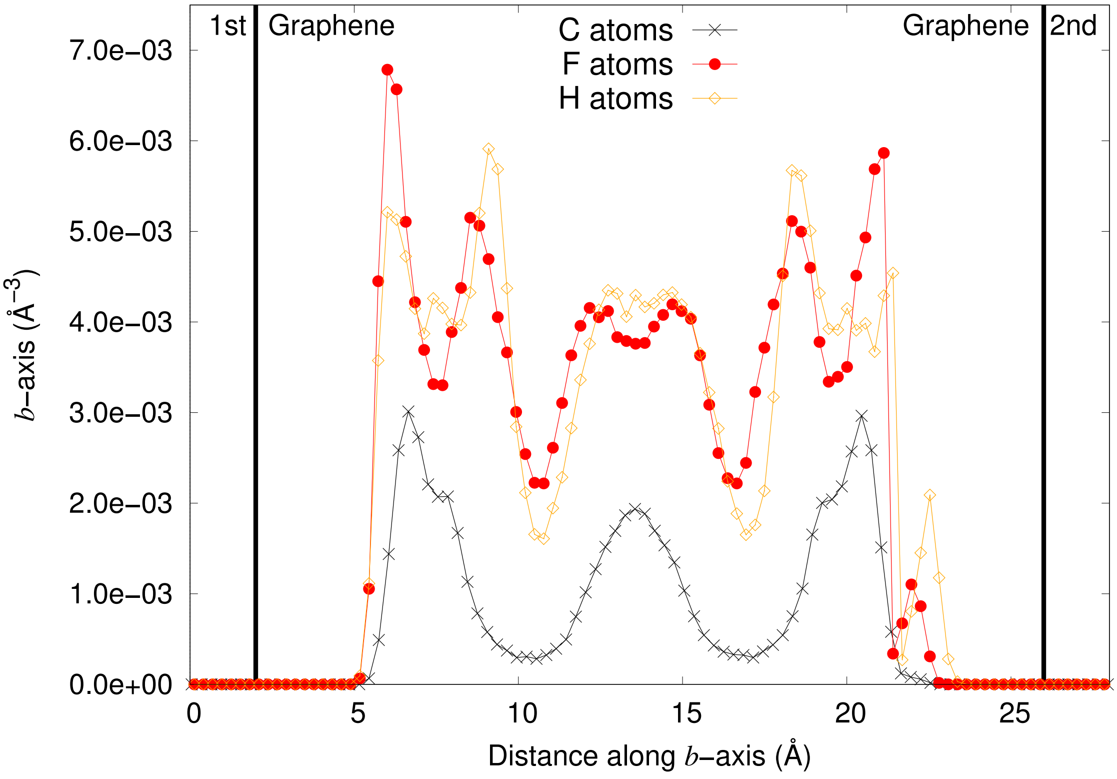

Fig. 6.7 Atoms distribution as function of space on the surface b-axis of the computed replica having two graphene sheets with Q: 0 using the B&S FF.

The observation of atoms distribution as function of distance from the graphene sheet surface (referenced from the bottom of the simulation box to the top on the b-axis) showed interesting results as different atomic species dispersed differently in space with a growing distinct atom species layering as the surface were higher. Figures 6.7, 6.10, 6.11 and 6.12 reported the atoms distribution as function of space along the b-axis of the four computed replicas with Q: 0, 0.025, 0.05 and 0.1, respectively. Figure 6.7 reported the atom distribution of the negative control (no charges on the two graphene sheets) which appeared similar to the atoms distribution of Figure 6.2, characteristic of an amorphous melt of PVDF oligomers where all atoms were dispersed homogeneously along the whole simulation box as the uncharged graphene sheets did not showed preference in attracting any atom species more than others.

A remarkable difference between Figures 6.7 and 6.2 which both showed atoms distribution of the liquid surface models along the surface b-axis was that in Figure 6.2 (surface

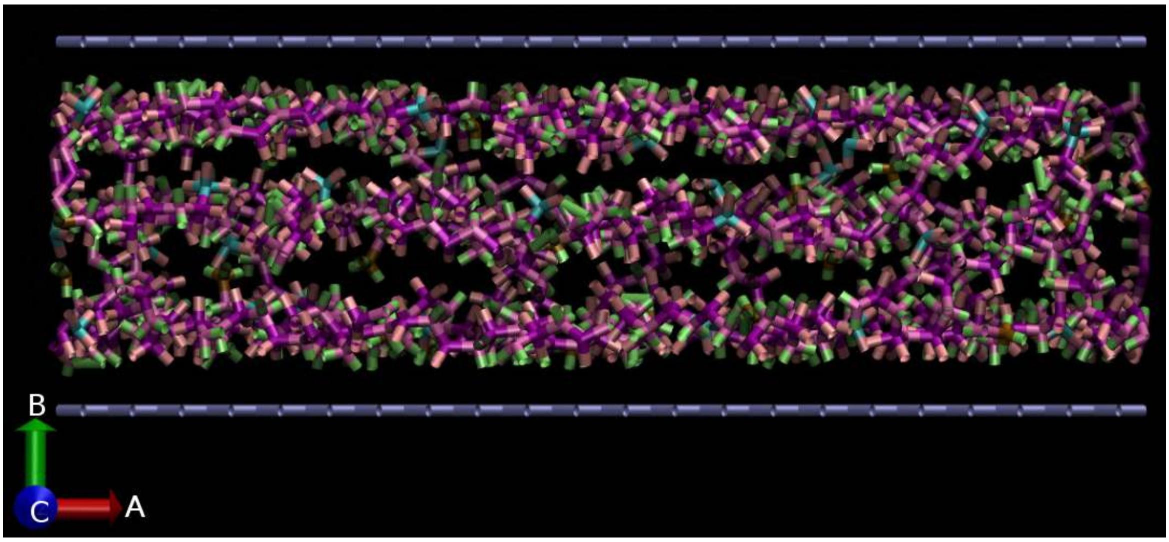

Fig. 6.8 Trajectory snapshot side view of the computed replica with Q: 0 at the liquid phase equilibrium showing a generally disordered state of PVDF oligomers. Green: Hydrogen; Purple, Cyan: Carbon; Pink: Fluorine.

model with one neutral graphene sheet) all atoms species were distributed along the *b*-axis with almost identical density profiles while in Figure 6.7 hydrogen and fluorine atoms separated in two peaks per every carbon atoms peak (especially visible on the first and last PVDF layers), which was attributed to the increased density of the system and to the layer stratification more consistent in the surface model with two neutral graphene sheets of Figure 6.7. Indeed, in Figure 6.6 the simulation snapshot showed an amorphous liquid phase with no clear PVDF layer stratification (surface model with one neutral graphene sheet), while in Figures 6.8 and 6.9, which shows side and top view, respectively, of the amorphous liquid phase of the surface model with two uncharged graphene sheets showed a distinct PVDF layer stratification with coiled chains having random conformations that made fluorine and hydrogen atoms to disperse less homogeneously along the *b*-axis.

Progressively, Figures 6.10, 6.11 and 6.12 which reported the atoms distribution as function of space along the *b*-axis of the three charged replicas, showed a more distinct separation of atom species distribution peaks as the surface charges were increased, meaning that a higher surface charge made the surface to repel strongly the incompatible charged atom species and attracting more intensely the compatible charged atom species, as distinctive sign of PVDF chains order.

In Figures 6.10, 6.11 and 6.12, all atomic species were grouped in three layered peaks per each atom species, as meaning that there were only three layers of chains deposited on the graphene surface. Although, the crystal model was build in a 6 × 6 chains frame, after the model became liquid and fully disordered, the surface charges restored crystallinity

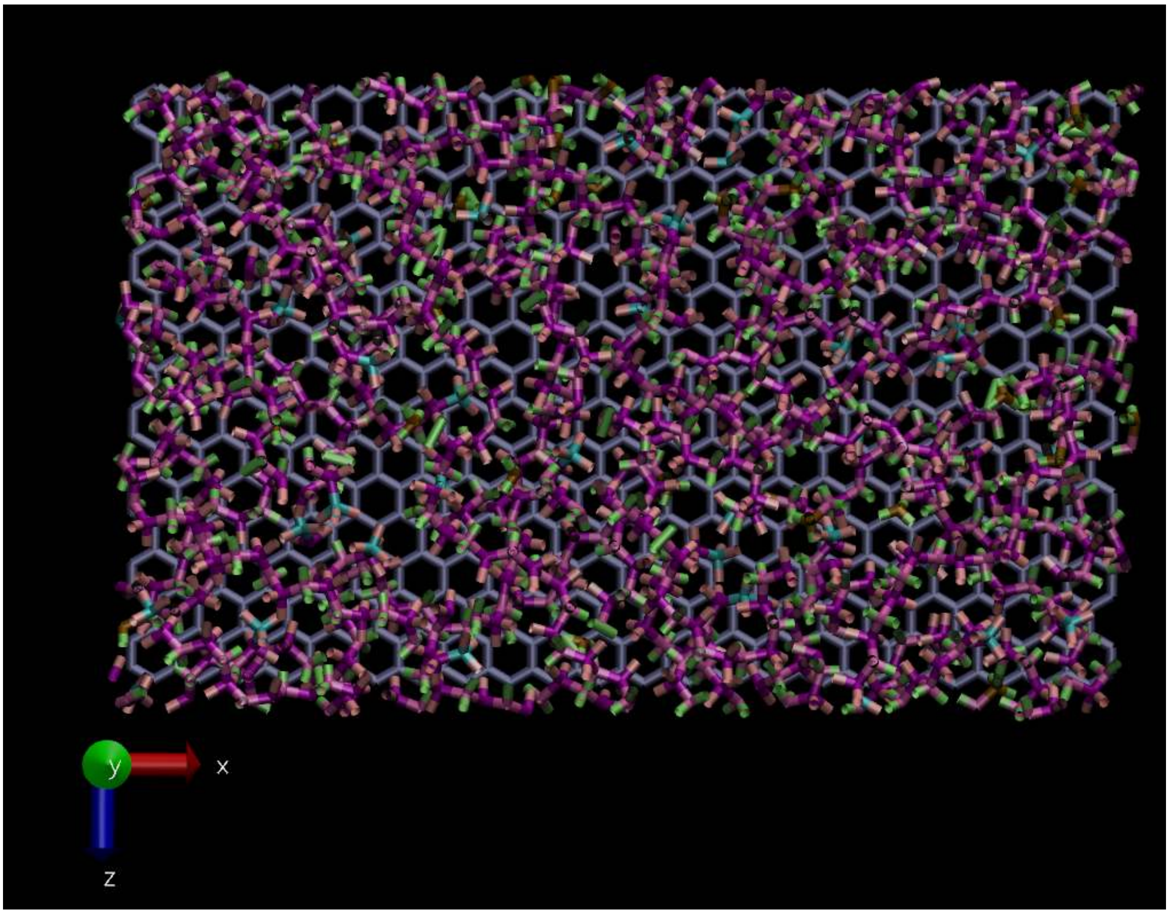

Fig. 6.9 Trajectory snapshot top view of the computed replica with Q: 0 at the liquid phase equilibrium showing a generally disordered state of PVDF oligomers. Green: Hydrogen; Purple, Cyan: Carbon; Pink: Fluorine.

but without restoring the 6 layers which would be the distinctive geometry of the β-phase. Figures 6.8, 6.13, 6.15 and 6.17 showed the PVDF chains conformation were influences by the graphene surface charges, as higher were the surface charges and more ordered were the PVDF oligomers sitting on the surface became (see Figures 6.9, 6.14, 6.16 and 6.18 for respective top view of the simulation trajectories snapshots). By looking at the trajectory snapshots, the computed models which have two graphene sheets with charges of 0.1 e, the PVDF oligomers appeared to have the distinctive β-phase shape rich in trans bonds. Although, the original β-PVDF geometry was not restored, PVDF oligomers deposited nearer to each others forming three layers of PVDF chains with a backbone conformations fully made of trans bonds maximising the number of compatible charged atoms in contact with the surface as Figure 6.17 showed.

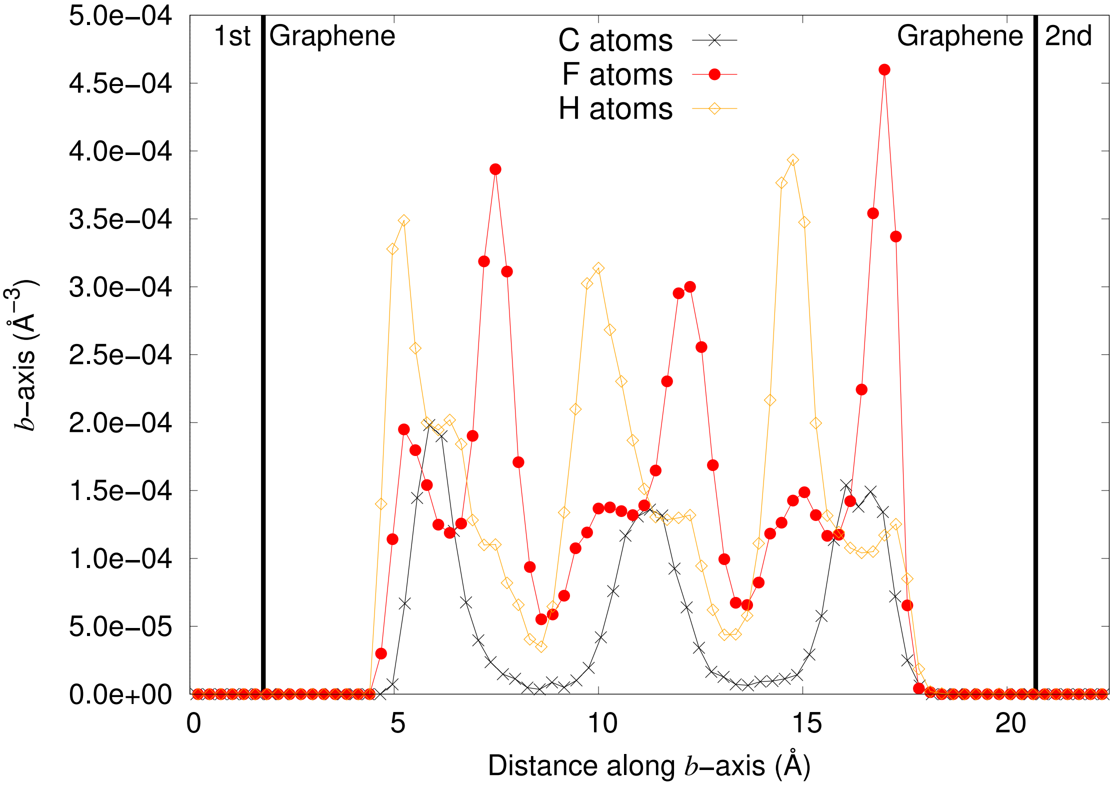

Fig. 6.10 Atoms distribution as function of space on the surface *b*-axis of the computed replica having two graphene sheets with Q: 0.025 using the B&S FF.

It was also noticed that between Figures 6.10, 6.11 and 6.12 there was a growing trend where fluorine atoms were more attracted by the second graphene layer than the first layer with higher and narrower peaks as the graphene sheets charges were higher. Such trend was attributed to the affinity of fluorine atoms charges (negatively charged) for the second graphene layer (positively charged) being higher than the first layer (negatively charged). Indeed, in Figures 6.10, 6.11 and 6.12 it became clear that the first graphene layer (negatively charged) showed affinity in attracting hydrogen atoms (positively charged and represented with yellow lines in each Figure) and the second graphene layer (positively charged) in attracting fluorine atoms (negatively charged and represented with red lines in each Figure). As in the B&S FF the fluorine atoms brought significantly higher charges than hydrogen atoms (see Table 3.5), the attraction on the second graphene layer resulted to be stronger, making fluorine atoms to compact tighter near to the second charged graphene sheet. The fluorine atoms are bonded to the backbone carbon atoms which also possess hydrogen atoms and the fluorine atoms attraction manifested with bigger peaks near to the second graphene sheet showed to alter the ditribution of the whole last PVDF chains layer as reported in

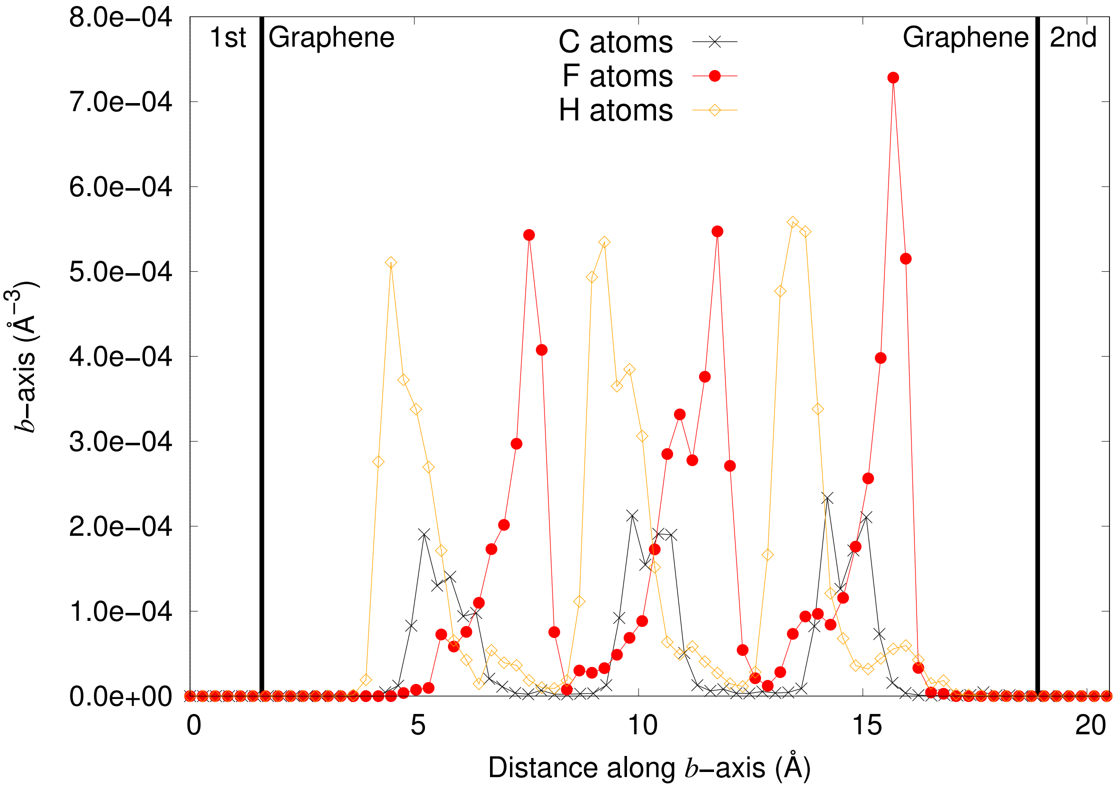

Fig. 6.11 Atoms distribution as function of space on the surface *b*-axis of the computed replicas having two graphene sheets with Q: 0.05 using the B&S FF.

Figures 6.10, 6.11 and 6.12 (effect visible especially on side chain atoms for the surface model with two graphene sheets charged at 0.1 *e* of Figure 6.12).

Table 6.3 also reported the R_g and R_e properties of the liquid phase of the four computed replicas with two graphene sheets. In Table 6.3 it was evinced that the application of charges played an important role on the PVDF chains conformation properties, indeed, R_g and R_e increased as the graphene sheets charges grown from a Q of 0 to 0.1 (elementary charges *e*). At Q of 0 the system properties resembled the averaged properties of the equilibrated liquid surface model with only one neutral graphene sheet as reported in Table 5.8 and Figures 6.8 and 6.9 (side and top vies respectively) verified the amorphous state of the surface model with two uncharged graphene sheets (the negative control). For the surface models with two charged graphene sheets Table 6.3 showed that the R_g and R_e properties increased with higher charges present on the graphene sheets, meaning that chains were becoming more linear as the graphene sheets charges were higher. Indeed, the initial crystalline surface model showed to have the R_g and R_e properties of 9.05 Å and 29.78 Å (Table 5.6), respectively. In Table 6.3 for the case of having the graphene sheets charges set at Q 0.05 *e* and 0.1 *e*, the R_g

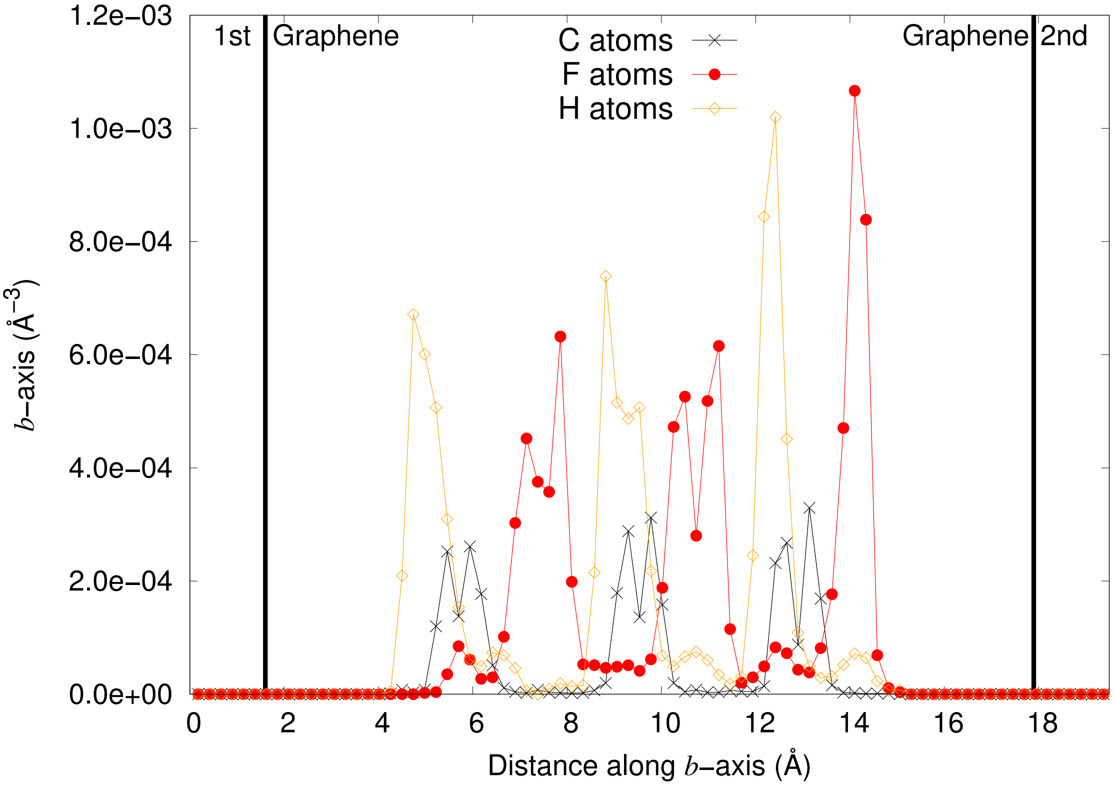

Fig. 6.12 Atoms distribution as function of space on the surface *b*-axis of the computed replica having two graphene sheets with Q: 0.1 using the B&S FF.

and R_e became bigger than the original crystalline properties of Table 5.6 indicating that the charges on the graphene sheets induced PVDF oligomers to a modest chains stretch due to the maximisation of charge screening between the graphene sheets and the PVDF side chain atoms.

The conformation tensor comparison between Tables 5.8 and 6.3 also evidenced how the presence of charges significantly limited chains mobility and atoms diffusivity as the values of the C_{xx}, C_{yy} and C_{zz} conformers significantly deviated from one. Also in this case the averaged properties of the liquid phase equilibrium of four computed replica with two graphene sheets became independent by time and by starting from the same initial liquid phase configuration, the different magnitude of charges applied on the graphene sheets allowed to reach new and different averaged properties independent by time as reported in Table 6.3 and Figure A.27 (Figure A.27 shows density as function of time of the four computed replica).

Moreover, the dihedral backbone distribution also agreed that the surface charges significantly affected the PVDF oligomers backbone conformation. Indeed, Figure 6.19 reported

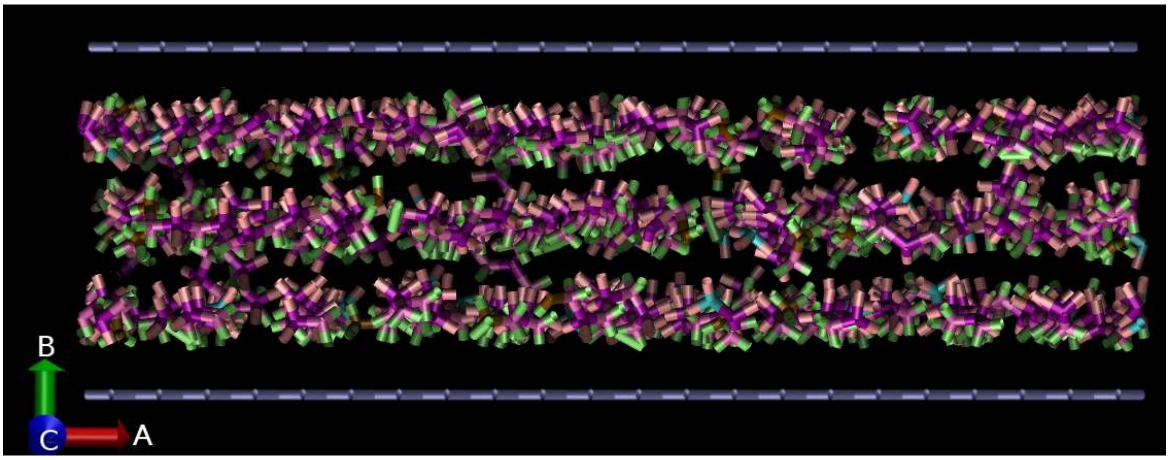

Fig. 6.13 Representative trajectory image side view of the computed replica with Q: 0.025 showing PVDF oligomers assuming the β-phase chains conformation on a charged graphene surface. Green: Hydrogen; Purple, Cyan: Carbon; Pink: Fluorine.

the dihedral distribution of the four computed replicas with charged graphene sheets and the negative control. The dihedral distribution of the negative control showed a dihedral distribution of trans and gauche bonds almost as 1:1:1 in Figure 6.19, a distribution even more random than what was observed in Figure 6.5 for the surface model with one neutral graphene sheet, as indicating that the addition of the second graphene sheet without any charge broke the modest effect in affecting the dihedrals distribution observed in the case of one neutral graphene sheet.

Visibly in Figure 6.19, as the surface charge increased, the gauche dihedrals diminished almost to zero in favour of the trans dihedrals (*e.g.* 180°), meaning that the PVDF oligomers conformation were mainly made of β chains and as Figure 6.17 confirmed, in fact, surface electrostatics made PVDF chains to become almost completely crystalline especially when the surface charge was set to Q: 0.1. As discussed in the previous chapter, the dihedrals backbone distribution could not be retained sufficient as a standalone proof that PVDF oligomers reached a backbone conformation characteristic of the β-phase. However, together the atom density distribution as function of space and the averaged properties of R_g and R_e as discussed previously, it became evident that PVDF oligomers backbone became linear due to the charges present on the two graphene sheets and all these evidences together demonstrated that charges played a major role in restoring PVDF oligomers chains order and Figure 6.17 strengthen such observations showing completely linear chains in the computed replica which had graphene sheets charged at 0.1 *e* (the two graphene sheets had same charged magnitude of opposite sign).

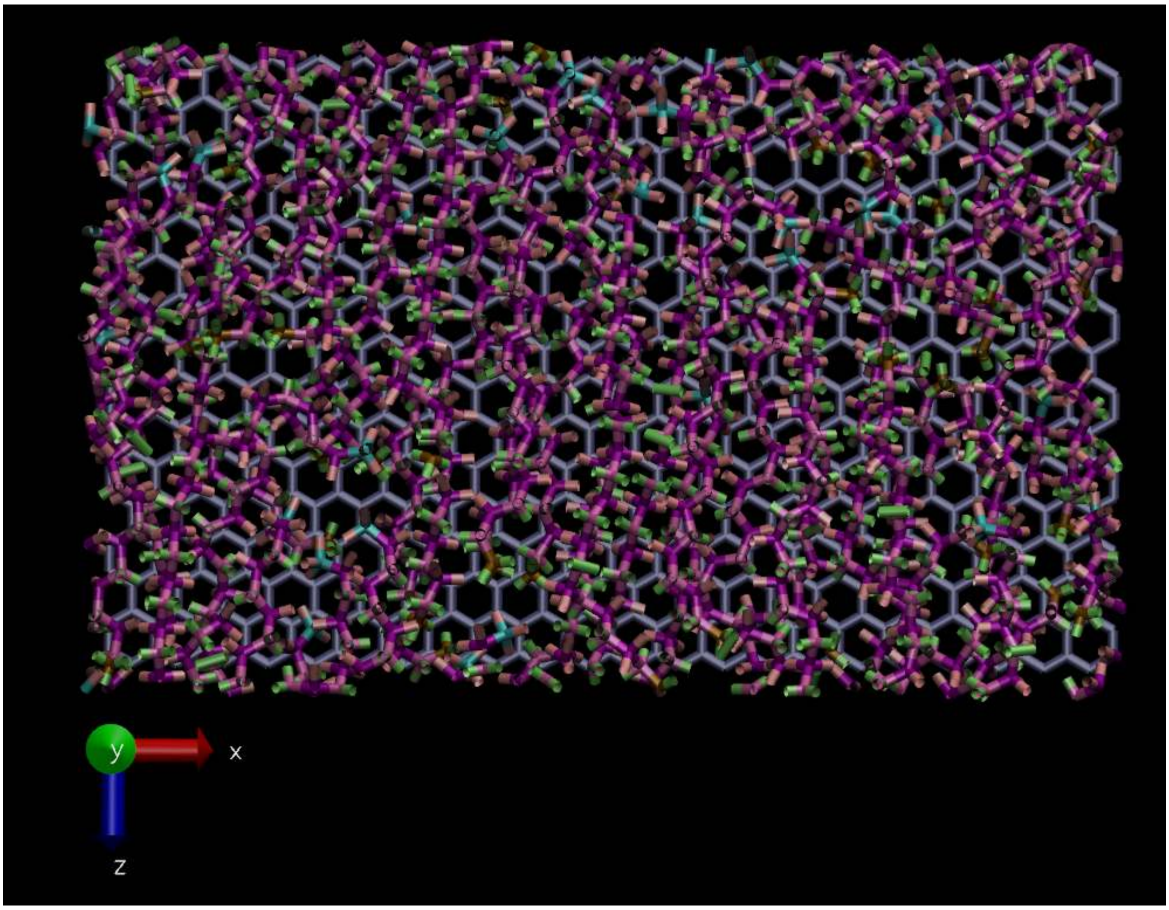

Fig. 6.14 Representative trajectory image top view of the computed replica with Q: 0.025 showing PVDF oligomers assuming the β-phase chains conformation on a charged graphene surface. Green: Hydrogen; Purple, Cyan: Carbon; Pink: Fluorine.

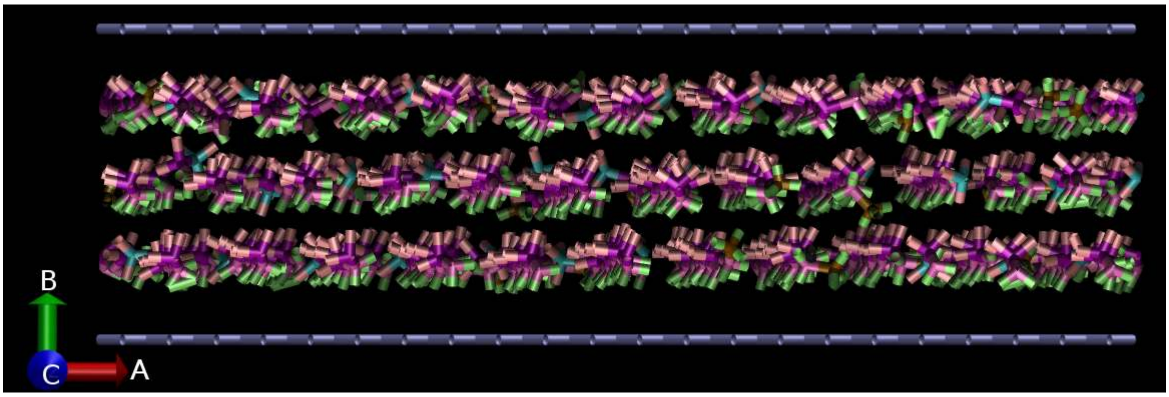

Fig. 6.15 Representative trajectory image side view of the computed replica with Q: 0.05 showing PVDF oligomers assuming the β-phase chains conformation on a charged graphene surface. Green: Hydrogen; Purple, Cyan: Carbon; Pink: Fluorine.

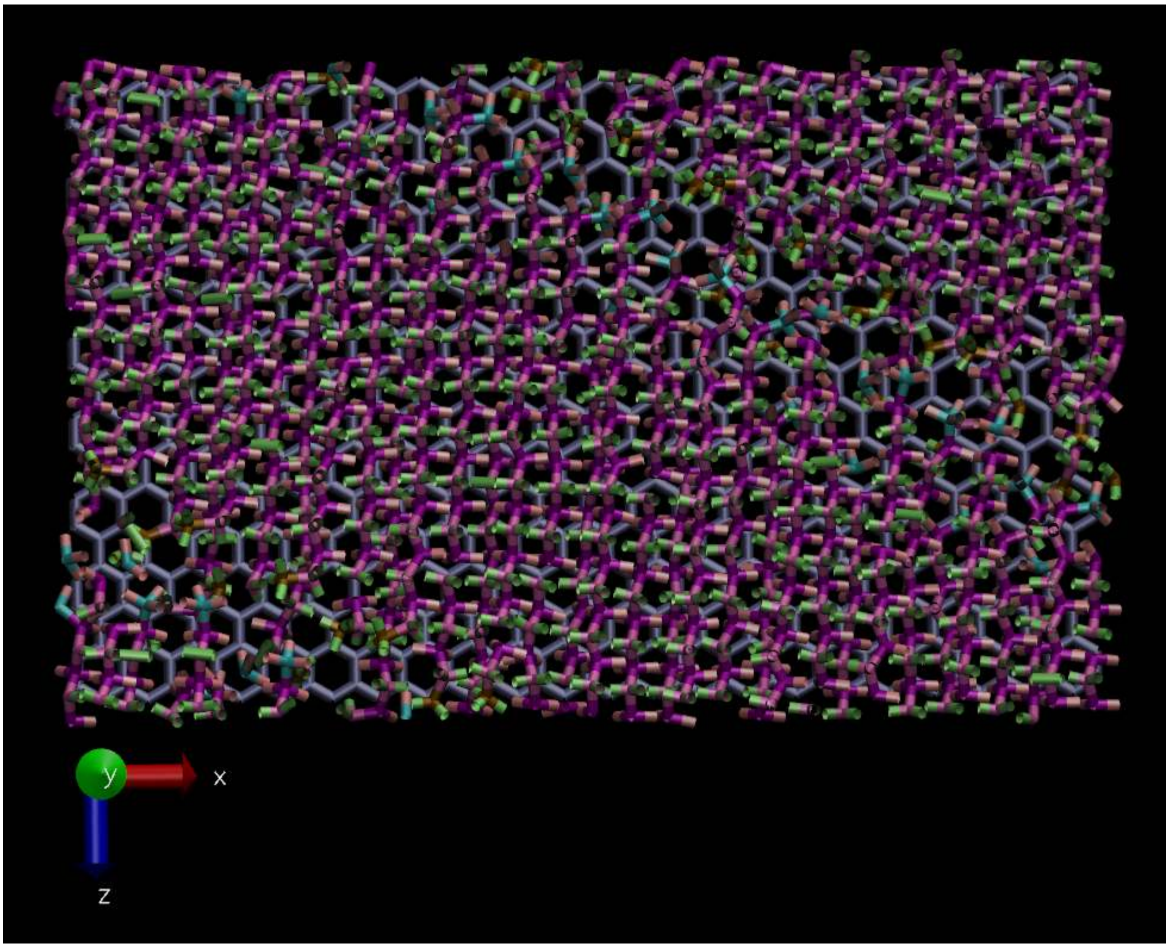

Fig. 6.16 Representative trajectory image top view of the computed replica with Q: 0.05 showing PVDF oligomers assuming the β-phase chains conformation on a charged graphene surface. Green: Hydrogen; Purple, Cyan: Carbon; Pink: Fluorine.

This evidence allowed to appreciate that the negative control of two uncharged graphene sheets was not generating crystalline artifacts, therefore, the charges on the graphene sheets really made the difference in restoring the β chains conformation. The effect of charges appeared indeed to be effective in restoring crystallinity out of an amorphous liquid phase equilibrium proportionally with the increase of charges as showed in Figure 6.19 which reported the increase of trans bonds as the surface charges were higher, where in the case of the graphene layers having carbon atoms charged at Q of 0.1 almost only trans bonds were found. The averaged properties finite temperatures dynamics of the liquid phase equilibrium of the surface model with two charged graphene sheets provided solid evidences that surface electrostatics was what influenced the β chains conformation to form out of an initially amorphous liquid phase of PVDF oligomers.

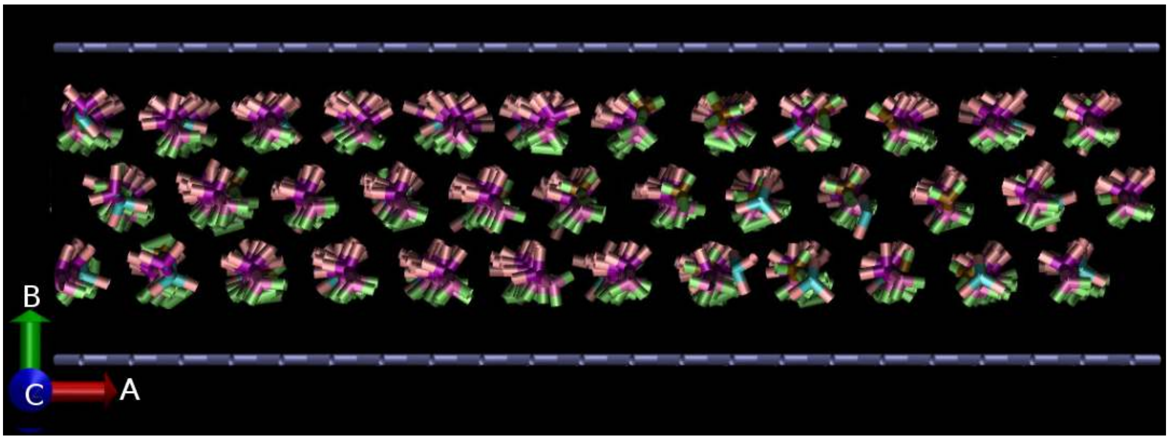

Fig. 6.17 Representative trajectory image side view of the computed replica with Q: 0.1 showing PVDF oligomers assuming the β-phase chains conformation on a charged graphene surface. Green: Hydrogen; Purple, Cyan: Carbon; Pink: Fluorine.

6.4 Summary

Results of the B&S FF described the surface model with encouraging results since it appeared clearly that the nanoconfinement was not a crucial surface to polymer interaction which enhanced PVDF oligomers conformation in favour of any crystalline geometry. Furthermore, it was observed that surface electrostatics played an effect on PVDF oligomers conformation bringing an amorphous liquid phase of coiled chains to be linear and highly organised similarly as the β-phase. In conclusion, it was the charges presence which made the surface able to interact with PVDF side chain atoms charges which promoted the crystalline formation of ordered and linear chains as only the β-phase could be. Indeed, a full trans backbone chain is the only chain conformation that displays all hydrogen atoms on one side of the chain and all fluorine atoms on the other side of the chain, the only geometry which maximises the charges of PVDF side chain atoms to interact compatibly with the graphene surface charges.

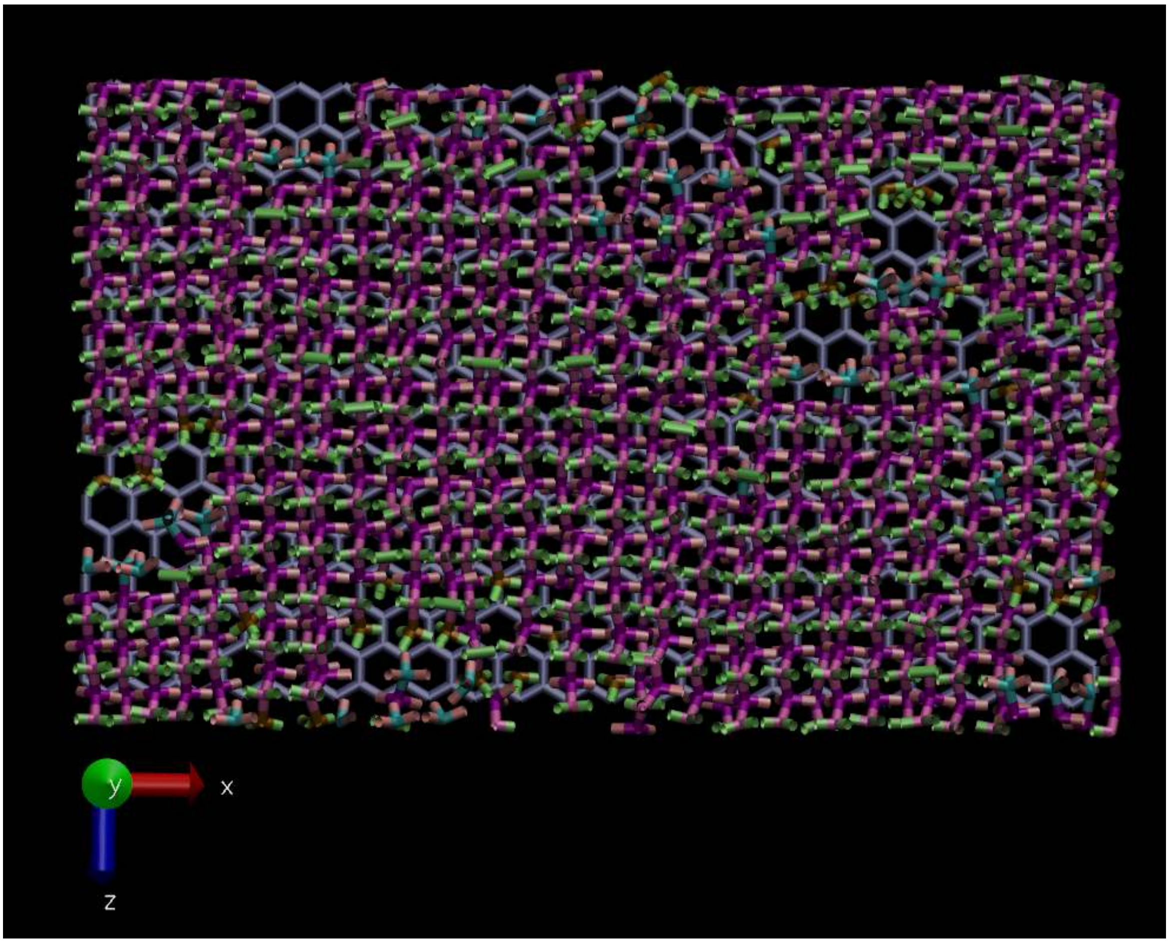

Fig. 6.18 Representative trajectory image top view of the computed replica with Q: 0.1 showing PVDF oligomers assuming the β-phase chains conformation on a charged graphene surface. Green: Hydrogen; Purple, Cyan: Carbon; Pink: Fluorine.

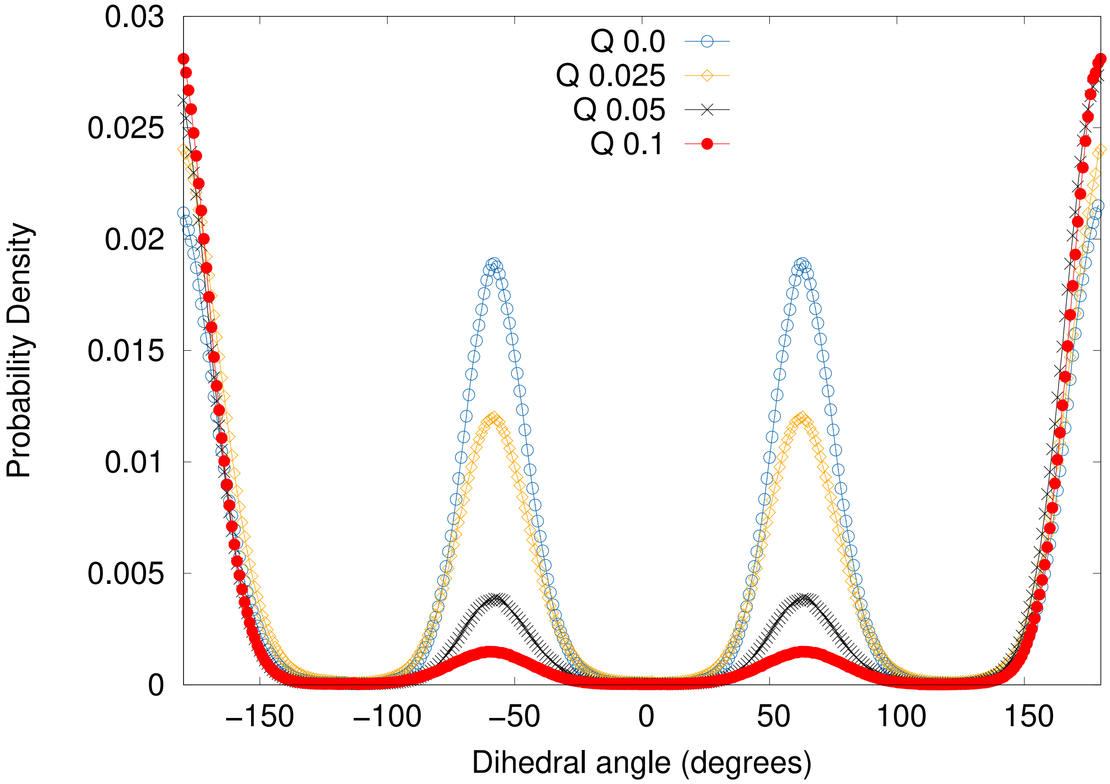

Fig. 6.19 Dihedral distribution of the last 15 ns of the liquid phase equilibrium at 500 K of the four computed replica with two graphene sheets bringing different charges using the B&S FF.

Chapter 7

Conclusions

The present research project saw at the beginning a vast incomplete literature knowledge about PVDF crystal polymorphs and the understanding of what surface property is necessary to control during PVDF samples manufacturing to increase the β-phase crystalline content. The aims of the present study were based on studying PVDF crystal properties with DFT completing the missing knowledge from literature and calculating the dynamical properties of PVDF liquid phase bulk and surface systems to understand which property of a surface drives the nucleation of the β-PVDF. The DFT study found satisfactory outcomes as the main XC-f available at the time of the computational investigation have been tested to find the best XC-f for predicting polymers properties. The vdW-DF functional resulted to be the functional more suited to predict the properties of PVDF as observed in experiments. The physical properties of PVDF investigated with the vdW-DF resulted to be the most consistent between the prediction of lattice structures, energetics, spontaneous polarisation and vibrational frequencies of PVDF crystals in comparison with experimental evidences.

In the DFT study it emerged that lattice structures well agreed with experimental observations, the spontaneous polarisation of the β-PVDF is in good agreement with recent experimental observations, and the vibrational frequencies of PVDF crystals found less agreement with previous computations and experimental observations, since previous authors computed with lower convergence thresholds the lattice structure used to calculate phonons, hence, discrepancies of wavelengths peak have been attributed to such lower DFT accuracy due to low convergence thresholds. The comparison with previous experimental observations and the present characterisation of the vibrational frequencies of the PVDF crystals remained in the range of accuracy between DFT and experiments as in experiments impurities, structural defects and amorphous regions of the sample alter the accuracy of experimental IR spectra[3] and fluctuations of 40-80 cm^{-1} in observed and computed peaks are considered normal.

The novelty of the present study allowed to determine that the ζ-phase is the sixth metastable PVDF crystal structure, which implies that how the β-phase crystalline content of a PVDF sample is addressed experimentally can not be based any more on the trans bond content of the sample since there two crystal structures of PVDF having a full trans backbone. Moreover, the ζ-phase also explain the discrepancies by the crystalline grade estimated with FTIR spectra and the spontaneous polarisation observed from such sample (a 100% crystalline β-phase defect free should have the same spontaneous polarisation of the DFT prediction). It has been proven that per each FE crystal, it exists a non FE crystal sharing the same backbone structure. Furthermore, the high rigour of the present study allowed to address that per the $T_3G^+T_3G^-$ backbone there are not only 2 crystals, of which one is expected to be FE and the other non FE, but per each crystal there are two distinguishable structural variants expanding to 8 the number of PVDF polymorphs. The present study saw a complete investigation of PVDF crystal matured in 8 crystals such as the α, β, δ, γ_{uu}, γ_{ud}, ε_{uu}, ε_{ud} and ζ phases.

The predicted geometries of PVDF crystals using different FFs resulted to be consistent with the present DFT study and previous experimental observations. The phase and cohesive energies of PVDF crystals predicted with MD resulted to be inconsistent between different FFs and also compared to the present DFT computations. Indeed, the MD study on PVDF found some weak point as it emerged that the FF development for describing PVDF accordingly to experiments is still missing. The MSSX FF resulted to be a difficult FF to implement in modern MD codes such as LAMMPS and such FF showed the inability of describing liquid phase properties of PVDF. The OPLS FF was a more modern and generalised FF which resulted to not describe liquid phase properties of PVDF accordingly to experiments. Indeed, both MSXX and OPLS failed to reach the liquid phase equilibrium of bulk PVDF models, furthermore, the OPLS FF even showed to produce crystalline artefacts in bulk systems recovering crystallinity of PVDF chains melted using the B&S FF. The B&S FF succeeded in reaching the liquid phase equilibrium of the PVDF bulk model, however, it has been necessary to simulated short PVDF chains of 12 monomers each to make the FF able to predict the liquid phase properties accordingly to experiments. This lacks of consistency underlines that it is necessary to keep developing the B&S FF to reach a more consistent FF able to predict the liquid phase properties of long or infinite PVDF chains are more consistent with real PVDF chain lengths.

The COMPASS FF was available from literature but not used in the present study since it was necessary to reduce the amount of work to remain suitable for the time available in the project. Moreover, COMPASS was not considered of main interest since it is a generalised FF for MD simulations, hence, not specific for PVDF as OPLS was. The OPLS FF was kept in the project since there was surface literature work available studying PVDF while for COMPASS only bulk studies were performed, and using two generalised FFs was considered out of scope for the present project. The most important investigation of understanding the surface effects on PVDF chains to find the surface/polymer interaction that promotes the β-PVDF nucleation has been conducted using the B&S FF, although, it resulted to be not perfect, it was still the most reliable FF to study liquid phase properties of PVDF.

Using the B&S FF to reach the liquid phase equilibrium of the bulk model, such properties were and intended to be compared with the liquid phase properties of the surface models, to underline structural properties modification depending on the conditions simulated. In merit to the surface model, two interaction mechanisms were investigated, where in the first case the nanoconfinement was the putative effect to be verified as a plausible FE crystals nucleation enhancer. To examine such hypothesis, one neutral graphene sheet sandwiched PVDF chains within 23 Å and results showed that no crystal geometries were formed out from a liquid phase of PVDF confined within a neutral graphene sandwich. The second hypothesis was to determine the surface electrostatics effects on the FE crystalline formation out of a liquid phase of PVDF short chains. In such case a graphene sandwich with two oppositely charged graphene sheets (one sheet on the bottom of the surface b-axis and the other on the top) were used to keep the overall system neutral offering to PVDF side chain atoms electrostatics surface charges to interact with, remarkably, surface electrostatics are a surface phenomena which is usually present found on material edges, however, the entity of the electrostatics charges needed to enchance the β-phase nucleation were unknown, as well as it was unknown if the surface electrostatics were a dominant interaction for driving the formation of β-crystals.

In the case of two charged graphene sheets it was concluded that electrostatics played a role in the formation of linearised β-like PVDF chains with a side atoms displacement typical of the β-phase. Therefore, within such study it has been discovered that the interaction surface mechanism which promotes the formation of the FE β-phase was the electrostatics interaction of the surface with the charges of PVDF side chain atoms. Previously than the present study, the real mechanism able to promote the β-phase formation was unclear as different authors proposed different mechanisms, not directly verified with proof of concepts, but only supported by observing that certain conditions promoted the β-phase formation with different efficacies, without determining the real nature of the FE nucleation enhancer. Within this study it has been possible to determine that the surface electrostatics are the surface/polymer interaction mechanism which promotes the β-PVDF nucleation making the β-phase conformation the most preferred in interacting with a charged surface. The present study provided precious knowledge about gaining control of the PVDF crystal phase formation, as depositing PVDF chains on a surface with appropriate electrostatics charges does enhance crystalline formation of the β-phase.

7.1 Future work

The present research project needed an extensive testing of DFT XC-fs and MD FFs to find the best computational set ups for calculating the properties of PVDF at the quantum and classical mechanics level. This however, reduced the amount of time possible to be spent on simulating more complex and large systems. Indeed, an interesting future work would be to extend the DFT study observing how the electron charge density of PVDF chains does change when in contact with a surface. Designing materials to reverse engineering in the materials the properties needed to enhance the β-PVDF crystallinity. The same study remains of interest when using MD although the level of theory would be different, both approaches should be used for completeness of the study.

Moreover when using MD, several aspects were neglected in the present computational study for lack of time. Indeed, the system computed with MD were rather small to keep the computational cost of the simulation light, hence, several further investigations could be considered by increasing the system size. Expanding the simulation box to include a bigger surface area and more PVDF chains, building thicker PVDF films, would make possible to appreciate how the surface electrostatics affects PVDF chains in the long range, appreciating the region of space where PVDF chains becomes to behave as a bulk system, or verifying that electrostatics have a very long range effects on PVDF chains enhancing the β-PVDF crystal structure also in portion of the simulation box distant from the surface.

Another aspect to be considered is the realistic structure of a surface modelled with MD, indeed, the present graphene sheet has been modelled to be a perfect flat sheet defects free. But it certain that if the preparation of a graphene surface is approached experimentally, several defects will be present such as holes, chemical modifications, vacancies, wanted or unwanted chemical functionalisation, surface roughness and deformations which would significantly change the graphene sheet geometry and physical properties, hence, the electrostatics magnitude possessed by a real graphene sheet, consequently also the effect that electrostatics charges would have on PVDF chains would be different. Hence, a considerable amount of work can be dedicated building more realistic graphene sheets as surface of interest. When such considerable amount of work would be terminated, the same approach could repeated with other surface types, and instead of trying randomly different surfaces, it would become very interesting to reverse engineering the properties of surface to make them as wanted to increase the crystalline enhancement effect on PVDF chains.

When considering the state of the art of the present available FFs, there is still space for developing and improving the current PVDF FFs. Especially evaluating the long range vdW potential and its efficacy in predicting PVDF properties accordingly to experiments, as long range forces defined the cohesiveness of PVDF chains, if it would results that the present FFs overestimate such energy interaction, a refinement of the parameters which feed long range potentials would help in reducing the strong entanglement effects found for example in the modern B&S FF. Indeed, the B&S FF is not able to reproduce the liquid phase properties of PVDF infinite chains and the long range potential could be further developed to avoid such FF issue. Moreover, the surface parameterisation is another weak point of the B&S FF as no surfaces are already parametrised, and in the present study the graphene surface was limited as a frozen sheet interacting with PVDF only with non bonded potentials, hence, several FF developments would be beneficial for the future research on PVDF.

Finally, applying the knowledge gathered along the present computational study to test in experiments the best conditions which promote the β-phase formation and ferroelectric behaviour could represent an important study. The experimental observation of electrostatics surface potential using the dynamic contact electrostatic force microscopy (DC-EFM) technique, IR spectra and spontaneous polarisation measurement would help finding the best surface/polymer interaction conditions to increase the crystalline content of the β-phase. By finding the best material substrate for the β-PVDF formation would be a remarkable investigation that would confirm the current results obtained with computational modelling, which would also provide a definitive work flow to prepare high crystalline grade samples of β-PVDF.

References

[1] M. Broadhurst, G. Davis, J. McKinney, and R. Collins, “Piezoelectricity and pyroelectricity in polyvinylidene fluoride-A model,” *Journal of Applied Physics*, vol. 49, no. 10, pp. 4992–4997, 1978.

[2] S. J. Kang, Park, Y. Jung, Sung, Jinwoo, Jo, P. Sung, Park, Cheolmin, Kim, K. Jin, Cho, and Beong, “Spin cast ferroelectric beta poly(vinylidene fluoride) thin films via rapid thermal annealing,” *Applied Physics Letters*, vol. 92, no. 1, 2008.

[3] X. Cai, T. Lei, D. Sun, and L. Lin, “A critical analysis of the alpha, beta and gamma phases in poly(vinylidene fluoride) using ftir,” *RSC Adv.*, vol. 7, pp. 15382–15389, 2017.

[4] L. Caihong, H. Bing, X. Ruijie, Q. Cai, and W. Shi, “Influence of room-temperature-stretching technology on the crystalline morphology and microstructure of pvdf hard elastic film,” 15th November 2013.

[5] S. F. Mendes, C. M. Costa, C. Caparros, V. Sencadas, and S. Lanceros-Méndez, “Effect of filler size and concentration on the structure and properties of poly(vinylidene fluoride)/batio3 nanocomposites,” *Journal of Materials Science*, vol. 47, pp. 1378–1388, Feb 2012.

[6] Mandal, Dipankar, Kim, K. Jin, and J. Soon, “Simple synthesis of palladium nanoparticles, β-Phase formation, and the control of chain and dipole orientations in palladium-doped poly(vinylidene fluoride) thin films,” *Langmuir*, vol. 28, no. 28, pp. 10310–10317, 2012. PMID: 22747424.

[7] V. Cauda, B. Torre, A. Falqui, G. Canavese, S. Stassi, T. Bein, and M. Pizzi, “Confinement in oriented mesopores induces piezoelectric behavior of polymeric nanowires,” *Chemistry of Materials*, vol. 24, no. 21, pp. 4215–4221, 2012.

[8] L. Kang, L. Wonho, K. Sun, S. Joo, S. Cho, G. Song, S. Hwan, B. Jeong, I. Hwang, A. Jong-Hyun, Y. Young-Jun, T. Shin, S. Kwak, S. Kang, and C. Park, “Epitaxial growth of thin ferroelectric polymer films on graphene layer for fully transparent and flexible nonvolatile memory,” *Nano Letters*, vol. 16, no. 1, pp. 334–340, 2016. PMID: 26618802.

[9] K. Foreman, N. Hong, C. Labedz, M. Shearer, S. Ducharme, and S. Adenwalla, “Ferroelectric characterization and growth optimization of thermally evaporated vinylidene fluoride thin films,” *Journal of Physics D: Applied Physics*, vol. 49, no. 1, p. 015301, 2015.

[10] W. Kohn and L. J. Sham, “Self-consistent equations including exchange and correlation effects,” *Phys. Rev.*, vol. 140, pp. A1133–A1138, Nov 1965.

[11] N. Ashcroft and N. Mermin, *Solid State Physics*. Philadelphia: Saunders College, 1976.

[12] P. Giannozzi, S. Baroni, N. Bonini, M. Calandra, R. Car, C. Cavazzoni, D. Ceresoli, G. L. Chiarotti, M. Cococcioni, I. Dabo, A. D. Corso, S. de Gironcoli, S. Fabris, G. Fratesi, R. Gebauer, U. Gerstmann, C. Gougoussis, A. Kokalj, M. Lazzeri, L. Martin-Samos, N. Marzari, F. Mauri, R. Mazzarello, S. Paolini, A. Pasquarello, L. Paulatto, C. Sbraccia, S. Scandolo, G. Sclauzero, A. Seitsonen, A. Smogunov, P. Umari, and R. Wentzcovitch, “Quantum espresso: a modular and open-source software project for quantum simulations of materials,” *Journal of Physics: Condensed Matter*, vol. 21, no. 39, p. 395502, 2009.

[13] W. Setyawan and S. Curtarolo, “High-throughput electronic band structure calculations: Challenges and tools,” *Computational Materials Science*, vol. 49, no. 2, pp. 299 – 312, 2010.

[14] R. M. Martin, *Electronic structure: basic theory and practical methods*. The Edinburgh Building, Cambridge CB2 2RU, UK: Cambridge University Press, 2004.

[15] J. Ziman, *Electrons and Phonons: The Theory of Transport Phenomena in Solids*. Oxford Classic Texts, 2001.

[16] D. Rapaport, *The Art of Molecular Dynamics Simulation*. 2004.

[17] S. Hari, *Ferroelectric Polymers: Chemistry, Physics, and Apllications*. 1995.

[18] C. gang Duan, W. N. Mei, J. R. Hardy, S. Ducharme, J. Choi, and P. A. Dowben, “Comparison of the theoretical and experimental band structure of poly(vinylidene fluoride) crystal,” *EPL (Europhysics Letters)*, vol. 61, no. 1, p. 81, 2003.

[19] B. Berge, A. Wicker, J. Lajzerowicz, and J. F. Legrand, “Second-harmonic generation of light and evidence of phase matching in thin films of p(vdf-trfe) copolymers,” *EPL (Europhysics Letters)*, vol. 9, no. 7, p. 657, 1989.

[20] H. T. Stokes and D. M. Hatch, “FINDSYM: program for identifying the space-group symmetry of a crystal,” *Journal of Applied Crystallography*, vol. 38, pp. 237–238, Feb 2005.

[21] M. Bachmann, W. L. Gordon, S. Weinhold, and J. B. Lando, “The crystal structure of phase iv of poly(vinylidene fluoride),” *Journal of Applied Physics*, vol. 51, no. 10, pp. 5095–5099, 1980.

[22] B. Mohammadi, A. Yousefi, and S. Bellah, “Effect of tensile strain rate and elongation on crystalline structure and piezoelectric properties of pvdf thin films,” *Polymer Testing*, vol. 26, no. 1, pp. 42 – 50, 2007.

[23] A. Lopes, C. Costa, C. Tavares, I. Neves, and S. Lanceros-Mendez, “Nucleation of the electroactive γ phase and enhancement of the optical transparency in low filler content poly(vinylidene)/clay nanocomposites,” *The Journal of Physical Chemistry C*, vol. 115, no. 37, pp. 18076–18082, 2011.

[24] A. Lopes, C. Caparros, J. G. Ribelles, I. Neves, and S. Lanceros-Mendez, “Electrical and thermal behavior of γ-phase poly(vinylidene fluoride)/nay zeolite composites,” *Microporous and Mesoporous Materials*, vol. 161, no. 0, pp. 98 – 105, 2012.

[25] Ramasundaram, Subramaniyan, Yoon, Sun, Kim, K. Jin, Park, and Cheolmin, “Preferential formation of electroactive crystalline phases in poly(vinylidene fluoride)/organically modified silicate nanocomposites,” *Journal of Polymer Science Part B: Polymer Physics*, vol. 46, no. 20, pp. 2173–2187, 2008.

[26] N. Karasawa and W. I. Goddard, “Force fields, structures, and properties of poly(vinylidene fluoride) crystals,” *Macromolecules*, vol. 25, no. 26, pp. 7268–7281, 1992.

[27] O. G. Byutner and G. D. Smith, “Quantum chemistry based force field for simulations of poly(vinylidene fluoride),” *Macromolecules*, vol. 33, no. 11, pp. 4264–4270, 2000.

[28] S. Guryel, M. Walker, P. Geerlings, F. De Proft, and M. R. Wilson, “Molecular dynamics simulations of the structure and the morphology of graphene/polymer nanocomposites,” *Phys. Chem. Chem. Phys.*, vol. 19, pp. 12959–12969, 2017.

[29] Noda, Kei, Ishida, Kenji, Kubono, Atsushi, Horiuchi, Toshihisa, Yamada, Hirofumi, Matsushige, and Kazumi, “Remanent polarization of evaporated films of vinylidene fluoride oligomers,” *Journal of Applied Physics*, vol. 93, no. 5, pp. 2866–2870, 2003.

[30] Y. Bormashenko, R. Pogreb, O. Stanevsky, and E. Bormashenko, “Vibrational spectrum of {PVDF} and its interpretation,” *Polymer Testing*, vol. 23, no. 7, pp. 791 – 796, 2004.

[31] T. Boccaccio, A. Bottino, G. Capannelli, and P. Piaggio, “Characterization of pvdf membranes by vibrational spectroscopy,” *Journal of Membrane Science*, vol. 210, no. 2, pp. 315 – 329, 2002.

[32] S. Nakhmanson, R. Korlacki, J. Travis, Ducharme, Stephen, Ge, Zhongxin, Takacs, and M. James, “Vibrational properties of ferroelectric β-poly-vinylidene fluoride polymers and oligomers,” *Phys. Rev. B*, vol. 81, p. 174120, May 2010.

[33] P. J. Mohr, D. B. Newell, and B. N. Taylor, “Codata recommended values of the fundamental physical constants: 2014,” *Rev. Mod. Phys.*, vol. 88, p. 035009, Sep 2016.

[34] L. Pardo and J. Ricote, *Multifunctional polycrystalline ferroelectric materials: processing and properties*, vol. 140. Springer Science & Business Media, 2011.

[35] J. F. Scott, *Ferroelectric Memories*, vol. 3. Springer Series in Advanced Microelectronics, 2000.

[36] C. Petzold, *Code: the hidden language of computer hardware and software*. DV-Undefined, Microsoft Press, 2000.

[37] J. R. Contreras, H. Kohlstedt, U. Poppe, R. Waser, C. Buchal, and N. A. Pertsev, “Resistive switching in metal–ferroelectric–metal junctions,” *Applied Physics Letters*, vol. 83, no. 22, pp. 4595–4597, 2003.

[38] T. Sakurai and A. R. Newton, “Alpha-power law mosfet model and its applications to cmos inverter delay and other formulas,” *IEEE Journal of Solid-State Circuits*, vol. 25, pp. 584–594, Apr 1990.

[39] Senanayak, P. Satyaprasad, S. Guha, and K. Narayan, “Polarization fluctuation dominated electrical transport processes of polymer-based ferroelectric field effect transistors,” *Phys. Rev. B*, vol. 85, p. 115311, Mar 2012.

[40] M. Poulsen, “Why ferroelectric polyvinylidene fluoride is special,” *Stephen Ducharme Publications*, vol. 17, no. 4, pp. 1028–1035, 2010.

[41] J. Li, Dong, Hong, Seungbum, Gu, Shiyuan, Choi, YoonYoung, S. Nakhmanson, H. Nakhmanson, Olle, Karpeev, and D. Kwangsoo, “Polymer piezoelectric energy harvesters for low wind speed,” *Applied Physics Letters*, vol. 104, no. 1, pp. –, 2014.

[42] B. Thomas, V. Demczuk, W. Piekarski, D. Hepworth, and B. Gunther, “A wearable computer system with augmented reality to support terrestrial navigation,” in *Wearable Computers, 1998. Digest of Papers. Second International Symposium on*, pp. 168–171, Oct 1998.

[43] M. Caironi and Y.-Y. Noh, *Large Area and Flexible Electronics*, vol. 1. Wiley-VCH Verlag GmbH Publication, 2015.

[44] S. Ducharme, *Why are Ferroelectric Polymers Difficult to Find – And Difficult to Verify*. University of Nebraska, Academic, 2008.

[45] V. Fridkin and S. Ducharme, *Ferroelectricity at the Nanoscale*, vol. 1. Springer-Verlag Berlin Heidelberg, 2014.

[46] J. F. Scott, C. A. Araujo, H. B. Meadows, L. D. McMillan, and A. Shawabkeh, “Radiation effects on ferroelectric thin−film memories: Retention failure mechanisms,” *Journal of Applied Physics*, vol. 66, no. 3, pp. 1444–1453, 1989.

[47] Sághi-Szabó, Gotthard, Cohen, E. Ronald, Krakauer, and Henry, “First-principles study of piezoelectricity in $\mathrm{PbTiO_3}$,” *Phys. Rev. Lett.*, vol. 80, pp. 4321–4324, May 1998.

[48] K. Matyjaszewski, *Controlled Radical Polymerization*. Washington, DC: American Chemical Society, 1998.

[49] T. M. K. W. M. Davidson, A.K. Hughes, *Contemporary Boron Chemistry*. Royal Society of Chemistry, 1999.

[50] S. Nakhmanson, M. Nardelli, and J. Bernholc, “*Ab Initio* studies of polarization and piezoelectricity in vinylidene fluoride and bn-based polymers,” *Phys. Rev. Lett.*, vol. 92, p. 115504, Mar 2004.

[51] K. Kremer and G. S. Grest, “Dynamics of entangled linear polymer melts a molecular dynamics simulation,” *The Journal of Chemical Physics*, vol. 92, no. 8, pp. 5057–5086, 1990.

[52] P. Southgate, “Room−temperature poling and morphology changes in pyroelectric polyvinylidene fluoride,” *Applied Physics Letters*, vol. 28, no. 5, pp. 250–252, 1976.

[53] R. B. Bird, R. C. Armstrong, and O. Hassager, *Dynamics of Polymeric Liquids, Volume 1: Fluid Mechanics, 2nd Edition*. 464.

[54] R. B. Bird, R. C. Armstrong, and O. Hassager, *Dynamics of Polymeric Liquids, Volume 2: Kinetic Theory, 2nd Edition*. 672.

[55] R. Kepler and R. Anderson, “Ferroelectric polymers,” *Advances in Physics*, vol. 41, no. 1, pp. 1–57, 1992.

[56] C. Purvis and P. Taylor, “Piezoelectricity and pyroelectricity in polyvinylidene fluoride: Influence of the lattice structure,” *Journal of Applied Physics*, vol. 54, no. 2, 1983.

[57] V. Cauda, S. Stassi, B. Katarzyna, and G. Canavese, “Nanoconfinement: an effective way to enhance pvdf piezoelectric properties,” *ACS Applied Materials & Interfaces*, vol. 5, no. 13, pp. 6430–6437, 2013. PMID: 23777739.

[58] T. Furukawa, “Ferroelectric properties of vinylidene fluoride copolymers,” *Phase Transitions*, vol. 18, no. 3-4, pp. 143–211, 1989.

[59] A. J. Lovinger, “Ferroelectric polymers,” *Science*, vol. 220, no. 4602, pp. 1115–1121, 1983.

[60] R. Kepler and R. Anderson, “Piezoelectricity and pyroelectricity in polyvinylidene fluoride,” *Journal of Applied Physics*, vol. 49, no. 8, 1978.

[61] P. Flory, *Principles of Polymer Chemistry*. Baker lectures 1948, Cornell University Press, 1953.

[62] J. B. Lando, H. G. Olf, and A. Peterlin, “Nuclear magnetic resonance and x-ray determination of the structure of poly(vinylidene fluoride),” *Journal of Polymer Science Part A-1: Polymer Chemistry*, vol. 4, no. 4, pp. 941–951, 1966.

[63] A. Lovinger, “Unit cell of the γ phase of poly(vinylidene fluoride),” *Macromolecules*, vol. 14, no. 2, pp. 322–325, 1981.

[64] A. Lovinger, “Annealing of poly(vinylidene fluoride) and formation of a fifth phase,” *Macromolecules*, vol. 15, no. 1, pp. 40–44, 1982.

[65] M. Kobayashi, K. Tashiro, and H. Tadokoro, “Molecular vibrations of three crystal forms of poly(vinylidene fluoride),” *Macromolecules*, vol. 8, no. 2, pp. 158–171, 1975.

[66] Pei, Yong, Zeng, and X. Cheng, “Elastic properties of poly(vinyldene fluoride) (PVDF) crystals: A density functional theory study,” *Journal of applied physics*, vol. 109, no. 9, 2011.

[67] Takahashi, Yasuhiro, Tadokoro, and Hiroyuki, “Crystal structure of form iii of poly(vinylidene fluoride),” *Macromolecules*, vol. 13, no. 5, pp. 1317–1318, 1980.

[68] M. Bachmann, W. Gordon, S. Weinhold, and J. Lando, “The crystal structure of the γ-phase of the poly(vinylidene fluoride),” vol. 13, 1980.

[69] L. Mengyuan, J. Harry, Spijkman, Mark-Jan, Asadi, Kamal, Katsouras, Ilias, Blom, W. Paul, and D. de Leeuw, "Revisiting the δ-phase of poly(vinylidene fluoride) for solution-processed ferroelectric thin films," 2013.

[70] H. Kawai, "The piezoelectricity of poly (vinylidene fluoride)," *Japanese Journal of Applied Physics*, vol. 8, no. 7, p. 975, 1969.

[71] C. gang Duan, W. N. Mei, W.-G. Yin, J. Liu, J. R. Hardy, M. Bai, and S. Ducharme, "Theoretical study on the optical properties of polyvinylidene fluoride crystal," *Journal of Physics: Condensed Matter*, vol. 15, no. 22, p. 3805, 2003.

[72] J. E. McKinney, G. T. Davis, and M. G. Broadhurst, "Plasma poling of poly(vinylidene fluoride): Piezo$-$ and pyroelectric response," *Journal of Applied Physics*, vol. 51, no. 3, pp. 1676–1681, 1980.

[73] Milani, A. Castiglioni, C. Radice, and Stefano, "Joint experimental and computational investigation of the structural and spectroscopic properties of poly(vinylidene fluoride) polymorphs," *The Journal of Physical Chemistry B*, vol. 119, no. 14, pp. 4888–4897, 2015. PMID: 25775384.

[74] G. Strobl, "Crystallization and melting of bulk polymers: new observations, conclusions and a thermodynamic scheme," *Progress in Polymer Science*, vol. 31, no. 4, pp. 398$--$442, 2006.

[75] H. R., T. Y., C. Y., and T. H., "Crystal structures of three crystalline forms of poly(vinylidene fluoride)," *Polym J*, vol. 3, no. 5, pp. 600–610, 1972.

[76] W. Li, Q. Meng, Z. Yuansuo, Z. Zhang, W. Xia, and Z. Xu, "Electric energy storage properties of poly(vinylidene fluoride)," vol. 96, 05 2010.

[77] M. Brodta, R. Wyciska, N. Daleb, and P. Pintauro, "Power output and durability of electrospun fuel cell fiber cathodes with pvdf and nafion/pvdf binders," *Journal of The Electrochemical Society*, vol. 5, no. 163, pp. 401$--$410, 2016.

[78] C. Costa, V. Sencadas, I. Pelicano, F. Martins, J. Rocha, and S. Lanceros-Mendez, "Microscopic origin of the high-strain mechanical response of poled and non-poled poly(vinylidene fluoride) in the β-phase," *Journal of Non-Crystalline Solids*, vol. 354, no. 32, pp. 3871–3876, 2008.

[79] V. Sencadas, S. Lanceros-Méndez, and J. Mano, "Characterization of poled and non-poled β-pvdf films using thermal analysis techniques," *Thermochimica Acta*, vol. 424, no. 1–2, pp. 201 – 207, 2004.

[80] W. Demtröder, *Laser Spectroscopy 2: Experimental Techniques*. Springer, 2015.

[81] N. J. Ramer, C. M. Raynor, and K. A. Stiso, "Vibrational frequency and LO$-$TO splitting determination for planar$-$zigzag β-poly(vinylidene fluoride) using density-functional theory," *Polymer*, vol. 47, no. 1, pp. 424 – 428, 2005.

[82] N. J. Ramer, T. Marrone, and K. A. Stiso, "Structure and vibrational frequency determination for α-poly(vinylidene fluoride) using density-functional theory," *Polymer*, vol. 47, no. 20, pp. 7160 – 7165, 2006. Containing: Structure and Dynamics of Complex Polymeric Materials. Commemorating Tadeusz Pakula.

[83] I. Yoo and S. Desu, “Mechanism of fatigue in ferroelectric thin films,” *physica status solidi (a)*, vol. 133, no. 2, pp. 565–573, 1992.

[84] L. Li, M. Zhang, M. Rong, and W. Ruan, “Studies on the transformation process of pvdf from alpha to beta phase by stretching,” *RSC Adv.*, vol. 4, pp. 3938–3943, 2014.

[85] K. Matsushige, K. Nagata, S. Imada, and T. Takemura, “The ii-i crystal transformation of poly(vinylidene fluoride) under tensile and compressional stresses,” *Polymer*, vol. 21, no. 12, pp. 1391 – 1397, 1980.

[86] A. Salimi and A. Yousefi, “Analysis method: Ftir studies of β-phase crystal formation in stretched pvdf films,” *Polymer Testing*, vol. 22, no. 6, pp. 699 – 704, 2003.

[87] M. Arrigoni, F. Bauer, S. Kerampran, J. Le Clanche, and M. Monloubou, “Development of a pvdf pressure gauge for blast loading measurement,” *Human Factors and Mechanical Engineering for Defense and Safety*, vol. 2, p. 2, Apr 2018.

[88] F. Bauer and R. Graham, “Very high pressure behavior of precisely-poled pvdf,” *Ferroelectrics*, vol. 171, no. 1, pp. 95–102, 1995.

[89] J. Gregorio and D. Borges, “Effect of crystallization rate on the formation of the polymorphs of solution cast poly(vinylidene fluoride),” *Polymer*, vol. 49, no. 18, pp. 4009 – 4016, 2008.

[90] A. Salimi and A. A. Yousefi, “Conformational changes and phase transformation mechanisms in pvdf solution-cast films,” *Journal of Polymer Science Part B: Polymer Physics*, vol. 42, no. 18, pp. 3487–3495, 2004.

[91] N. Takashi, A. Ryosuke, Y. Takahashi, and T. Furukawa, “Intrinsic switching characteristics of ferroelectric ultrathin vinylidene fluoride/trifluoroethylene copolymer films revealed using au electrode,” *Japanese Journal of Applied Physics*, vol. 44, no. 10L, p. L1385, 2005.

[92] J. Yang, T. Ryu, Y. Lansac, Y. Jang, and B. Lee, “Shear stress-induced enhancement of the piezoelectric properties of pvdf-trfe thin films,” *Organic Electronics*, vol. 28, pp. 67–72, 2016.

[93] A. Gebrekrstos, M. Sharma, G. Madras, and S. Bose, “Critical insights into the effect of shear, shear history, and the concentration of a diluent on the polymorphism in poly(vinylidene fluoride),” *Crystal Growth & Design*, vol. 17, no. 4, pp. 1957–1965, 2017.

[94] Wu, Ying, Hsu, S. Ling, Honeker, Christian, Bravet, J. David, and S. Darryl, “The role of surface charge of nucleation agents on the crystallization behavior of poly(vinylidene fluoride),” *The Journal of Physical Chemistry B*, vol. 116, no. 24, pp. 7379–7388, 2012. PMID: 22646047.

[95] R. Song, G. Xia, X. Xing, L. He, Q. Zhao, and Z. Ma, “Modification of polymorphisms in polyvinylidene fluoride thin films via water and hydrated salt,” *Journal of Colloid and Interface Science*, vol. 401, pp. 50 – 57, 2013.

[96] C. Ederer and N. A. Spaldin, "Effect of epitaxial strain on the spontaneous polarization of thin film ferroelectrics," *Phys. Rev. Lett.*, vol. 95, p. 257601, Dec 2005.

[97] O. N. Oliveira, "Langmuir–Blodgett films – properties and possible applications," *Brazilian Journal of Physics*, vol. 22, no. 2, p. 10, 1992.

[98] M. Bai, M. Poulsen, A. V. Sorokin, S. Ducharme, C. M. Herzinger, and V. M. Fridkin, "Infrared spectroscopic ellipsometry study of vinylidene fluoride (70%)-trifluoroethylene (30%) copolymer langmuir–blodgett films," *Journal of Applied Physics*, vol. 94, no. 1, pp. 195–200, 2003.

[99] T. Reece, Ducharme, S. Sorokin, A. Sorokin, Poulsen, and Matt, "Nonvolatile memory element based on a ferroelectric polymer Langmuir–Blodgett film," *Applied Physics Letters*, vol. 82, no. 1, 2003.

[100] M. Achaby, F. Arrakhiz, S. Vaudreuil, E. Essassi, and A. Qaiss, "Piezoelectric β-polymorph formation and properties enhancement in graphene oxide – {PVDF} nanocomposite films," *Applied Surface Science*, vol. 258, no. 19, pp. 7668 – 7677, 2012.

[101] Itoh, Akira, Takahashi, Yoshiyuki, Furukawa, Takeo, Yajima, and Hirofumi, "Solid-state calculations of poly(vinylidene fluoride) using the hybrid DFT method: spontaneous polarization of polymorphs," *Polymer Journal*, vol. 46, pp. 207–211, APR 2014.

[102] N. Ramer and K. Stiso, "Structure and born effective charge determination for planar-zigzag β-poly(vinylidene fluoride) using density-functional theory," *Polymer*, vol. 46, no. 23, pp. 10431 – 10436, 2005.

[103] S. Nakhmanson, M. B. Nardelli, and J. Bernholc, "Collective polarization effects in $\beta-$polyvinylidene fluoride and its copolymers with tri$-$ and tetrafluoroethylene," 2005.

[104] H. Su, A. Strachan, and W. Goddard, "Density functional theory and molecular dynamics studies of the energetics and kinetics of electroactive polymers: Pvdf and p(vdf-trfe)," *Phys. Rev. B*, vol. 70, pp. 64–101, Aug 2004.

[105] K. Tashiro, Y. Itoh, M. Kobayashi, and H. Tadokoro, "Polarized raman spectra and lo-to splitting of poly(vinylidene fluoride) crystal form i," *Macromolecules*, vol. 18, no. 12, pp. 2600–2606, 1985.

[106] K. Tashiro, M. Kobayashi, and H. Tadokoro, "Vibrational spectra and disorder-order transition of poly(vinylidene fluoride) form iii," *Macromolecules*, vol. 14, no. 6, pp. 1757–1764, 1981.

[107] Takahashi, Yasuhiro, Matsubara, Yoshiaki, Tadokoro, and Hiroyuki, "Crystal structure of form ii of poly(vinylidene fluoride)," *Macromolecules*, vol. 16, no. 10, pp. 1588–1592, 1983.

[108] W. Zhi-Yin, F. Hui-Qing, S. Ke-He, and W. Zhen-Yi, "Structure and piezoelectric properties of poly(vinylidene fluoride) studied by density functional theory," *Polymer*, vol. 47, no. 23, pp. 7988 – 7996, 2006.

[109] K. C. Satyanarayana and K. Bolton, “Molecular dynamics simulations of α to $\beta-$poly(vinylidene fluoride) phase change by stretching and poling,” *Polymer*, vol. 53, no. 14, pp. 2927 – 2934, 2012.

[110] N. Karasawa and W. A. Goddard, “Dielectric properties of poly(vinylidene fluoride) from molecular dynamics simulations,” *Macromolecules*, vol. 28, no. 20, pp. 6765–6772, 1995.

[111] E. Erdtman, K. C. Satyanarayana, and K. Bolton, “Simulation of α- and β-pvdf melting mechanisms,” *Polymer*, vol. 53, no. 14, pp. 2919 – 2926, 2012.

[112] S. Güryel, M. Alonso, B. Hajgató, Y. Dauphin, G. Van Lier, P. Geerlings, and F. De Proft, “A computational study on the role of noncovalent interactions in the stability of polymer/graphene nanocomposites,” *Journal of Molecular Modeling*, vol. 23, p. 43, Feb 2017.

[113] M. Dion, H. Rydberg, E. Schröder, D. Langreth, and B. Lundqvist, “van der Waals density functional for general geometries,” *Phys. Rev. Lett.*, vol. 92, p. 246401, Jun 2004.

[114] J. Kleis, B. Lundqvist, and D. Langreth, “Towards a working density-functional theory for polymers: First-principles determination of the polyethylene crystal structure,” *Phys. Rev. B*, vol. 76, p. 100201, 2007.

[115] K. Lee, E. D. Murray, L. Kong, B. I. Lundqvist, and D. C. Langreth, “Higher-accuracy van der waals density functional,” *Phys. Rev. B*, vol. 82, p. 081101, Aug 2010.

[116] Argaman, Nathan, Makov, and Guy, “Density functional theory: An introduction,” *American Journal of Physics*, vol. 68, no. 1, 2000.

[117] M. J. Abraham, T. Murtola, R. Schulz, S. Páll, J. C. Smith, B. Hess, and E. Lindahl, “Gromacs: High performance molecular simulations through multi-level parallelism from laptops to supercomputers,” *SoftwareX*, vol. 1–2, pp. 19 – 25, 2015.

[118] J. C. Phillips, R. Braun, W. Wang, J. Gumbart, E. Tajkhorshid, E. Villa, C. Chipot, R. D. Skeel, L. Kalé, and K. Schulten, “Scalable molecular dynamics with namd,” *Journal of Computational Chemistry*, vol. 26, no. 16, pp. 1781–1802, 2005.

[119] S. Plimpton, “Fast parallel algorithms for short-range molecular dynamics,” *Journal of Computational Physics*, vol. 117, no. 1, pp. 1 – 19, 1995.

[120] H. Eschrig, *The Fundamentals of Density Functional Theory*. Vieweg+Teubner Verlag, 1996.

[121] P. Koskinen and V. Mäkinen, “Density-functional tight-binding for beginners,” *Computational Materials Science*, vol. 47, no. 1, pp. 237 – 253, 2009.

[122] R. Haydock, “The recursive solution of the schrödinger equation,” *Computer Physics Communications*, vol. 20, no. 1, pp. 11 – 16, 1980.

[123] S. Grimme, “Improved second-order møller–plesset perturbation theory by separate scaling of parallel- and antiparallel-spin pair correlation energies,” *The Journal of Chemical Physics*, vol. 118, no. 20, pp. 9095–9102, 2003.

[124] C. Møller and M. S. Plesset, "Note on an approximation treatment for many-electron systems," *Phys. Rev.*, vol. 46, pp. 618–622, Oct 1934.

[125] S. Grimme, "Improved third-order møller–plesset perturbation theory," *Journal of Computational Chemistry*, vol. 24, no. 13, pp. 1529–1537, 2003.

[126] C. Kittel, *Introduction to Solid State Physics*. New York: John Wiley & Sons, Inc., 6th ed., 1986.

[127] W. Kohn, *Fundamentals of density functional theory*, pp. 1–7. Berlin, Heidelberg: Springer Berlin Heidelberg, 1998.

[128] M. Stone, "Born-oppenheimer approximation and the origin of wess-zumino terms: Some quantum-mechanical examples," *Phys. Rev. D*, vol. 33, pp. 1191–1194, Feb 1986.

[129] R. Woolley and B. Sutcliffe, "Molecular structure and the born—oppenheimer approximation," *Chemical Physics Letters*, vol. 45, no. 2, pp. 393 – 398, 1977.

[130] G. Kresse and J. Hafner, "Norm-conserving and ultrasoft pseudopotentials for first-row and transition elements," *Journal of Physics: Condensed Matter*, vol. 6, no. 40, p. 8245, 1994.

[131] D. Vanderbilt, "Soft self-consistent pseudopotentials in a generalized eigenvalue formalism," *Phys. Rev. B*, vol. 41, pp. 7892–7895, Apr 1990.

[132] G. Kresse and D. Joubert, "From ultrasoft pseudopotentials to the projector augmented-wave method," *Phys. Rev. B*, vol. 59, pp. 1758–1775, Jan 1999.

[133] S. Fujita and K. Ito, *Bloch Theorem*. New York, NY: Springer New York, 2007.

[134] E. Gross and W. Kohn, "Local density-functional theory of frequency-dependent linear response," *Phys. Rev. Lett.*, vol. 55, pp. 2850–2852, Dec 1985.

[135] Paier, Joachim, Hirschl, Robin, Marsman, Martijn, Kresse, and Georg, "The perdew–burke–ernzerhof exchange-correlation functional applied to the g2-1 test set using a plane-wave basis set," *The Journal of Chemical Physics*, vol. 122, no. 23, 2005.

[136] J. P. Perdew, K. Burke, and M. Ernzerhof, "Generalized gradient approximation made simple," *Phys. Rev. Lett.*, vol. 77, pp. 3865–3868, Oct 1996.

[137] S. Sholl and J. Steckel, *Density Functional Theory: A Practical Introduction*. 2009.

[138] S. Grimme, "Semiempirical gga-type density functional constructed with a long-range dispersion correction," *Journal of Computational Chemistry*, vol. 27, no. 15, pp. 1787–1799, 2006.

[139] A. Tkatchenko and M. Scheffler, "Accurate molecular van der waals interactions from ground-state electron density and free-atom reference data," *Phys. Rev. Lett.*, vol. 102, p. 073005, Feb 2009.

[140] N. Spaldin, "A beginner's guide to the modern theory of polarization," *Journal of Solid State Chemistry*, vol. 195, pp. 2–10, 2012. Polar Inorganic Materials: Design Strategies and Functional Properties.

[141] W. Jorgensen, D. Maxwell, and J. Tirado-Rives, "Development and testing of the opls all-atom force field on conformational energetics and properties of organic liquids," *Journal of the American Chemical Society*, vol. 118, no. 45, pp. 11225–11236, 1996.

[142] P. Pernot, B. Civalleri, D. Presti, and A. Savin, "Prediction uncertainty of density functional approximations for properties of crystals with cubic symmetry," *The Journal of Physical Chemistry A*, vol. 119, no. 21, pp. 5288–5304, 2015. PMID: 25626469.

[143] F. D. Proft, J. M. Martin, and P. Geerlings, "On the performance of density functional methods for describing atomic populations, dipole moments and infrared intensities," *Chemical Physics Letters*, vol. 250, no. 3, pp. 393 – 401, 1996.

[144] W. Kim, M. Han, Y.-H. Shin, H. Kim, and E. Lee, "First-principles study of the $\alpha - \beta$ phase transition of ferroelectric poly(vinylidene difluoride): Observation of multiple transition pathways," *J. Phys. Chem. B*, vol. 120, pp. 3240–3249, 2016.

[145] M. A. Bachmann, W. L. Gordon, J. Koenig, and J. B. Lando, "An infrared study of phase$-$iii poly(vinylidene fluoride)," *Journal of Applied Physics*, vol. 50, no. 10, pp. 6106–6112, 1979.

[146] F. W. B. Jr., "Lattice energy of crystalline polyethylene," *Journal of Applied Physics*, vol. 28, no. 10, pp. 1114–1118, 1957.

[147] V. Ranjan, L. Yu, M. Nardelli, and J. Bernholc, "Phase equilibria in high energy density pvdf-based polymers," *Phys. Rev. Lett.*, vol. 99, p. 047801, Jul 2007.

[148] D. Mao, B. Gnade, and M. Quevedo-Lopez, "Ferroelectric properties and polarization switching kinetic of poly (vinylidene fluoride-trifluoroethylene) copolymer," *Ferroelectrics - Physical Effects*, 2011.

[149] K. Nakamura, M. Nagai, T. Kanamoto, Y. Takahashi, and T. Furukawa, "Development of oriented structure and properties on drawing of poly(vinylidene fluoride) by solid-state coextrusion," *Journal of Polymer Science Part B: Polymer Physics*, vol. 39, no. 12, pp. 1371–1380, 2001.

[150] J. Choi, P. A. Dowben, S. Pebley, A. V. Bune, S. Ducharme, V. M. Fridkin, S. P. Palto, and N. Petukhova, "Changes in metallicity and electronic structure across the surface ferroelectric transition of ultrathin crystalline poly(vinylidene fluoride-trifluoroethylene) copolymers," *Phys. Rev. Lett.*, vol. 80, pp. 1328–1331, Feb 1998.

[151] K. Tashiro, K. Takano, M. Kobayashi, Y. Chatani, and H. Tadokoro, "Phase transition at a temperature immediately below the melting point of poly(vinylidene fluoride) from i: A proposition for the ferroelectric curie point," *Polymer*, vol. 24, no. 2, pp. 199 – 204, 1983.

[152] G. J. Cestari and M. Cestari, "Effect of crystallization temperature on the crystalline phase content and morphology of poly(vinylidene fluoride)," *Journal of Polymer Science Part B: Polymer Physics*, vol. 32, no. 5, pp. 859–870, 1994.

[153] M. Glazer, *Preface*. Oxford: Academic Press, third edition ed., 2013.

[154] L. Mengyuan, I. Katsouras, K. Asadi, W. Blom, M. Dago, and D. Leeuw, "Low voltage extrinsic switching of ferroelectric $\delta-$pvdf ultra$-$thin films," 2013.

[155] R. Gregorio and R. C. Capitão, "Morphology and phase transition of high melt temperature crystallized poly(vinylidene fluoride)," *Journal of Materials Science*, vol. 35, no. 2, pp. 299–306, 2000.

[156] M. Doi and S. F. Edwards, "Dynamics of concentrated polymer systems," *J. Chem. Soc., Faraday Trans. 2*, vol. 74, pp. 1789–1801, 1978.

[157] K. C. Satyanarayana, M. Bohlén, A. Lund, R. W. Rychwalski, and K. Bolton, "Analysis of the torsion angle distribution of poly(vinylidene fluoride) in the melt," *Polymer*, vol. 53, no. 5, pp. 1109 – 1114, 2012.

[158] K. Ichi, Matsumoto, and K. Maki, "Molecular orientation in thin film grown on au, ag, al and si substrates by vacuum evaporation of copolymer of vinylidene fluoride and tetrafluoroethylene," *Ferroelectrics*, vol. 171, no. 1, pp. 163–176, 1995.

[159] C. Seoul, Y.-T. Kim, and C.-K. Baek, "Electrospinning of poly(vinylidene fluoride)/dimethylformamide solutions with carbon nanotubes," *Journal of Polymer Science Part B: Polymer Physics*, vol. 41, no. 13, pp. 1572–1577, 2003.

[160] J. Yamashita, M. Shioya, T. Kikutani, and T. Hashimoto, "Activated carbon fibers and films derived from poly(vinylidene fluoride)," vol. 39, pp. 207–214, 02 2001.

[161] O. Leenaerts, B. Partoens, and F. M. Peeters, "Adsorption of h_2O, Nh_3, co, No_2, and no on graphene: A first-principles study," *Phys. Rev. B*, vol. 77, p. 125416, Mar 2008.

[162] A. Berg, C. Peter, and K. Johnston, "Evaluation and optimization of interface force fields for water on gold surfaces," *Journal of Chemical Theory and Computation*, vol. 13, no. 11, pp. 5610–5623, 2017. PMID: 28992416.

[163] A. De Virgiliis, A. Milchev, V. G. Rostiashvili, and T. A. Vilgis, "Structure and dynamics of a polymer melt at an attractive surface," *The European Physical Journal E*, vol. 35, p. 97, Sep 2012.

Appendix A

Plots, Tables and Figures

A.1 Convergence tests

Figures A.1, A.2 and A.3 reported the convergence test needed to define the cutoffs parameters such as kwfc and krho and the number of k-points for integrating the total energy of the system in the Brillouin zone. The parameters chosen to perform the DFT study were reported in Table 3.1.

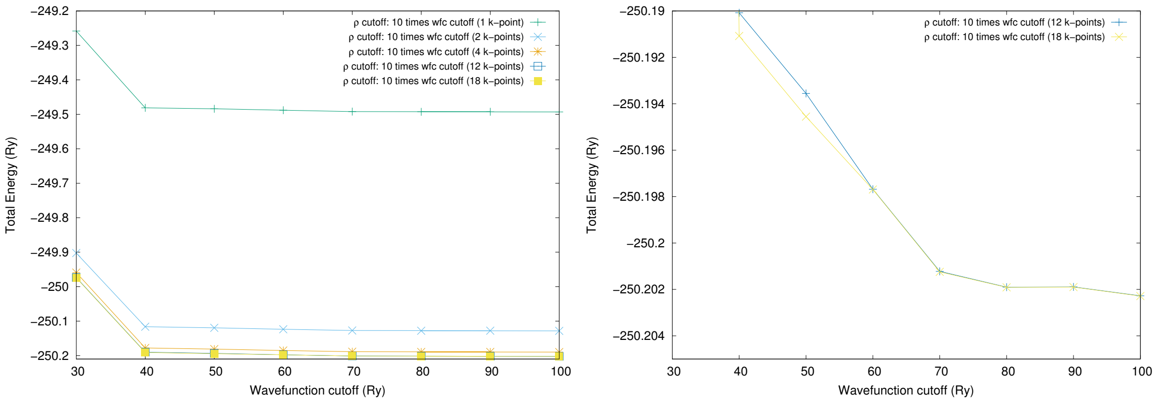

Fig. A.1 Convergence tests for the full trans backbone structure such as the β and ζ phases (12 atoms models: 12 milli Rydbergs tollerance), with the ideal kinetic energy cutoff of the charge density ten times the kinetic energy cutoff of the wavefunction (for US pseudopotentials). Left: Convergence overview; Right: Convergence zoomed in the milli Rydbergs range were cutoffs were accepted.

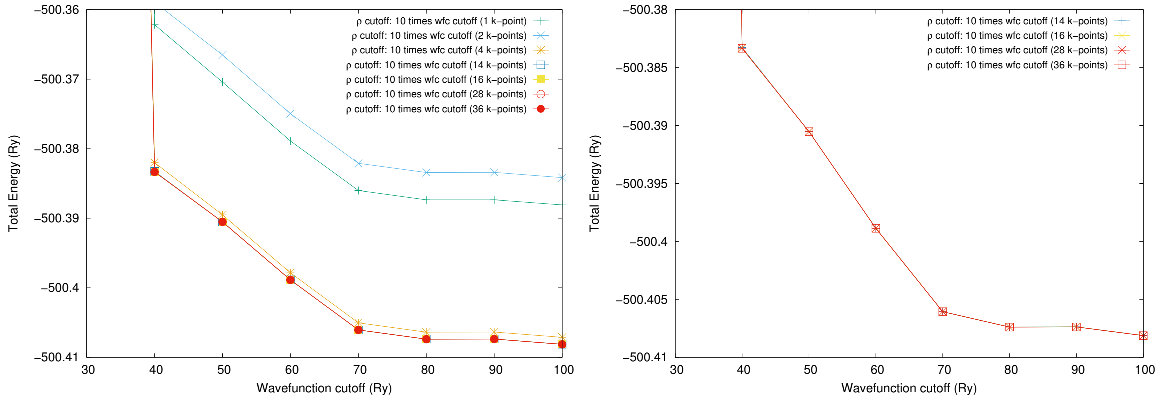

Fig. A.2 Convergence tests for the full trans backbone structure such as the α and δ phases (24 atoms models: 24 milli Rydbergs tollerance), with the ideal kinetic energy cutoff of the charge density ten times the kinetic energy cutoff of the wavefunction (for US pseudopotentials). Left: Convergence overview; Right: Convergence zoomed in the milli Rydbergs range were cutoffs were accepted.

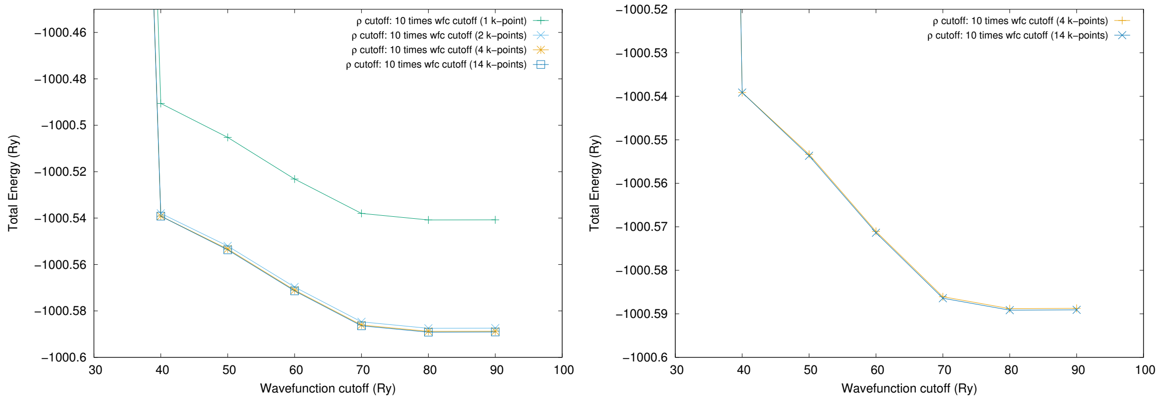

Fig. A.3 Convergence tests for the full trans backbone structure such as the γ and ε phases (48 atoms models: 48 milli Rydbergs tollerance), with the ideal kinetic energy cutoff of the charge density ten times the kinetic energy cutoff of the wavefunction (for US pseudopotentials). Left: Convergence overview; Right: Convergence zoomed in the milli Rydbergs range were cutoffs were accepted.

A.2 Table of conversions and calculations

Table A.1 reported the constants used to convert the magnitude and metric of specific values along data gathered from simulations and reported where appropriate in the thesis body. The R$_g$ is calculated per every single axis weighting every atomic coordinate of that axis r_j with the atomic weight m_j of the specie and divided by the molecule mass n to have the 3D coordinate of the centre of mass of the molecule and calculating the average distance of every atom from such centre for a, b and c axes ($\langle ... \rangle_{x,y,z}$), retrieving the R$_g$ of a molecule (the iterator j is the atom index). The R$_e$ is calculated by getting the euclidean space distance between an atom found at one end of the molecule to an atom found to the other end of the molecule. The conformation tensor is calculated by appreciating the averaged distance that every atom within the simulation box walked across the period of time considered normalised by the R$_e$^{2}, repeated per every axis (e.g. C$_{xx}$, C$_{xy}$, C$_{xz}$,C$_{yx}$,C$_{yy}$, etc).

Table A.1 Table of conversion constants and calculations used in the thesis taken from the NIST CODATA database[33]. Std.: Standard deviation; R$_g$: Radius of gyration; R$_e$: End to end distance; Tensor: Conformation tensor

Conversions constants		
From	To	Exact constant value
Ry	eV	13.605691930242388
Ry	kJ mol^{-1}	1312.7496997450642
eV	kJ mol^{-1}	96.48533288249876
kcal mol^{-1}	kJ mol^{-1}	4.184
Bohr	Å	0.52917721067
Calculations		
Std.	$\sigma = \sqrt{\frac{1}{N} \Sigma_1^N (x_i - \mu)^2}$	
R$_g$	$\langle \Sigma_0^j \, \frac{\lvert r_j - \Sigma_0^j \frac{r_j m j}{n} \rvert}{j} \rangle_{x,y,z}$	
R$_e$	$euclidean = \lvert (x_{ja}, y_{ja}, z_{ja}), (x_{jb}, y_{jb}, z_{jb}) \rvert$	
Tensor	$\langle \frac{3RR}{\langle R_e^2 \rangle} \rangle$	

A.3 DFT additional data

A.3.1 Partial DOS using the PBE functional

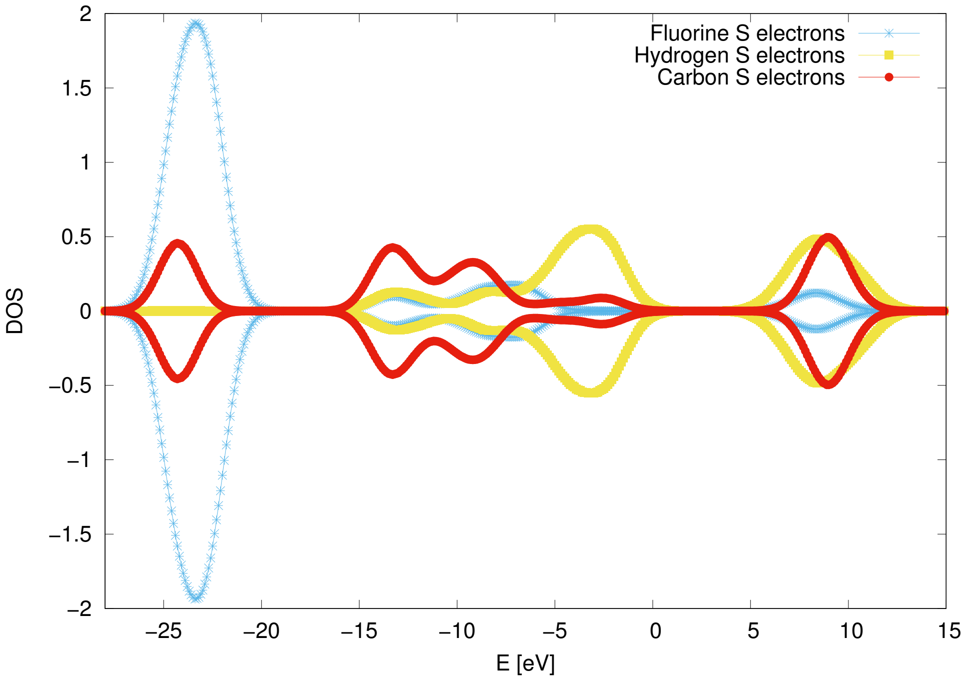

Fig. A.4 Partial DOS *s* electrons projection of the β-phase using PBE.

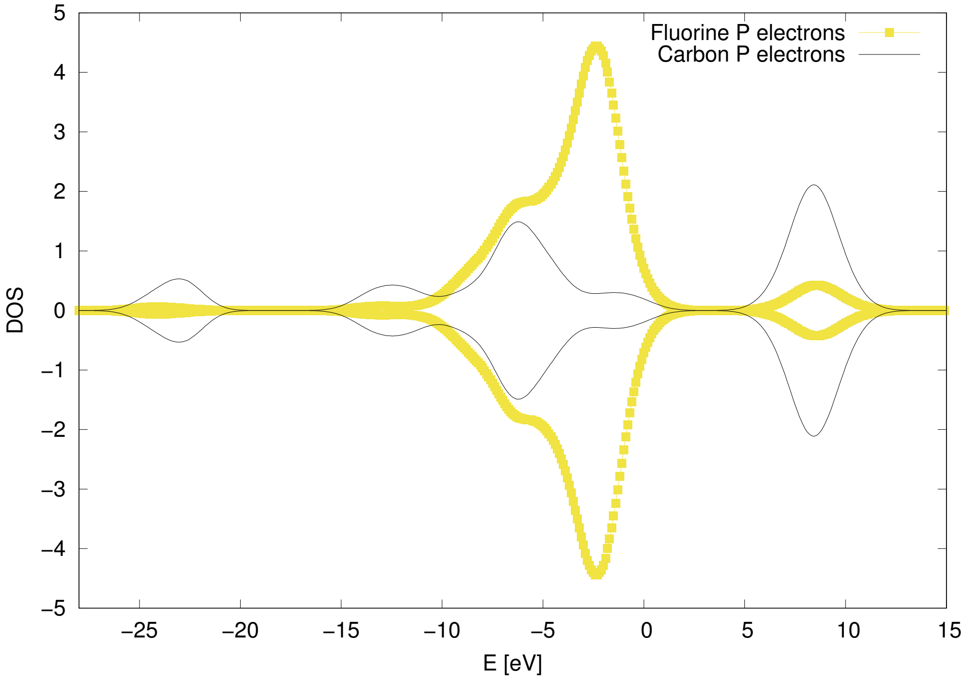

Fig. A.5 Partial DOS p electrons projection of the β-phase using PBE.

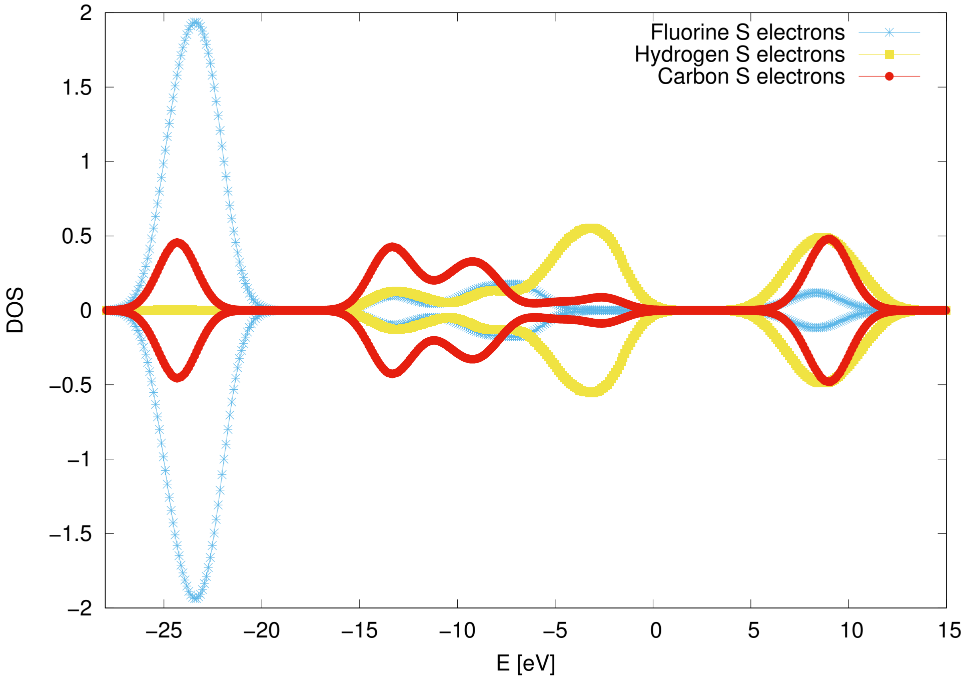

Fig. A.6 Partial DOS s electrons projection of the ζ-phase using PBE.

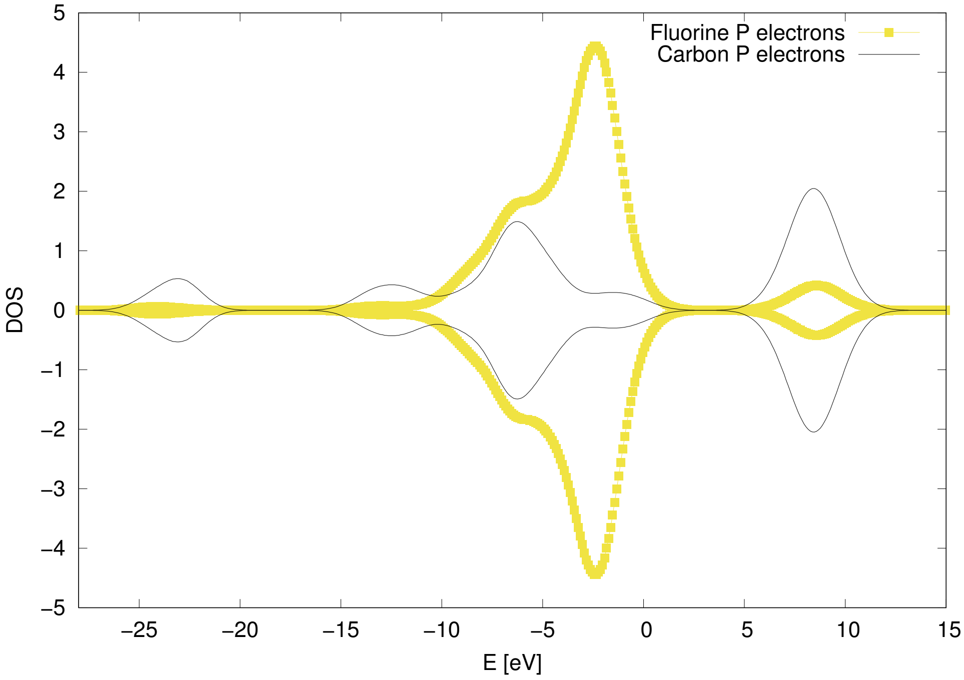

Fig. A.7 Partial DOS p electrons projection of the ζ-phase using PBE.

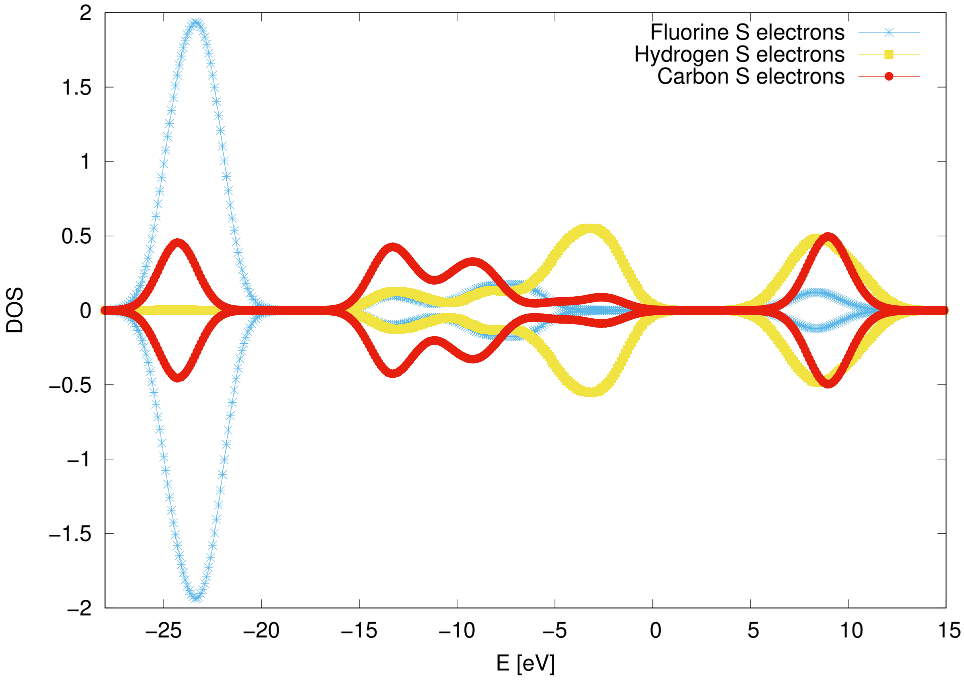

Fig. A.8 Partial DOS s electrons projection of the α-phase using PBE.

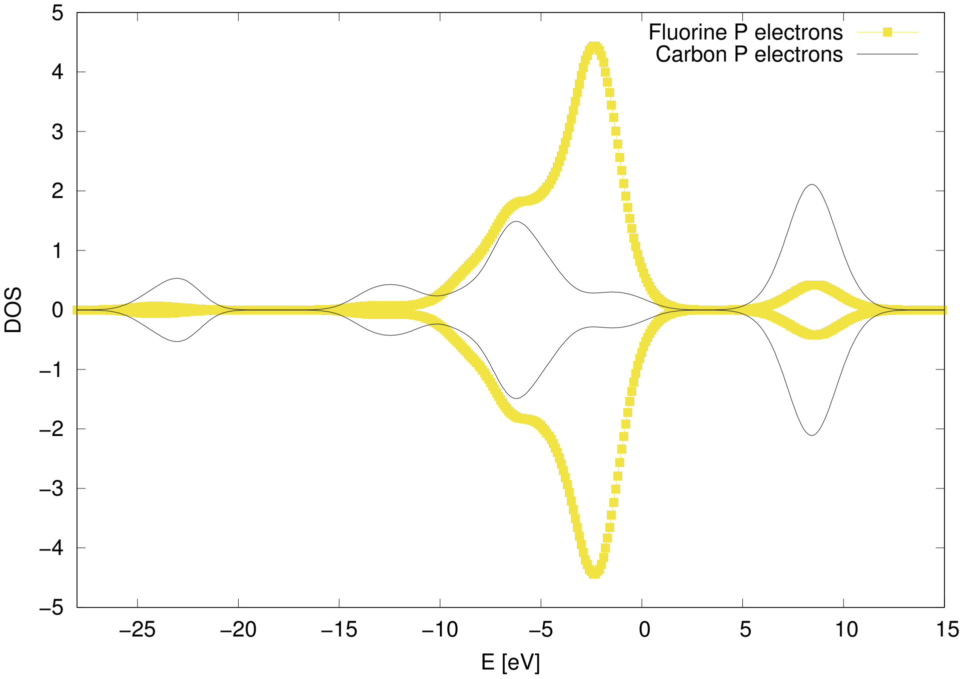

Fig. A.9 Partial DOS p electrons projection of the α-phase using PBE.

A.3.2 Electronic structures performed with vdW-DF

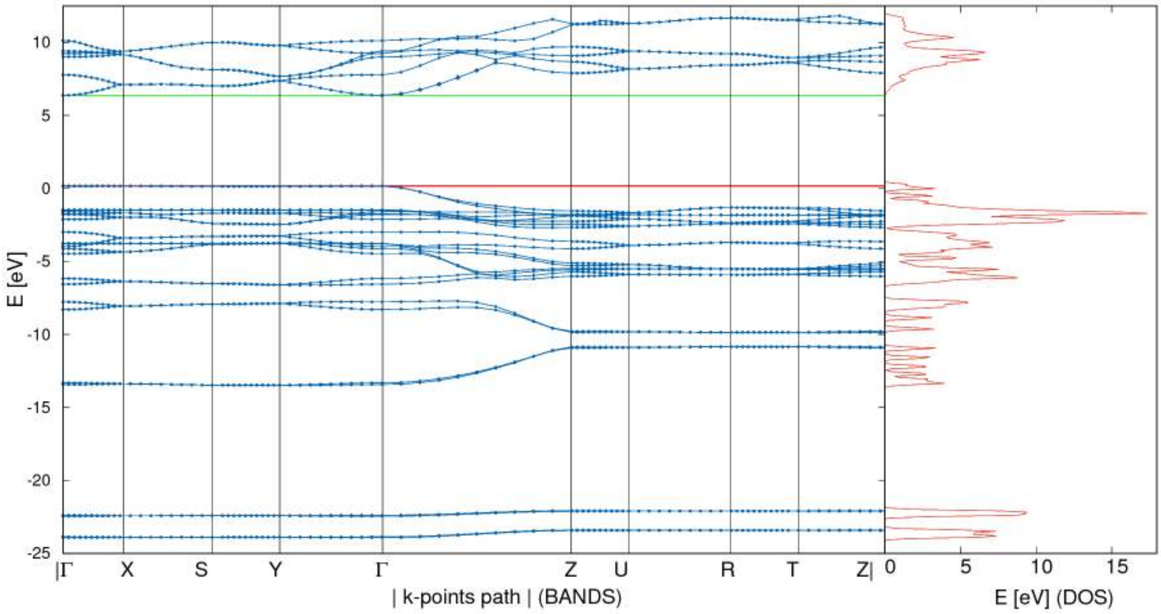

Fig. A.10 Bands structure and DOS states of the β-phase using vdW-DF.

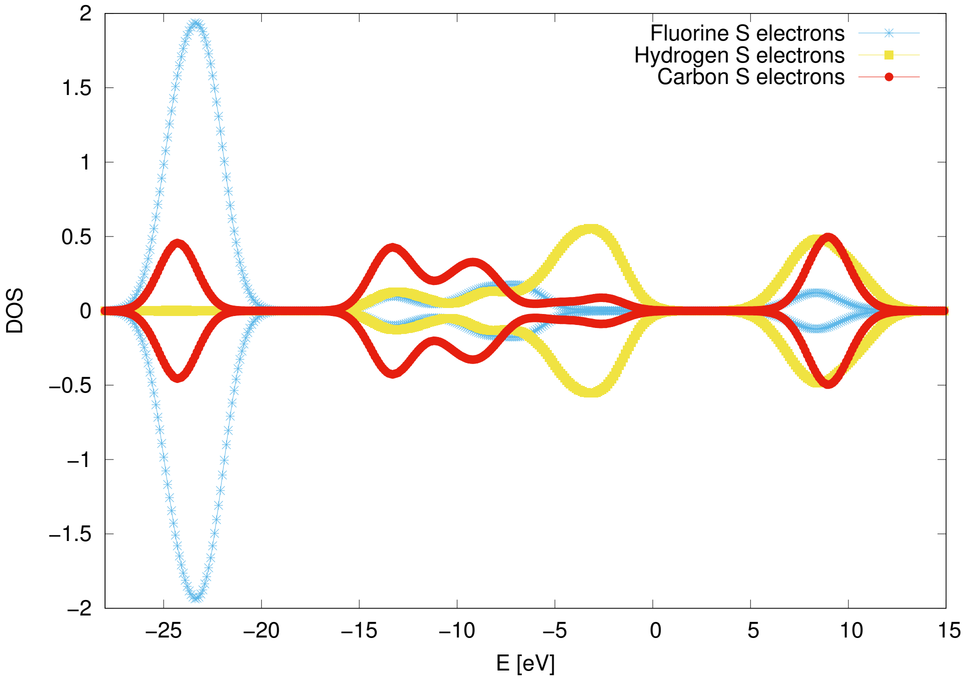

Fig. A.11 Partial DOS *s* electrons projection of the β-phase using vdW-DF.

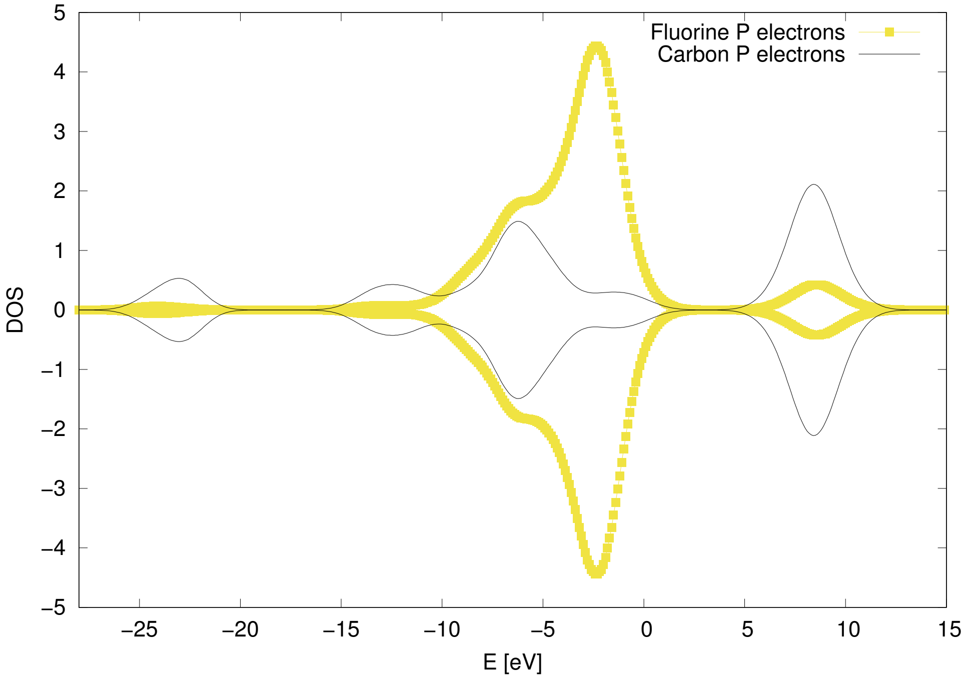

Fig. A.12 Partial DOS p electrons projection of the β-phase using vdW-DF.

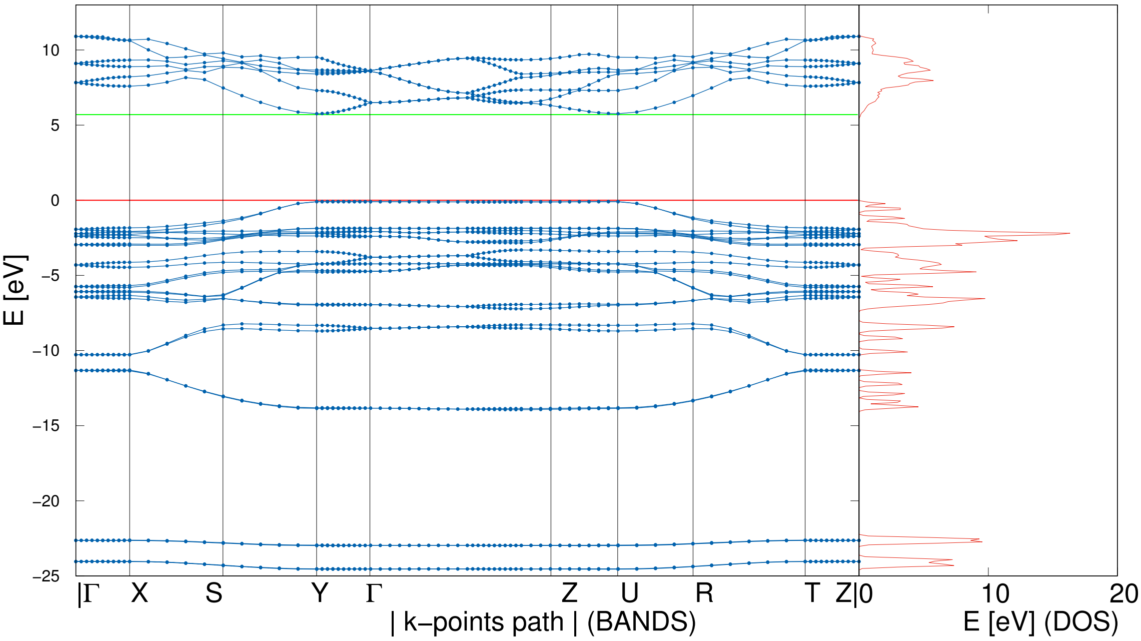

Fig. A.13 Bands structure and DOS states of the ζ-phase using vdW-DF.

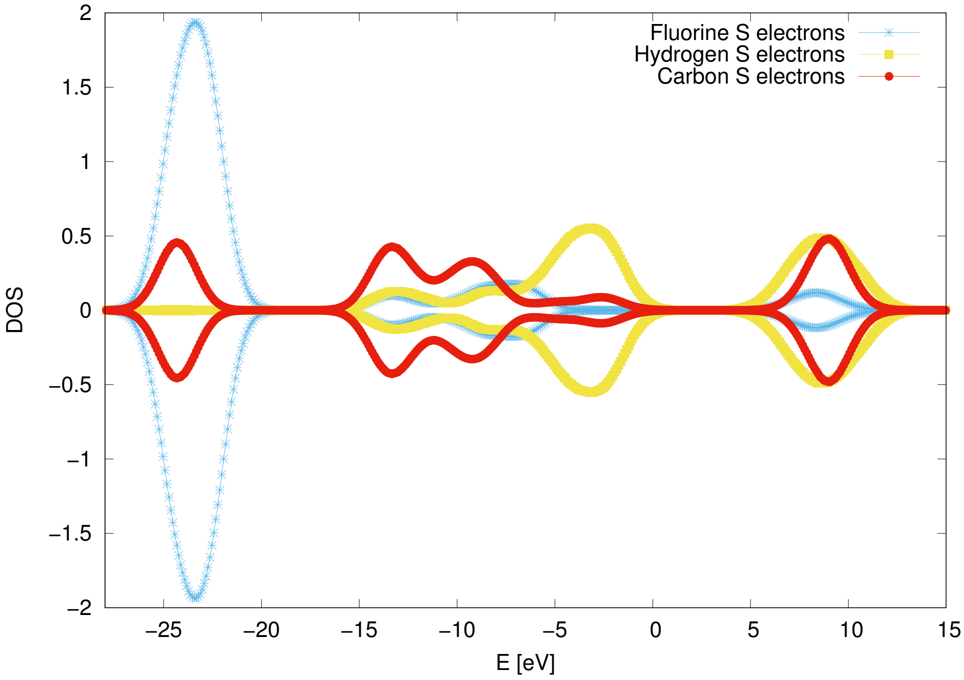

Fig. A.14 Partial DOS *s* electrons projection of the ζ-phase using vdW-DF.

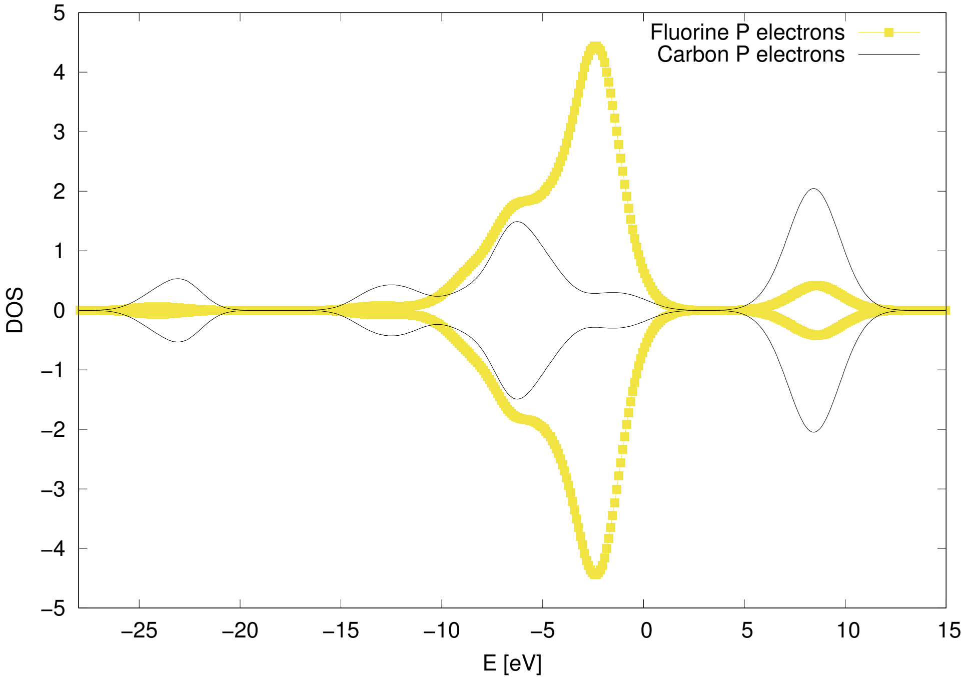

Fig. A.15 Partial DOS *p* electrons projection of the ζ-phase using vdW-DF.

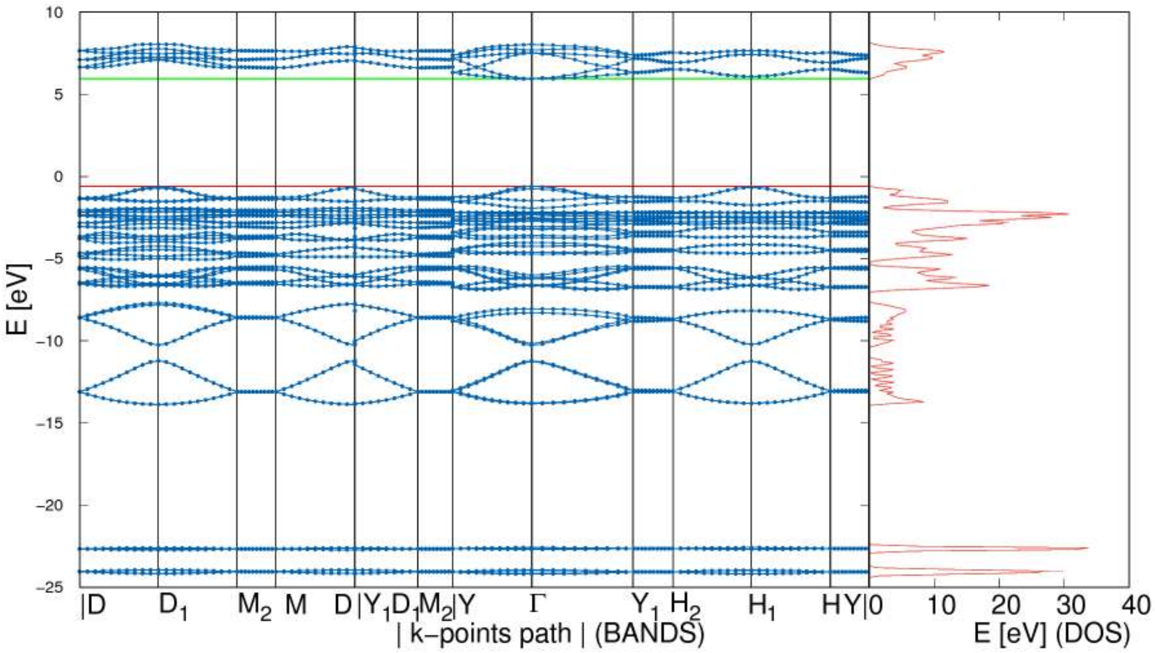

Fig. A.16 Bands structure and DOS states of the α-phase using vdW-DF.

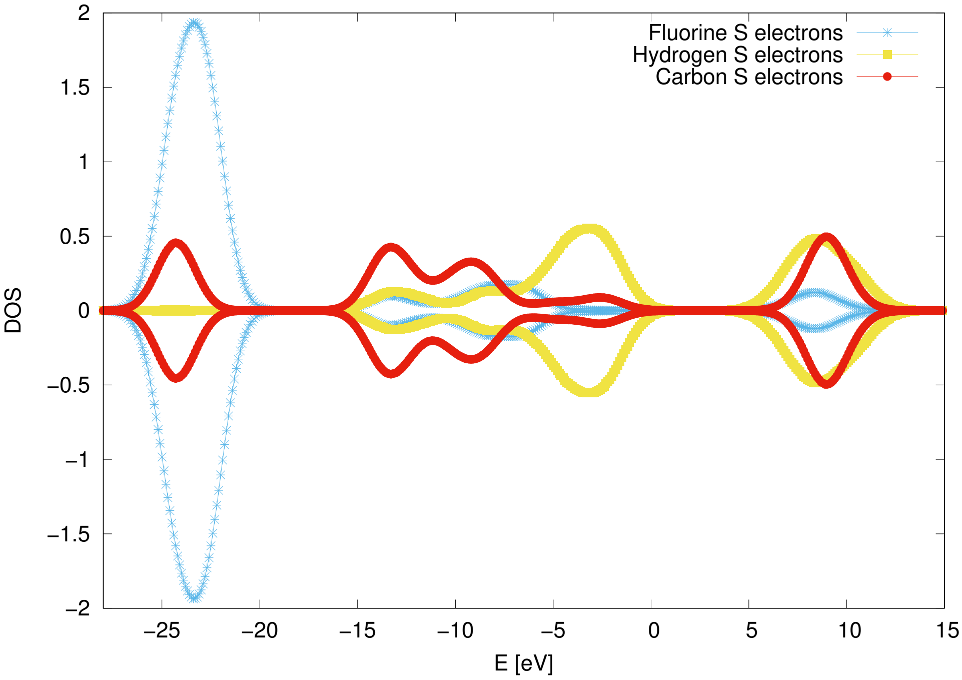

Fig. A.17 Partial DOS s electrons projection of the α-phase using vdW-DF.

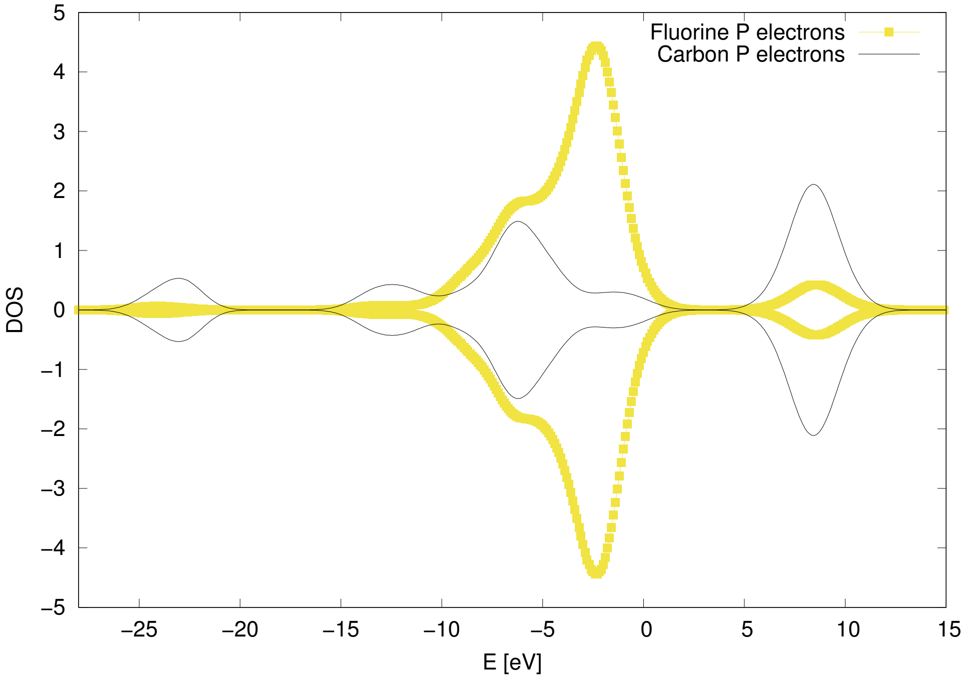

Fig. A.18 Partial DOS *p* electrons projection of the α-phase using vdW-DF.

A.3.3 Correlation Plots

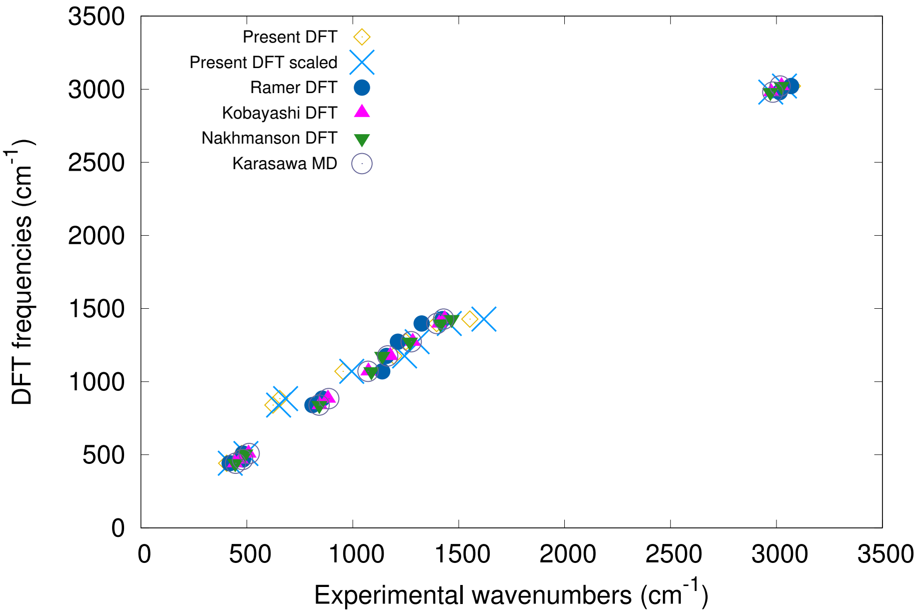

Fig. A.19 Correlation plot of the computed β-phase frequencies with the experimental frequencies.

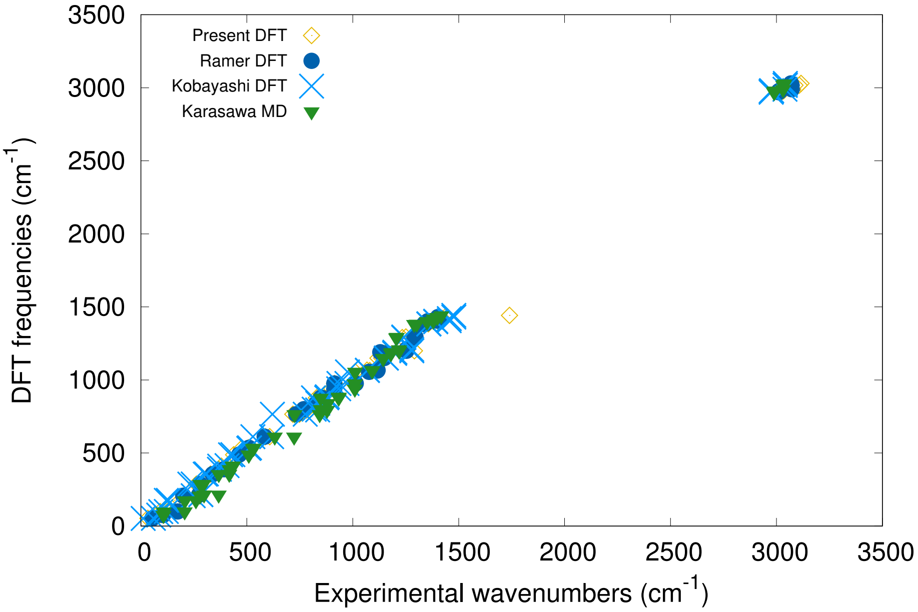

Fig. A.20 Correlation plot of the computed α-phase frequencies with the experimental frequencies.

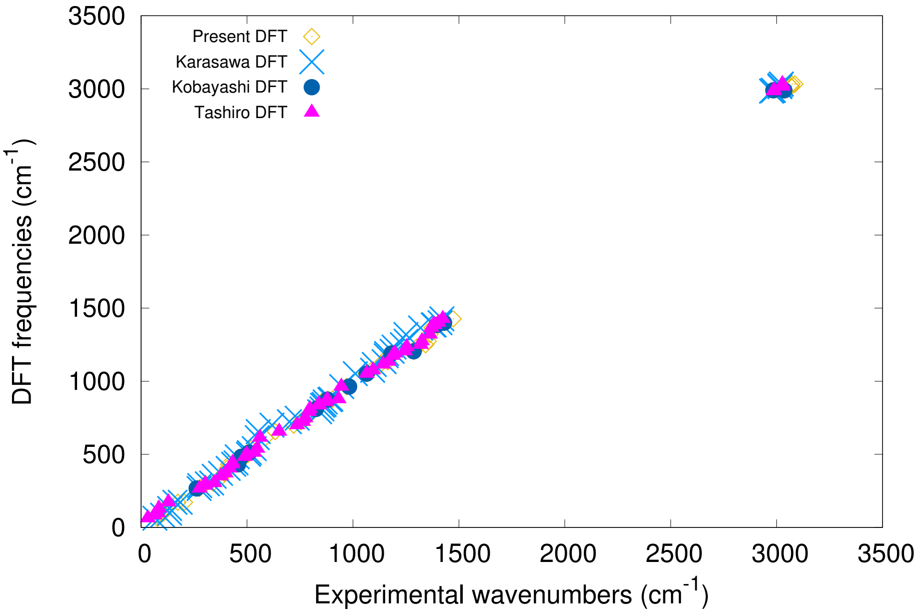

Fig. A.21 Correlation plot of the computed γ-phase frequencies with the experimental frequencies.

A.3.4 Vibrational frequencies of the ε_{uu} and ε_{ud} crystals

Table A.2 Vibrational frequencies of the ε_{uu}-PVDF.

(cm^{-1}) Present ε_{uu}	Modes	IR
3083	$\nu_a(CH_2)$	0.10
3075	$\nu_a(CH_2)$	0.37
3071	$\nu_a(CH_2)$	0.13
3065	$\nu_a(CH_2)$	0.11
3031	$\nu_s(CH_2)$	0.04
3022	$\nu_s(CH_2)$	0.09
3014	$\nu_s(CH_2)$	0.13
3011	$\nu_s(CH_2)$	0.07
1501	$\delta(CH_2)+w(CH_2)$	0.06
1414	$\delta(CH_2)$	0.05
1404	$\delta(CH_2)$	0.09
1393	$\delta(CH_2)$	0.19
1384	$\delta(CH_2)+w(CH_2)$	0.29
1364	$w(CH_2)$	0.32
1352	$w(CH_2)$	0.07
1346	$w(CH_2)$	1.22
1302	$t(CH_2)$	0.16
1281	$w(CH_2)$	0.18
1252	$w(CH_2)$	0.09
1223	$w(CH_2)+\delta(CCC)$	1.49
1198	$w(CH_2)+\delta(CCC)$	0.10
1183	$w(CH_2)+\delta(CCC)-\nu_s(CC)$	4.71
1158	$\delta(CCC)+r(CH_2)$	0.56
1136	$\delta(CCC)+r(CH_2)-\nu_s(CC)$	18.0
1113	$w(CH_2)+\nu_s(CC)$	5.34
1090	$\delta(CCC)+w(CH_2)$	0.49
1069	$\delta(CCC)+w(CH_2)$	0.41
3080	$\nu_a(CH_2)$	0.12
3074	$\nu_a(CH_2)$	0.13
3067	$\nu_a(CH_2)$	0.04
3064	$\nu_a(CH_2)$	0.01
3023	$\nu_s(CH_2)$	0.09
3021	$\nu_a(CH_2)$	0.13
3011	$\nu_s(CH_2)$	0.00
3010	$\nu_s(CH_2)$	0.02
1415	$\delta(CH_2)$	0.10
1407	$\delta(CH_2)$	0.55
1399	$\delta(CH_2)$	0.62
1392	$\delta(CH_2)$	0.10
1366	$w(CH_2)+w(CH_2)$	0.65
1361	$\delta(CH_2)+w(CH_2)$	14.0
1348	$w(CH_2)$	3.24
1337	$w(CH_2)$	1.60
1301	$w(CH_2)$	0.11
1278	$w(CH_2)$	0.44
1244	$w(CH_2)$	0.14
1221	$w(CH_2)+\delta(CCC)$	3.50
1185	$w(CH_2)+\delta(CCC)$	12.7
1180	$w(CH_2)+\delta(CCC)-\nu_a(CC)$	7.43
1150	$\delta(CCC)+r(CH_2)$	11.67
1124	$\delta(CCC)+w(CH_2)$	5.14
1104	$w(CH_2)+\nu_s(CC)$	1.00
1073	$\delta(CCC)+w(CH_2)$	0.77
1065	$\delta(CCC)+w(CH_2)-\nu_s(CC)$	2.11

1049	$\delta(CCC) + w(CH_2) - \nu_s(CC)$	0.18	1033	$\delta(CCC)+w(CH_2)$	2.01
1027	$\delta(CCC)+w(CH_2)$	4.62	1024	$\delta(CCC)+t(CH_2)$	0.26
1008	$t(CH_2)$	0.42	999	$t(CH_2)-\nu_s(CC)$	2.36
974	$t(CH_2)-\delta(CCC)$	0.02	971	$t(CH_2) + w(CH_2) - \delta(CCC)$	0.03
896	$t(CH_2)+\delta(CCC)$	0.18	896	$w(CH_2)+\delta(CCC)$	0.14
869	$w(CH_2)$	0.29	865	$w(CH_2)$	0.47
862	$w(CH_2)$	0.82	844	$w(CH_2)$	1.60
842	$w(CH_2)+r(CH_2)$	2.50	837	$t(CH_2)+r(CH_2)$	0.69
835	$r(CH_2)+t(CH_2)$	0.03	834	$t(CH_2)$	1.09
828	$r(CH_2)+w(CH_2)$	0.36	824	$r(CH_2)+w(CH_2)$	12.48
806	$\nu_a(CF_2) + w(CH_2) - \delta(CCC)$	1.81	790	$\nu_a(CF_2) + \nu_s(CF_2) + \delta(CCC)$	1.16
779	$\delta(CCC)$	0.86	776	$\delta(CCC)+\nu_s(CF_2)$	0.75
759	$\delta(CCC)+\nu_s(CF_2)$	0.84	750	$\delta(CCC)$	0.68
747	$\delta(CCC) + w(CF_2) + r(CH_2)$	1.41	732	$\delta(CCC) + w(CF_2) + r(CH_2)$	2.08
700	$r(CH_2)+\delta(CCC)$	0.09	690	$r(CH_2)+\delta(CCC)$	0.05
588	$r(CH_2)+r(CF_2)$	0.55	539	$\delta(CCC)+\delta(CF_2)$	0.21
525	$\delta(CCC) + \delta(CF_2) - r(CH_2)+w(CH_2)$	0.20	523	$\delta(CCC)+\delta(CF_2)$	0.05
520	$\delta(CCC) + \delta(CF_2) + r(CH_2)$	0.01	516	$\delta(CF_2) + \delta(CCC) + r(CH_2)$	0.21
515	$\delta(CF_2) + \delta(CCC) + r(CH_2)$	0.76	505	$\delta(CF_2)+w(CH_2)$	0.24
487	$\delta(CF_2)+r(CH_2)$	1.12	467	$\delta(CF_2)+w(CH_2)$	0.93
459	$w(CH_2)$	1.74	449	$w(CH_2)-\delta(CF_2)$	1.18
424	$w(CH_2)+w(CF_2)$	0.51	409	$w(CH_2)+w(CF_2)$	0.02
406	$w(CH_2)-w(CF_2)$	0.24	402	$w(CH_2)$	0.09
389	$w(CH_2)$	0.03	386	$w(CH_2)+w(CF_2)$	0.02
378	$w(CH_2)+w(CF_2)$	0.02	377	$w(CH_2)+w(CF_2)$	0.06
353	$w(CH_2)+w(CF_2)$	0.17	343	$w(CH_2)$	0.02
318	$w(CH_2)+w(CF_2)$	0.02	308	$w(CH_2)+w(CF_2)$	0.05
297	$w(CH_2) + w(CF_2) - \delta(CCC)$	0.05	290	$\delta(CCC)+\delta'(CCC)$	0.16

285	$\delta(CCC)+w(CF_2)$	0.10	271	$w(CF_2)$	0.03
252	$\delta(CCC)$	0.03	252	$\delta(CCC)+w(CH_2)$	0.00
246	$\delta(CCC)+w(CH_2)$	0.00	238	$\delta(CCC)$	0.00
224	$\delta(CCC)$	0.00	218	$\delta(CCC)+\delta'(CCC)$	0.03
217	$\delta(CCC)+r(CH_2)$	0.00	208	$\delta(CCC)+r(CH_2)$	0.01
189	$\delta(CCC)+w(CH_2)+w(CF_2)$	0.00	176	$w(CH_2)+w(CF_2)$	0.08
157	$\delta(CCC)+\delta'(CCC)$	0.16	128	$w(CH_2)$	0.01
121	$w(CH_2)+w(CF_2)$	0.02	113	$L(T_c)$	0.05
109	$L(T_c)$	0.04	107	$L(T_c)$	0.03
102	$L(T_c)$	0.07	79	$L(T_b)$	0.06
71	$L(T_a)$	0.45	70	$L(T_a)$	0.06
39	τ_a	0.08	34	τ_a	0.03
29	τ_s	0.02	26	τ_s	0.02
14	τ_s	0.04	7	τ_a	0.00

Table A.3 Vibrational frequencies of the ε_{ud}-PVDF.

(cm^{-1})			(cm^{-1})		
Present	Modes	IR	Present	Modes	IR
	ε_{ud}		ε_{ud}		
3079	$\nu_a(CH_2)$	0.07	3073	$\nu_a(CH_2)$	0.24
3071	$\nu_a(CH_2)$	0.66	3071	$\nu_a(CH_2)$	0.21
3061	$\nu_a(CH_2)$	0.01	3053	$\nu_a(CH_2)$	0.05
3053	$\nu_a(CH_2)$	0.17	3052	$\nu_a(CH_2)$	0.10
3022	$\nu_s(CH_2)$	0.06	3021	$\nu_s(CH_2)$	0.03
3019	$\nu_s(CH_2)$	0.43	3017	$\nu_s(CH_2)$	0.12
3002	$\nu_s(CH_2)$	0.02	2999	$\nu_s(CH_2)$	0.01
2998	$\nu_s(CH_2)$	0.08	2997	$\nu_s(CH_2)$	0.10
1437	$\delta(CH_2)$	0.13	1433	$\delta(CH_2)$	0.15
1423	$\delta(CH_2)$	0.00	1411	$\delta(CH_2)$	0.46
1409	$\delta(CH_2)$	0.71	1405	$\delta(CH_2)$	0.15
1402	$\delta(CH_2)$	0.04	1401	$\delta(CH_2)$	0.05
1381	$w(CH_2)$	0.78	1365	$w(CH_2)$	2.46
1353	$w(CH_2)$	7.26	1352	$w(CH_2)$	0.05
1342	$w(CH_2)$	2.83	1341	$w(CH_2)$	4.24

1337	$w(CH_2)$	0.07	1332	$w(CH_2)$	1.19
1309	$w(CH_2)$	0.55	1306	$w(CH_2)$	0.13
1285	$w(CH_2)$	0.65	1281	$w(CH_2)$	0.06
1252	$t(CH_2)$	0.64	1246	$t(CH_2)$	0.56
1238	$w(CH_2)$	2.04	1229	$w(CH_2)$	0.16
1198	$w(CH_2)+\delta(CCC)$	2.64	1192	$\nu_a(CC)$	8.73
1191	$\nu_a(CC)$	10.74	1173	$w(CH_2)$	16.75
1159	$r(CH_2)$	3.48	1152	$r(CH_2)-\nu_s(CC)$	0.96
1140	$\delta(CCC)$	18.80	1139	$\delta(CCC)$	0.01
1104	$\nu_a(CC)+w(CH_2)$	0.58	1097	$\nu_a(CC)-r(CH_2)$	2.69
1087	$w(CH_2)+w(CF_2)$	1.64	1083	$w(CH_2)$	0.49
1072	$w(CH_2)$	0.36	1067	$w(CH_2)$	2.68
1056	$w(CH_2)$	0.20	1045	$w(CH_2)-\nu_a(CC)$	1.15
1034	$\nu_a(CC)+\nu_a(CH_2)$	3.14	1029	$r(CH_2)$	2.48
1008	$w(CH_2)$	0.21	1001	$w(CH_2)$	1.36
972	$w(CH_2)$	0.26	968	$w(CH_2)$	0.02
916	$w(CH_2)$	0.10	914	$w(CH_2)$	0.48
870	$w(CH_2)$	0.05	865	$t(CH_2)$	0.46
862	$t(CH_2)$	0.16	855	$t(CH_2)$	0.08
849	$t(CH_2)$	3.58	838	$r(CH_2)$	1.01
837	$r(CH_2)$	0.03	834	$w(CH_2)-w(CH_2)$	3.57
830	$t(CH_2)$	0.75	827	$t(CH_2)$	10.83
797	$r(CH_2)$	0.87	791	$r(CH_2)+\nu_s(CF_2)$	1.70
781	$r(CH_2)+\nu_s(CF_2)$	2.35	777	$r(CH_2)+\nu_s(CF_2)$	0.24
760	$r(CH_2)-\nu_a(CF_2)$	0.29	750	$r(CH_2)-\nu_a(CF_2)$	0.54
740	$r(CH_2)+\nu_a(CF_2)$	1.35	736	$r(CF_2)+r(CH_2)$	0.48
700	$r(CF_2)-r(CH_2)$	0.04	695	$r(CH_2)$	0.02
602	$r(CF_2)+r(CH_2)$	0.16	569	$\nu_s(CC)$	0.57
529	$r(CH_2)-\delta(CF_2)$	0.08	529	$r(CH_2)+\delta(CF_2)$	0.09
515	$\delta(CF_2)-\delta(CH_2)$	0.00	514	$\delta(CF_2)$	0.01
512	$r(CH_2)+\delta(CF_2)$	1.07	512	$r(CH_2)+\delta(CF_2)$	0.16
487	$r(CH_2)+\delta(CF_2)-\nu_a(CC)$	0.77	480	$\delta(CF_2)+\delta(CCC)$	0.19
459	$t(CH_2)$	3.55	455	$t(CH_2)$	0.27
419	$t(CH_2)$	0.07	408	$t(CH_2)$	0.05
404	$t(CH_2)$	0.45	399	$t(CH_2)$	0.15

386	$t(CH_2)+t(CF_2)$	0.01	383	$t(CH_2)$	0.04
381	$t(CH_2)$	0.01	376	$t(CH_2)$	0.01
347	$t(CH_2)-t(CF_2)$	0.05	347	$t(CH_2)-t(CF_2)$	0.00
326	$t(CH_2)+t(CF_2)$	0.00	303	$t(CH_2)+\delta(CCC)$	0.02
292	$\delta(CCC)$	0.00	288	$\delta(CCC)+w(CF_2)$	0.09
283	$w(CF_2)$	0.30	280	$t(CF_2)$	0.04
251	$w(CH_2)$	0.00	251	$w(CF_2)$	0.00
242	$w(CH_2)$	0.00	240	$\delta(CCC)$	0.03
228	$\nu_s(CC)$	0.01	221	$\delta(CCC)$	0.02
200	$\delta(CCC)+\delta'(CCC)$	0.00	199	$\delta(CCC)$	0.03
196	$t(CH_2)$	0.02	194	$r(CH_2)$	0.01
151	$\delta'(CCC)$	0.01	143	$\delta(CCC)$	0.16
139	$\delta(CCC)$	0.00	107	$w(CH_2)$	0.04
106	$r(CH_2)$	0.07	97	$L(T_c)$	0.01
86	τ_a	0.04	85	τ_a	0.00
62	τ_a	0.02	59	τ_s	0.01
43	τ_a	0.01	38	τ_s	0.01
37	$L(T_b)$	0.11	24	$L(T_b)$	0.04
21	τ_a	0.12	15	τ_a	0.05

A.4 Additional data of the liquid bulk equilibration phase

The Table A.4 shows that the system kept steady at 500 K further cooled with the same 10 ns ramp at 400 K and 300 K and kept stable at both temperatures for 30 ns for each case brought the system conformation tensor to significantly diverge from the identity matrix which is synonymous of a liquid system randomly disordered, hence, assumed to be at the liquid phase equilibrium. In Table A.4-A is possible to appreciate that the steady state at 400 K was described by a conformation tensor which diverge from the identity matrix, and even more divergent in Table A.4-B the conformation tensor of the steady state at 300 K was found, meaning that in such cases the molecule's mobility within the system progressively decreased with the temperature decrease and brought the system to be solid, even thought, the system remained amorphous.

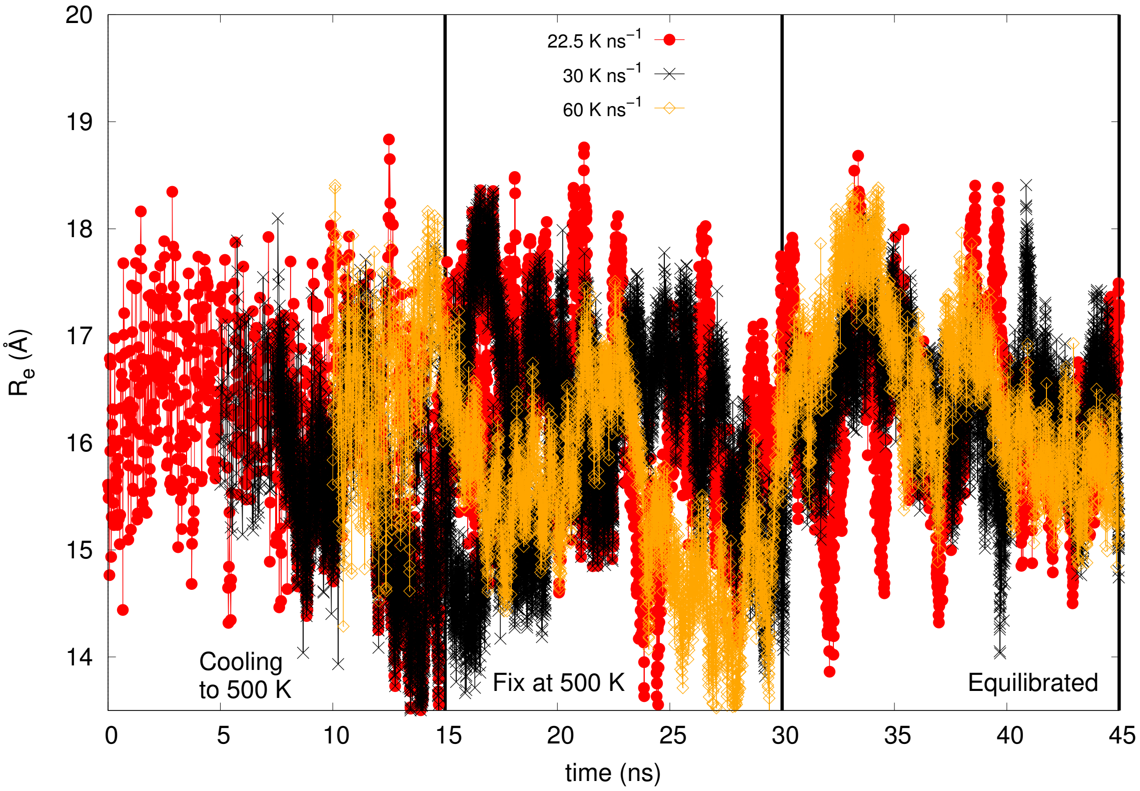

Fig. A.22 R_e as function of time of bulk PDVF annealed at 800 K and cooled to to 500 K using 3 different cooling rates using the B&S FF.

Table A.4 Conformation tensor for the B&S force field during fixed temperature dynamics runs. A: system cooled at 400 K in 10 ns after the 30 ns steady at 500 K and kept for 30 ns at 400 K where here the last 15 ns were showed; B:system cooled at 300 K in 10 ns after the 30 ns steady at 400 K and kept for 30 ns at 300 K where here the last 15 ns were showed.

	A	B
C_{xx}	0.597	0.260
C_{yy}	1.451	1.882
C_{zz}	1.399	1.741

Table A.5 Conformation tensor for the B&S force field during fixed temperature dynamics runs. A: constant heating at 600 K per 40 ns; B: cooling at 500 K in 10 ns; C: 15 ns stable at 500 K; D: extra 15 ns stable at 500 K.

	A	B	C	D
C_{xx}	1.102	1.220	1.720	1.747
C_{yy}	1.160	0.789	0.371	0.327
C_{zz}	0.949	1.760	0.914	0.585

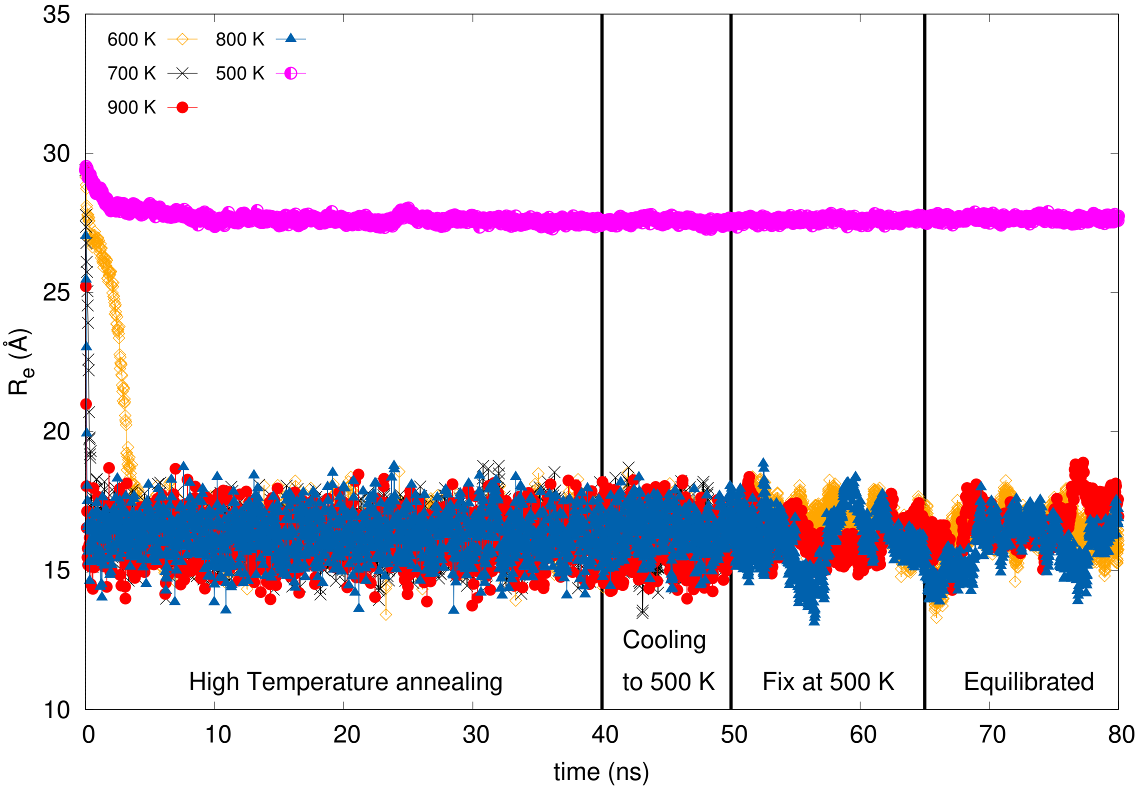

Fig. A.23 R_e as function of time of the annealing temperatures from 500 K up to 900 K using the B&S FF.

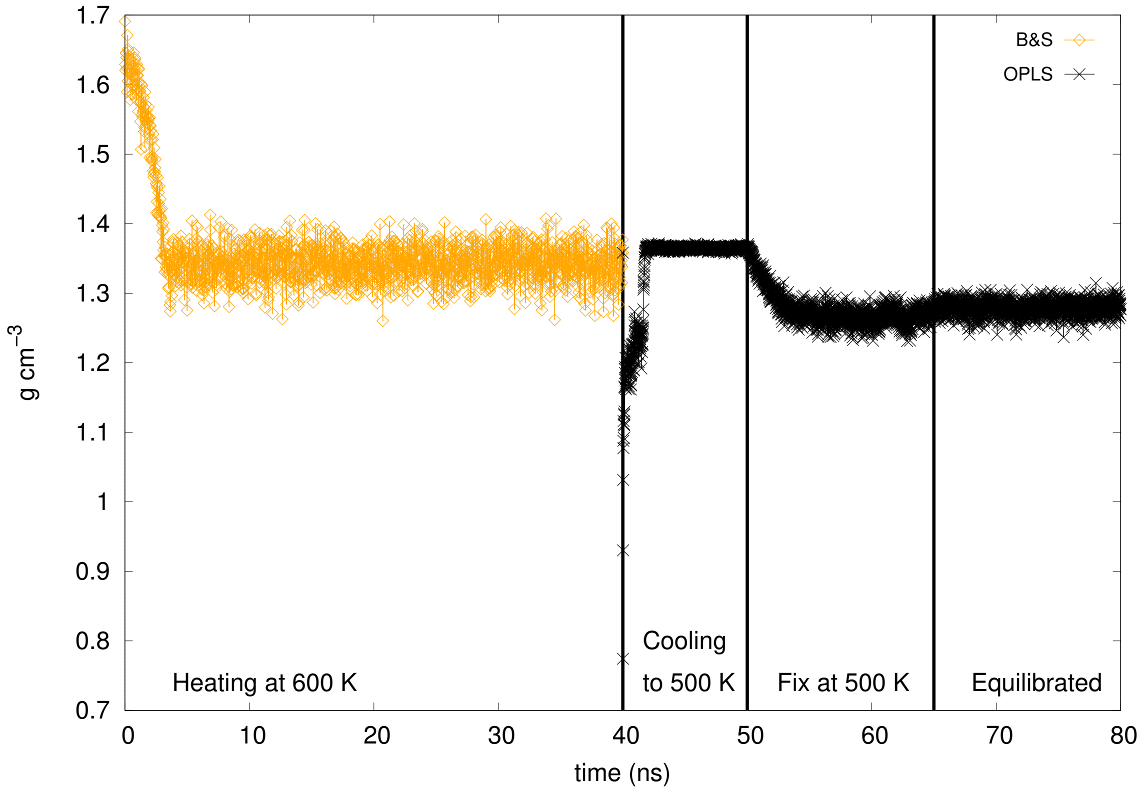

Fig. A.24 Density versus time of bulk β-PDVF short chains during hybrid equilibration procedure where the melted system was gathered from B&S force field dynamic at 600 K and passed into OPLS to cooling such disordered system steadily at 500 K. Heating at 600 K: thermal treatment at 600 K to melt the chains; Cooling: cooling process to bring the system to 500 K; Fix at 500 K: steady dynamic run at the fixed temperature of 500 K; Equilibrium: Equilibrium of the liquid phase.

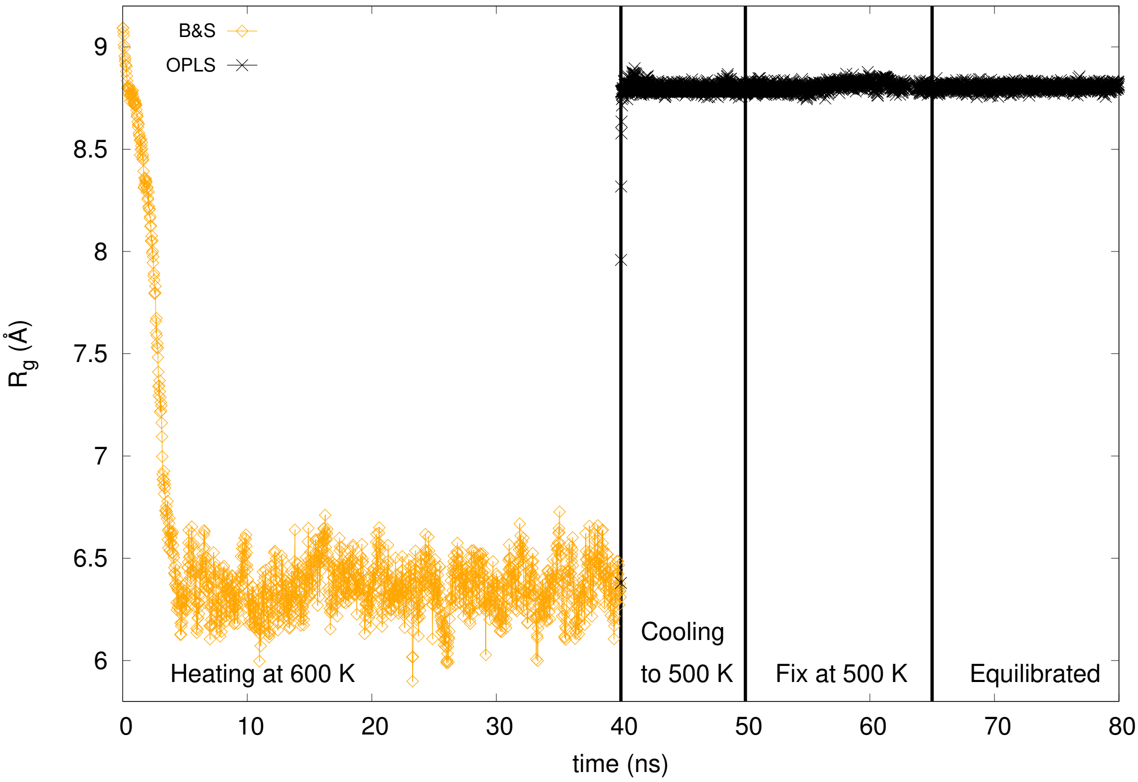

Fig. A.25 Radius of gyration versus time of bulk β-PDVF short chains during hybrid equilibration procedure where the melted system was gathered from B&S force field dynamic at 600 K and passed into OPLS to cooling such disordered system steadily at 500 K. Heating at 600 K: thermal treatment at 600 K to melt the chains; Cooling: cooling process to bring the system to 500 K; Fix at 500 K: steady dynamic run at the fixed temperature of 500 K; Equilibrium: Equilibrium of the liquid phase.

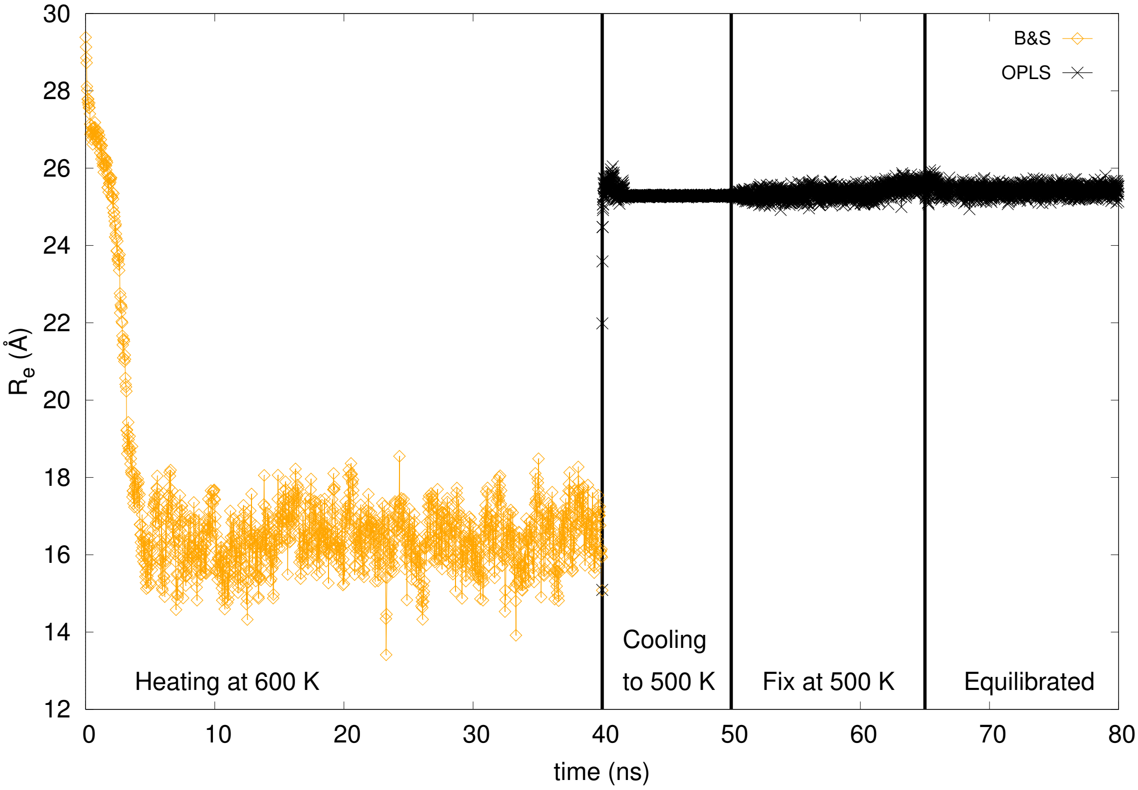

Fig. A.26 End to end distance versus time of bulk β-PDVF short chains during hybrid equilibration procedure where the melted system was gathered from B&S force field dynamic at 600 K and passed into OPLS to cooling such disordered system steadily at 500 K. Heating at 600 K: thermal treatment at 600 K to melt the chains; Cooling: cooling process to bring the system to 500 K; Fix at 500 K: steady dynamic run at the fixed temperature of 500 K; Equilibrium: Equilibrium of the liquid phase.

A.5 Additional data of the two graphene sheets surface model MD dynamics

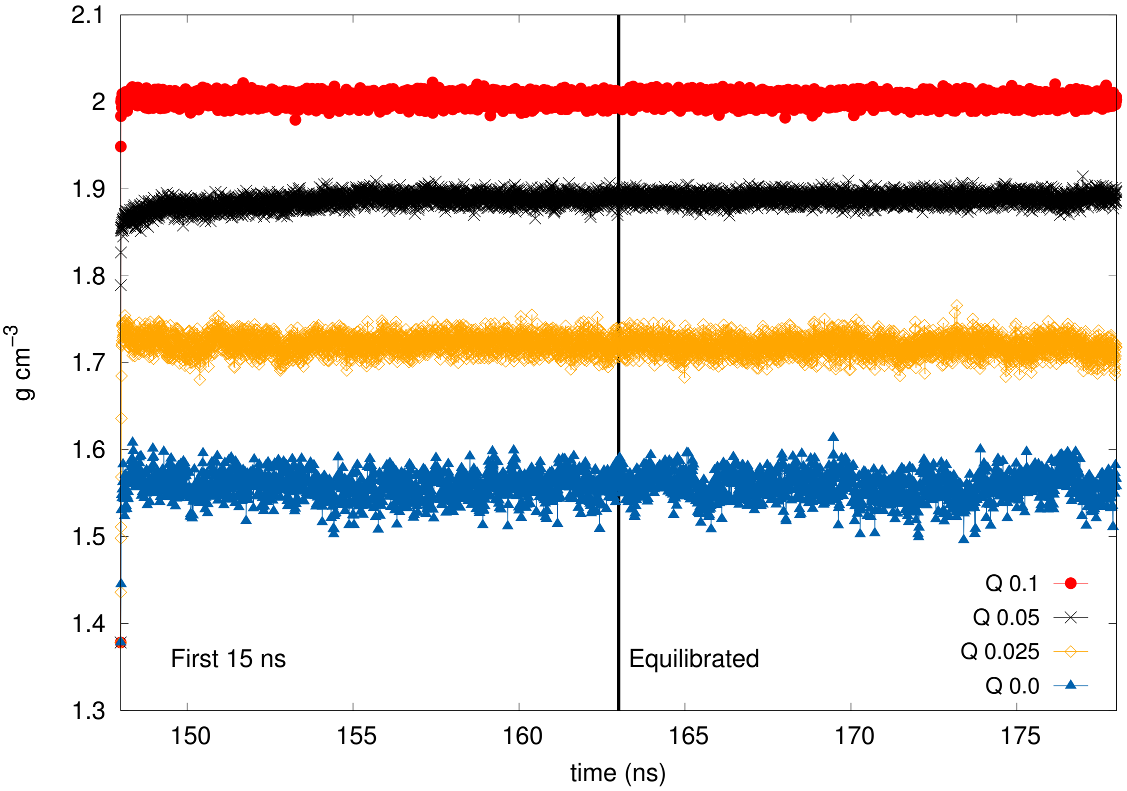

Fig. A.27 Density as function of time of the four computed replica with graphene layers differently charged from a Q of 0 up to 0.1 (*e*) using B&S FF.

Appendix B

Papers published, due to submission and future publications

B.1 Publications of chapter 4

B.1.1 PVDF crystal structure study of α, δ and β phases using first principle vdW (published)

Eur. Phys. J. Special Topics
© EDP Sciences, Springer-Verlag 2016
DOI: 10.1140/epjst/e2016-60133-8

THE EUROPEAN
PHYSICAL JOURNAL
SPECIAL TOPICS

Regular Article

A van der Waals density functional theory study of poly(vinylidene difluoride) crystalline phases

F. Pelizza[1,a], B.R. Smith[2], and K. Johnston[1,b]

[1] Department of Chemical and Process Engineering, University of Strathclyde,
75 Montrose Street, Glasgow G1 1XJ, UK
[2] WestCHEM, Department of Pure and Applied Chemistry, University of Strathclyde,
Thomas Graham Building, 295 Cathedral Street, Glasgow G1 1XL, UK

Received 25 April 2016 / Received in final form 9 June 2016
Published online 18 July 2016

Abstract. Ferroelectric polymers, such as poly(vinylidene difluoride) (PVDF), have many potential applications in flexible electronic devices. PVDF has six experimentally observed polymorphs, three of which are ferroelectric. In this work we use density functional theory to investigate the structural properties, energetics and polarisation of the stable α-phase, its ferroelectric analogue, the δ-phase, and the β-phase, which has the best ferroelectric properties. The results from a variety of exchange and correlation functionals were compared and it was found that van der Waals (vdW) interactions have an important effect on the calculated crystal structures and energetics, with the vdW-DF functional giving the best agreement with experimental lattice parameters. The spontaneous polarisation was found to strongly correlate with the unit cell volumes, which depend on the functional used. While the relative phase energies were not strongly dependent on the functional, the cohesive energies were significantly underestimated using the PBE functional. The inclusion of vdW interactions is, therefore, important to obtain the correct lattice structures, polarisation and energetics of PVDF polymorphs.

1 Introduction

Ferroelectric (FE) materials exhibit a spontaneous electric dipole moment that is switchable by an applied electric field and, hence, they play an important role in electronic devices, such as transistors, non-volatile memory, sensors, etc., [1]. To provide lightweight and flexible consumer devices, inflexible crystalline FE materials, such as perovskites, need to be replaced by low density, flexible FE materials, such as FE polymers, which have the additional benefit of being easy and potentially inexpensive to process [2,3].

---

[a] e-mail: `francesco.pelizza@strath.ac.uk`
[b] e-mail: `karen.johnston@strath.ac.uk`

Poly(vinylidene difluoride) (PVDF) is a particularly promising FE polymer due to its chemical stability and good ferroelectric, piezoelectric and pyroelectric properties [4]. The FE properties arise from a strong electric dipole moment in the PVDF monomer unit, which is due to the high electronegativity difference between fluorine and hydrogen atoms combined with a small enough monomer to allow switching at low coercive fields. Other polymers, such as poly(vinylidene dichloride) (PVDC), poly(vinylidene cyanide), and poly(aminodifluoroborane) also have monomer dipole moments but are not useful in FE devices due to either steric effects, which increase the coercive field, or chemical reactivity [4].

PVDF can exist in at least six known crystalline polymorphs, as well as in amorphous melt or glassy phases. The α-phase, which is thermodynamically stable at ambient conditions, is non-ferroelectric and chains have a $\mathrm{TG}^{+}\mathrm{TG}^{-}$ structure, where T and $\mathrm{G}^{+/-}$ stand for trans and ±gauche, respectively. The individual chains in this phase do have a dipole moment but are aligned antiparallel, which gives a zero net dipole moment of the crystal. If the chains are aligned parallel, this gives the ferroelectric δ-phase [5,6]. The β-phase has an (all-trans) planar zig-zag chain structure and is the polymorph with the highest spontaneous polarisation.

After crystallisation from melt or solution and subsequent thermal treatment, PVDF often exists as a mixture of polymorphs [7]. To estimate the fraction of each polymorph in a sample, experimentalists analyse diffraction patterns or vibrational spectra using information available about known crystal phases. Simulations are useful for providing information about the ideal crystal structures, and density functional theory (DFT) has been used to study crystalline phases of PVDF. Previous DFT studies have determined lattice parameters and polarisation of the β-phase [8,9], phase energetics [10,11], chain rotational barriers [9,12], elastic constants [13], structural and electronic properties of thin films [14] and vibrational spectra [15–17]. While these studies provided valuable insight into PVDF crystalline phases, most did not account for van der Waals (vdW) interactions, which are important for weakly bonded systems [18]. Only the study by Pei et al. [13] used the semi-empirical DFT-D2 vdW correction [19]. No one has previously applied the first-principles vdW-DF [20] or vdW-DF2 [21] functionals to studies of PVDF. A DFT vdW-DF study of polyethylene [18] showed that vdW interactions were essential to obtain accurate lattice parameters and cohesive energies and the results were in good agreement with experimental values.

The goal of this work is to investigate the structure and energetics of three common polymorphs of PVDF. We use density functional theory (DFT) with a variety of exchange and correlation (XC) functionals and vdW correction methods. We obtain crystal structures for the α, δ and β-phases and show that vdW interactions have an important impact on lattice parameters and cohesive energies. In addition, the value of the spontaneous polarisation for the β and δ-phases was found to correlate strongly with the calculated unit cell volume. The inclusion of vdW interactions is thus crucial for providing accurate information about PVDF crystal structures from DFT calculations.

Method

All calculations were performed with Quantum ESPRESSO (QE) [22], versions 5.2 and 5.3, which implements density functional theory using a planewave basis set. The study investigated the performance of different exchange and correlation (XC) functionals including the LDA, the PBE generalised gradient approximation (GGA) [23], the long range van der Waals (vdW) functionals vdW-DF [20,24,25] and vdW-DF2 [21], and the PBE-D2 [19] vdW correction scheme.

Table 1. Lattice constants, angle β, and volume, V, for the α-phase for different functionals compared to DFT calculations and experimental results available in the literature.

		Lattice parameters					
Method	XC	a (Å)	b (Å)	c (Å)	Angle β (°)	V (Å^3)	Reference
Exp	-	4.96	9.64	4.62	90	220.9	[29]
DFT	LDA	4.65	8.95	4.58	90.9	190.3	Present
DFT	PBE	5.21	10.00	4.68	90.7	243.7	Present
DFT	vdW-DF	4.99	9.57	4.69	90.6	224.0	Present
DFT	vdW-DF2	4.85	9.39	4.69	90.7	213.6	Present
DFT	PBE-D2	4.80	9.27	4.65	90.8	206.9	Present
DFT	PBE	5.18	10.30	4.70	91	250.7	[16]
DFT	PBE	5.02	9.77	4.67	90	229.0	[13]
DFT	PBE-D2	4.75	9.24	4.64	90	203.7	[13]
DFT	PBE0 hybrid	5.03	9.98	4.65	90.4	233.4	[31]

We tested both ultrasoft (US) pseudopotentials (PSPs) and projector augmented waves (PAW) and found that the results were not significantly dependent on the PSP. Therefore, in the results section we present results using only US PSPs. Only PSPs available from the QE website that were classification verified were used. The kinetic energy cutoffs were 80 Ry and 800 Ry for the wave function and for the charge density, respectively. These high cutoff energies were required to reach a total energy convergence of 1 mRy per atom. The Brillouin zone was sampled using a Monkhorst-Pack mesh of $2\times3\times4$ for the β phase and $3\times2\times4$ for the α and δ phases. In all cases, the self-consistent calculations were considered converged when the estimated energy error was less than 10^{-8} Ry. Cell and ionic relaxations were considered complete when the convergence threshold on the energy was 10^{-4} Ry and when forces less than 10^{-3} a.u. were reached.

The spontaneous polarisation was calculated using the modern theory of polarisation [26,27]. For all polymorphs we used 11 k-points in the dimensional reduced grid and 120 bands, which gave converged results for all cases.

2 Results and discussion

2.1 Crystal structure

2.1.1 α phase

The α-phase is monoclinic with space group $P2_1/c$ [28] and has a $\mathrm{TG^+TG^-}$ chain structure with the dipoles aligned antiparallel resulting in a non-polar centrosymmetric structure. The chains have an antiparallel orientation along the c direction (chain axis), which corresponds to the experimentally determined space group [13,28–30].

The lattice parameters for the α-phase for various functionals are shown alongside previous calculations and experimental values from literature in Table 1. The c lattice parameter is along the chain and the a and b parameters are in the interchain directions. The LDA is seen to underestimate the a and b lattice constants by 6–7% but is in good agreement with the c lattice constant. In contrast, PBE significantly overestimates the a and b lattice constants by 4–5% but again is in reasonable agreement with the c lattice constant, which is in good agreement with previous PBE results [13,16]. The lattice constant in the c direction is determined by the carbon backbone and this length is less sensitive to the functional. However, the polymer chains are

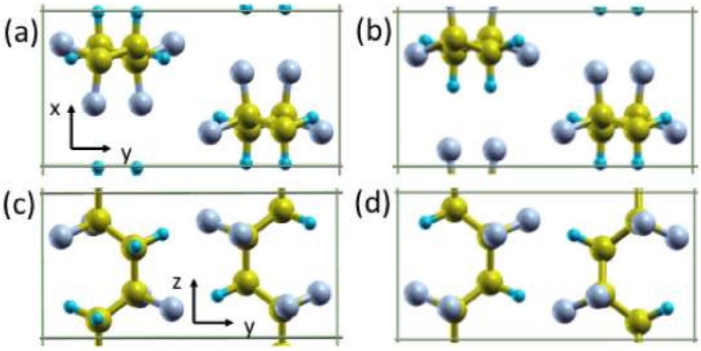

Fig. 1. α-phase in the a) xy-plane and c) yz-plane. δ-phase in the b) xy-plane and d) yz-plane. For an orthorhombic cell xyz directions correspond to abc lattice vectors.

only weakly held together by van der Waals interactions and it is well known that for molecular systems the LDA overbinds, whereas the GGA underbinds.

All calculations with vdW functionals or corrections give lattice constants that are much closer to experimental results. The vdW-DF2 and PBE-D2 calculations underestimate the experimental values by 2–4% for a and b lattice constants. The vdW-DF agrees with the experimental values to within 1% for a and b lattice constants and 1.5% for c. Our results for PBE-D2 are in close agreement to previously published results [13]. The type of pseudopotential used only has a small effect on the lattice constants compared to the effect of the exchange and correlation functional, with PAW giving slightly larger volumes than US. In this space group the α and γ-angles are fixed by symmetry to 90° but the β-angle is not constrained to be 90° [16]. Our results for all functionals show a small deviation from 90°, similar to previous DFT calculations [16,31]. However, this is a small deviation that is within the DFT limits of accuracy.

2.1.2 δ phase

The α-phase can be transformed into the δ-phase by application of a strong electric field [5,6]. The δ-phase is similar to the α-phase except that the dipoles are aligned so that there is a net spontaneous dipole moment, as shown in Fig. 1(b). The crystal structure of δ is orthorhombic with space group $Pna2_1$ (or equivalently $P2_1cn$) [5,6], which corresponds to an antiparallel chain orientation [13]. The lattice parameters for the δ-phase are presented in Table 2. All angles in this space group are equal to 90^o. The lattice parameters of the δ-phase are similar to those of the α-phase. The trends shown by the various functionals are similar to the trends observed for the α-phase.

2.1.3 β phase

The β-PVDF structure is the crystal form with the highest spontaneous polarisation and therefore the most studied structure. The chain has an all-trans structure and the dipoles are in parallel alignment, as shown in Fig. 2.

The lattice constants for the β-phase are shown in Table 3. First, we note that in the interchain directions, LDA overbinds by 7% and 9% for a and b, respectively, and PBE underbinds by 4% and 2% for a and b respectively. Our PBE calculation results in a considerably larger value for $a = 8.95$ Å than the PBE values reported previously,

Table 2. Lattice constants and volume, V, for the δ-phase for different functionals compared to DFT calculations and experimental results available from literature.

		Lattice parameters				
Method	XC	a (Å)	b (Å)	c (Å)	V (Å^3)	Reference
Exp	-	4.96	9.64	4.62	220.9	[5]
DFT	LDA	4.62	8.92	4.58	188.6	Present
DFT	PBE	5.17	10.09	4.69	244.4	Present
DFT	vdW-DF	4.98	9.53	4.70	223.2	Present
DFT	vdW-DF2	4.85	9.32	4.69	211.9	Present
DFT	PBE-D2	4.80	9.21	4.65	205.6	Present
DFT	PBE	5.02	9.71	4.67	227.6	[13]
DFT	PBE-D2	4.79	9.10	4.65	202.7	[13]
DFT	PBE0 hybrid	5.01	10.00	4.65	233.0	[31]

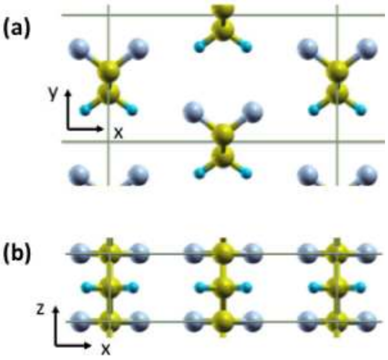

Fig. 2. View of the β-phase in the (a) xy-plane and (b) xz-plane. The xyz directions correspond to abc lattice vectors.

Table 3. Lattice constants for the β-phase from compared to previous DFT calculations and experimental results.

Method	XC	a (Å)	b (Å)	c (Å)	V (Å^3)	Reference
Expt	-	8.58	4.91	2.56	107.8	[28]
DFT	LDA	7.97	4.46	2.54	90.2	Present
DFT	PBE	8.95	5.00	2.59	115.7	Present
DFT	vdW-DF	8.62	4.80	2.60	107.5	Present
DFT	vdW-DF2	8.40	4.66	2.60	101.8	Present
DFT	PBE-D2	8.27	4.55	2.58	97.0	Present
DFT	PBE	8.55	4.83	2.58	106.5	[17]
DFT	PBE	8.69	4.85	2.58	108.7	[13]
DFT	PBE-D2	8.22	4.51	2.58	95.6	[13]
DFT	PBE0 hybrid	8.69	4.89	2.57	109.2	[31]

which gave $a = 8.69$ Å [13] and $a = 8.55$ Å [17]. We attribute this to methodological differences, such as lower plane wave energy cutoffs of ≈ 38 Ry (500 eV) [13] and 30 Ry [17]. We tested this by decreasing the plane wave cutoff from 80 Ry to 40 Ry and this resulted in a decrease in the a lattice parameter from 8.95 Å to 8.57 Å and a decrease in the volume from 115.7 Å^3 to 106.6 Å^3.

The vdW calculations lie between the two extremes of the LDA and GGA. Our results for the PBE-D2 calculations are in close agreement with the previous D2 calculations of Pei et al. [13]. Of the vdW calculations, vdW-DF gives the best overall

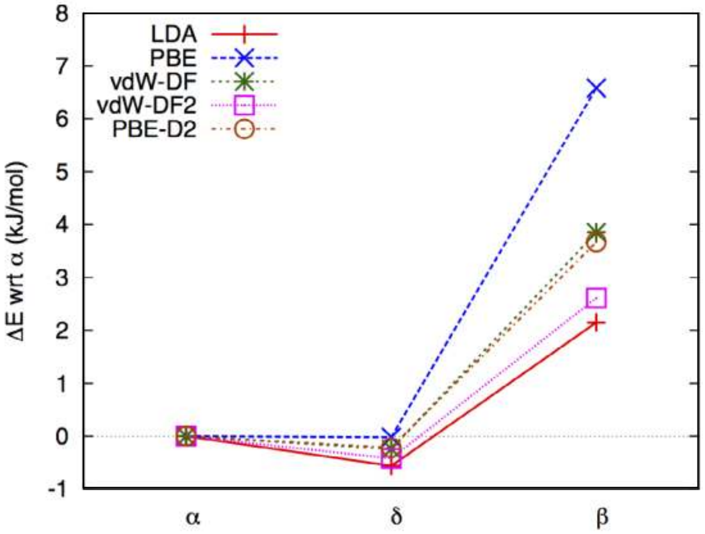

Fig. 3. Energy difference per monomer of PVDF polymorphs relative to α-phase.

agreement with experimental values, with a volume of 107.5 Å^3, compared to the experimental volume of 107.8 Å^3 [28].

2.2 Polymorph energetics

2.2.1 Phase energies

To compare the relative stability of the different polymorphs of PVDF we calculated the energy per monomer using the various functionals. The energy differences relative to the α-phase are presented in Fig. 3.

First we note that all functionals predict the δ-phase to be the lowest energy polymorph, although the energy difference of less than 1 kJ/mol is marginal and within the margin of error for these calculations. The β-phase has the highest energy, ranging from 2 kJ/mol for LDA up to 7 kJ/mol for PBE. Our results agree with previous PBE results [10], which found δ to be marginally stable, and a very small energy range of less than 5 kJ/mol between the polymorphs studied. Another DFT study calculated the energy difference between the α and β-phases and found the α-phase to be 4.4 kJ/mol per monomer (23 meV per carbon atom) lower than the β-phase [11]. Another PBE study found that the α-phase is 2.6 kJ/mol (0.027 eV) per monomer lower in energy than the β-phase [16]. A study using the PBE0 functional found that the α, β, δ-phases differ in energy by less than 3 kJ/mol, with the α-phase being only marginally lower in energy than δ [31]. A study into the possible routes from α to β-phase transformations found the α and δ-phases to be almost equi-energetic, and the β-phase to have a higher energy of 3.4 kJ/mol [32].

2.2.2 Cohesive energies

We expect the inclusion of vdW interactions to have a significant effect on the cohesive energy of the polymorphs. We define the cohesive energy per monomer of the

Table 4. Cohesive energies and energy difference between the TG^+TG^- and all trans chains, denoted ΔE_{chain}. Units are kJ/mol per monomer.

Functional	α	δ	β	ΔE_{chain}	Ref
LDA	−25.5	−26.0	−41.7	−18.3	Present
PBE	−8.1	−8.1	−17.5	−16.0	Present
vdW-DF	−33.7	−34.0	−47.5	−17.6	Present
vdW-DF2	−30.9	−31.3	−46.8	−18.5	Present
PBE-D2	−27.0	−27.2	−41.6	−18.2	Present
PBE	−2.6	−2.8	−17.6	−19.9	[10]
PBE	−15.8	−14.5	−46.3	-	[13]
PBE-D2	−54.0	−54.0	−84.9	-	[13]

polymorphs to be

$$E_{\text{coh}} = \frac{E_{\text{cry}} - N_{\text{chain}} E_{\text{chain}}}{N_{\text{mon}} N_{\text{chain}}}$$

where E_{cry} is the total energy of the crystal, E_{chain} is the total energy of one relaxed chain in vacuum, N_{chain} is the number of chains in the crystal unit cell and N_{mon} is the number monomers per chain.

The isolated chains were relaxed in a box with $a = b = 19$ Å and with the c lattice parameter (backbone direction) allowed to vary. The TG^+TG^- chain is stable for all functionals, with the all-trans chain ranging from $\approx 16 - 19$ kJ/mol per monomer higher in energy than the TG^+TG^- chain. The chain energy differences, shown in Table 4, are similar for all functionals, which is expected since this is due to bonded interactions rather than van der Waals interactions. Su et al. [10] also found the TG^+TG^- chain structure to be stable, with the all-trans chain to be 19.9 kJ/mol per monomer (2.38 kcal/mol per C atom) higher in energy.

The cohesive energies are shown in Table 4. For all functionals the β-phase has the strongest cohesion, in agreement with previous results. It is clear that the PBE functional gives the smallest cohesive energies, which is not surprising as it is known to underbind. The vdW methods result in slightly stronger cohesive energies than the LDA. These three functionals give very similar results, with vdW-DF giving slightly stronger cohesion and PBE-D2 giving weaker cohesion. We note that our cohesive energies for PBE and PBE-D2 are approximately half of the cohesive energies reported by Pei et al. [13]. However, we note that their PBE values are much larger than both our results and the results of Su et al. [10]. There is no experimental data on the cohesive energy for PVDF. However, we can compare our results qualitatively with a similar study on polyethylene [18]. GGAs gave cohesive energies of less than 1 kJ/mol per CH_2, compared to LDA, which gave ≈ 11 kJ/mol per CH_2. vdW-DF gave a result of ≈ 10 kJ/mol/CH_2, which is slightly smaller than the LDA and in good agreement with the experimental value of 7.8 kJ/mol/CH_2 [33].

Polarisation

In this subsection we investigate the polarisation of the polar phases for various XC functionals and vdW corrections. To calculate the polarisation using the Berry phase method it is necessary to construct a non-polar reference structure (see for example the description by Spaldin [34]). For PVDF, the non-polar reference state for the β-phase was constructed by fixing the dimensions of the unit cell and rotating one of the chains by 180° along the chain axis so that there is a zero net dipole moment in the unit cell. A similar approach was taken for the δ-phase. Our results for the

Table 5. Spontaneous polarisation, P (μC cm^{-2}), for the β-phase compared experimental results and previous DFT data.

P (μC cm^{-2})	Method	Reference
7.6	Plasma poling	[35]
10.0	Extrusion	[36]
13.0	VDF oligomers	[37]
18.1	DFT PBE	[38]
17.8	DFT PBE	[9]
17.6	DFT PBE0 hybrid	[31]
26.6	DFT LDA	Present
16.8	DFT PBE	Present
19.8	DFT vdW-DF	Present
22.6	DFT vdW-DF2	Present
22.3	DFT PBE-D2	Present

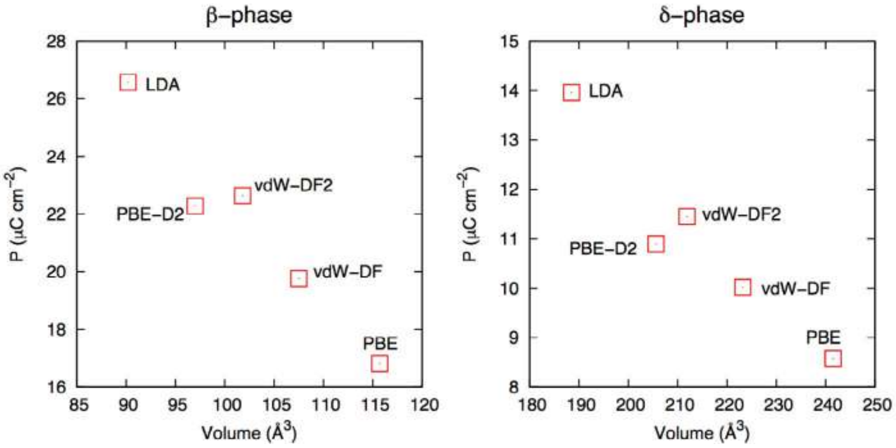

Fig. 4. Variation of polarisation with the volume of the unit cell for β-phase (left) and δ-phase (right).

spontaneous polarisation of the β-phase are shown in Table 5 alongside the results from previous calculations and experiments.

The β-phase has the highest spontaneous polarisation of all the known polymorphs of PVDF. In our DFT calculations the polarisation ranges from a maximum of 26.6 μC cm^{-2} for the LDA to a minimum of 16.8 μC cm^{-2} for PBE. Since the LDA and PBE give the smallest and largest unit cells, respectively, it is expected that their polarisations (dipole moment per unit volume) would be the largest and smallest, assuming that there is no significant change in dipole moment. The spontaneous polarisation is plotted against unit cell volume in Fig. 4. The results from the LDA, PBE, vdW-DF and vdW-DF2 functionals show an approximately linear trend, and the PBE-D2 falls below this trend.

It is well known that the experimentally measured polarisation is lower than the value predicted by DFT calculations. This is normally attributed to the fact that DFT calculations use perfect PVDF crystal structures, whereas, experimentally, PVDF exhibits thermal fluctuations and can be partially amorphous or exist in several polymorphs simultaneously. However, there are many experimental studies focused on improving the crystallinity and purity of the β-phase. For example, Noda et al. [37] formed thin films of VDF oligomers and measured a spontaneous polarisation of 13 μC cm^{-2}. Further work to control the crystallinity may result in experimental measurements of the polarisation to become even closer to the computationally predicted values.

The polarisation of the δ-phase is shown in Fig. 4 as a function of the unit cell volume and ranges from $8.6\,\mu\mathrm{C\,cm^{-2}}$ for PBE to $14.0\,\mu\mathrm{C\,cm^{-2}}$ for LDA. Similar to the β-phase there is a strong correlation between the polarisation and the volume. An experimental value for the polarisation of the δ-phase is 7 μC cm^{-2} [6] (see their Supplementary Information) and a previous DFT result using the PBE0 hybrid functional gave 8.5 μC cm^{-2} [31].

3 Conclusions

Structural properties, energetics and polarisation of three polymorphs of PVDF were studied using DFT calculations with various XC functionals and vdW corrections. The studied polymorphs were the α-phase, its polar analogue the δ-phase and the β-phase. For all phases it was found that vdW interactions were essential in predicting the correct interchain distances and corresponding lattice constants. Of the functionals studied, the vdW-DF functional was found to give the best agreement with experimental lattice constants.

The spontaneous polarisation for the polar phases, β and δ, was calculated for the different functionals. The variation in polarisation with functional/correction is primarily due to the different unit cell volumes and the spontaneous polarisation varies linearly with unit cell volume. The PBE-D2 method predicts a smaller polarisation for the predicted volume than the other functionals.

The relative energetics of the different polymorphs were compared with respect to the α-phase. All functionals predict that the δ-phase is slightly more stable than the α-phase, and that the β-phase is between 2–7 kJ/mol higher than α. However, the vdW corrections have an important effect on the cohesive energies, with the vdW cohesive energies being similar to or stronger than the LDA cohesive energies for all three phases. As expected, PBE predicts much weaker cohesive energies. In all cases the β-phase was found to have the strongest cohesive energies, in agreement with previous studies.

In summary, it is clear that the inclusion of vdW interactions is essential for predicting the lattice structure and energetics of PVDF polymorphs and future studies into phase transformations and new polymorphs should take vdW interactions into account.

This paper is dedicated to Prof. Kurt Kremer on the occasion of his 60th birthday. Francesco Pelizza would like to thank Alan Kennedy for help with space group identification. Results were obtained using the EPSRC funded ARCHIE-WeSt High Performance Computer (`www.archie-west.ac.uk`). EPSRC grant no. EP/K000586/1. Input files for PVDF crystal structures are available from `http://dx.doi.org/10.15129/26e38705-5d3d-47c2-9b15-b2aef53641a2`. Files are embargoed until 31/05/17.

References

1. J.F. Scott, Science **315**, 954 (2007)
2. T. Someya, Y. Kato, T. Sekitani, S. Iba, Y. Noguchi, Y. Murase, H. Kawaguchi, T. Sakurai, PNAS **102**, 12321 (2005)
3. V. Cauda, G. Canavese, S. Stassi, J. Appl. Poly. Sci., 41667 (2015)
4. M. Poulsen, S. Ducharme, IEEE Trans. Dielectr. Electr. Insul. **17**, 1028 (2010)
5. M. Bachmann, W.L. Gordon, S. Weinhold, J.B. Lando, J. Appl. Phys. **51**, 5095 (1980)

6. M. Li, H.J. Wondergem, M.-J. Spijkman, K. Asadi, I. Katsouras, P.W.M. Blom, D.M. de Leeuw, Nat. Mater. **12**, 433 (2013)
7. R. Gregorio Jr., E.M. Ueno, J. Mat. Sci. **34**, 4489 (1999)
8. S.M. Nakhmanson, M.B. Nardelli, J. Bernholc. Phys. Rev. Lett. **92**, 115504 (2004)
9. S.M. Nakhmanson, M.B. Nardelli, J. Bernholc. Phys. Rev. B **72**, 115210 (2005)
10. H. Su, A. Strachan, W.A. Phys. Rev. B **70**, 064101 (2004)
11. V. Ranjan, L. Yu, Phys. Rev. Lett. **99**, 047801 (2007)
12. W. Wang, H. Fan, Y. Ye, Polymer **51**, 3575 (2010)
13. Y. Pei, X.C. Zeng, J. Appl. Phys. **109**, 093514 (2011)
14. J.C. Li, R.Q. Zhang, C.L. Wang, N.B. Wong, Phys. Rev. B **75**, 155408 (2007)
15. N.J. Ramer, C.M. Raynor, K.A. Stiso, Polymer **47**, 424 (2006)
16. N.J. Ramer, T. Marrone, K.A. Stiso, Polymer **47**, 7160 (2006)
17. S.M. Nakhmanson, R. Korlacki, J.T. Johnston, S. Ducharme, Z. Ge, J.M. Takacs, Phys. Rev. B **81**, 174120 (2010)
18. J. Kleis, B.I. Lundqvist, D.C. Langreth, E. Schröder, Phys. Rev. B **76**, 100201(R) (2007)
19. S. Grimme J. Comput. Chem. **27**, 1787 (2006)
20. M. Dion, H. Rydberg, E. Schröder, D.C. Langreth, B.I. Lundqvist, Phys. Rev. Lett. **92**, 246401 (2004)
21. K. Lee, E.D. Murray, L. Kong, B.I. Lundqvist, D.C. Langreth, Phys. Rev. B **82**, 081101(R) (2010)
22. P. Giannozzi, S. Baroni, N. Bonini, et al., J. Phys. Condens. Matter **21**, 395502 (2009)
23. J.P. Perdew, K. Burke, M. Ernzerhof, Phys. Rev. Lett. **77**, 3865 (1996)
24. T. Thonhauser, V.R. Cooper, S. Li, A. Puzder, P. Hyldgaard, D.C. Langreth, Phys. Rev. B **76**, 125112 (2007)
25. R. Sabatini, E. Kucukbenli, B. Kolb, T. Thonhauser, S. de Gironcoli, J. Phys.: Condens. Matter **24**, 424209 (2012)
26. R.D. King-Smith, D. Vanderbilt, Phys. Rev. B **47**, 1651 (1993)
27. R. Resta, Rev. Mod. Phys. **66**, 899 (1994)
28. M. Kobayashi, K. Tashiro, H. Tadokoro, Macromol. **8**, 158 (1974)
29. R. Hasegawa, Y. Takahashi, Y. Chatani, H. Tadokoro, Polymer J. **3**, 600 (1972)
30. Y. Takahashi, H. Tadokoro, Macromol. **16**(12), 1880 (1983)
31. A. Itoh, Y. Takahashi, T. Furukawa, H. Yajima, Polymer J. **46**, 207 (2014)
32. W.J. Kim, M.H. Han, Y.-H. Shin, H. Kim, E.K. Lee, J. Phys. Chem. B (2016)
33. F.W. Billmeyer Jr., J. Appl. Phys. **28**, 1114 (1957)
34. N.A. Spaldin, J. Solid. State. Chem. **195**, 2 (2012)
35. J.E. McKinney, G.T. Davis, M.G. Broadhurst, J. Appl. Phys. **51**, 1676 (1980)
36. K. Nakamura, M. Nagai, T. Kanamoto, Y. Takahashi, T. Furukawa, J. Polymer Science Part B: Polymer Physics **39**(12), 1371 (2001)
37. K. Noda, K. Ishida, A. Kubono, T. Horiuchi, H. Yamada, K. Matsushige, J. Appl. Phys. **93**, 2866 (2003)
38. N.J. Ramer, K.A. Stiso, Polymer **46**, 10431 (2005)

B.1.2 PVDF crystal structure study of γ, ε and ζ crystals using first principle vdW (submitted)

A density functional theory study of PVDF crystalline phases

Francesco Pelizza and Karen Johnston

March 28, 2018

Abstract

The structure and energetics of crystalline phases of PVDF were investigated using density functional theory (DFT). In particular, we present data on non-polar analogues of the β and γ phases that have not yet been experimentally characterised. The results from a variety of exchange and correlation functionals were compared and it was found that van der Waals (vdW) interactions have an important effect on the calculated crystal structures. While the relative phase energies were not strongly dependent on the functional, the cohesive energies were significantly affected.

1 Introduction

Ferroelectric (FE) materials, particularly thin films are widely used in electronic devices as non-volatile memory, capacitors and sensors [1]. The replacement of FE ceramics with FE polymers is desirable as polymers are compatible with a wide range of substrates, are easier to process and have mechanical flexibility. Poly(vinylidene difluoride) (PVDF) is the most promising FE polymer due to its chemical stability, low coercive field, large remnant polarisation and high Curie temperature [2, 3].

PVDF has six main crystal phases and native PVDF samples are typically composed of a mixture of these crystalline phases within amorphous regions. The PVDF crystalline phases, have three different chain structures with parallel or antiparallel chain orientations. If the chains are aligned to give a net dipole moment, then the crystal is polar, and since the direction of the dipole moment can be switched by an electric field the crystal is FE. If the chain dipoles are antiparallel then the crystal

Figure 1: Structures of a) all-trans all-T chain (4 repeat units), b) $TG^{+}TG^{-}$ chain (2 repeat units), c) $T_3G^{+}T_3G^{-}$ chain (1 repeat unit). The black arrow shows the dipole orientation perpendicular to the chain axis.

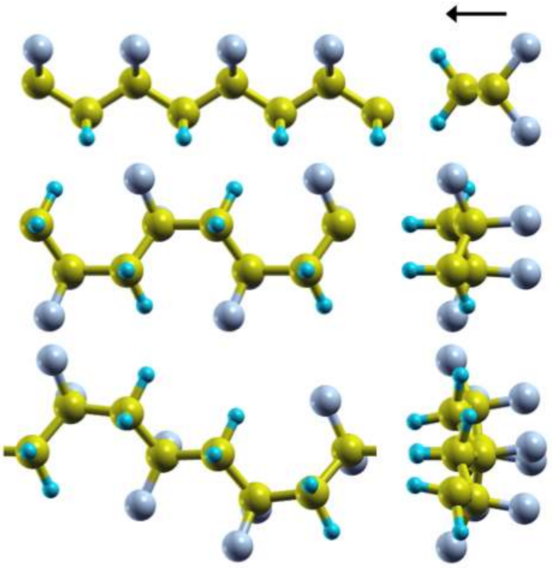

is non-polar and, therefore, non-FE. Figure 1 shows the all-trans (T) backbone, the trans-gauche $TG^{+}TG^{-}$ backbone and the more complex $T_3G^{+}T_3G^{-}$ backbone.

The β phase is the most desirable PVDF phase, as it has the highest spontaneous polarisation of any FE polymer. There is a large body of experimental research focused on finding the optimal processing procedures for the formation of the β phase. However, since multiple phases are often present experimentally, accurate sample characterisation will depend on knowing the properties of all crystal phases. To date the non-polar analogue of the β phase, denoted here by ζ, has not been characterised by either experiment or simulation. In addition, only a few DFT studies have investigated the $T_3G^{+}T_3G^{-}$ polar γ and non-polar ϵ phases. However, the DFT studies for the ϵ phases did not account for van der Waals interactions, which is known to be important for molecular crystals, including polymers [4, 12].

In this paper we present the first calculations of the properties of the non-polar PVDF ζ and ϵ phases using DFT that includes van der Waals (vdW) interactions. In addition, we calculated the γ phases and compare our results for lattice structures, polarisation, relative phase energies, and cohesive energies to previous work on PVDF crystal phases.

2 Method

All calculations were performed using the Quantum Espresso DFT software package (QE versions 5.3 and 5.4) [6] that is implemented using a planewave basis set. The adopted threshold values were 80 Ry for the wavefunction and 800 Ry for the charge density. Several exchange and correlation (XC) functionals were used, including the local density approximation (LDA), the PBE generalised gradient approximation (GGA) [7], the an der Waals (vdW) functionals vdW-DF [5] and vdW-DF2 [8] and the semi-empirical vdW correction scheme DFT-D2 [9]. The Brillouin zone was sampled using a Monkhorst-Pack mesh of $2 \times 3 \times 4$ for the ζ phase, and $3 \times 1 \times 2$ for the γ and ϵ phases. For core electrons we used ultrasoft pseudopotentials available on the QE website [10]. For the PBE, vdW-DF, vdW-DF2 and DFT-D2 XC functionals we used F.pbe-n-rrkjus_Psl.0.1.UPF, C.pbe-n-rrkjus.UPF and H.pbe-n-rrkjus.UPF, and for the LDA functional we used F.pz-van_asa.UPF, C.pz-van_ak.UPF and H.pz-van_ak.UPF.

For structural relaxations of the γ and ϵ phases, the thresholds were set to be 10^{-4} a.u. (atomic units) for the atomic forces and 10^{-5} Ry for the total energy. The self-consistency convergence threshold was 10^{-8} a.u. The ζ phase characterisation was performed with both force and total energy thresholds increased up to one order of magnitude in respect to what was used for the γ and ϵ phases.

Space groups were determined using the FINDSYM code [11]. The spontaneous polarisation was calculated using Berry phase method implemented in Quantum Espresso. The Berry phase calculations used 11 k-points with 120 bands along the direction of the polarisation.

3 Results and Discussion

3.1 Structure of ζ-phase

The main difference between the β and ζ phases, is that in the β phase the chain dipole moments are parallel, whereas the ζ phase the chain dipole moments are antiparallel resulting in a non-polar phase. The initial structure for the ζ phase was obtained from the β phase by reflecting one of the chains in the y-direction (defined as the direction of the chain dipole moment) and relaxing the system. Upon relaxation of the ζ phase the two chains become coplanar in the xz plane, as shown in Figure 2. The ζ phase has orthorhombic spacegroup *Pmma* (number 51) and the lattice parameters for the ζ-phase are presented in Table 1. Experimental characterisation for the ζ phase is not available.

Figure 2: Unit cell of the PVDF ζ-phase, showing that the chains have become coplanar in the xy-plane.

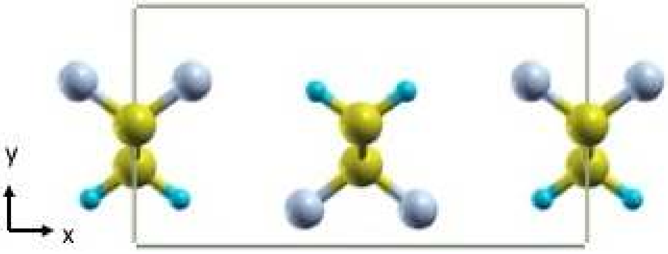

Table 1: Lattice constants for the ζ-phase using different exchange and correlation functionals.

a (Å)	b (Å)	c (Å)	V (Å^3)	Method
7.96	4.45	2.54	89.9	LDA
8.99	5.00	2.59	116.2	PBE
8.65	4.77	2.60	107.1	vdW-DF
8.42	4.64	2.60	101.5	vdW-DF2
8.26	4.56	2.58	97.0	DFT-D2

Despite the structural differences between the β and ζ phases, the ζ lattice parameters are very similar to the β-phase lattice parameters [12]. As observed in this previous study of PVDF, the XC functional has a significant effect, with LDA predicting the smallest volume and PBE predicting the largest volume.

The only other simulation study that considered a non-polar all-trans phase was the DFT PBEsol [13] phase transition study by Kim *et al* [14]. Their structure, denoted $\beta(I_a)$, was proposed as a transition state from the non-polar α phase to the polar δ phase. However, this transition state differs from our proposed ζ structure. In their $\beta(I_a)$ phase the chains were not aligned but were positioned similar to the β phase. They did note that this structure was unstable, and perhaps due to constraints imposed by the NEB method, they did not observe a relaxation to a coplanar structure.

3.2 Structure of γ- and ϵ-phases

The γ and ϵ phases have a $T_3G^+T_3G^-$ backbone structure, and are shown in Fig. 3. The γ-phase has parallel chain dipole moments, making it FE, whereas the ϵ-phase has antiparallel chain dipoles and is non-polar. There are two further variations in the crystal structures, so that the γ and ϵ phases can each be represented by two very similar crystal structures. Fig. 3 shows how the two variants of the same PVDF crystal phase differ from each other by a 180° rotation in the xz-plane of one of the chains with respect to the other. The distinction between these two variants within the same crystal phase is made from now on with the annotation uu (up-up) for parallel chains and ud (up-down) for anti-parallel chains. The γ and ϵ phases are thus sub-distinguished as γ_{uu}, γ_{ud}, ϵ_{uu} and ϵ_{ud} as shown in Fig. 3.

Figure 3: Assembly of crystal structures of PVDF phases γ_{uu}, γ_{ud} ϵ_{uu} and ϵ_{ud}. Top panels show the view in the xy plane where the dipole moment is in the y direction and the bottom panels show along the chain in the xz plane, highlighting the difference in up-up and up-down structures.

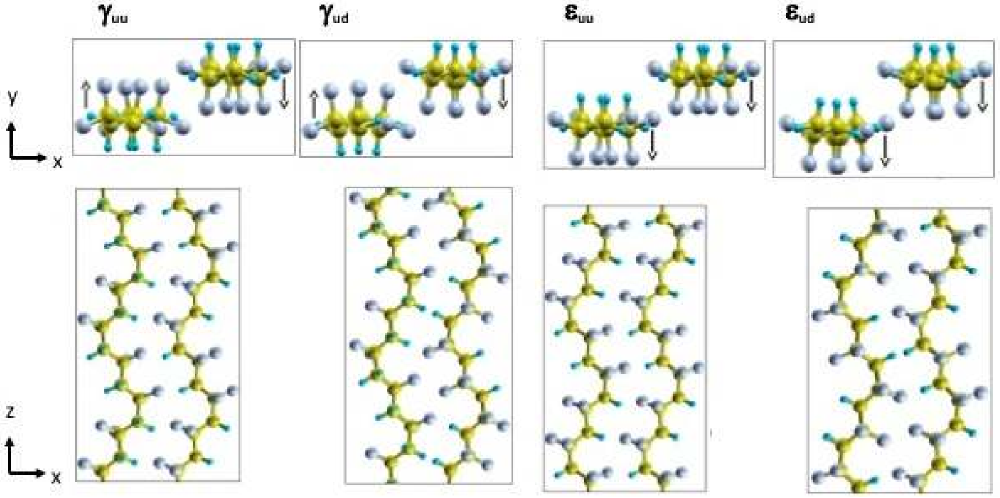

We constructed the different crystal structures by applying symmetry operations to a $T_3G^+T_3G^-$ chain in an orthorhombic cell. γ_{uu} was obtained by translation of the chain by ($\frac{1}{2}$,$\frac{1}{2}$,0) to give a structure with space group Cc (number 9). γ_{ud} was obtained by rotating the chain around the y-axis followed by the above translation to get space group $Pna2_1$ (number 33). To obtain the $\epsilon_{\rm uu}$ structure, we rotated the chain by 180°around the chain axis (z-axis) followed by the above translation to give space group $Pca2_1$ (number 29). Finally, to get $\epsilon_{\rm ud}$, the chain was rotated around the z-axis, then rotated around the y-axis, and finally translated to obtain a structure with space group $P2_1/c$ (number 14). Our starting structures have the same space groups as those reported by Karasawa *et al* [15]. Pei *et al* [16] agreed with all $T_3G^+T_3G^-$crystal structures, except for $\epsilon_{\rm ud}$, where they reported a space group of $P2_{c_1}/c$. We were unable to identify this space group and we surmise that this may be a typo, and should refer to $P2_1/c$.

The lattice parameters for all γ- and ϵ-phases are shown in Table 2. In all cases, the LDA functional gives the smallest lattice parameters and volumes and the PBE functional gives the largest lattice parameters for interchain directions and volumes. For all phases, our calculations using PBE give larger a and b lattice parameters, and a larger unit cell volume compared the PBE results of Pei *et al* [16]. We attribute this difference to methodological differences since Pei *et al* used a lower wavefunction cutoff ($\approx$ 38 − 40 Ry) than this study (80 Ry) and we note that a similar effect was previously observed for the α and δ-phases [12]. The vdW-DF, vdW-DF2 and DFT-D2 functionals give lattice parameters in between those of the LDA and PBE functionals. This is the expected trend and is similar to the results for the ζ-phase and also for previous results for the β, α and δ-phases [12].

Experimentally, the γ-phase was first predicted to have an orthorhombic structure with space group $C2_{\rm cm}$ [17] and experimental samples contained both up-up (parallel) and up-down (antiparallel) chain packing. However, later studies showed that the structure is monoclinic [18, 19]. The calculated structures of $\gamma_{\rm uu}$ and $\gamma_{\rm ud}$ phases both have monoclinic structures in agreement with experiment. The β angle of the $\gamma_{\rm uu}$ structures is in good agreement with experiment at a few degrees over 90°. The $\gamma_{\rm ud}$ phase has the β angle at around 90° indicating that experimentalists observed $\gamma_{\rm uu}$.

The $\epsilon_{\rm uu}$ phase is orthorhombic with a negligible deviation of the β angle from 90° for some functionals, while the $\epsilon_{\rm ud}$ phase is monoclinic with negligible deviations of the α and γ angles from 90°. There are no experimental measurements of the structure of ϵ-phase, other than a report of its existence [20]. We know of only two studies of the ϵ phase, a DFT study by Pei *et al* [16] and a classical force field study by Karasawa and Goddard [15]. Although we agree with the space groups, we disagree with the crystal structure for $\epsilon_{\rm ud}$. Both the previous studies give an angle of $\beta \approx 120°$, whereas our structure is close to orthorhombic with all angles $\approx 90°$. We did attempt to create a structure with $\beta = 120°$ by modifying our $\epsilon_{\rm ud}$ structure, but we were unable to obtain a stable structure. However, we note that our results are in line with the structures of the other $T_3G^+T_3G^-$ phases.

Table 2: Lattice parameters a, b and c, unit cell volume, V, and angles α, β and γ for the $\gamma_{\rm uu}$, $\gamma_{\rm ud}$, $\epsilon_{\rm uu}$ and $\epsilon_{\rm ud}$ phases.

Phase	a (Å)	b (Å)	c (Å)	V (Å^3)	α (°)	β (°)	γ (°)	Method
γ	9.66	4.97	9.18	440.7	90.0	90.0	90.0	Expt. [17]
	9.58	4.96	9.23	437.5	90.0	92.9	90.0	Expt. [18]
	9.67	4.96	9.20	440.1	90.0	93	90.0	Expt. [19]
$\gamma_{\rm uu}$	9.09	4.59	9.09	379.1	90.0	93.0	90.0	LDA
	10.18	5.18	9.29	489.0	90.0	92.7	90.0	PBE
	9.71	4.95	9.34	447.7	90.0	94.4	90.0	vdW-DF
	9.41	4.85	9.33	424.8	90.0	94.5	90.0	vdW-DF2
	9.38	4.78	9.24	414.2	90.0	93.3	90.0	DFT-D2
	9.69	5.00	9.34	452.5	90.0	91.5	90.0	PBE [16]
	9.26	4.76	9.25	407.7	90.0	93.1	90.0	DFT-D2 [16]
	9.53	5.02	9.14	436.1	90.0	93.0	90.0	MSXX [15]
$\gamma_{\rm ud}$	8.79	4.81	9.22	389.7	90.0	90.0	90.0	LDA
	10.78	5.29	9.39	534.6	90.0	91.7	90.0	PBE
	9.38	5.16	9.46	457.0	90.0	90.0	90.0	vdW-DF
	9.12	5.04	9.45	434.3	90.0	89.8	90.0	vdW-DF2
	9.09	4.96	9.33	420.2	90.0	89.9	90.0	DFT-D2
	9.75	5.17	9.39	463.5	90.0	90.0	90.0	PBE [16]
	9.27	5.24	9.28	450.8	90.0	90.0	90.0	MSXX [15]
$\epsilon_{\rm uu}$	9.16	4.61	9.08	383.1	90.2	90.0	90.0	LDA
	10.09	5.18	9.30	486.2	90.1	90.0	90.0	PBE
	9.79	4.95	9.32	451.8	90.0	90.0	90.0	vdW-DF
	9.55	4.83	9.32	429.5	90.1	89.9	90.0	vdW-DF2
	9.52	4.75	9.23	417.6	90.1	90.0	90.0	DFT-D2
	9.78	5.08	9.33	463.5	90.0	90.0	90.0	PBE [16]
	9.68	4.98	9.13	440.1	90.0	90.0	90.0	MSXX [15]
$\epsilon_{\rm ud}$	8.87	4.84	9.17	393.8	90.0	93.0	90.1	LDA
	10.71	5.38	9.34	538.5	90.1	95.2	90.0	PBE
	9.46	5.18	9.41	460.4	90.0	93.0	90.0	vdW-DF
	9.18	5.07	9.41	438.0	90.0	93.3	90.0	vdW-DF2
	9.21	4.95	9.30	424.2	90.2	91.2	90.1	DFT-D2
	9.68	6.17	9.38	560.2	90.0	121.9	89.9	PBE [16]
	9.26	6.04	9.01	-	90.0	120.0	90.0	MSXX [15]

Polarisation of the γ phase

The modern theory of the polarisation was used to determine the spontaneous polarisation of the γ phases. To do this, it is necessary to have reference crystal structures to investigate. The first reference is a centrosymmetric crystal, therefore non-polar, and the second reference is a crystal with all atoms rotated by 180° around the chain axis. In this study we have reported the polarisation in the direction perpendicular to the chains.

The results for the spontaneous polarisation of γ_{uu} and γ_{ud} phases are shown in Table 3. For both γ_{uu} and γ_{ud} phases the same spontaneous polarisation prediction trend of different functionals was observed. The highest spontaneous polarisation values were reached with the LDA functional. The vdW-DF and PBE XC functionals predicted the spontaneous polarisation being within the mid range of values reached within this characterisation. The vdW-DF2 and DFT-D2 functionals saw the spontaneous polarisation being towards the bottom range of predicted values.

γ_{uu}	γ_{ud}	Method
13.2	16.0	LDA
8.2	9.1	PBE
8.4	10.7	vdW-DF
6.9	5.8	vdW-DF2
7.8	7.0	DFT-D2
7.1	-	PBE0 [21]
0.2-0.3		Expt. [22]

Table 3: Spontaneous polarisation (μC cm^{-2}) of γ_{uu} and γ_{ud} phases.

Itoh *et al* [21] used the PBE0 XC functional and showed the spontaneous polarisation of the the γ phase being 7.1 μC cm^{-2} for a Cc space group, which is in line with our results. An experimental study by Zhao *et al* on PVDF thin films found a very small polarisation of 0.2-0.3 μC cm^{-2} for the γ phase (see Fig. 5c in their paper). It is typical that experimental measurements have a much smaller polarisation due to disorder in the sample.

3.3 Phase and Cohesive Energies

The total energy per monomer of the ζ, γ and ϵ PVDF phases relative to the stable α phase were calculated for different functionals, and are reported in Table 4. The energetic ordering of the crystal phases depends on the XC functional. For example, LDA predicts that the γ_{ud} and ϵ_{ud} are higher in energy than ζ but PBE predicts that ζ has the highest energy. All vdW functionals predict that γ_{ud} and ϵ_{ud} are highest in energy, followed by ζ, followed by ϵ_{uu} and then γ_{uu}. However, we note that the energy differences here are very small and are within the DFT error.

ζ	γ_{uu}	γ_{ud}	ϵ_{uu}	ϵ_{ud}	Method
4.93	0.54	10.26	4.63	10.14	LDA
6.76	0.97	4.55	1.14	4.63	PBE
3.95	0.23	5.99	0.92	6.03	vdW-DF
2.67	0.25	7.18	1.20	7.20	vdW-DF2
3.38	0.77	5.54	1.25	5.39	DFT-D2
6.75	-	-	-	-	PBEsol [14]
-	0.67	-	1.76	-	PBE [23]
-	0.2	-	-	-	PBE [21]
-	-2.30	4.39	-1.63	1.46	MSXX [15]

Table 4: PVDF phase energies in kJ/mol per monomer relative to the α phase.

The ζ phase has not previously been calculated but we can compare its relative phase energy to a non-polar all-trans structure, calculated by Kim *et al* [14]. They obtained an relative phase energy of 70 meV (6.75 kJ/mol) per monomer. While the phase energy is in good agreement with our PBE value, we note that their structure differs as it did not come from a structural relaxation, but rather from an intermediate transition state (image 5 in their paper) in a nudged elastic band calculation. The ζ phase energies are also very similar to previously reported β phase energies for all functionals [12].

There are two studies that have calculated the phase energy of the γ phase. Itoh *et al* calculated the phase energy per monomer for γ_{uu} to be 0.2 kJ/mol. Su *et al* calculated the relative phase energy for γ_{uu} as 0.08 kcal/mol per carbon atom (equivalent to 0.67 kJ/mol per monomer) and the relative phase energy for ϵ_{uu} as 0.21 kcal/mol per carbon atom (equivalent to 1.76 kJ/mol per monomer). Our PBE results are slightly higher for γ_{uu} and slightly lower for ϵ_{uu}, but again we note these energy differences are very small and overall our results are in good agreement with literature. Based on present and previously published results [12], all phase energies per monomer vary within a range of less than 10 kJ/mol for all XC functionals. This narrow energy range at least partially explains why multiple phases are found within PVDF samples.

Cohesive energies were calculated to understand further the effect of vdW dispersion forces. The isolated, infinite chains were relaxed in a box with $a = b = 19$ Å and with the c lattice parameter (backbone direction) allowed to vary. The cohesive energy per monomer, E_{coh}, of ζ, γ and ϵ phases are defined as:

$$E_{\mathrm{coh}} = \frac{E_{\mathrm{crys}} - N_{\mathrm{chain}} E_{\mathrm{chain}}}{N_{\mathrm{chain}} M_{\mathrm{chain}}} \tag{1}$$

where E_{crys} is the lattice of the crystal, E_{chain} is the total energy of one isolated chain in vacuum, N_{chain} is the number of chains in the crystal unit cell, and M_{chain} is the number of monomers in a chain.

The difference between the $T_3G^+T_3G^-$ and all-T chain energies, $\Delta E_{\mathrm{chain}}$, for the different functionals are shown in Table 5. $\Delta E_{\mathrm{chain}}$ is similar for all functionals, although slightly lower for LDA and DFT-D2, which is expected since the differences depend on intrachain properties rather than interchain, so vdW would not play a strong role. These values are in line with previous calculation of -1.41 kcal per C atom (-11.8 kJ/molper monomer) by Su *et al* [23].

Table 5: Cohesive energies of the different phases in kJ/mol per monomer. $\Delta E_{\mathrm{chain}}$ energy (kJ/mol per monomer) is the energy of the $T_3G^+T_3G^-$ chain relative to the all-T chain.

ζ	γ_{uu}	γ_{ud}	ϵ_{uu}	ϵ_{ud}	$\Delta E_{\mathrm{chain}}$	Method
-41.8	-32.8	-23.1	-28.7	-23.2	-13.4	LDA
-17.4	-10.5	-6.9	-10.3	-6.8	-12.6	PBE
-47.4	-38.5	-32.8	-37.8	-32.7	-12.6	vdW-DF
-46.7	-36.5	-29.5	-35.5	-29.5	-12.7	vdW-DF2
-41.7	-30.2	-25.4	-29.7	-25.6	-14.2	DFT-D2
-	-10.0	-	-8.6	-	-11.8	PBE [23]
-	-18.1	-	-	-	-	PBE [16]
-	-59.8	-	-	-	-	DFT-D2 [16]

The cohesive energies calculated using the various XC functionals are shown in Table 5. E_{coh} were weakest for PBE, while vdW-DF and vdW-DF2 gave the strongest cohesive energies. LDA gave very similar results to DFT-D2. Our PBE results for γ_{uu} and γ_{ud} are similar to the PBE results calculated by Su *et al* and slightly lower than the PBE result of -18.1 kJ/mol for γ_{uu} by Pei *et al* [16].

The cohesive energies for the ζ phase are very similar to previous results for the β phase [12] and these two all-T phases have the strongest cohesive energies of all the phases. We observe that both TG^+TG^- structures reported previously have very similar energies. For the $T_3G^+T_3G^-$ phases we note that the two up-up structures have similar energies, and the two up-down structures have similar cohesive energies, but that γ_{ud} and ϵ_{ud} have higher cohesive energies than their γ_{uu} and ϵ_{uu} counterparts. Since the up-down phases have larger interchain lattice parameters, particularly the a lattice parameter, this results in weaker interchain interactions and hence lower cohesive energies.

4 Conclusions

The properties of several PVDF phases have been determined using density functional theory with a variety of XC functionals. The choice of functional significantly influenced the lattice parameters, particularly in the interchain crystal directions, and the cohesive energies. For the γ phase the vdW functionals resulted in lattice parameters that agreed well with experimental values. In all phases studied, the PBE functional was found to significantly overestimate the interchain lattice parameters.

We predicted the structure for the non-polar all-trans ζ phase and found it to have a *Pmma* space group with the chains being coplanar in direction of the chain dipole moments. For the $T_3G^+T_3G^-$ phases we determined the space groups of our structures, in agreement with previous literature. However, for ϵ_{ud} we report a monoclinic angle just over 90°, compared to the 120° angle predicted by previous studies [15, 16].

The energetic ordering of the phases was strongly dependent on the XC functional. PBE predicted that the ζ phase had a higher energy than all $T_3G^+T_3G^-$ phases, whereas all other functionals found that γ_{ud} and ϵ_{ud} had the highest energies. All functionals found that the up-down variants of the γ and ϵ phases have higher energy than the up-up structures. This is mainly due to the low cohesive energy of these structures, which have larger interchain lattice parameters.

In conclusion, we investigated the experimentally uncharacterised ϵ and ζ phases using DFT. This will provide information that will aid future experimental characterisation of mixed PVDF samples.

Acknowledgements

Results were obtained using the EPSRC funded ARCHIE-WeSt High Performance Computer (www.archie-west.ac.uk) EPSRC grant number EP/K000586/1. FP would like to thank Prof. Alan Kennedy for useful discussions on crystallography.

References

[1] N. Setter, D. Damjanovic, L. Eng, G. Fox, S. Gevorgian, S. Hong, A. Kingon, H. Kohlstedt, N. Y. Park, G. B. Stephenson, I. Stolitchnov, A. K. Tagantsev, D. V. Taylor, T. Yamada, and S. Streiffer. Ferroelectric thin fils: Review of materials, properties, and applications. *J. Appl. Phys.*, 100:051606, 2006.

[2] Matthew Poulsen and Stephen Ducharme. Why Ferroelectric Polyvinylidene Fluoride is Special. *IEEE Transactions on Dielectrics and Electrical Insulation*, 17:1028–1035, 2010.

[3] R. Korlacki, J. Travis Johnston, Jihee Kim, Stephen Ducharme, Daniel W. Thompson, V. M. Fridkin, Zhongxin Ge, and James M. Takacs. Oligo(vinylidene fluoride) Langmuir-Blodgett films studied by spectroscopic ellipsometry and the density functional theory. *J. Chem. Phys.*, 129:064704, 2008.

[4] J. Kleis, B. I. Lundqvist, D. C. Langreth, and E. Schröder. Towards a working density-functional theory for polymers: First-principles determination of the polyethylene crystal structure. *Phys. Rev. B*, 76:100201(R), 2007.

[5] M. Dion, H. Rydberg, E. Schroeder, D. C. Langreth, and B. I. Lundqvist. Van der waals density functional for general geometries. *Phys. Rev. Lett.*, 92(24):246401, 2004.

[6] Paolo Giannozzi, Stefano Baroni, Nicola Bonini, Matteo Calandra, Roberto Car, Carlo Cavazzoni, Davide Ceresoli, Guido L. Chiarotti, Matteo Cococcioni, Ismaila Dabo, Andrea Dal Corso, Stefano de Gironcoli, Stefano Fabris, Guido Fratesi, Ralph Gebauer, Uwe Gerstmann, Christos Gougoussis, Anton Kokalj, Michele Lazzeri, Layla Martin-Samos, Nicola Marzari, Francesco Mauri, Riccardo Mazzarello, Stefano Paolini, Alfredo Pasquarello, Lorenzo Paulatto, Carlo Sbraccia, Sandro Scandolo, Gabriele Sclauzero, Ari P. Seitsonen, Alexander Smogunov, Paolo Umari, and Renata M. Wentzcovitch. QUANTUM ESPRESSO: a modular and open-source software project for quantum simulations of materials. *J. Phys.: Condens. Matter*, 21(39):395502, 2009.

[7] J.P. Perdew, Burke, Kieron, and Matthias Ernzerhof. Generalized gradient approximation made simple. *Phys. Rev. Lett.*, 77:3865–3868, Oct 1996.

[8] Kyuho Lee, Eamonn D. Murray, Lingzhu Kong, Bengt I. Lundqvist, and David C. Langreth. Higher-accuracy van der Waals density functional. *Phys. Rev. B*, 82:081101(R), 2010.

[9] S. Grimme. Semiempirical GGA-type density functional constructed with a long-range dispersion correction. *Journal of Computational Chemistry*, 27:1787, 2006.

[10] Quantum espresso website.

[11] H. T. Stokes and D. M. Hatch. FINDSYM: Program for Identifying the Space Group Symmetry of a Crystal. *J. Appl. Cryst.*, 38:237, 2005.

[12] F. Pelizza, B.R. Smith, and K. Johnston. A van der waals density functional theory study of poly(vinylidene difluoride) crystalline phases. *The European Physical Journal Special Topics*, 225:1733, 2016.

[13] J. P. Perdew, A. Ruzsinzky, G. I. Csonka, O. A. Vydrov, G. E. Scuseria, L. A. Constantin, X. Zhou, and K. Burke. Restoring the Density-Gradient Expansion for Exchange in Solids and Surfaces. *Phys. Rev. Lett.*, 100:136406, 2008.

[14] Won June Kim, Myung Hoon Han, Young-Han Shin, Hyungjun Kim, and Eok Kyun Lee. First-Principles Study of the $\alpha - \beta$ Phase Transition of Ferroelectric Poly(vinylidiene difluoride): Observation of Multiple Transition Pathways. *J. Phys. Chem. B*, 120(12):3240–3249, 2016.

[15] Naoki Karasawa and William A. Goddard III. Force Fields, Structures and Properties of Poly(vinylidene fluoride) Crystals. *Macromolecules*, 25:7268, 1992.

[16] Y. Pei and X. C. Zeng. Elastic properties of poly(vinyldene fluoride) (PVDF) crystals: A density functional theory study. *Journal of Applied Physics*, 109:093514, 2011.

[17] S. Weinhold, M.H. Litt, and J.B. Lando. The crystal structure of the γ-phase of the poly(vinylidene fluoride). *Macromolecules*, 13:1178, 1980.

[18] Yasuhiro Takahashi, Masaki Kohyama, Yoshiaki Matsubara, Hisashi Iwane, and Hiroyuki Tadokoro. Tilting Phenomena in Forms II and III of Poly(vinylidene fluoride): Evidence for Monoclinic Structures. *Macromolecules*, 14:1841–1842, 1981.

[19] A.J. Lovinger. Unit cell of the phase of poly(vinylidene fluoride). *Macromolecules*, 14(2):322–325, 1981.

[20] A. J. Lovinger. Annealing of Poly(viny1idene fluoride) and Formation of a Fifth Phase. *Macromol.*, 15:40–44, 1982.

[21] Akira Itoh, Yoshiyuki Takahashi, Takeo Furukawa, and Hirofumi Yajima. Solid-state calculations of poly(vinylidene fluoride) using the hybrid DFT method:spontaneous polarization of polymorphs. *Polymer Journal*, 46:207–211, 2014.

[22] Yuetao Zhao, Wenyao Yang, Yujiu Zhou, Yan Chen, Xin Cao, Yajie Yang, Jianhua Xu, and Yadong Jiang. Effect of crystalline phase on the dielectric and energy storage properties of poly(vinylidene fluoride). *J. Mater Sci: Mater Electron*, 27:7280–7286, 2016.

[23] Haibin Su, Alejandro Strachan, and William A. Goddard III. Density functional theory and molecular dynamics sturies of the energetics and kinetics of electroactive polymers: PVDF and P(VDF-TrFE). *Phys. Rev. B*, 70:064101, 2004.

B.1.3 Vibrational frequencies of PVDF polymorphs (future publication)

The last part of chapter 4 will represent a third paper to be published about DFT results showing the vibrational frequencies of each PVDF crystal structure completing the circle of publications about the DFT results gathered along the present study.

B.2 Publication of chapter 5 (future publication)

Chapter 5 will become a standing paper to show benchmarks of MSXX-noX, B&S and OPLS FFs in crystal and cohesive energies prediction of PVDF crystal structures and the compatibility of the FFs used in performing a liquid phase equilibration of PVDF bulk model reporting that the B&S FF resulted to be the best FF for equilibrating PVDF systems.

B.3 Publication of chapter 6 (future publication)

Chapter 6 will become a standing paper showing the outcomes of MD simulations using the B&S FF about the liquid phase properties of PVDF models in bulk compared to graphene surface models studied to show that electrostatics is the driving force which shapes PVDF chains to form ordered backbones of the ferroelectric β-phase.